

UC Santa Cruz

UC Santa Cruz Electronic Theses and Dissertations

Title

Synthesis, Characterization, and Ultrafast Dynamics of Metal, Metal Oxide, and Semiconductor Nanomaterials

Permalink

<https://escholarship.org/uc/item/959757bk>

Author

Wheeler, Damon Andreas

Publication Date

2013

Peer reviewed|Thesis/dissertation

UNIVERSITY OF CALIFORNIA
SANTA CRUZ

**SYNTHESIS, CHARACTERIZATION, AND ULTRAFAST DYNAMICS OF
METAL, METAL OXIDE, AND SEMICONDUCTOR NANOMATERIALS**

A dissertation submitted in partial satisfaction
of the requirements for the degree of

DOCTOR OF PHILOSOPHY

in

CHEMISTRY

by

Damon A. Wheeler

June 2013

The Dissertation of Damon A. Wheeler
is approved:

Professor Jin Z. Zhang, Chair

Professor Shaowei Chen

Assistant Professor Yat Li

Tyrus Miller
Vice Provost and Dean of Graduate Studies

Copyright © by
Damon A. Wheeler
2013

TABLE OF CONTENTS

LIST OF FIGURES.....	xii
ABSTRACT.....	xviii
DEDICATION.....	xx
ACKNOWLEDGEMENTS.....	xxi
CHAPTER 1: SURFACE ENHANCED RAMAN SCATTERING.....	1
1.1 Abstract.....	1
1.2 Introduction.....	1
1.3 Background.....	2
1.3.1 Raman Scattering.....	2
1.3.2 SERS: History and Nomenclature.....	6
1.4 Surface Plasmons.....	7
1.5 SERS Enhancement Mechanisms.....	13
1.5.1 Electromagnetic and Chemical Enhancement Mechanisms.....	13
1.6 Nanoengineered Substrates.....	18
1.6.1 Core/Shell Structures.....	19
1.6.2 Nanoengineered Dimers and Trimers.....	23
1.6.3 Nanolithography.....	27
1.7 Current Applications.....	28
1.8 Recent Advances.....	34
1.8.1 Single Molecule SERS.....	34

1.8.2	Union of Ultrafast Spectroscopy and SERS.....	37
1.8.3	UV SERS.....	41
1.9	Conclusion.....	42
1.10	References.....	42
CHAPTER 2. Optical Properties and Persistent Spectral Hole Burning of Near Infrared-Absorbing Hollow Gold Nanospheres.....		
53		
2.1	Abstract.....	53
2.2	Introduction.....	54
2.3	Methods and Materials.....	57
2.3.1	HGN Synthesis.....	57
2.3.2	Spectral Hole Burning.....	58
2.3.3	UV-Vis and Electron Microscopy Measurements.....	59
2.3.4	Theoretical Calculations.....	59
2.4	Results.....	60
2.4.1	UV-Vis Spectra.....	60
2.4.2	TEM.....	63
2.4.3	Persistent Spectral Hole Burning.....	66
2.4.4	Calculation of Extinction Efficiencies and Electric $ E ^2$ Fields.....	76
2.5	Discussion.....	80
2.5.1	Theoretical Calculations of Extinction Spectra of HGNS.....	80
2.5.2	Mechanism of Femtosecond Hole Burning.....	86
2.6	Conclusion.....	89

2.7 References.....	90
CHAPTER 3. Optical Properties and Coherent Vibrational Oscillations of Gold Nanostars.....	95
3.1 Abstract.....	95
3.2 Introduction.....	95
3.3 Methods and Materials.....	97
3.3.1 Synthesis of AuNP Seeds.....	97
3.3.2 Synthesis of AuNS.....	97
3.3.3 UV-Vis and Electron Microscopy (EM).....	97
3.3.4 Femtosecond Transient Absorption System.....	98
3.4 Results.....	100
3.4.1 UV-Vis Spectra and Persistent Spectral Hole Burning.....	100
3.4.2 SEM and TEM.....	105
3.4.3 Ultrafast Pump-Probe Transient Absorption.....	108
3.4.4 Theoretical Modeling and Calculation of Periodic Oscillations.....	115
3.5 Discussion.....	115
3.5.1 Experimental and Calculated Oscillations.....	115
3.5.2 Persistent Spectral Hole Burning.....	117
3.6 Conclusion.....	120
3.7 References.....	120
CHAPTER 4. Nanostructured Hematite: Synthesis, Characterization, Charge Carrier Dynamics, and Photoelectrochemical Properties.....	125

4.1 Abstract.....	125
4.2 Introduction.....	125
4.3 Synthesis.....	129
4.3.1 Solution-phase Synthetic Methods.....	129
4.3.2 Vapor-phase Deposition Methods.....	133
4.3.3 Thermal Oxidation and Thermal Pyrolysis.....	138
4.3.4 Electrochemical Methods.....	142
4.4 Structural and Morphological Properties.....	145
4.5 Optical and Electronic Properties.....	153
4.5.1 Optical Absorption in near UV to near IR.....	153
4.5.2 Size and Shape Effect on Optical Transition.....	157
4.5.3 Photoluminescence.....	159
4.5.4 XPS and EXAFS.....	163
4.5.5 Theoretical Studies of Electronic Band Structure.....	164
4.6 Charge Carrier Dynamics in Hematite.....	165
4.6.1 Background on Time-resolved Studies of Nanostructures.....	165
4.6.2 Carrier Dynamics of Hematite Nanostructures.....	167
4.6.3 Dependence of Dynamics on Crystal Structure and Surface.....	167
4.6.4 Size Dependence.....	171
4.6.5 Nanoparticle Shape Dependence.....	171
4.6.6 Effect of Crystallinity.....	172
4.6.7 Effect of Doping.....	173

4.6.8	Charge Carrier Kinetics of α -Fe ₂ O ₃ for Water Oxidation.....	188
4.7	Photoelectrochemistry of Fe ₂ O ₃	190
4.8	Conclusion.....	208
4.9	References.....	208
CHAPTER 5. Ultrafast Charge Carrier Dynamics and Photoelectrochemical		
Properties of Hydrogen-Treated TiO₂ Nanowire Arrays.....		
5.1	Abstract.....	239
5.2	Introduction.....	239
5.3	Experiment.....	241
5.3.1	TiO ₂ Nanowire Array Synthesis.....	241
5.3.2	Hydrogen Treatment.....	241
5.3.3	Electron Microscopy (EM), UV-Vis, and Raman Measurements....	242
5.3.4	Photoelectrochemical Measurements.....	242
5.3.5	Femtosecond Transient Absorption System.....	243
5.4	Discussion.....	243
5.5	Conclusion.....	261
5.6	References.....	261
CHAPTER 6. Structural, Optical, Electronic, and Ultrafast Properties of		
Hydrogen-Treated TiO₂ Nanowires.....		
6.1	Abstract.....	264
6.2	Introduction.....	265
6.3	Experimental.....	268

6.3.1	TiO ₂ Nanowire Synthesis.....	268
6.3.2	Hydrogen Treatment of TiO ₂ Nanowires.....	269
6.3.3	UV-Vis, Electron Microscopy, and Electron Spin Resonance.....	269
6.3.4	Photoelectrochemical Measurements.....	269
6.3.5	Time-resolved Fluorescence.....	269
6.3.6	Femtosecond Transient Absorption System.....	270
6.4	Results.....	271
6.5	Discussion.....	288
6.6	Conclusion.....	299
6.7	References.....	299
CHAPTER 7. Magnetic Fe₃O₄-Au Core-Shell Nanostructures for Surface		
Enhanced Raman Scattering.....		
7.1	Abstract.....	308
7.2	Introduction.....	309
7.3	Experimental.....	311
7.3.1	Gold Nanoparticles (AuNPs).....	312
7.3.2	Fe ₃ O ₄ Synthesis.....	312
7.3.3	Fe ₃ O ₄ -Au Synthesis.....	313
7.3.4	UV-Vis, Electron Microscopy, and Raman Systems.....	314
7.4	Results.....	315
7.4.1	Optical Properties and EM Characterization.....	315
7.4.2	SERS Spectra.....	325

7.5 Discussion.....	331
7.5.1 SPR Properties of Gold-coated Fe ₃ O ₄	331
7.5.2 Mechanism of Enhanced SERS of Magnetically-Induced Aggregates.....	332
7.6 Conclusion.....	336
7.7 References.....	336
CHAPTER 8. Exciton Dynamics in Semiconductor	
Nanocrystals.....	349
8.1 Abstract.....	349
8.2 Introduction.....	349
8.3 Optical Properties.....	352
8.3.1 Linear Optical Absorption and Emission.....	352
8.3.2 Nonlinear Optical Absorption and Emission.....	363
8.4 Charge Carrier Dynamics.....	366
8.4.1 Basic Properties of Excitons.....	366
8.4.2 Ultrafast Time-Resolved Laser Techniques.....	370
8.4.3 Exciton Dynamics.....	372
8.4.3.1 Electronic Dephasing.....	378
8.4.3.2 Intraband Relaxation.....	383
8.4.3.3 Charge Carrier Trapping.....	386
8.4.3.4 Interband Electron-Hole Recombination.....	388
8.4.4 Nonlinear Exciton Dynamics.....	394

8.4.5	Modeling of Exciton Dynamics.....	411
8.5	Concluding Remarks.....	423
8.6	References.....	423
CHAPTER 9.	Ultrafast Exciton Dynamics in Silicon Nanowires.....	449
9.1	Abstract.....	449
9.2	Introduction.....	449
9.3	Results.....	451
9.4	Discussion.....	464
9.5	Conclusion.....	471
9.6	Methods.....	472
9.6.1	SiNW Preparation.....	472
9.6.2	UV-Vis, Electron Microscopy (EM) and PL Measurements.....	472
9.6.3	Femtosecond Laser System and Transient Absorption Measurement.....	473
9.7	References.....	473
9.8	Supporting Information.....	481
9.8.1	Kinetic Modeling of Charge Carrier Dynamics.....	481
9.8.2	Supporting Information References.....	493
CHAPTER 10.	Ultrafast Exciton Relaxation Dynamics of PbS and Core/Shell PbS/CdS Quantum Dots.....	495
10.1	Abstract.....	495
10.2	Introduction.....	496

10.3 Experimental.....	498
10.3.1 Synthesis of PbS Quantum Dots.....	498
10.3.2 UV-Vis, Photoluminescence, Electron Microscopy, and ICP- OES.....	499
10.3.3 Femtosecond Laser and Transient Absorption.....	500
10.4 Results.....	500
10.5 Discussion.....	517
10.6 Conclusion.....	520
10.7 References.....	521

LIST OF FIGURES

CHAPTER 1

Figure 1: Energy diagram illustrating SERS process.....	4
Figure 2: Shape dependence of SPR of Ag nanostructures.....	10
Figure 3: Spectral location of SPR dependent upon chemical composition.....	11
Figure 4: Diagram of SERS electromagnetic mechanism.....	14
Figure 5: Resonances of crystalline and aggregate nanomaterials.....	22
Figure 6: Correlated structural, finite-element, and SERS characterization of a gold nanotrimer.....	26
Figure 7: AgFON schematic and associated SERS spectra.....	31
Figure 8: SM-SERS spectra of crystal violet isotopologues.....	36
Figure 9: Schematic illustrating femtosecond stimulated Raman scattering.....	40

CHAPTER 2

Figure 1: UV-Vis spectrum of as-prepared HGNs.....	62
Figure 2: TEM images of as-prepared and hole burned HGNs.....	65
Figure 3: UV-Vis spectra of as-prepared and hole burned HGNs.....	68
Figure 4: UV-Vis spectra of HGNs exposed to CW laser.....	72
Figure 5: Illustration of conversion pathways for HGNs after laser illumination.....	75
Figure 6: Theoretical and experimental extinction efficiencies of HGNs of varying aspect ratio.....	79
Figure 7: Electric field of 50 nm radius HGNs at corresponding resonance wavelengths.....	85

CHAPTER 3

Figure 1: UV-Vis spectrum of AuNS.....	103
Figure 2: SEM and TEM of as-prepared AuNS.....	107
Figure 3: Ultrafast relaxation dynamics of AuNS and accompanying FFT data.....	111
Figure 4: 3D plot of transient bleach followed by coherent vibrational oscillations of AuNS.....	114

CHAPTER 4

Figure 1: SEM image of 3D flower-like and nanorod α -Fe ₂ O ₃ nanostructure.....	132
Figure 2: Cross-sectional SEM images of 500 nm thick mesoporous Si-doped α -Fe ₂ O ₃ films.....	135
Figure 3: Schematic illustration and TEM images of Fe ₂ O ₃ -TiSi ₂ core@shell structure.....	137
Figure 4: Schematic illustration and SEM images of mesoporous α -Fe ₂ O ₃ films...	141
Figure 5: Top view and side view of α -Fe ₂ O ₃ nanotube arrays.....	144
Figure 6: Bright field TEM images and AFM images of Fe ₂ O ₃ particles of various sizes.....	147
Figure 7: Low resolution and high resolution TEM images of Fe ₂ O ₃ nanowires....	150
Figure 8: Absorption and (b) reflectance spectra of the α -Fe ₂ O ₃ nanocrystals of different sizes.....	156
Figure 9: Absorption and emission spectra of γ -Fe ₂ O ₃ and α -Fe ₂ O ₃	162
Figure 10: Ultrafast transient absorption decay profiles of γ -Fe ₂ O ₃ nanoparticles..	170
Figure 11: Ultrafast transient absorption decay profiles of undoped and Ti-doped Fe ₂ O ₃ films.....	176
Figure 12: Ultrafast transient absorption decay profiles of hematite nanowires.....	179

Figure 13: Ultrafast transient absorption for hematite hetero-nanostructure electrodes.....	183
Figure 14: Transient absorbance spectra of hematite before and 500 fs after excitation.....	186
Figure 15: Energy diagram of <i>n</i> -type hematite photoanode.....	193
Figure 16: Comparison of potential curves of planar Fe ₂ O ₃ and Fe ₂ O ₃ /TiSi ₂ heterostructures.....	197
Figure 17: Comparison of photocurrent densities of undoped and Ti-doped α-Fe ₂ O ₃ films.....	201
Figure 18: PEC performance of unmodified and IrO ₂ -modified hematite photoanode.....	204
Figure 19: Calcination-temperature dependence of <i>I-V</i> curves for α-Fe ₂ O ₃ solar cells.....	207

CHAPTER 5

Figure 1: SEM image of vertically aligned H:TiO ₂ nanowire arrays.....	245
Figure 2: Raman spectra of TiO ₂ and H:TiO ₂ annealed in a hydrogen atmosphere.....	248
Figure 3: Voltammogram collected from pristine TiO ₂ nanowires and H:TiO ₂ nanowires.....	251
Figure 4: Transient absorption decay profile of H ₂ -treated TiO ₂ nanowires.....	256
Figure 5: Band diagram model of the dynamics of TiO ₂ as compared to H:TiO ₂	258
Figure 6: IPCE spectra of pristine TiO ₂ and H:TiO ₂ nanowires prepared at 350°C.....	260

CHAPTER 6

Figure 1: UV-Vis spectra of TiO ₂ and H:TiO ₂ NWs annealed at various temperatures.....	273
Figure 2: Representative HRTEM images of TiO ₂ NWs and H:TiO ₂ NWs.....	276

Figure 3: ESR of untreated and hydrogen-treated TiO ₂ NW.....	280
Figure 4: Intensity vs. time PL data of TiO ₂ and H:TiO ₂ NWs.....	283
Figure 5: Transient bleach relaxation traces of TiO ₂ and H:TiO ₂ NWs.....	287
Figure 6: Proposed model for energy levels related to optical properties and dynamics studies.....	298

CHAPTER 7

Figure 1: UV-Vis spectra of Fe ₃ O ₄ , Au, Fe ₃ O ₄ -Au , and magnetically-induced aggregates.....	318
Figure 2: STEM image of as-prepared Fe ₃ O ₄ , Fe ₃ O ₄ -Au and HRTEM image of Fe ₃ O ₄ -Au.....	321
Figure 3: EDX mapping and associated spectrum of Fe ₃ O ₄ -Au nanoparticles.....	324
Figure 4: SERS spectra of R6G adsorbed onto AuNPs and Fe ₃ O ₄ -Au nanoparticles.....	327
Figure 5: SERS spectra of R6G adsorbed on Fe ₃ O ₄ -Au in the presence of a magnetic field.....	330

CHAPTER 8

Figure 1: Illustration of the quantum confinement ranging from atoms to bulk materials.....	355
Figure 2: UV-Vis and PL spectra of CdTe QDs capped with thioglycolic acid in aqueous solution.....	358
Figure 3: Schematic illustration of a strongly-bound and weakly-bound photogenerated exciton.....	369
Figure 4: Illustration of key dynamic processes in a QD and related transient absorption measurement.....	375
Figure 5: Peak shift data for CdSe-CdS, CdSe-CdS-CdZnS-ZnS, and CdSe-CdS-ZnS.....	382

Figure 6: Rising population at varying probe wavelengths for a 1.7 nm sample of CdSe.....	385
Figure 7: Representative femtosecond pump-probe TA spectra of colloidal CdSe QDs.....	391
Figure 8: A plot of exciton density as a function of time for CdSe NCs.....	399
Figure 9: Quantum yield vs. $h\nu/E_g$ for PbSe QDs indicating MEG.....	403
Figure 10: Transient bleach decay data for CdSe and 44% CdSe/56%TiO ₂ arrays.....	410
Figure 11: Populations of individual states over time and experimental data vs. modeled data.....	414
Figure 12: Growth of the total population of all single exciton states.....	418
Figure 13: Illustration of the kinetic model used to support experimental observations.....	422

CHAPTER 9

Figure 1: SEM and TEM images of 1D silicon nanowires.....	454
Figure 2: Electronic absorption and fluorescence spectra of SiNWs.....	457
Figure 3: 3D transient bleach relaxation traces of 1D SiNWs.....	460
Figure 4: Transient bleach relaxation traces of 1D SiNWs.....	463
Figure 5: Proposed model for energy levels related to the optical properties and dynamics studies.....	468
Figure 6: Populations of individual states as a function of time.....	486
Figure 7: Experimental data vs. modeled data using a 30/30/20/20 split.....	489
Figure 8: Experimental data vs. modeled data using a 40/40/10/10 split.....	492

CHAPTER 10:

Figure 1: TEM image of PbS and PbS/CdS QDs.....	502
--------------------------------------------------------	-----

Figure 2: UV-Vis absorption spectra of PbS and PbS/CdS nanoparticles.....	505
Figure 3: PL spectra of PbS and PbS/CdS QDs.....	508
Figure 4: Transient absorption relaxation traces of PbS and PbS/CdS.....	511
Figure 5: 3D plots of the transient absorption decay profiles of PbS QDs and PbS/CdS QDs.....	513
Figure 6: Transient absorption decay profiles for three different pump powers for the PbS and PbS/CdS QDs.....	516

SYNTHESIS, CHARACTERIZATION, AND ULTRAFAST DYNAMICS OF METAL, METAL OXIDE, AND SEMICONDUCTOR NANOMATERIALS

Damon A. Wheeler

ABSTRACT

The optical properties of each of the three main classes of inorganic nanomaterials, metals, metal oxides, and semiconductors differ greatly due to the intrinsically different nature of the materials. These optical properties are among the most fascinating and useful aspects of nanomaterials with applications spanning cancer treatment, sensors, lasers, and solar cells. One technique which is central to understanding the optical properties and subsequently allowing exploitation of them is femtosecond transient absorption (TA) which specifically aids in explicating the kinetics of photoexcited charge carriers. In this dissertation, their respective syntheses, optical (*e.g.*, steady-state) characterizations, and TA (*e.g.*, time-resolved) dynamics were explored in order to obtain a fundamentally deeper understanding of their photophysical properties and to provide a deeper understanding of the nature of the underlying photophysics of each class of nanomaterial. For hollow gold nanospheres (HGNs), their ability to absorb high-peak-power femtosecond laser pulses was investigated and was found to be dependent upon average power of the laser. Additionally, gold nanostars (AuNS) were found to exhibit coherent vibrational oscillations arising from phonon relaxation following hot electron relaxation of ~ 2 ps, dependent upon peak power. Metal oxides likewise were

explored with TA techniques in order to probe their excited state kinetics. Specifically, TA was used to study the ultrafast charge carrier dynamics of hydrogen-treated TiO₂ nanowires which contains a singly-occupied oxygen vacancy within the bandgap unlike pristine TiO₂. Following UV irradiation, the charge carrier recombination of the hydrogen-treated TiO₂ NWs was slower than that of pristine TiO₂. These ultrafast results indicate that the presence of the oxygen vacancy significantly slows the charge carrier recombination within the hydrogen-treated TiO₂ relative to pristine TiO₂. The combination of metal oxides and metal, in the form of Fe₃O₄-Au core-shell NPs, combined the modalities of magnetism from the metal oxide and surface plasmon resonance from the metal. This was done to explore the surface enhanced Raman scattering (SERS) properties of the resultant core-shell nanomaterial, in which magnetically-induced aggregation of the NPs was observed to enhance greatly their SERS response by a factor of 7× *via* the generation of more “hot spot” sites as well as improved scattering from the aggregates overall. Finally, TA was utilized to study the exciton dynamics and relaxation pathways of porous silicon nanowires, for which a power-dependence was found and the initial recombination increased in amplitude and decreased in time for increasing laser power, due to exciton-exciton annihilation. Similar results were found for PbS and PbS/CdS core/shell quantum dots. Knowledge of the charge carrier relaxation dynamics in these semiconductor materials may lead to an improved understanding of the origin of the photoluminescence (PL) and how to optimize better and exploit more fully that property for future applications.

DEDICATION

I dedicate this magnum opus to my family:

Your tireless support and unending love has made this endeavor possible. I cannot express to you what this has meant to me.

*“For as our intellect draws near its goal,
it opens to such depths of understanding
as memory cannot plumb within the soul.”*

-Dante Alighieri, The Paradiso

ACKNOWLEDGEMENTS

Men far wiser than I have remarked before that joy lies not in the destination, but in the journey itself. And what better way to take *any* journey than with those whom you respect and love.

Firstly, I would like to thank my advisor, mentor, and friend, Professor Jin Z. Zhang, for his help and guidance throughout my four years at UCSC. He has been a perpetual source of knowledge, wisdom, and guidance to me. I am truly in awe of his abilities and drive and will carry with me forever his kind messages. I would also like to acknowledge my committee members, Professors Shaowei Chen and Yat Li, for their advice and support.

I am indebted greatly to Professors Holger Schmidt, Jin Z. Zhang, and the other co-PIs of the W.M. Keck Center for Nanoscale Opto-fluidics. Their mastery of their respective disciplines was instrumental in UCSC securing the Keck Center's most generous fellowship, for which I was awarded for my first year of residency. Having that fellowship was key in my successes as a first-year graduate student.

I am inestimably fortunate in having matriculated through my graduate career alongside some of the finest scientists and best friends I've yet had in my life. Bob Fitzmorris, Jason Cooper, and Sheraz Gul have been constant companions along my doctoral studies. Together we have navigated the wild ride of graduate school, learning together and made the lab an exciting, upbeat place in which to work. During times when we saw more of each other than our own families, we have become a family for each other. I want to thank them for their friendship and

scientific support. I also want to thank the other current members of the Zhang Lab, including Staci Adams, Sarah Lindley, Liat Zavokivker, and the many undergraduate workhorses we've hosted. Thank you for having made the laboratory memorable and an overall wonderful experience. In addition, the former members of the Zhang Lab that I have had the pleasure of working alongside, including Dr. Jennifer Hensel, Dr. Carley Corrado, Dr. Rebecca Newhouse, Dr. Abraham Wolcott, Prof. Sandy Preciado-Flores, and Dr. Liping Liu. I feel especially indebted to Dr. Rebecca Newhouse who was my patient guide and mentor when I was a junior student. You made the process of learning the ins and outs of the femtosecond laser system so enjoyable.

I have had the joy of collaborating with many accomplished researchers and would like to thank particularly Prof. Shengli Zou, Haining Wang, Prof. Kenneth Knappenberger, Prof. Luis Liz-Marzán, Prof. S.T. Lee, Jian-An Huang, Prof. Claire Gu, and Dr. Xuan Yang. Prof Zou and Haining Wang performed theoretical calculations for my work on the HGNs and AuNS. Prof. Knappenberger was instrumental in measuring the coherent vibrational oscillations of the AuNS, while Prof. Liz-Marzán was key in their synthesis. Prof. Lee and Dr. Huang provided the SiNW samples and some TEM images. Finally, Prof. Gu, the outside member of my qualifying examination, and Dr. Yang, have been excellent collaborators in some fine SERS work we've conducted together.

I have appreciated greatly the camaraderie and togetherness from other graduate students in the Chemistry Department at UCSC, including Clive Kittredge, Yashar Abdollahian, and Kenny Ikei.

Dr. David Stockwell has been, simultaneously, a teacher, mentor, and friend. Without his patience, expertise, and friendship, I would not be the person I am today. Thank you for being there for me.

Finally, I am indebted eternally to my family. Collectively, you are the cornerstones to the absolute best parts of myself. Mom and Dad, your wisdom and love know no bounds. You have no idea how amazing it is knowing you are a phone call away for a quick splash of encouragement, guidance, and unrequited love and support. You are my greatest champions, my idols, and are the people I strive to emulate daily. Simply, you are the two finest people I know. Period. Yasmin and Sean, your patience and guidance have been key to my successes and have been instrumental to me. You always knew what I was going through and were always ready, willing, and able to talk and provide support and encouragement. Your patience, your caring, and your love have been catalysts for me. I could not have done this without you. At all. English, I feel, does not have sufficient wording as to express my love for each of you and what you mean to me. You have collectively carried me through my lows and cheered me on as I rocketed to my highest of highs. Your unending concert of encouragement has spurred me to my triumphs, and helped me soar.

I can only hope I've made each and every one of you proud with my work ethic, drive, and competitive spirit. *Ad astra per aspera!*

The text of this dissertation includes reprints of the following previously published material:

Chapter 1: “Surface Enhanced Raman Scattering,” Wheeler, D.A., Schwartzberg, A.M., Zhang, J.Z. *Dekker Encyclopedia of Nanoscience and Nanotechnology*, **2013**, Ed. 2.

Chapter 2: “Optical Properties and Persistent Spectral Hole Burning of Near Infrared-Absorbing Hollow Gold Nanospheres,” Wheeler, D.A., Newhouse, R.J., Wang, H., Zou, S., Zhang, J.Z., *J. Phys. Chem. C.*, **2010**, 114, 18126-18133.

Chapter 3: “Optical Properties and Coherent Vibrational Oscillations of Gold Nanostars,” Wheeler, D.A., Green, T.D., Wang, H., Fernández-López, C., Liz-Marzán, L., Zou, S., Knappenberger, K.L., Zhang, J.Z. *Chem. Phys. Lett.*, **2012**, 524, 127-132.

Chapter 4: “Nanostructured Hematite: Synthesis, Characterization, Charge Carrier Dynamics, and Photoelectrochemical Properties,” Wheeler, D.A., Wang, G., Ling, Y., Li, Y., and Zhang, J.Z. *Energy & Environmental Science*, **2012**, 5, 6682-6702.

Chapter 5: “Ultrafast Charge Carrier Dynamics and Photoelectrochemical Properties of Hydrogen-Treated TiO₂ Nanowire Arrays,” Wheeler, D.A., Wang, G., Fitzmorris, B.C., Adams, S.A., Li, Y., and Zhang, J.Z. *MRS Proc.*, **2012**, 1387, e04-e07.

Chapter 7: “Magnetic Fe₃O₄-Au Core-shell Nanostructures for Surface Enhanced Raman Scattering,” Wheeler, D.A., Adams, S.A., López-Luke, T., Torres-Castro, A., Zhang, J.Z. *Annalen der Physik*, **2012**, 524, 670-679.

Chapter 8: “Exciton Dynamics in Semiconductors,” Wheeler, D.A. and Zhang, J.Z. *Advanced Materials*, **2013**, VOL, PAGE.

Chapter 9: “Ultrafast Exciton Dynamics in Silicon Nanowires,” Wheeler, D.A., Huang, J.A., Newhouse, R.J., Lee, S.T., Zhang, J.Z. *J. Phys. Chem. Lett.*, **2012**, 3, 766-771.

Chapter 11: “Ultrafast Exciton Dynamics of PbS and Core/Shell PbS/CdS Quantum Dots,” Wheeler, D.A., Fitzmorris, B.C., Zhao, H., Ma, D., and Zhang, J.Z. *Science China Chemistry*, **2011**, 54, 2009-2015.

CHAPTER 1. Surface Enhanced Raman Scattering

1.1 Abstract

Surface enhanced Raman scattering is a powerful analytical technique that allows for a highly sensitive “fingerprint” detection of molecules through the electromagnetic (EM) enhancement of electric fields generated by the excitation of surface plasmons. Since its inception, SERS has progressed from a little-understood phenomenon into one of the most widely-used laboratory tools that is employed across a wide variety of disciplines. In this chapter, we present an overview of the background of Raman scattering and SERS, with an emphasis on surface plasmon resonance and the enhancement mechanisms. We then highlight the impact of substrates before discussing representative applications and recent advances in the development of the SERS technique.

1.2 Introduction

Surface-enhanced Raman scattering (SERS) is a form of Raman spectroscopy (RS) in which a highly amplified Raman scattering signal is achieved when an analyte molecule is on or near a roughened metallic surface. In the intervening 36 years since its discovery in 1977,^{1,2} it has emerged as an extremely useful method for chemical and biochemical analysis and detection for a wide variety of disciplines.³

Because of the widespread potential of this technique for applications, considerable work has been preformed with SERS as the centerpiece. This chapter

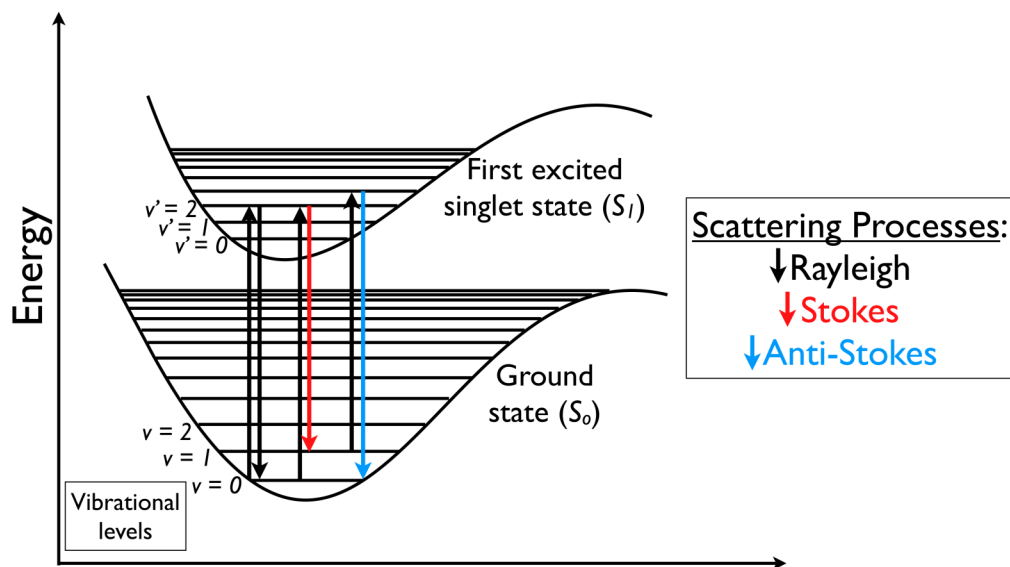
will cover the background of SERS by reviewing Raman scattering, surface plasmon resonance (SPR), and the two main mechanisms behind the SERS enhancement. We then provide an overview of the importance of SERS substrates before discussing current applications and finally the advancements in experimental technique in SERS.

1.3 Background

1.3.1 Raman Scattering

Raman scattering is an optical effect first discovered by C.V. Raman in 1928,⁴ garnering Raman the Noble prize in physics in 1930. It has since become famous for its scientific versatility, with applications spanning art, archaeology, biosciences, analytical chemistry, solid state physics, liquids and liquid interactions, nanomaterials, phase transitions, pharmaceutical studies, and forensic science.³ Raman scattering is an inelastic, light scattering process, and affords a non-destructive technique whereby the vibrational “fingerprint” of an analyte molecule is measured following its photoexcitation and a subsequent change in its molecular polarization (Fig. 1).⁵

Figure 1. Energy diagram illustrating the scattering scheme related to the various scattering mechanisms that are possible: elastic Rayleigh scattering (black arrow), Stokes scattering (red arrow) in which the emitted photon has a lower energy than the absorbed photon, and anti-Stokes scattering (blue arrow) in which the emitted photon is of higher energy than the absorbed photon.



The energetic difference between the incident light and the scattered light is called the Raman shift and corresponds to a molecularly unique set of vibrational frequencies. In this manner, RS is similar to conventional infrared (IR) spectroscopy. However, because IR spectroscopy is predicated upon IR absorption, a non-zero-background measurement, and RS is a zero-background measurement that is detected most commonly at visible wavelengths, RS is far more sensitive than IR spectroscopy.

One of the major limitations to RS has been its small cross-section, $\sim 10^{-30}$ cm²/molecule,⁶ or low quantum yield, about 10^{-7} . Because of this, Raman signals are often challenging to detect. Due to that, a great deal of work has focused on the enhancement of RS signals. Two main approaches have been developed: resonance Raman scattering (RRS) and surface enhanced Raman scattering (SERS). In RRS, the light excitation is resonant with the electronic transition of the analyte which typically results in an enhancement factor of 10^2 - 10^4 ,⁷⁻⁹ or even as high as 10^6 .⁹ However, RRS can be complicated by fluorescence from the electronic transition that interferes with the Raman signal.¹⁰

SERS is a method in which normal Raman scattering signals are enhanced by the strong electromagnetic (EM) field due to an analyte molecule being adsorbed onto (or close to) a roughened noble metal substrate that absorbs light. This is linked to other phenomenon, including surface plasmon resonance, examined in a later section. Nevertheless, the chemical nature of the substrate becomes important since the substrate's surface plasmon resonance (SPR) is mainly responsible for the intensified EM field. The net result is a huge enhancement relative to normal Raman, with an ensemble averaged enhancement factor on the order of 10^{6-11} or higher (10^{13}).¹²

Many books and review article on SERS have been published previously.¹³⁻¹⁸ This work will therefore focus on some of the latest developments, including a brief history of SERS, an overview of the most current understanding of its two main enhancement mechanisms, current applications, and recent advancements to the techniques of SERS.

1.3.2 SERS: History and Nomenclature

SERS was first discovered in 1974 by Fleischmann using roughened silver electrodes which amplified the Raman signal of pyridine¹⁹ and was borne out a few years later by Albrecht¹ and Jeanmaire.² It had been surmised incorrectly that the enhanced signal was due to the increased surface area of the silver electrode. Later, Creighton and van Duyne reasoned that another effect was occurring which accounted for the enhancement, and attributed it to a “plasma resonant enhancement.” In this account, the phenomenon was thought to be due to the Raman component of

the resonant scattering in which the polarizability of the metal particles was modulated by the vibrations of the adsorbed analyte.²⁰ Eventually, Moskovits interpreted the data correctly in surmising the true nature of the effect lay with the excitation of surface plasmons.^{21,22} That particular insight was instrumental since SERS would be observed among metal colloids and that the intensity would scale with the ability of the metal substrate to provide a strong plasmon enhancement.

Generally speaking, the name of “SERS” denotes well the underpinnings of the effect:

- Surface: SERS is a spectroscopic technique which requires the adsorption of analyte molecules onto or very near the surface (within a few nm at most) of a noble metal substrate
- Enhanced: the signal enhancement is predicated upon surface plasmon excitation of the noble metal substrate. This is most effectively achieved by illumination of the substrate with laser light. The substrates which have typically achieved the best enhancements are those with high surface area and roughness, namely nanoparticles.
- Raman: the enhanced signals are still subject to the Raman effect, which involves the inelastic scattering of light and can provide great detail and insight into their vibrational structure, as mentioned above
- Scattering: this word emphasizes the optical effect which is in play. Conversely, “spectroscopy” can be used if one prefers to emphasize the technique itself.

1.4 Surface Plasmons

Plasmons are the quantized and collective oscillations of free electrons of noble metal nanoparticles that occur upon the illumination of the nanoparticles with resonant light.²³⁻²⁷ Surface plasmons are, therefore, those that are confined to surfaces.²⁸⁻³⁰ An incident field polarizes the nanoparticle, shifting the electrons collectively to one side of the system. This is only possible in metal particles with high electron mobility in the lattice such as gold, silver, copper, and to some extent, platinum. After their initial perturbation, the electrons will oscillate. The frequency of this oscillation corresponds to the energy at which photons will be most strongly absorbed. Because of this, the surface plasmon absorption is strongly dependent on the nature of the nanoparticle material and its structure including size, shape, and interparticle interaction (Fig. 2).

Figure 2. Extinction efficiency of a silver cube, truncated cube (TC), cuboctahedron (CO), icosahedron (IH), and a sphere.

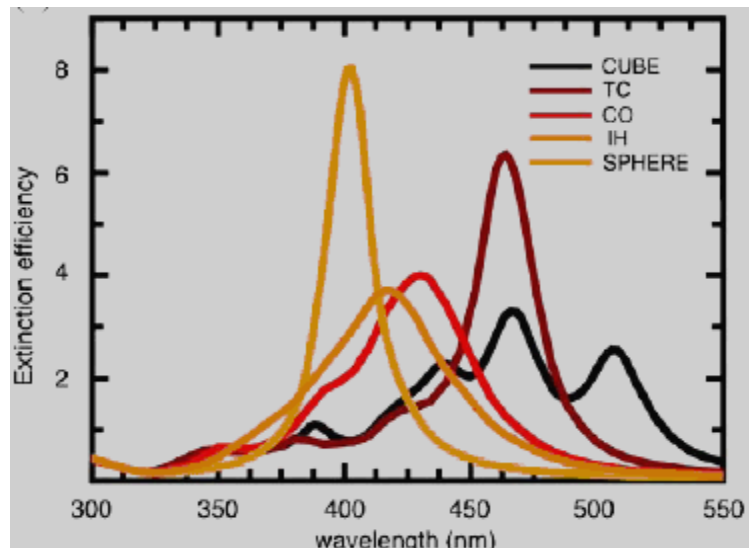


Figure 3. Calculated absorption spectra of (a) Ag, (b) Au, and (c) Cu NPs with cuboctahedral (blue curve with label 1), truncated octahedral (pink curve with label 2), decahedral (red curve with label 3), and icosahedral (green curve with label 4) morphologies. The spectrum calculated for one single sphere (black curve with label 5) is plotted in each graph for comparison with the other shapes.

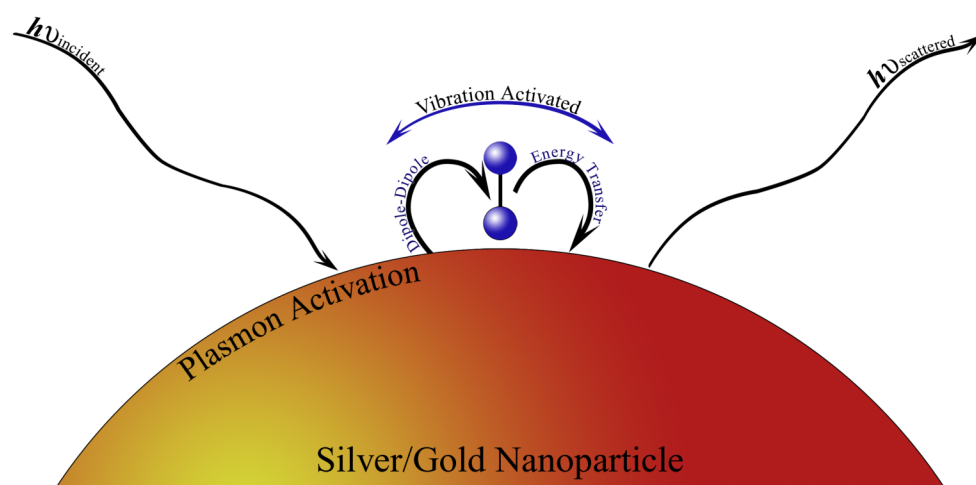
Likewise, as shown in Figure 3, the chemical identity of the metal can influence strongly the SPR peak position. By changing the shape or size of the nanoparticle or interparticle separation, it is possible to change the resonance energy of the plasmon mode. For example, by elongating the nanoparticle into a nanorod, two directions now exist along which the electrons may resonate; the so called transverse (short axis) and longitudinal (long axis) axes. Any deviation from the spherical geometry will induce multiple resonances, including nanoshells,³¹⁻³⁴ and nanoparticle aggregates.³⁵⁻⁴¹ In fact, based on optical absorption alone, it is impossible to discern between nanoshells, nanorods, and nanoparticle aggregates.⁴² This will be discussed in greater detail later.

1.5 SERS Enhancement Mechanisms

1.5.1 Electromagnetic and Chemical Enhancement Mechanisms

There are two principal contributing mechanisms to the SERS effect: electromagnetic and chemical. The general consensus is that the electromagnetic mechanism is the dominant contributing factor to the enhancement of Raman signals. Electromagnetically, analytes that are in close proximity to the surface of the roughened metallic substrate will experience the field generated by the SPR of the metal and thus “feel” a much larger resulting EM field (Fig. 4).

Figure 4. A diagram of the SERS electromagnetic mechanism. Incident light, $h\nu_{\text{incident}}$, is absorbed by the nanoparticle activating the plasmon mode, energy is transferred by means of dipole-dipole interaction to the molecule. A vibration is activated in the molecule and energy is transferred back into the particle. The particle then emits a photon with new energy $h\nu_{\text{scattered}}$.



The chemical enhancement centers on a metal-molecule charge transfer process which increases the resonance with the Raman excitation laser.^{43]} However, the subject of chemical enhancement is somewhat controversial at present.^{44,45}

Because the electromagnetic mechanism is the dominant contributing force to SERS which relies on the substrate's SPR excitation, the identity and morphology of the metal substrate is key in producing maximized SERS signals. Substrates composed of gold or silver are the most popular since their SPRs lie in visible wavelengths, giving them the potential for achieving resonance with excitation laser wavelengths, most of which are also in the visible. Nevertheless, it is the roughened surface of the metal substrate and/or the formation of junction sites between nanoparticles that lead to the generation of so-called "hot spots" that produce strong enhancement. For example, it has been demonstrated that hot spots contribute nearly 24% of the total SERS intensity, even though, on average, only 63 out of 1 million sites are hot spot sites.¹¹

Mathematical models have been developed to illustrate the electromagnetic scattering mechanism in SERS.⁴⁶ Consider an analyte located in close proximity to a metal nanostructure. Behaving like an amplifying device (*e.g.*, an "antenna"), the nanostructure intensifies the incoming field, E_{inc} , of the frequency ω_l , by a factor f_l , generating a local field, E_{loc} , in its proximity:

$$E_{loc} = f_l E_{inc}; \quad (1)$$

The nanostructure also intensifies the scattering from the analyte/metal system at the Raman-shifted frequency ω_2 by an enhancement factor f_2 . The field, denoted as E_{AOA} , is scattered off the analyte *via* the antenna is consequently given by:

$$E_{AOA} \propto f_2 E_{loc} = f_1 f_2 E_{inc} \quad (2)$$

The index AOA signifies the course of scattering: the incident light first polarizes the antenna A, the local field of which polarizes the analyte molecule O, and finally the local field of the analyte re-scatters from the antenna A, which radiates as a result of the interaction. When the difference between ω_1 and ω_2 is small, the approximation of $f_1 \approx f_2 \approx f$ can be made. When this occurs, the antenna-intensified field scattered off the analyte/metal system, E_{AOA} , is proportional to the square of the local field enhancement:

$$E_{AOA} \propto f^2 \quad (3)$$

Importantly, equation (3) is applicable principally in the scenario of surface-enhanced elastic scattering where ω_1 is exactly equivalent to ω_2 . For a full examination of the scattering process, the fully complex nature of the field enhancement must be borne out:

$$f = |f| e^{i\Delta\varphi_f} \quad (4)$$

Here, $|f|$ is the scalar value of the EM enhancement and $\Delta\varphi_f$ is the phase shift produced by the antenna with respect to the incident field. From (3) and (4), it is seen that the scattered intensity $I_{AOA} \propto |E_{AOA}|^2$ scales with the fourth power of the magnitude of the local field enhancement:

$$I_{AOA} \propto |f|^{14} \quad (5)$$

The chemical effect, meanwhile, can provide an enhancement of around 100× to the overall Raman signal intensity. The chemical effect is less understood than the electromagnetic enhancement and thus is the source of minor controversy. Nevertheless, an analyte molecule adsorbed onto the substrate will inevitably interact with that surface. The chemical enhancement exists because of this interaction, for which several explanations have been used to describe the interaction. One prominent explanation states that the metal-adsorbate proximity may allow for routes of electronic coupling from which different charge-transfer intermediates materialize that have larger RS cross-sections than the analyte alone, *e.g.*, when not adsorbed onto the surface.¹⁴ Effectively, this is similar to the RRS effect. An alternative interpretation is that the molecular orbitals of the adsorbate broaden into the conducting electrons of the metal, thereby altering the analyte's chemistry.⁴⁷ Direct studies of the chemical enhancement are difficult because most nanostructured surfaces are nanoscopically featured and a separation of the electromagnetic and chemical effects cannot be easily accomplished. Nevertheless, the chemical effect has been studied *via* adsorbed analyte on an atomically flat copper surface. The EM contributions to the substrate were minor and well-understood, rendering the chemical mechanism easier to analyze. An overall enhancement of 30× was detected and subsequently described as a RR-type phenomenon.⁴⁸

1.6 Nanoengineered Substrates

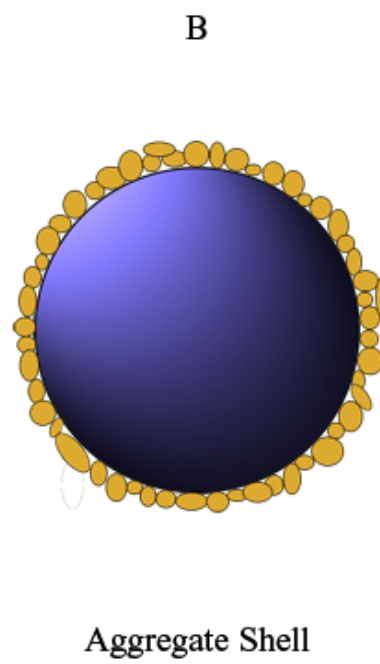
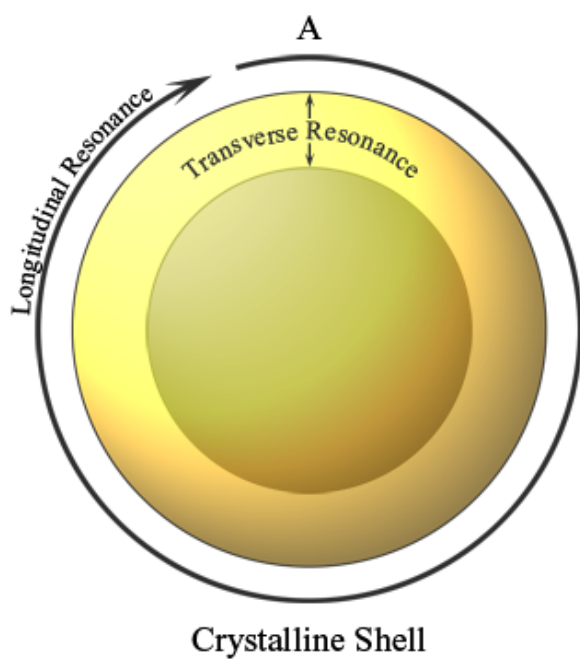
1.6.1 Core/Shell Structures

Core/shell structures are creating a significant stir in SERS research today due to their excellent optical and SERS properties.³⁴ Optically, they are advantageous due to the near infrared (NIR) absorption which is highly desirable for *in vivo* studies as tissue absorbs weakly in this region.⁴⁹ Because SERS requires excitation resonance with nanoparticle absorption, purely spherical nanoparticles of gold or silver will not absorb in the NIR region making nanoshells a unique substrate for biological applications. Their SERS properties are also interesting. While they do not have excessively large enhancements, they are highly uniform which is advantageous for single molecule/single particle studies.⁵⁰ Often in single particle SERS one would want reproducible signals from particle to particle, however, most substrates that are aggregated have random shapes and sizes leading to slight variations. While in theory core/shell systems could provide a solution to this problem, there are several complications.

The first major problem with this type of system is determining that core/shell particles are present at all. As stated earlier, a core/shell system can have very similar optical absorption as an aggregated system.⁴² Therefore, without significant analytical work it is difficult to prove whether a synthesis is producing aggregates or core/shell particles. The other complicating factor is that even with the proper analytical techniques like high resolution transmission electron microscopy (HRTEM) it may still be difficult to determine if the shell is a single crystal (Fig. 5A) or merely a conglomeration of small nanoparticles on the surface of the core (Fig.

5B).^{35,36} While this may not seem like a big distinction, the photophysics and SERS properties of the system are entirely dependent on this.

Figure 5. Diagram of the crystalline shell (A) and aggregate shell (B) core shell structures. Figure A shows schematically the path which the longitudinal and transverse resonances take.



In a core/shell particle with a single crystal shell, the NIR or longitudinal absorption is due to resonance around the particle as in Figure 5A. However, if the shell is made up of aggregated particles the transverse band originates in the individual particles while the longitudinal mode is due to aggregation of the nanoparticles. This is essentially a nanoparticle aggregate system and will not have the same properties or advantages as a true core-shell particle. While many report the synthesis of core-shell nanoparticles, few are truly able to show conclusively that this is the case.⁴²

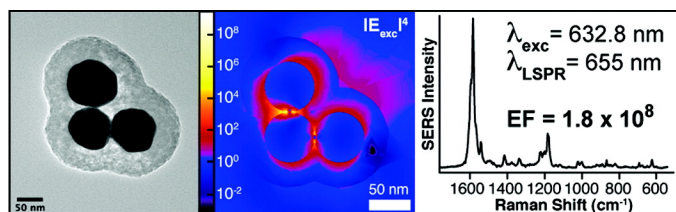
1.6.2 Nanoengineered Dimers and Trimers

As mentioned before, the generation of hot spots is crucial to obtaining a maximal exploitation of all that SERS has to afford. Hot spots occur most commonly on both the roughened surface of the nanostructured substrate as well as at interparticle junction sites. Furthermore, hot spots are customarily developed haphazardly, *e.g.*, in nanoparticle aggregates, rendering them difficult to produce accurately and reliably. Because the size and architecture of the nanoparticle substrate has an influence on the SERS activity,⁵¹ irreproducibility in hot spot location and/or density can frequently result in unstable SERS results. Due to this, research is currently underway to bolster the reproducibility and consistency of SERS substrates and structures. One propitious solution to address the matter of irregularity of hot spots lies with engineered substrates, where the arrangement of plasmonic

materials can be guided more deliberately than with traditional wet-chemical methods.

One current example of engineered substrates is that of dimers and trimers of nanoparticles with a concomitantly tightly controlled interparticle distance. Dimers facilitate profoundly strong plasmonic coupling, particularly when the interparticle distances are affixed in the sub-5 nm scale.⁵² Several intriguing engineered dimer and trimer systems have been generated,⁵³⁻⁵⁶ all of which result in enhancement factors ranging from 10^6 to 10^9 (Fig. 6).

Figure 6. Correlated structural, finite-element, and SERS characterization of an individual gold nanotrimer material, showing an overall SERS enhancement factor (EF) of 1.8×10^8 .



Nevertheless, because they are synthesized *via* wet-chemical methods, variations in the spectral position and magnitude of the resulting SPR can emerge due to inhomogeneities in the size, shape, interparticle spacing, composition, and local dielectric.

1.6.3 Nanolithography

Because of the above issue of variances in spectral positioning and magnitude, nanoengineered patterning techniques, *e.g.* nanolithography, have become increasingly wide-spread for fabricating SERS substrates with better structural controls.⁵⁷⁻⁵⁹ One unique, high-throughput advancement, termed on-wire lithography (OWL), allows for single-nanometer control of interparticle spacing.^{60,61} In OWL, template-directed synthesis, electrochemical deposition, and wet-chemistry etching are combined to generate architectures with single nanometer control over the interparticle spacing. With such intricate control over the particle size and interparticle spacing, it becomes possible to tune the resonance band to the same wavelength as the excitation laser. Such OWL substrates produce enhancement factors approaching 10^9 , which is supported by DDA calculations for similar structures.⁶²

Nanolithography has recently led to the generation of nanohole arrays (NHAs) and dot arrays as SERS substrates. NHAs are appealing in that they couple incident light with surface plasmons on one side of the film with an accompanying evanescent

transfer of light through the holes and subsequent decoupling on the other side of the film.⁶³ The net result is several resonance peaks which have higher transmission than that of the incident light when normalized to the aperture area. NHAs likewise display highly accentuated electric fields, in proximity to the holes themselves, within the structure at resonant wavelengths.⁶⁴ Concurrently, dot arrays also have had initial successes. As with NHAs, dot arrays can be generated with lithographic or pulsed laser ablation techniques. By precisely controlling the number of laser pulses incident upon the sample as well as the pressure of the inert atmosphere in which the ablation occurs, nanometric silver⁶⁵ or gold⁶⁶ dot arrays can be synthesized with consistent interparticle spacing, resulting in red-shifted plasmonic bands that match well with Raman laser excitation wavelengths. Despite being in its relative infancy, nanolithographic techniques have indeed demonstrated the capability of producing SERS substrates with high reproducibility and high sensitivity.⁶⁶

1.7 Current Applications

SERS has established itself as one of the most potent trace molecule detection methods available today. From biomolecules to chemical warfare agent detection, there are virtually endless possibilities for this technology. There is, however, a major hurdle which, to date, has hindered wider practical SERS applications. The nanoparticle-analyte co-location requirement mentioned earlier causes many difficulties. For molecules that bind strongly onto silver and gold surfaces, SERS detection is simple and straightforward. These include amine and thiol-containing

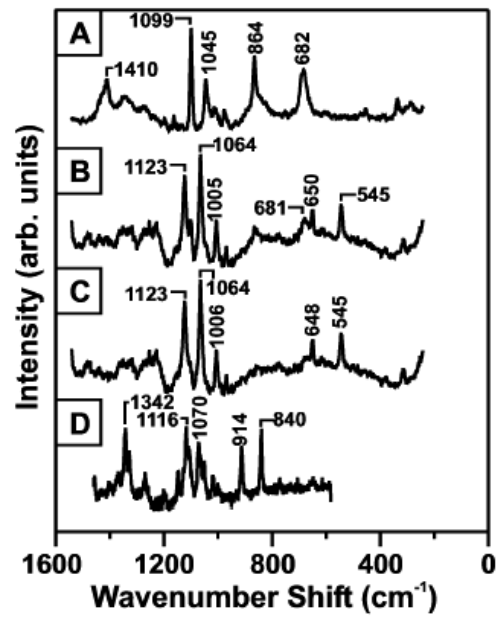
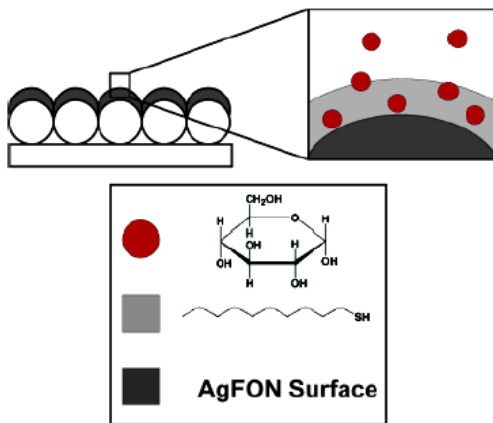
compounds; however, to devise a detection device for a wide variety of analytes, this limitation must be overcome.

For example, one of the most desired molecules for detection is glucose due to the prevalence of diabetes. Millions of people suffer from this disease, yet little advancement has been made in terms of accurate glucose detection using SERS. Blood must still be drawn, and for serious cases this can be required multiple times per day, an inconvenient and painful lifestyle. The development of an in-vitro, implantable, glucose detection device could revolutionize the lives of millions.

To this end there has been steady progress in the field of SERS glucose detection. The first work to demonstrate the possibility of glucose detection did so by utilizing a kind of sandwich method. A layer of glucose is dried between two layers of silver nanoparticles effectively forcing the glucose inside a silver aggregate inducing strong SERS. This is not practical for building devices as it is not stable or usable for real time detection.

More recently, Van Duyne *et al.* have shown significant progress in practical SERS detection of glucose.^{67,68} This is achieved by first producing a stable silver substrate on silica by using latex nanospheres as a template. The substrate is then covered with a self-assembled monolayer (SAM) which acts as a partition between the free solution and the silver. A diagram of this configuration is shown in Figure 7 as well as the RS signal achieved.

Figure 7. (a) Schematic showing hypothetical glucose concentration gradient created by 1-decanethiol (1-DT) partition layer. (b) Spectra used in quantitative analysis in Ref 42 & 43. (A) 1-DT monolayer on AgFON substrate. (B) Mixture of 1-DT monolayer and glucose partitioned from a 100 mM solution. (C) Residual glucose spectrum produced by subtracting (A) from (B). (D) Normal Raman spectrum of crystalline glucose for comparison.



In this configuration glucose can be detected within the biological range with reasonable accuracy. This is due to glucose settling into the SAM close enough to the surface to feel enhancement. This substrate could practically be used in device applications being robust and simple to reproduce consistently by nanotemplating.

Another important application is explosive compound recognition, which requires large enhancements from a technique like SERS to detect trace molecules. SERS also has much higher molecular specificity than other current detection techniques; molecules as similar as enantiomers can be differentiated by SERS. This is important when searching for explosives due to their structural similarity to many other compounds, namely nitrate fertilizers, and can lead to false positive results. Several reports using varying techniques have attempted to detect TNT and similar compounds. The first study was done using electrochemically roughened gold films in which TNT at concentrations in vapor as low as 5 ppb were detected.⁶⁹ By blowing a vaporized sample over the film and monitoring the SERS via a RS fiber probe this low detection limit was possible. Nevertheless, a significant amount of post acquisition work was still required to extract the signal from the data. A more recent study utilized oriented arrays of pyramidally-tipped silver nanowires to detect the explosive 2,4-dinitrotoluene (DNT). While they do not report a detection limit, they do report an enhancement of 5 orders of magnitude, enough for low concentration detection.⁷⁰ It is theorized that the enhancement is increased by the pointed tips of the wires which concentrate the electric field strongly. Both studies show that explosives

detection with SERS is a viable technique and allows the detection of low concentrations of explosives with high spectral resolution.

One major problem which must be overcome for SERS to be a practical technique for *in vivo* or explosive and warfare agents is portability, mobility, and ruggedness of the substrate. Currently, most SERS studies are done with a tabletop RS instrument in a laboratory with colloidal solution or one time use films. There are portable RS instruments; however, a SERS substrate that is portable, reusable, and sensitive has not yet been available. Recently, Vo-Dinh *et al.* have demonstrated a reusable fiber optic tip SERS substrate.^{71,72} With this they are able to obtain SERS spectra from the fiber by merely touching it to a dry surface. It is clear that there is a large enhancement by mere contact. This is achieved by tapering the fiber and depositing silver island films on the surface. This configuration lends itself well to localized, nondestructive experiments while maintaining high spatial resolution due to the small size of the fiber tip. Also, the ability to detect SERS through dry contact is a major advantage over any other currently known system. This type of a device could be used as a sensing probe for SERS detection in a wide variety of situations, whether in the body or in the field.

Many of these fiber detection applications have extremely low sample volume, and a commensurate low signal. Recently in our lab we have built a new detection system utilizing a D-shaped, high surface area fiber SERS sensor. By polishing down one side of the fiber to the core, light can be coupled into metal particles on the surface and activate SERS. This represents an increase in active

SERS surface area of $\sim 2800\times$ from end polished sensors, greatly increasing the total intensity.⁷³

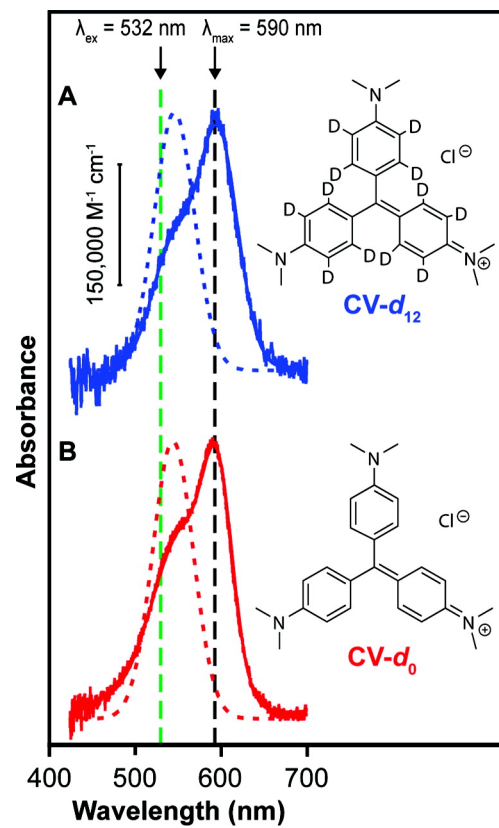
The studies presented above represent a very few of the myriad works being done today. In biological detection significant advances have been made in detection of cancer,⁷⁴⁻⁸⁰ HIV,⁸¹ insulin,^{82,83} and many other exciting areas including amino acids, drugs and vitamins in human samples.⁸⁴⁻⁸⁹ Also the detection of pollution in sea water has been explored, important for rapid monitoring of environmental conditions.^{90,91} Even illicit drugs and uranyl ions have been detected via SERS.^{92,93} This speaks to the vast potential of SERS detection and what can be looked forward to in the future.

1.8 Recent Advances

1.8.1 Single Molecule SERS

Due to the extremely large SERS enhancement and thus potentially high detection sensitivity, there is intense interest in reducing the detection limit to the single molecule level, *i.e.* to develop single-molecule SERS (SM-SERS). Ever since Nie and Emory⁹⁴ and Kneipp⁹⁵ published the first studies of SM-SERS, research interest in the area has exploded. SM-SERS is innately challenging to affirm due to its intrinsically small signal and many possible complications. Recent work on SM-SERS using isotope-substituted analyte molecules has provided perhaps the most convincing result (Fig. 8).^{96,97}

Figure 8. Left panel: representative SM-SERS spectra obtained using a 532 nm excitation laser and 5 second acquisition time of (a) two isotopologues of crystal violet (CV- d_0 and CV- d_{12}), (b) only CV- d_0 , and (c) only CV- d_{12} . Right panel: structures of CV isotopologues as well as simulated (TDDFT, gas phase, dashed line) and experimental ($\sim 10^{-6}$ M (aq) solution, solid line) visible absorbance spectra of crystal violet isotopologues (A) CV- d_{12} and (B) CV- d_0 . No major perturbation of the electronic structure upon deuteration is observed.



Other recent work incorporating the aforementioned nanoengineered dimers has gained interest due to the dimers' ability to provide a known and fixed hot spot location that could be promising for SM-SERS. Likewise, the recent advances in nanofluidics could potentially facilitate the development SM-SERS.^{98,99} However, one drawback to all these approaches is that they do not adequately address the issue of how to position the molecule in a location where SM-SERS may be reliably and reproducibly observed (*e.g.*, the hot spot). This is especially important in order to study the phenomenon and provide key insights into the mechanism behind it. Initial progress on this issue is being made in the field of tip- enhanced Raman spectroscopy (TERS). Convincing demonstrations of SM-TERS have been shown in ultrahigh vacuum¹⁰⁰ and under ambient conditions¹⁰¹ by imaging single molecules with an STM prior to spectrum collection. The latter is especially exciting since it allows for the potential to witness TERS imaging of chemical reactions.

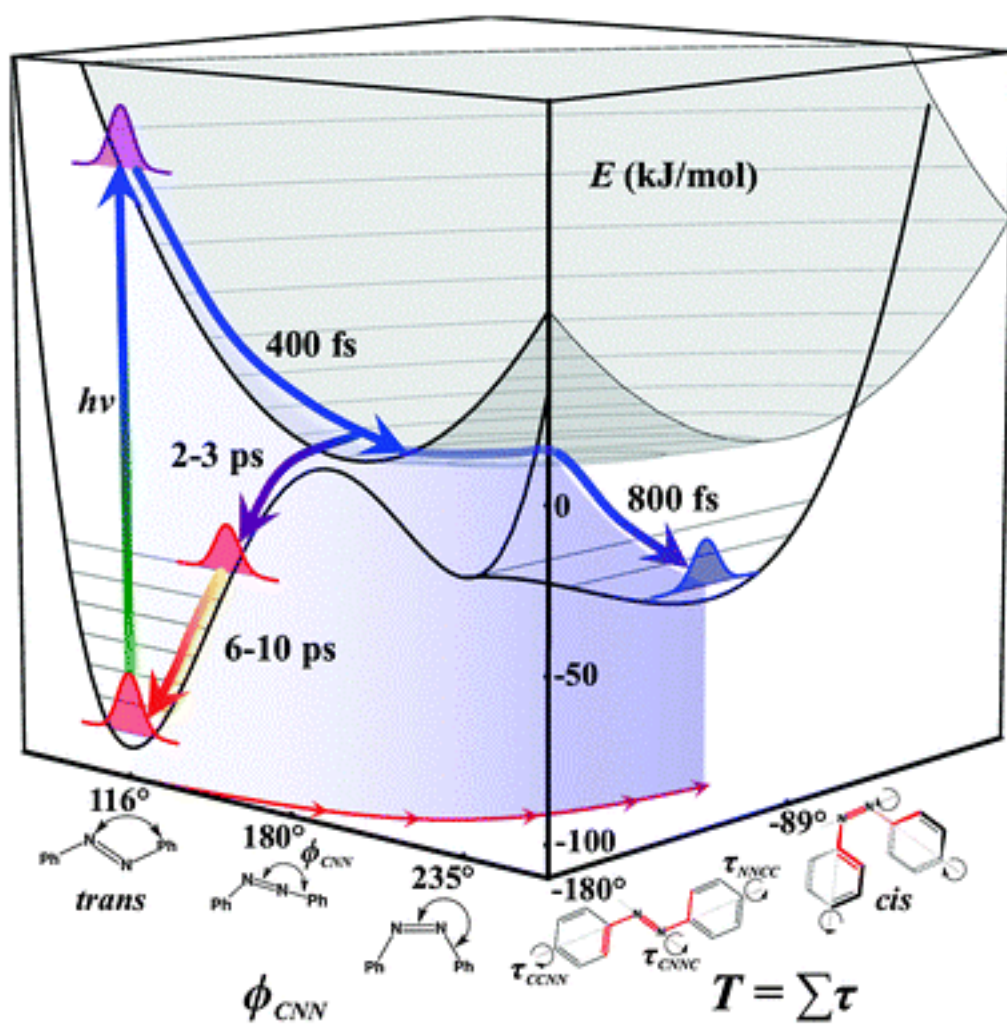
1.8.2 Union of Ultrafast Spectroscopy and SERS

An area of dynamic research has been the combination of the numerous advantages afforded by SERS with ultrafast spectroscopy. The strongest motivator for this is to obtain a more complete understanding of the mechanism behind SERS, especially since predicted enhancement factors as high as 10^{20} have been made¹⁰² and a more complete understanding of the mechanism could help achieve experimentally these remarkable predictions. Prior attempts have been made to observe enhanced Raman signals using femtosecond and stimulated spectroscopies, however many of

these were relegated to individual vibrational peaks with concomitant enhancement factors below 10^4 .¹⁰³⁻¹⁰⁵

Recently, however, Van Duyne's group has incorporated the modalities of surface enhancement with femtosecond stimulated Raman spectroscopy (FSRS). FSRS produces temporally highly-resolved Raman spectra from either ground or excited states of molecules^{106,107} and it has been used to probe the structural dynamics of several photocatalyzed reactions (Fig. 9).¹⁰⁸⁻¹¹⁰

Figure 9. Schematic potential energy surface for the photoinitiated *trans* \rightarrow *cis* isomerization of 4-nitro-4'-dimethylamino-azobenzene (NDAB). The bottom black curve represents the S_0 surface while the higher gray one represents the S_1 surface. The carbon-nitrogen-nitrogen (CNN) bending coordinate is shown on the left of the figure and is represented by the CNN angle (Φ_{CNN}). The collective torsional coordinate is shown on the right and is represented by the sum of the CCNN, CNNC and NNCC dihedral angles ($T = \tau_{CCNN} + \tau_{CNNC} + \tau_{NNCC}$). The hypothetical reaction coordinate is indicated by the red projection. The initially prepared wave packet quickly leaves the Frank Condon region, within 400 fs, through dilation of Φ_{CNN} . Near the 180° point the population meets an S_1/S_0 seam and bifurcates. A small portion continues forward along the bending coordinate (Φ_{CNN}) and a combination of phenyl torsional motions (T) to the *cis* product state effectively completing the reaction within 800 fs. The remainder moves back along Φ_{CNN} and appears as vibrationally excited reactant on the ground state surface after 2–3 picoseconds. The hot ground state reactant continues to cool in the *trans* potential well for the next 6–10 picoseconds.



Typically, a narrow-band (1-3 ps) pump pulse produces Raman excitations, while a continuum (~40 fs) Stokes-based probe pulse interrogates the electronic states.¹¹¹ By using these short-duration optical pulses, Frontiera *et al.* obtained high-quality signal from 600-1800 cm^{-1} of bis-pyridyl-ethylene adsorbed onto gold-silica core-shell substrates with enhancement factors as high as 10^6 .¹¹² This is particularly exciting since it has the potential to provide key insights into the chemistry of surfaces.

1.8.3 UV SERS

Because detection of most biomolecules relies greatly upon excitation in the ultraviolet (UV) regime of the EM spectrum and if one is to take advantage of the resonance effect, UV SERS has emerged as one way to potentially detect biological samples, including proteins, bacteria, DNA, and viruses. It has been challenging to find a metallic substrate that exhibits surface enhancement in the UV. Current attempts to achieve UV SERS have been conducted with varying colloids, including Pd, Pt, Au, Ag, Au-Ag core-shell and Ag-Au core-shell with variant morphologies,¹¹³ aluminum nanohole arrays,¹¹⁴ and metallic gratings,¹¹⁵ which have shown initial promise with enhancement factors on the order of 10^5 . Some reports indicate premature substrate oxidation inhibiting the SERS performance since oxide layers can red-shift absorption maxima, thereby diminishing the resonance of the substrate with the excitation source. Nevertheless, the potential benefits of UV SERS will likely continue to stimulate research interest in this area.

1.9 Conclusion

The discovery of SERS over three decades ago enacted widespread and intense research into what has become an invaluable spectroscopic tool that can identify and provide a unique fingerprinting of analyte molecules due to vast EM field enhancements afforded by the metal substrate. While some lingering questions remain surrounding its implementation, recent work has nonetheless shown that it is highly sensitive, molecularly specific, and non-destructive. In this chapter, the fundamentals of Raman scattering, the SERS mechanisms, and recent applications in the field of SERS have been presented. Challenges related to the SERS substrate have been put forth as well as new developments were discussed, along with some perspective on possible future research directions.

1.10 References

- [1] M. G. Albrecht; J. A. Creighton, *Journal of the American Chemical Society* **1977**, *99*, 5215.
- [2] D. L. Jeanmaire; R. P. Van Duyne, *Journal of Electroanalytical Chemistry* **1977**, *84*, 1.
- [3] W. Kiefer, *Journal of Raman Spectroscopy* **2007**, *38*, 1538-1553.
- [4] C. V. Raman; K. Krishnan, *Nature* **1928**, *121*, 501-502.
- [5] A. Jorio; R. Saito; G. Dresselhaus; M. S. Dresselhaus. Quantum Description of Raman Scattering. In *Raman Spectroscopy in Graphene Related Systems*; Wiley-VCH Verlag GmbH & Co. KGaA, 2011; pp 103-119.

- [6] S. Šašić; Y. Ozaki *Raman, Infrared, and Near-Infrared Chemical Imaging*; Wiley Online Library, 2010.
- [7] B. Schrader *Infrared and Raman spectroscopy*; Wiley-VCH, 2008.
- [8] J. R. Ferraro; K. Nakamoto; C. W. Brown *Introductory raman spectroscopy*; Academic Pr, 2003.
- [9] J. G. Grasselli; B. J. Bulkin *Analytical Raman Spectroscopy*; Wiley, 1991.
- [10] D. Weitz; S. Garoff; J. Gersten; A. Nitzan, *The Journal of Chemical Physics* **1983**, 78, 5324-5338.
- [11] Y. Fang; N. H. Seong; D. D. Dlott, *Science* **2008**, 321, 388-392.
- [12] A. Otto, *Journal Of Raman Spectroscopy* **2005**, 36, 497-509.
- [13] M. Moskovits, *Reviews of Modern Physics* **1985**, 57, 783.
- [14] K. Kneipp; H. Kneipp; I. Itzkan; R. R. Dasari; M. S. Feld, *Chemical Reviews* **1999**, 99, 2957-2976.
- [15] D. Drescher; J. Kneipp, *Chemical Society Reviews* **2012**,
- [16] R. P. Van Duyne, *Physical Chemistry Chemical Physics* **2012**,
- [17] B. Sharma; R. R. Frontiera; A. I. Henry; E. Ringe; R. P. Van Duyne, *Materials Today* **2012**, 15, 16-25.
- [18] P. B. Etchegoin; E. C. Le Ru, *Annual Review of Physical Chemistry* **2012**, 63,
- [19] M. Fleischmann; P. Hendra; A. McQuillan, *Chemical Physics Letters* **1974**, 26, 163-166.

- [20] J. A. Creighton; C. G. Blatchford; M. G. Albrecht, *Journal of the Chemical Society, Faraday Transactions 2: Molecular and Chemical Physics* **1979**, *75*, 790-798.
- [21] M. Moskovits, *The Journal of Chemical Physics* **1978**, *69*, 4159-4161.
- [22] M. Moskovits, *Solid State Communications* **1979**, *32*, 59-62.
- [23] F. J. G. de Abajo, *Nature* **2012**, *483*, 417-418.
- [24] K. M. Mayer; J. H. Hafner, *Chemical Reviews* **2011**, *111*, 3828.
- [25] J. Zuloaga; E. Prodan; P. Nordlander, *Nano Letters* **2009**, *9*, 887-891.
- [26] S. Lal; J. H. Hafner; N. J. Halas; S. Link; P. Nordlander, *Accounts of Chemical Research* **2012**,
- [27] M. Piliarik; J. Homola, *Optics Express* **2009**, *17*, 16505-16517.
- [28] S. Zeng; X. Yu; W.-C. Law; Y. Zhang; R. Hu; X.-Q. Dinh; H.-P. Ho; K.-T. Yong, *Sensors and Actuators B: Chemical* **2013**, *176*, 1128-1133.
- [29] P. Bharadwaj; A. Bouhelier; L. Novotny, *Physical Review Letters* **2011**, *106*, 226802.
- [30] M. Piliarik; H. Šípová; P. Kvasnička; N. Galler; J. R. Krenn; J. Homola, *Optics Express* **2012**, *20*, 672-680.
- [31] E. Prodan; P. Nordlander; N. Halas, *Nano Letters* **2003**, *3*, 1411-1415.
- [32] C. L. Nehl; N. K. Grady; G. P. Goodrich; F. Tam; N. J. Halas; J. H. Hafner, *Nano Letters* **2004**, *4*, 2355-2359.

- [33] L. M. Liz-Marzán; M. Giersig; P. Mulvaney, *Langmuir* **1996**, *12*, 4329-4335.
- [34] N. Halas, *GOLD BULLETIN-WORLD GOLD COUNCIL* **2004**, *37*, 137-137.
- [35] T. J. Norman; C. D. Grant; D. Magana; J. Z. Zhang; J. Liu; D. L. Cao; F. Bridges; A. Van Buuren, *Journal Of Physical Chemistry B* **2002**, *106*, 7005-7012.
- [36] T. J. Norman Jr; C. D. Grant; A. M. Schwartzberg; J. Z. Zhang, *Optical Materials* **2005**, *27*, 1197-1203.
- [37] B. Nikoobakht; M. A. El-Sayed, *The Journal of Physical Chemistry A* **2003**, *107*, 3372-3378.
- [38] M. Quinten; J. Stier, *Colloid & Polymer Science* **1995**, *273*, 233-241.
- [39] M. Quinten; A. Leitner; J. Krenn; F. Aussenegg, *Optics letters* **1998**, *23*, 1331-1333.
- [40] M. Quinten; U. Kreibig, *Applied optics* **1993**, *32*, 6173-6182.
- [41] M. Quinten, *Applied Physics B: Lasers and Optics* **2000**, *70*, 579-586.
- [42] J. Z. Zhang; A. M. Schwartzberg; T. Norman; C. D. Grant; J. Liu; F. Bridges; T. van Buuren, *Nano Letters* **2005**, *5*, 809-810.
- [43] D. Y. Wu; X. M. Liu; S. Duan; X. Xu; B. Ren; S. H. Lin; Z. Q. Tian, *The Journal of Physical Chemistry C* **2008**, *112*, 4195-4204.
- [44] A. Otto; A. Bruckbauer; Y. Chen, *Journal of Molecular Structure* **2003**, *661*, 501-514.

- [45] W. E. Doering; S. Nie, *The Journal of Physical Chemistry B* **2001**, *106*, 311-317.
- [46] P. Alonso-González; P. Albella; M. Schnell; J. Chen; F. Huth; A. García-Etxarri; F. Casanova; F. Golmar; L. Arzubiaga; L. Hueso, *Nature Communications* **2012**, *3*, 684.
- [47] A. Campion; P. Kambhampati, *Chem. Soc. Rev.* **1998**, *27*, 241-250.
- [48] A. Campion; J. E. Ivanecky; C. M. Child; M. Foster, *Journal of the American Chemical Society* **1995**, *117*, 11807-11808.
- [49] K. Kneipp; H. Kneipp; I. Itzkan; R. R. Dasari; M. S. Feld, *Journal of Physics: Condensed Matter* **2002**, *14*, R597.
- [50] J. Jackson; S. Westcott; L. Hirsch; J. West; N. Halas, *Applied Physics Letters* **2003**, *82*, 257-259.
- [51] J. M. McLellan; Z.-Y. Li; A. R. Siekkinen; Y. Xia, *Nano Letters* **2007**, *7*, 1013-1017.
- [52] N. J. Halas; S. Lal; W.-S. Chang; S. Link; P. Nordlander, *Chemical Reviews* **2011**, *111*, 3913-3961.
- [53] S. Toroghi; P. G. Kik, *Applied Physics Letters* **2012**, *100*, 183105-183105-183104.
- [54] C. G. Khoury; S. J. Norton; T. Vo-Dinh, *ACS Nano* **2009**, *3*, 2776-2788.
- [55] A. Pallaoro; G. B. Braun; N. O. Reich; M. Moskovits, *Small* **2010**, *6*, 618-622.

- [56] K. L. Wustholz; A. I. Henry; J. M. McMahon; R. G. Freeman; N. Valley; M. E. Piotti; M. J. Natan; G. C. Schatz; R. P. V. Duyne, *Journal of the American Chemical Society* **2010**,
- [57] S. Cataldo; J. Zhao; F. Neubrech; B. Frank; C. Zhang; P. V. Braun; H. Giessen, *ACS Nano* **2011**, *6*, 979-985.
- [58] M. Najiminaini; F. Vasefi; B. Kaminska; J. J. L. Carson, *Applied Physics Letters* **2012**, *100*, 063110-063110-063114.
- [59] J. Zhao; B. Frank; S. Burger; H. Giessen, *ACS Nano* **2011**,
- [60] K. D. Osberg; A. L. Schmucker; A. J. Senesi; C. A. Mirkin, *Nano Letters* **2011**,
- [61] L. Qin; S. Park; L. Huang; C. A. Mirkin, *Science* **2005**, *309*, 113-115.
- [62] J. M. McMahon; S. Li; L. K. Ausman; G. C. Schatz, *The Journal of Physical Chemistry C* **2012**, *116*, 1627-1637.
- [63] T. W. Ebbesen; H. J. Lezec; H. F. Ghaemi; T. Thio; P. A. Wolff, *Nature* **1998**, *391*, 667-669.
- [64] A. Krishnan; T. Thio; T. J. Kim; H. J. Lezec; T. W. Ebbesen; P. A. Wolff; J. Pendry; L. Martin-Moreno; F. J. Garcia-Vidal, *Optics Communications* **2001**, *200*, 1-7.
- [65] C. D'Andrea; F. Neri; P. Ossi; N. Santo; S. Trusso, *Sensors and Microsystems* **2011**, 137-143.

- [66] N. R. Agarwal; F. Neri; S. Trusso; A. Lucotti; P. M. Ossi, *Applied Surface Science* **2011**,
- [67] K. E. Shafer-Peltier; C. L. Haynes; M. R. Glucksberg; R. P. Van Duyne, *Journal of the American Chemical Society* **2002**, *125*, 588.
- [68] C. R. Yonzon; C. L. Haynes; X. Zhang; J. T. Walsh Jr; R. P. Van Duyne, *Analytical Chemistry* **2004**, *76*, 78-85.
- [69] J. M. Sylvia; J. A. Janni; J. Klein; K. M. Spencer, *Analytical Chemistry* **2000**, *72*, 5834-5840.
- [70] A. Tao; F. Kim; C. Hess; J. Goldberger; R. He; Y. Sun; Y. Xia; P. Yang, *Nano Letters* **2003**, *3*, 1229-1233.
- [71] D. L. Stokes; T. Vo-Dinh, *Sensors and Actuators B: Chemical* **2000**, *69*, 28-36.
- [72] D. L. Stokes; Z. Chi; T. Vo-Dinh, *Applied Spectroscopy* **2004**, *58*, 292-298.
- [73] Y. Zhang; C. Gu; A. M. Schwartzberg; J. Z. Zhang, *Applied Physics Letters* **2005**, *87*, 123105-123103.
- [74] L. R. Allain; T. Vo-Dinh, *Analytica Chimica Acta* **2002**, *469*, 149-154.
- [75] M. Culha; D. Stokes; T. Vo-Dinh, *Expert review of molecular diagnostics* **2003**, *3*, 669-675.
- [76] H. Morjani; J. F. Riou; I. Nabiev; F. Lavelle; M. Manfait, *Cancer Research* **1993**, *53*, 4784-4790.

- [77] I. Nabiev; H. Morjani; M. Manfait, *European biophysics journal* **1991**, *19*, 311-316.
- [78] K. Sokolov; J. Aaron; B. Hsu; D. Nida; A. Gillenwater; M. Follen; C. MacAulay; K. Adler-Storthz; B. Korgel; M. Descour, *Technology in cancer research & treatment* **2003**, *2*, 491.
- [79] T. Vo-Dinh; L. R. Allain; D. L. Stokes, *Journal of Raman Spectroscopy* **2002**, *33*, 511-516.
- [80] D. S. Grubisha; R. J. Lipert; H. Y. Park; J. Driskell; M. D. Porter, *Analytical Chemistry* **2003**, *75*, 5936-5943.
- [81] N. R. Isola; D. L. Stokes; T. Vo-Dinh, *Analytical Chemistry* **1998**, *70*, 1352-1356.
- [82] C. Ortiz; D. Zhang; Y. Xie; V. J. Davisson; D. Ben-Amotz, *Analytical biochemistry* **2004**, *332*, 245-252.
- [83] V. P. Drachev; M. D. Thoreson; E. N. Khaliullin; V. J. Davisson; V. M. Shalaev, *The Journal of Physical Chemistry B* **2004**, *108*, 18046-18052.
- [84] Y. Du, *SPECTROSCOPY AND SPECTRAL ANALYSIS* **2003**, *23*, 718-720.
- [85] P. D. O'Neal; G. L. Coté; M. Motamedi; J. Chen; W. C. Lin, *Journal of Biomedical Optics* **2003**, *8*, 33-39.
- [86] Y. Wang; Y. S. Li; Z. Zhang; D. An, *Spectrochimica Acta Part A: Molecular and Biomolecular Spectroscopy* **2003**, *59*, 589-594.

- [87] W. Premasiri; D. Moir; M. Klempner; N. Krieger; G. Jones II; L. Ziegler, *The Journal of Physical Chemistry B* **2005**, *109*, 312-320.
- [88] Y. Wang; Y. Li; Z. Zhang; D. An, *Guang pu xue yu guang pu fen xi= Guang pu* **2004**, *24*, 1376.
- [89] T. W. Koo; S. Chan; L. Sun; X. Su; J. Zhang; A. A. Berlin, *Applied Spectroscopy* **2004**, *58*, 1401-1407.
- [90] H. Schmidt; N. Bich Ha; J. Pfannkuche; H. Amann; H. D. Kronfeldt; G. Kowalewska, *Marine pollution bulletin* **2004**, *49*, 229-234.
- [91] B. Gu; J. Tio; W. Wang; Y. K. Ku; S. Dai, *Applied Spectroscopy* **2004**, *58*, 741-744.
- [92] B. Sägmüller; B. Schwarze; G. Brehm; G. Trachta; S. Schneider, *Journal of Molecular Structure* **2003**, *661-662*, 279.
- [93] L. Bao; S. Mahurin; R. Haire; S. Dai, *Analytical Chemistry* **2003**, *75*, 6614-6620.
- [94] S. M. Nie; S. R. Emery, *Science* **1997**, *275*, 1102-1106.
- [95] K. Kneipp; Y. Wang; H. Kneipp; L. T. Perelman; I. Itzkan; R. R. Dasari; M. S. Feld, *Physical Review Letters* **1997**, *78*, 1667-1670.
- [96] J. A. Dieringer; B. Robert; I. Lettan; K. A. Scheidt; R. P. Van Duyne, *Journal of the American Chemical Society* **2007**, *129*, 16249-16256.
- [97] S. L. Kleinman; E. Ringe; N. Valley; K. L. Wustholz; E. Phillips; K. A. Scheidt; G. C. Schatz; R. P. Van Duyne, *Journal of the American Chemical Society* **2011**,

- [98] I. Choi; Y. S. Huh; D. Erickson, *Microfluidics and Nanofluidics* **2012**, 1-7.
- [99] R. M. Connatser; L. A. Riddle; M. J. Sepaniak, *Journal of Separation Science* **2004**, 27, 1545-1550.
- [100] J. Steidtner; B. Pettinger, *Physical Review Letters* **2008**, 100, 236101.
- [101] M. D. Sonntag; J. M. Klingsporn; L. K. Garibay; J. M. Roberts; J. A. Dieringer; T. Seideman; K. A. Scheidt; L. Jensen; G. C. Schatz; R. P. Van Duyne, *The Journal of Physical Chemistry C* **2011**, 116, 478-483.
- [102] H. Chew; D. Wang; M. Kerker, *JOSA B* **1984**, 1, 56-66.
- [103] T. Ichimura; N. Hayazawa; M. Hashimoto; Y. Inouye; S. Kawata, *Journal of Raman Spectroscopy* **2003**, 34, 651-654.
- [104] P. Kukura; D. W. McCamant; R. A. Mathies, *Annual Review of Physical Chemistry* **2007**, 58, 461-488.
- [105] V. Namboodiri; M. Namboodiri; G. Diaz; M. Oppermann; G. Flachenecker; A. Materny, *Vibrational Spectroscopy* **2011**, 56, 9-12.
- [106] R. R. Frontiera; R. A. Mathies, *Laser & Photonics Reviews* **2011**, 5, 102-113.
- [107] G. V. P. Kumar; N. Rangarajan; B. Sonia; P. Deepika; N. Rohman; C. Narayana, *Bulletin of Materials Science* **2011**, 34, 207.
- [108] C. Fang; R. R. Frontiera; R. Tran; R. A. Mathies, *Nature* **2009**, 462, 200-204.

- [109] A. Weigel; N. P. Ernsting, *The Journal of Physical Chemistry B* **2010**, *114*, 7879-7893.
- [110] D. P. Hoffman; R. A. Mathies, *Physical Chemistry Chemical Physics* **2012**, *14*, 6298-6306.
- [111] S.-Y. Lee; D. Zhang; D. W. McCamant; P. Kukura; R. A. Mathies, *The Journal of Chemical Physics* **2004**, *121*, 3632-3642.
- [112] R. R. Frontiera; A.-I. Henry; N. L. Gruenke; R. P. Van Duyne, *The Journal of Physical Chemistry Letters* **2011**, *2*, 1199-1203.
- [113] E. Kämmer; T. Dörfer; A. Csáki; W. Schumacher; P. A. Da Costa Filho; N. Tarcea; W. Fritzsche; P. Rösch; M. Schmitt; J. Popp, *The Journal of Physical Chemistry C* **2012**, *116*, 6083-6091.
- [114] Z. L. Yang; Q. H. Li; B. Ren; Z. Q. Tian, *Chemical Communications* **2011**, *47*, 3909-3911.
- [115] N. Mattiucci; G. D'Aguanno; H. O. Everitt; J. V. Foreman; J. M. Callahan; M. C. Buncick; M. J. Bloemer, *Optics Express* **2012**, *20*, 1868-1877.

CHAPTER 2. Optical Properties and Persistent Spectral Hole Burning of Near Infrared-Absorbing Hollow Gold Nanospheres

2.1 Abstract

We report on the characteristics and mechanism of persistent spectral hole burning of hollow gold nanospheres (HGNs) with near IR (NIR) surface plasmon resonance (SPR) absorption induced by femtosecond (fs) laser pulses. The HGNs were exposed to pulsed laser light at 810 nm, on resonance with their absorption band, at various laser powers while the total photon flux incident on the samples was kept constant. Depletion of HGNs responsible for 830 nm absorption was observed while simultaneous growth of bluer-absorbing HGNs, solid gold nanoparticles (AuNPs), or a mixture thereof was observed. This occurred only with fs pulsed laser irradiation and did not occur with continuous wave (CW) laser irradiation. Based on combined UV-vis spectroscopy and transmission electron microscopy data, the mechanism behind the persistent hole burning with fs laser irradiation is proposed to involve two possible processes: (i) conversion of NIR-absorbing HGNs to bluer-absorbing HGNs, and (ii) breakdown of NIR-absorbing HGNs into solid AuNPs directly. The branching ratio between these two processes depends on the peak power of the fs laser pulses with higher peak power favoring the second process. This hole-burning study is useful for understanding and exploring the potential use of HGNs in drug delivery with a laser as a trigger for release. In conjunction, theoretical calculations have been carried out to gain further insight into the optical absorption of

HGNs, especially in terms of how the extinction coefficient depends on the structure of the HGNs in comparison to solid AuNPs. One interesting finding is that HGNs with thicker shells not only absorb at bluer wavelengths, but also have lower absorption as well as extinction coefficient. An HGN with the same outer diameter as a solid AuNP has a substantially larger extinction coefficient. These theoretical findings are supported by experimental results. The enhanced extinction coefficient is advantageous for applications such as photothermal ablation therapy (PTA) for cancer treatment. The dependence of the absorption coefficients on the HGN structure is also important for interpreting the hole-burning results that rely on changes in spectral position as well as intensity.

2.2 Introduction

Noble-metal nanoparticles have recently been the focus of intense research because of their fascinating optical properties, particularly the surface plasmon resonance (SPR) absorption due to collective oscillation of conduction band electrons in response to an electrical field such as light. Analytical methods based on SPR¹⁻⁸ and surface-enhanced Raman scattering (SERS)⁹⁻¹⁵ of metallic nanoparticles have garnered much attention because of their applications for chemical and biological analysis. A key factor that determines the SPR properties is the structure, especially shape, of the metal nanomaterials. Advancements in synthetic methodology have produced many interesting shapes of metal nanostructures, such as rods,^{16,17} prisms,^{18,19} cubes,^{20,21} triangles,^{22,23} cages,^{24,25} tubes,^{26,27} aggregates,^{28,29} and

frames.^{30,31} Different applications of these metal nanostructures have been studied, including photocatalysis,^{32,33} photovoltaics,^{34,35} metal-enhanced fluorescence,^{36,37} and imaging.^{38,39}

Recently, a unique class of noble-metal nanoparticles, termed hollow gold nanospheres (HGNs), has been developed. While isolated spherical solid gold nanoparticles (AuNPs) possess a single resonance centered near 520 nm,⁴⁰ HGNs have a broadly tunable SPR in the entire visible to near IR (NIR) dependent upon both their core diameters as well as shell thicknesses.^{41,42} This tunability is especially interesting for applications such as cancer therapy and detection based on photothermal ablation (PTA) that has been demonstrated successfully.^{43,44} The HGNs showed significantly improved PTA performance over AuNPs due to their strong and narrow NIR absorption. NIR light irradiation is preferred for PTA due to deeper tissue penetration.⁴⁵ The small size (30-50 nm) and spherical shape of the HGNs, in conjunction with the strong and tunable SPR in the NIR, make them unique and one of the most promising nanomaterials for PTA application.⁴⁶

Another interesting potential application of HGNs is for drug delivery with a drug either encapsulated inside the shell or attached to the outer surface. Very recently, Lu *et al.* bioconjugated HGNs with siRNA on the outer surface and triggered a photothermally induced siRNA release via pulsed laser irradiation with the result of downregulating the NF- κ B p65 transcription factor.⁴⁷ If drug molecules are encapsulated inside the HGNs, one would need a mechanism to trigger the release of the drug once reaching the target. One possible triggering method is laser-induced

fragmentation of the HGNs. Indeed, in the work reported by Lu et al.,⁴⁷ it was found that pulsed laser irradiation can lead to fragmentation of the HGNs. There were indications of solid AuNP formation upon HGN fragmentation, but the detailed fragmentation mechanism behind it is still not well understood. The concept of using pulsed lasers to affect the structure of metal nanoparticles has been investigated before.⁴⁸⁻⁵²

In this work, we conducted a systematic study of the effect of pulsed fs laser irradiation on HGNs to probe the effect of light on possible structural changes of HGNs using a combination of persistent spectral hole burning and transmission electron microscopy (TEM). With fs laser irradiation at 810 nm, the NIR- absorbing HGNs are converted into either bluer-absorbing HGNs or solid AuNPs. The branching ratio between the two conversion products depends on the peak power of the fs laser pulses, with higher peak power producing relatively more solid AuNPs. In order to quantify the spectral intensity changes in addition to spectral position changes associated with the hole burning, we quantitatively compare the extinction coefficients of different HGNs and solid AuNPs both experimentally and theoretically. The NIR-absorbing HGNs have larger extinction coefficients than bluer-absorbing HGNs, and HGNs have larger extinction coefficients than solid AuNPs with the same outer diameter, when normalized to a per HGN or NP basis. The results have important implications in various applications of HGNs, including PTA treatment of cancer, SERS, and potential drug delivery.

2.3 Methods and Materials

2.3.1 HGN Synthesis

Cobalt chloride hexahydrate ($\text{CoCl}_2 \cdot 6\text{H}_2\text{O}$, 99.99%), monosodium citrate trihydrate ($\text{Na}_3\text{C}_6\text{H}_5\text{O}_7 \cdot 3\text{H}_2\text{O}$, 99%), sodium borohydride (NaBH_4), and chloroauric acid trihydrate ($\text{HAuCl}_4 \cdot 3\text{H}_2\text{O}$, ACS reagent grade) were obtained from Fisher Scientific. All water used in the synthesis of HGNS was 18 M Ω ultrapure water.

The HGNS were synthesized according to the method established by Schwartzberg et al.,⁴² of which the NIR-absorbing HGN nanoparticles were made more facile and reproducible by Preciado-Flores *et al.*⁵³ in which solid cobalt nanoparticles were used as a sacrificial template in a galvanic replacement with gold ions. Throughout all of these steps, the utmost attention was paid to the exclusion of air from the system due to the predilection of cobalt to rapid oxidation in the presence of oxygen. Additionally, all glassware that was used was meticulously cleaned with soap solutions, aqua regia, and ultrapure water.

Briefly, in a two-necked round-bottom flask, 100 mL of water was combined with 100 μL of 0.4 M cobalt chloride hexahydrate and 400 μL of 0.1 M sodium citrate trihydrate, and the solution was deaerated by bubbling with argon gas for 40 min. To that deaerated solution, 100 μL of 1.0 M sodium borohydride was injected. Upon the addition of the sodium borohydride, the solution turned from a pale pink color to a brown color over the course of a few seconds. Simultaneous to the addition of the sodium borohydride, 500 μL of a 1% wt/wt solution of (poly)vinylpyrrolidone,

(C₆H₉NO)_n, (average *M_w* of 55 000) was injected. The as-formed cobalt nanoparticle solution was further deaerated by passing argon through the reaction flask for a further 40 min until the hydrolysis of the borohydride was complete. Magnetic stirring was avoided due to previous reports by Schwartzberg et al.,²⁷ which indicated that the presence of a magnetic field could induce the formation of cobalt nanotubes rather than colloidal spheres.

Subsequently, 30 mL of the cobalt nanoparticles were transferred, via cannula, to a stirring solution of 10 mL of water and 15 μL of 0.1 M chloroauric acid trihydrate. A galvanic replacement reaction occurred, reducing the gold ions onto the cobalt nanoparticles that were concurrently oxidized in a 3:2 ratio of cobalt-to-gold. The solution immediately turned green in color and was allowed to stir for another five minutes to complete the reaction.

2.3.2 Spectral Hole Burning

Hole-burning experiments were carried out on two different laser systems. Continuous wave (CW) light was generated from a Ti:sapphire laser with a 780 nm fundamental while femtosecond laser pulses were generated from a regeneratively amplified Er-doped fiber oscillator that delivered 1.0 mJ pulse energies centered at 810 nm with a repetition rate of 752 Hz. The beam size was approximately 2 mm in each case. Peak power in each case was varied by the usage of neutral density (ND) filters with values of 0.1, 0.3, and 0.5, while incident photon flux onto the samples was maintained at a constant value of 3.06×10^{18} photons/s by varying the amount of

time each sample was exposed to the laser light. In both CW and fs experiments, average incident laser power was maintained at 750 mW when no ND filters were used.

2.3.3 UV-Vis and Electron Microscopy (EM) Measurements

Absorption measurements were performed using a Varian Cary 50 UV-visible spectrophotometer with spectral resolution set to 2 nm. Associated spectra were fit using the Origin 8.0 suite. Samples were concentrated using a Sorval RC 5C Plus supercentrifuge that was spun at 14 000 rpm for 15 min at a constant temperature of 20 °C. Low-resolution transmission electron microscopy (TEM) was carried out using a JEOL model JEM-1200EX microscope. High-resolution TEM was performed on a Philips CM300-FEG at the National Center for Electron Microscopy at Lawrence Berkeley National Laboratory. Particle sizes were analyzed using imageJ software.⁵⁴

2.3.4 Theoretical Calculations

Generalized Mie theory was used to calculate the extinction and absorption spectra of the core shell Au particle and the electric and magnetic fields at different wavelengths.^{55,56} For a spherical core shell particle illuminated with a plane incident wave, the electric and magnetic fields of the incident light, scattered light, and those inside the particle core and shells can be expressed with vector spherical harmonics (VSH). By matching boundary conditions, the expansion coefficients of the VSH can

be obtained, and the optical properties of the particle can be calculated. The extinction and scattering cross section of the particle can be calculated using eqs 1 and 2:

$$C_{ext} = \frac{2\pi}{k^2} \sum_{n=1}^{\infty} (2n+1) \text{Re}(a_n + b_n) \quad (1)$$

$$C_{sca} = \frac{2\pi}{k^2} \sum_{n=1}^{\infty} (2n+1) (|a_n|^2 + |b_n|^2) \quad (2)$$

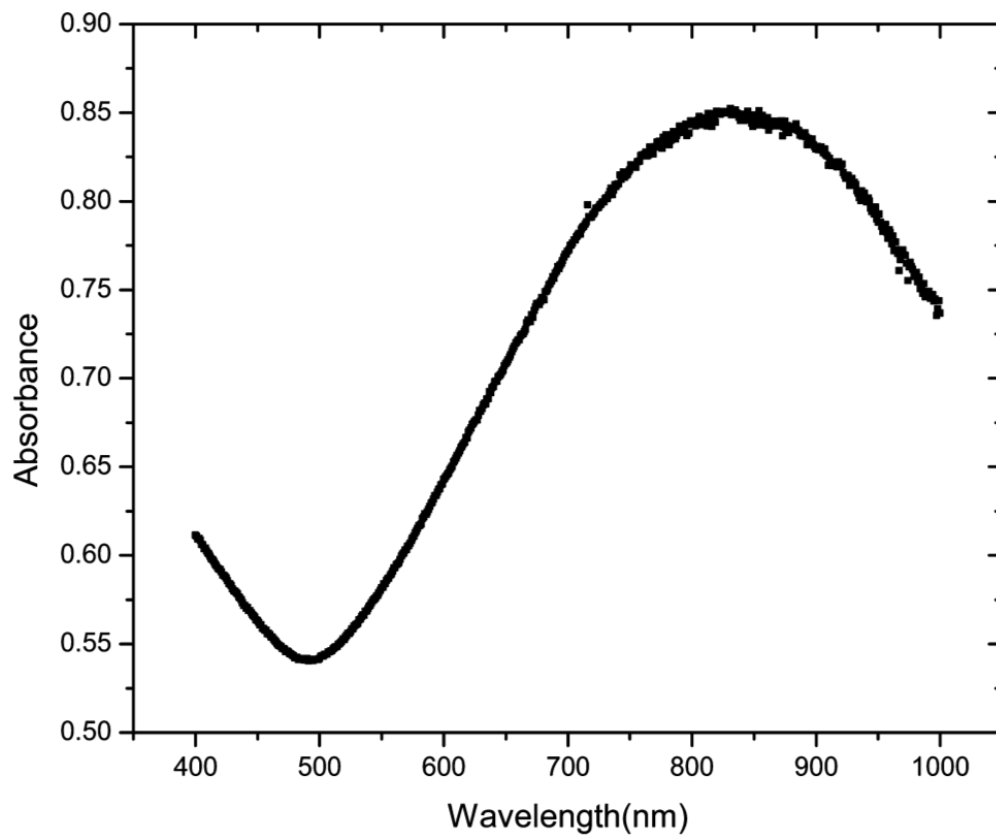
where k is the incident wave vector, n represents the excitation order, and a and b are the expansion coefficients for the transverse magnetic (TM) and transverse electric (TE) excitations. The absorption cross section is given as $C_{abs} = C_{ext} - C_{sca}$. The efficiencies of the spectra are obtained by dividing the cross section by the physical cross section of the particle.

2.4 Results

2.4.1 UV-Vis Spectra

The UV-vis spectrum of the as-prepared HGNs shows an absorption band centered at 830 nm with a full width at half-maximum (FWHM) of 300 nm (Figure 1). The surface plasmon resonance wavelength of the HGNs is red shifted into the NIR from the normal 520 nm peak position of typical solid AuNPs⁴⁰ and is indicative of the hollow nature of the nanoparticles as described in detail in previous studies.⁴² The as-prepared sample was concentrated from a stock solution.

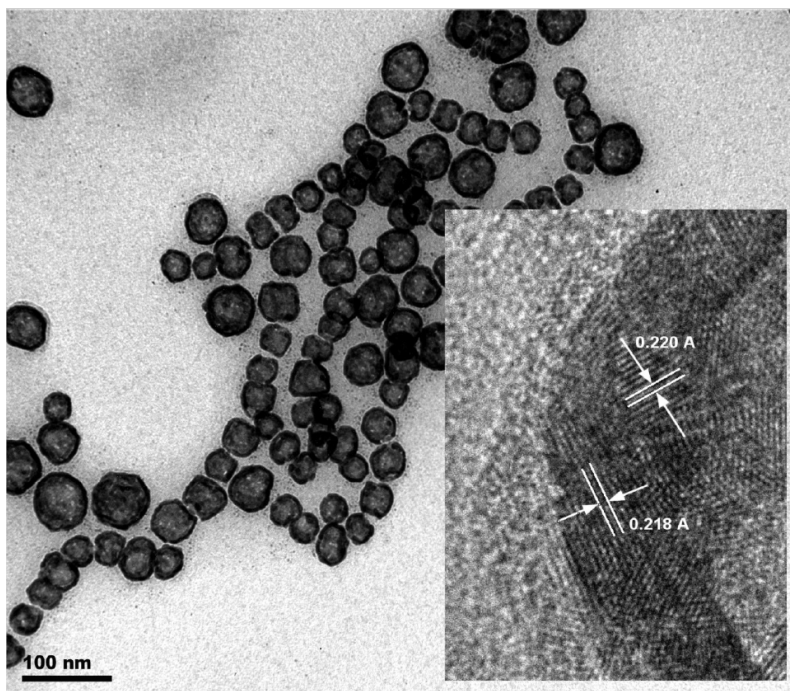
Figure 1. UV-Vis absorbance spectrum of HGNs with peak centered at 830 nm. It should be noted that the UV-Vis spectra reported experimentally are usually called absorption spectra in the spectroscopy community. Strictly speaking, the UV-Vis spectra are extinction spectra, since it contains contributions from both absorption and scattering. Scattering is often unimportant for small molecules but can be substantial for nanoparticles. For convenience, we will continue to call the UV-Vis spectra absorption spectra with the intensity labeled as OD (optical density).



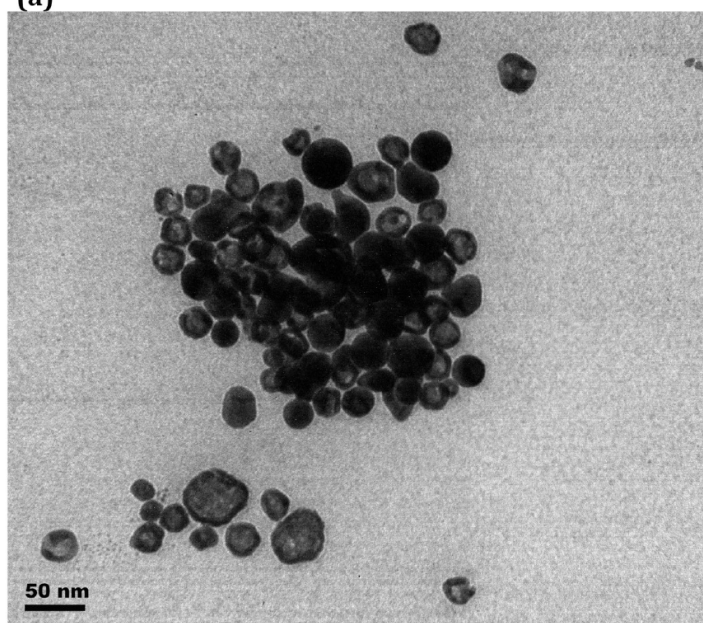
2.4.2 TEM

Low-resolution TEM images of the as-prepared HGNs show an average outer HGN particle diameter of 50 ± 7 nm with a shell thickness of 5 ± 1 nm (Figure 2a). A high-resolution TEM image of the as-prepared HGN, shown in the inset in Figure 2a, shows the lattice spacing of 2.19 Å indicative of the [111] planes of Au and illustrates the polycrystallinity of the HGN. Figure 2b is a low-resolution TEM image of the HGNs after laser irradiation at ND0.1 (indicating ND) 0.1 filter in the laser beam before the sample) and shows the abundance of AuNPs relative to thickened HGNs and as-prepared HGNs.

Figure 2. (a) Representative low-resolution TEM and high-resolution TEM (inset) images of as-prepared HGNs, and (b) TEM image of HGNs post hole burning for the ND0.1 experiment.



(a)

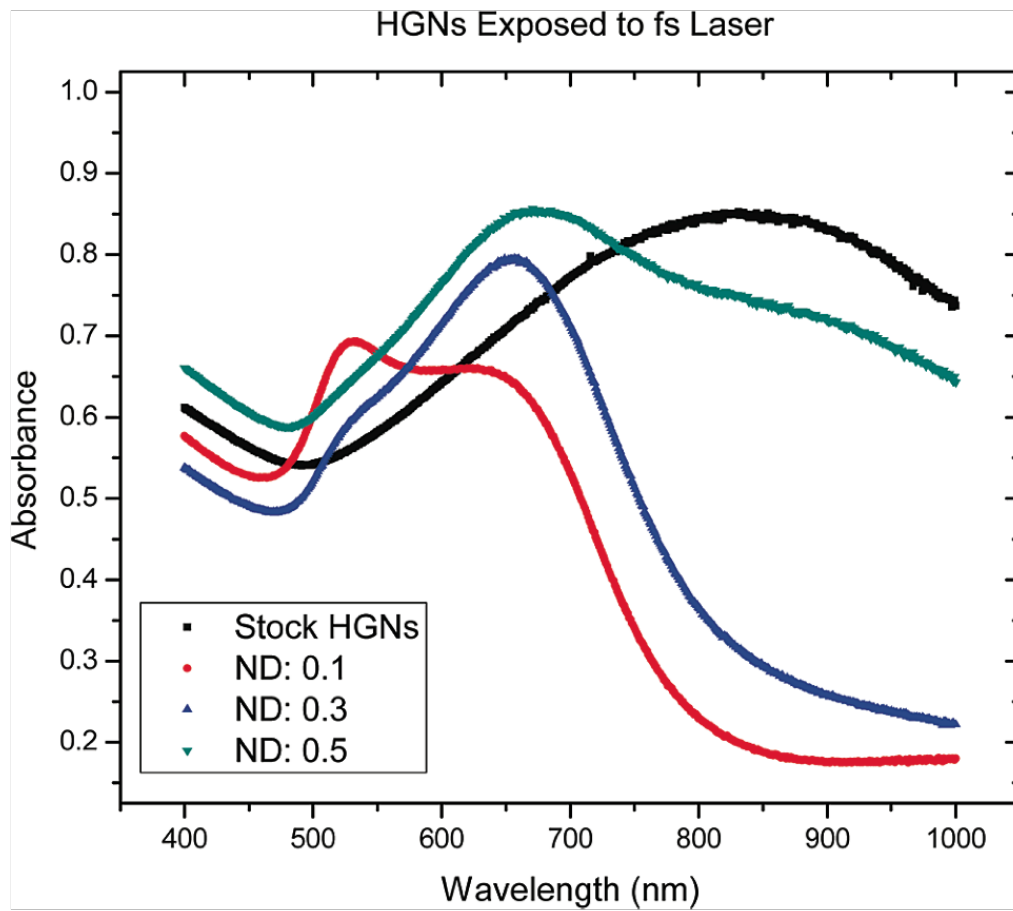


(b)

2.4.3 Persistent Spectral Hole Burning

Figure 3 shows UV-vis spectra of the HGNs after being exposed to fs laser irradiation with varying ND filters in front of the sample.

Figure 3. UV-Vis spectra of as-prepared and post hole-burning HGNs using different ND filters in the laser beam or different laser peak powers.



The as-prepared HGN sample has a broad band centered at 830 nm with an absorbance value of 0.85. The overall spectrum changed dramatically with laser irradiation, and the changes depend strongly on the amount of ND used in the laser beam, or the peak power used, since the average power used was kept the same by adjusting the exposure time on purpose. For ND_{0.5} irradiation, the optical density (OD) of the NIR region of the spectrum decreased by a value of 0.1 while the OD at a bluer region, for example, near 672 nm, grew by about 0.10. The decrease in absorption in the NIR region is indicative of the depletion of HGNS that absorb in that region, while the growth in the bluer region indicates an increase in population of HGNS that absorb there.

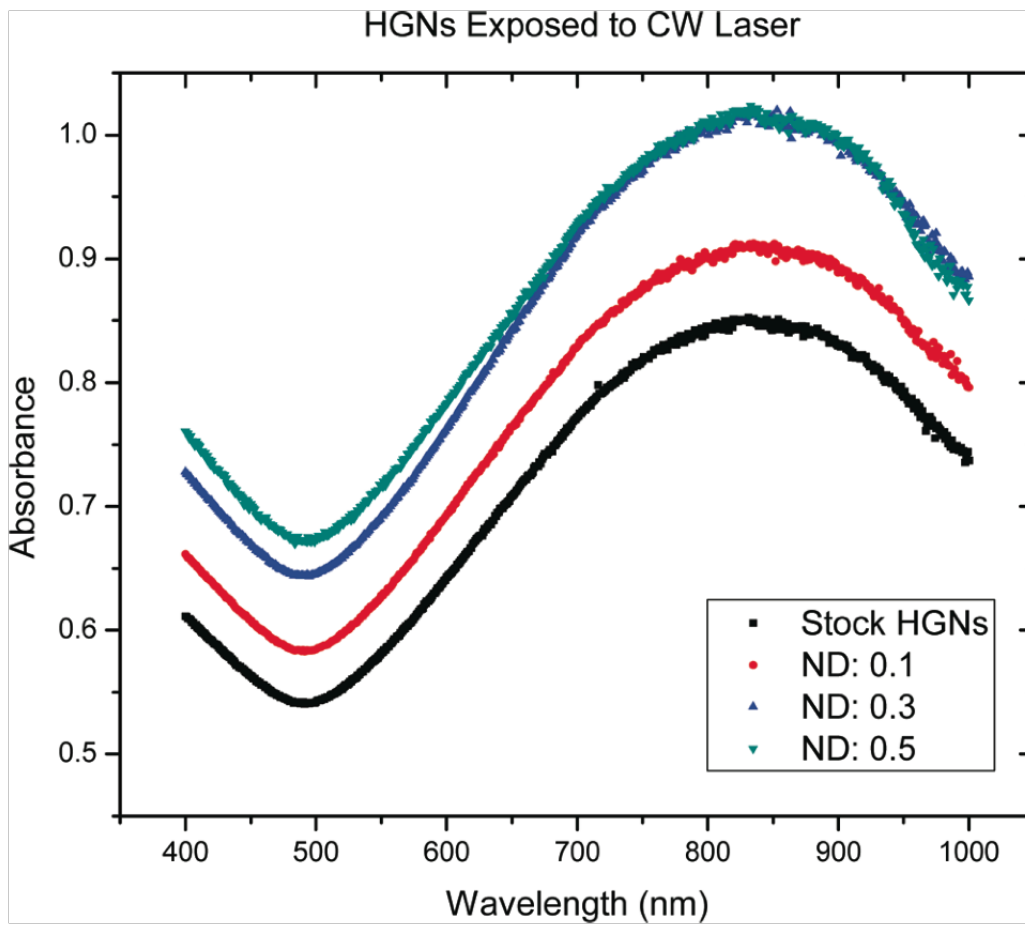
For ND_{0.3} irradiation, that is, increased laser peak power, the NIR depletion near 830 nm is much more pronounced, with a decrease in OD by about 0.55. However, the increase in OD at bluer wavelengths is not as pronounced, with a maximum increase of 0.08 OD occurring for the band centered at 650 nm. Interestingly, a shoulder centered near 520 nm can be seen to grow in, which indicates the formation of solid Au nanoparticles or AuNPs.⁴⁰

For ND_{0.1} irradiation, that is, further increase in peak power, the NIR region close to the laser wavelength of 810 nm shows deeper, and almost complete, depletion while the bluer region, centered at 640 nm, shows no increase in absorption or OD. As a matter of fact, the OD near 640 nm decreased by 0.07. This is likely due to the depletion of HGNS with SPR peaked near 830 nm but with an absorption tail in the 640 nm region because of the broad line shape of the 830 band. The drastic

decrease in absorption at the NIR (830 nm) indicates near complete disappearance of HGNs absorbing at those wave-lengths, while the decrease in the bluer region also indicates a decrease population of HGNs absorbing at 640 nm. The growth of the band centered at 520 nm, an OD increase of 0.14, is more pronounced in this case, indicating that more solid AuNPs have been generated with this laser power relative to the ND_{0.5} or ND_{0.3} experiment.

Figure 4 shows the UV-Vis spectra of the HGNs after being exposed to CW laser irradiation with varying ND filters placed before the sample.

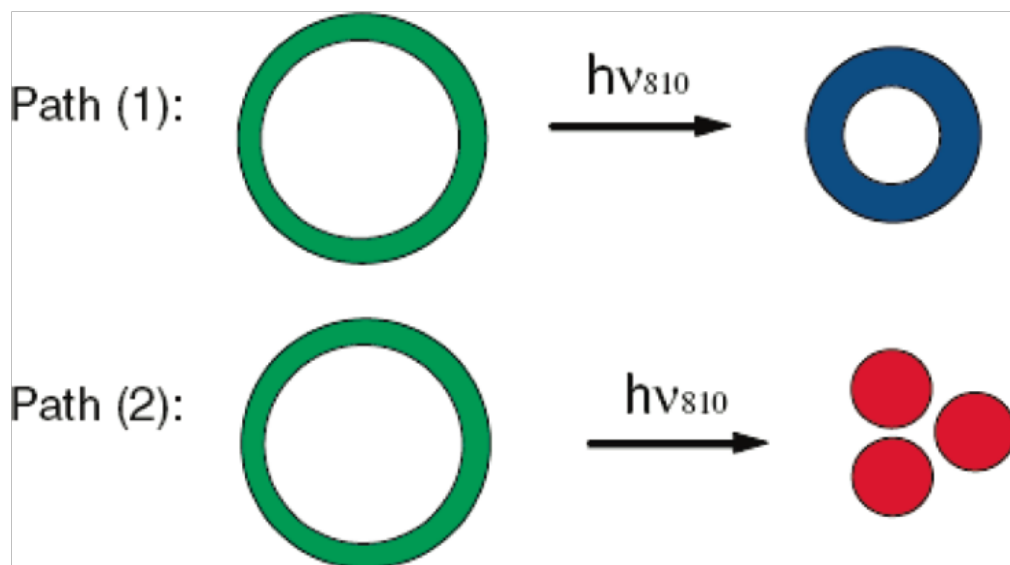
Figure 4. UV-Vis spectra of as-prepared HGNs and HGNs after continuous-wave (CW) hole-burning experiments with different ND filters in the laser beam.



The total power or photon flux is kept the same as in the fs laser hole-burning experiment by adjusting the illumination time. The peak position and FWHM of the broad SPR band did not change with CW laser irradiation. The OD of the spectra did vary somewhat; however, we believe this to be due to some solvent evaporation during the course of the experiment. The most important observation is that there is no hole burning or depletion of HGNs with CW laser irradiation.

The fs hole-burning results presented in Figure 3 have led us to propose a model, shown in Figure 5, based upon the overall structural change that occurs at varying laser peak powers. Two possible processes are believed to occur: (i) the conversion of NIR-absorbing HGNs into bluer HGNs upon NIR laser irradiation, and (ii) the conversion of NIR-absorbing HGNs into AuNPs directly. Path (1) describes results indicative of low peak power irradiation ($ND_{0.5}$ and $ND_{0.3}$ experiments), showing that the post hole-burning solution contains thickened, blue-shifted HGNs, while path (2) depicts results pinpointing higher peak power irradiation experiments ($ND_{0.1}$), showing a preponderance of solid AuNP formation relative to bluer HGNs. A more detailed explanation will be given in the Discussion section.

Figure 5. Schematic illustration of two conversion pathways in the persistent spectral hole burning of as-prepared HGNs with NIR irradiation. Process (2) becomes more dominant over process (1) at higher laser peak power.



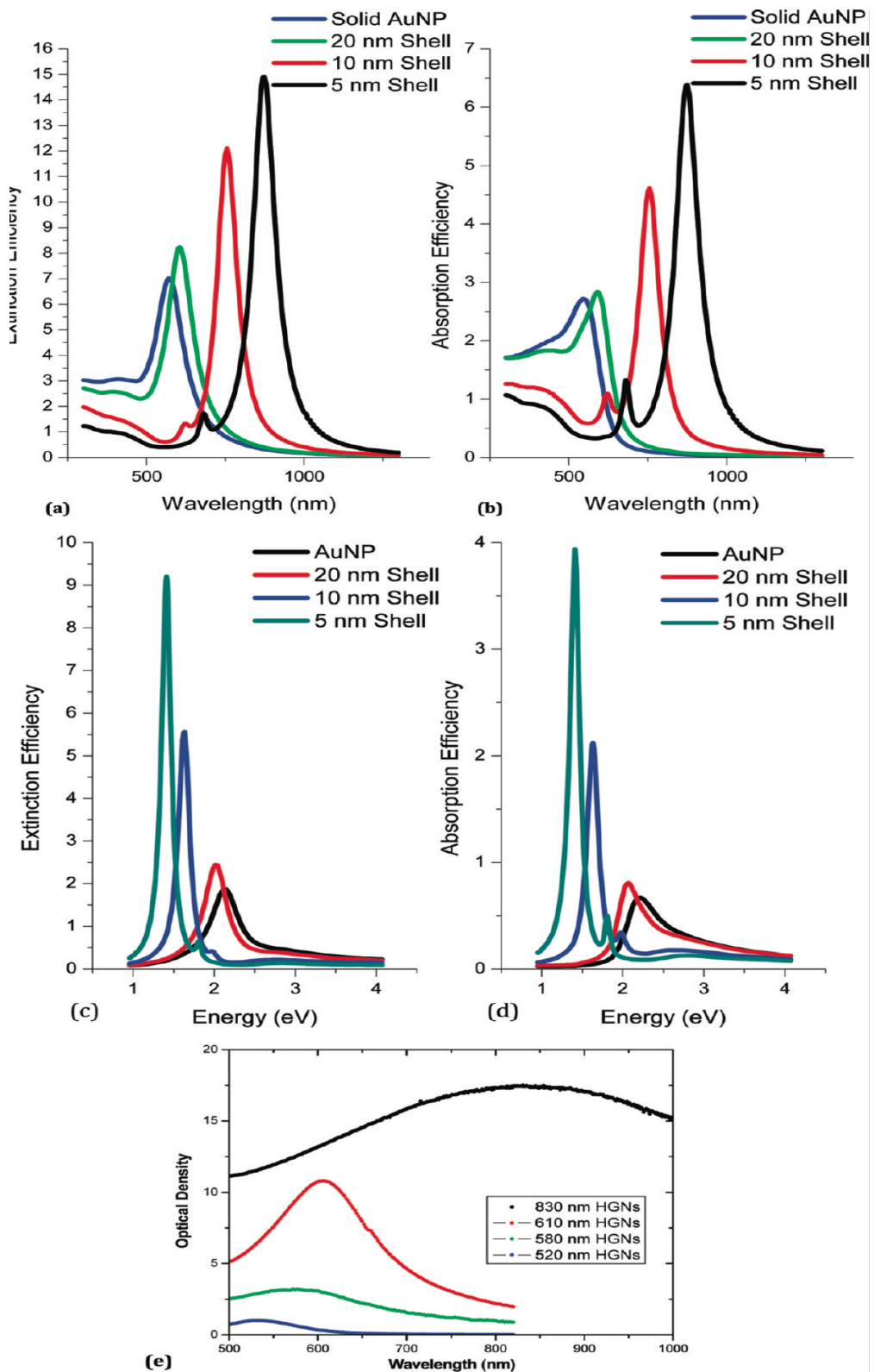
2.4.4 Calculation of Extinction Efficiencies and Electric $|\mathbf{E}|^2$ Fields

Figure 6a and b shows theoretical results from modeling the extinction and absorption efficiencies, respectively, of HGNs with various shell thicknesses as a function of wavelength in nanometers. The environment is taken as water, and the core is treated as water. The dielectric constants of Au are from Palik's book,⁵⁷ and we corrected the size effect using equations described by Coronado *et. al.*⁵⁸ The most notable feature is the substantial red shift of the SPR with decreasing shell thickness, consistent with previous theoretical and experimental results.^{42,59} The FWHM of the SPR seems to increase slightly with decreasing shell thickness.

Since energy difference is nonlinear with respect to wave-length difference ($\Delta E = \Delta\lambda/\lambda^2$), one may gain a different perspective when the spectra are viewed in energy (*e.g.*, eV) instead of in wavelength (nm). Figure 6c and d shows the same spectra shown in Figure 6a and b now as a function of energy given in electron volts. In these spectra, the FWHM measured in electron volts actually decreases as the shell thickness decreases. Figure 6e shows experimental results for several different HGN samples that show larger absorption coefficients and broader FWHM as the SPR red shifts. These results are qualitatively consistent with the theoretical prediction in changes of spectral intensity and FWHM (when Figure 6a and e are compared). Quantitatively, the experimental FWHM seems to be wider than that theoretically predicted. This is likely due to inhomogeneous broadening of the experimental data as a result of heterogeneity in shell diameter and thickness. Also, the shell diameter and thickness of the HGNS measured for Figure 6e are not quantitatively matched

with those calculated theoretically. It is the overall trend in change in FWHM and spectral intensity or extinction/absorption coefficients that are of primary interest here.

Figure 6. Theoretically calculated extinction (a) and absorption (b) efficiency or coefficient (defined as the cross section of the spectrum divided by the cross section of the particle's outer radius) of HGNs with a 50 nm outer radius and varying shell thicknesses, both plotted as a function of wavelength in nm. (c) and (d) are the same data plotted as a function of eV. UV-Vis spectra of four different HGN samples (e): 830 nm absorbing HGNs (50 nm \pm 7 nm core diameter with 5 \pm 1 nm shells), 610 nm absorbing HGNs (35 nm \pm 4 nm core diameter with 6.3 \pm 0.8 nm shells), 580 nm absorbing HGNs (28 nm \pm 2 nm core diameter with 6 \pm 0.5 nm shells), and AuNPs (50 nm \pm 5 nm diameter).



In order to gain some insight about the field distribution of HGNs upon light excitation, enhanced electric fields $|E|^2$ for HGNs of different thicknesses at corresponding resonance wavelengths have been calculated. Figure 7 shows representative results that clearly show a dependence of the field strength on the shell thickness of the HGN, as to be discussed further next. The enhancement is relative to the incident light that was set to be unity. These results are also helpful for understanding effects related to SPR and SERS for which the HGNs have been found to be useful.⁶⁰

2.5 Discussion

2.5.1 Theoretical Calculations of Extinction Spectra of HGNs

In order to properly interpret the spectral shift and intensity changes in the UV-Vis spectra associated with the fs hole-burning experiments, it is important to first understand how the UV-vis spectrum may depend on the detailed structure of the HGNs, for example, shell diameter and thickness. For this purpose, we turn to theoretical calculations for some guidance.

As shown in Figure 6, the extinction and absorption spectra of an HGN with an outer radius of 50 nm and different shell thickness exhibit a strong dependence on the shell thickness, especially in terms of the SPR position and intensity. The resonance wavelength red shifts with decreasing shell thickness, which has been shown experimentally.^{41,42} More importantly for the purpose of this work, the calculations also show that the extinction coefficients at the peak resonance wavelength increases

with decreasing shell thickness. The resonance extinction coefficient is increased from 7.0 for a solid AuNP to 12.3 when the HGN shell thickness is 10 nm. The intensity increases with further decreasing shell thickness down to 5 nm due to the dielectric constant correction (or surface scattering) when the shell thickness is less than the mean free path length of the conduction band electrons. There is a weak peak at around 700 nm when the shell thickness is 5 nm. This is due to the quadrupole excitation of the particle and not the coupling of states of the inner and outer surfaces of the shell. When we limit the excitation order to one (dipole only), this weak peak disappears.

Figure 6b indicates that a thinner shell may allow light to penetrate the particle and increase the absorption coefficient. The resonance absorption coefficient shows a monotonic increase with decreasing shell thickness. The resonance intensity is increased from 2.7 for a solid Au particle to 6.5 when the shell thickness is 5 nm. This is understandable, since surface plasmons are collective oscillations of conduction electrons that happen at the interface between a metal and a dielectric material. The bandwidth (*e.g.*, FWHM) does not seem to change noticeably with the change in shell thickness.

When the spectra are plotted as a function of energy, as shown in Figure 6c and d, the SPR peak intensity increases, and FWHM slightly decreases with decreasing shell thickness. As a result, the change for the integrated area under each band is not substantial. If one normalizes to the mass or amount of gold in the HGN, the thinner-shelled HGNs would have a much higher integrated spectral band or SPR intensity

per unit mass of gold. This feature is quite different from common molecular or atomic systems that usually have spectral intensity proportional to their mass. The difference is due to the unique properties of SPR caused by collective electron oscillation that is essentially classical in nature. The experimental results shown in Figure 6e qualitatively confirm the theoretical prediction that the HGNs with redder SPR, usually due to thinner shells, have larger absorption coefficients, especially when normalized to per mass unit of gold. More generally, HGNs with a decreased aspect ratio (defined as the ratio of the core diameter to shell thickness) display progressively blue-shifted SPR. Additionally, as the aspect ratio decreases, the optical density does as well, with solid AuNPs (aspect ratio of zero) having the most blue-shifted absorbance coupled with the lowest optical density for a given amount of gold. These results are in good qualitative agreement with theory presented above. The above understanding will be important for interpreting the hole-burning results later.

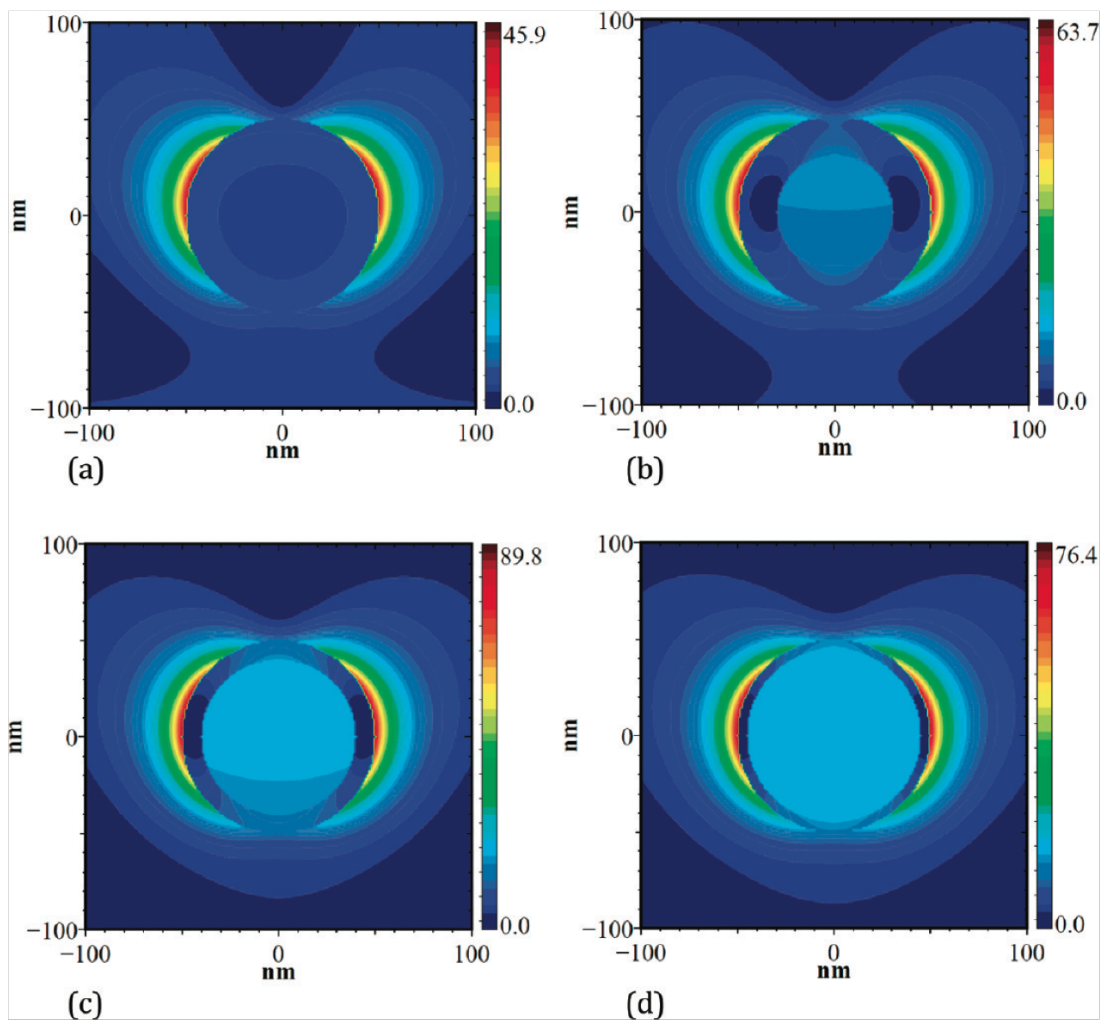
The fact that the thinnest HGNs have the reddest SPR and largest extinction/absorption coefficients is significant for various applications including SPR, SERS, and PTA, since all of these techniques rely heavily on light absorption and their performance is usually enhanced with stronger light absorption.⁴⁶ The thinner shells also require less gold, which is an added advantage.

The enhanced electric fields $|E|^2$ for particles of different thicknesses at corresponding resonance wavelengths shown in Figure 7 indicate that the enhanced local electric field is increased from 46 for a solid particle to 90 when the shell

thickness becomes 10 nm. The enhancement drops with further decreasing shell thickness. Generally speaking, the enhancement is greatest when the plasmon frequency is resonant with incident radiation. Theory can explain the effect of visible and NIR incident radiation for gold, since the plasmon resonance of gold falls within those wavelengths. This also provides deeper insight into the SPR location based on the shell thickness, since SPR is dependent upon the field distribution upon the HGNS.

As will be discussed next, the dependence of the extinction/ absorption coefficients on the HGN structure, for example, shell thickness, has ramifications for the interpretation of the hole-burning experiments.

Figure 7. Electric field $|E|^2$ of 50 nm radius Au core shell particles of different shell thicknesses at corresponding resonance wavelengths. The plot is in the plane determined by the incident wave vector and polarization direction and through the particle center. (a) Solid particle at 570 nm wavelength; (b) shell thickness) 20 at 650 nm wavelength; (c) shell thickness) 10 at 700 nm wavelength; (d) shell thickness) 5 at 880 nm wavelength. The code used for the calculation was written by one of the authors, Shengli Zou.



2.5.2 Mechanism of Femtosecond Hole Burning

As shown in Figure 3, after exposing HGNs to fs laser irradiation at 810 nm with an ND filter of 0.5, the OD at 830 nm (peak of the NIR SPR band) decreased by about 0.1 with a concomitant increase in OD for a band centered at 672 nm (by ~ 0.1 OD). The simplest explanation is that the HGNs absorbing near 830 nm have been destroyed by the laser while HGNs absorbing near 672 nm have been created. Based on the theoretical calculation discussed above, if there is a one-to-one correspondence in the destruction and creation of HGN absorption at the different wavelengths (830 nm vs 672 nm), the increase in OD at 672 nm should be less than the decrease in OD at 830 nm. It should be noted that the theoretical prediction is based on the same outer radius, which is not possible experimentally. When a hollow particle is destroyed and created, the mass is conserved, and the blue shift might be due to increase in thickness, which should be accompanied by a decrease of the outer diameter. Those two factors will both lead to blue shift. The conclusion that the increase in 672 nm should be less than the decrease in OD at 830 nm still holds. However, this did not seem to happen in the observed spectral change. One possible explanation is that the experimental results are more complicated than theoretical calculations, for example, in terms of band overlap and inhomogeneous broadening due to variations in HGN diameter and shell thickness. The most important point is that there is a good correlation in HGN destruction by the incident fs laser and creation of HGNs absorbing at other (bluer) wavelength. This process is illustrated as path (1) in Figure 5. The conversion is likely related to “melting” and shrinking of

the 830 nm absorbing HGNs. Evidence for the “melting” effect can be found in the EM images in Figure 2 that show more rounded HGNs following hole burning. Melting of metal nanostructures such as nanorods has been studied previously.⁴⁸⁻⁵²

For the ND_{0.3} experiment (higher peak power than the ND_{0.5} experiment), the decrease in OD at 830 nm is much more pronounced (by 0.55 OD), while the increase in OD of a bluer band centered at 652 nm is less pronounced compared to the ND_{0.5} experiment (changing by 0.08 OD). The latter is perhaps somewhat unexpected. There are two possible reasons for this. The first is the effect predicted by theory decreasing the OD for bluer SPR, and this effect should be more apparent now, since the peak position is further away from the 830 nm band. The second is the decrease in OD from HGNs that are destroyed by the hole-burning laser but have an absorption tail in the 652 nm region due to the typically broad nature of the SPR.

One of the most interesting observations in this hole-burning experiment is the increase in OD for a band centered at 520 nm that is indicative of the formation of solid AuNPs, as illustrated in path (2) in Figure 5. Thus, the destruction of the 830 nm absorbing HGNs results in not only the formation of 652 nm absorbing HGNs but also the formation of solid AuNPs. The formation of solid AuNPs apparently requires higher peak power than for that of 652 nm absorbing HGNs. The formation of solid AuNPs is most likely another reason for the unexpectedly small increase in OD at 652 nm.

Upon further reducing the ND in the laser beam to ND_{0.1} or increasing the peak power of the fs laser pulses, the OD of the 830 nm absorbing HGNs is almost

completely diminished, while, somewhat surprisingly, a band centered at 640 nm showed a decrease in OD, instead of increase as one may expect. The latter is certainly in contrast to the ND_{0.5} and ND_{0.3} experiments that showed an increase in OD for the bluer band. This decrease in OD for the 640 nm band could be caused by the same reasons discussed above for the relatively smaller increase in OD for the blue band when comparing the ND_{0.3} and ND_{0.5} experiments. Interestingly, the increase in OD for the 520 nm band is more dramatic. In this case, the formation of solid AuNPs apparently dominates over the formation of bluer-absorbing HGNs. Therefore, the branching ratio between processes (2) and (1) increases with peak power of hole-burning laser irradiation.

It should be pointed out that there is no indication of a sequential process, that is, going from red-absorbing HGNs to blue-absorbing HGNs and then to solid AuNPs. For this to occur, a shorter-wavelength laser matching the SPR of blue-absorbing HGNs would be required. Thus, the two processes illustrated in Figure 5 are considered to take place in parallel with path (2) becoming more dominant at higher peak power of the hole-burning laser irradiation in the red or NIR. For example, if the goal is to convert the NIR-absorbing HGNs into bluer-absorbing HGNs, one should choose lower peak power. However, CW laser clearly does not work, and pulsed laser irradiation is necessary to deposit enough energy per HGN and per unit time to generate the effect needed for restructuring of the HGNs.

The hole-burning studies provide useful insights in the possible design and utilization of HGNs as a potential carrier for drug delivery in biomedicine. Pulsed

laser irradiation can be used as a potential means for triggering drug release. Further research is needed to explore this idea for practical applications.

2.6 Conclusion

The persistent spectral hole-burning characteristics and mechanism of hollow gold nanospheres (HGNs) induced by fs laser pulses has been studied. Based on combined UV-vis spectroscopy and TEM data, the mechanism behind the hole burning seems to involve two processes: (i) conversion of NIR absorbing HGNs to bluer-absorbing HGNs upon NIR irradiation, and (ii) breakdown of NIR-absorbing HGNs into solid AuNPs directly. The branching ratio between these two processes is dependent upon the peak power of the fs laser pulses with lower peak power favoring process (i) and higher peak power favoring process (ii). The hole-burning study is instrumental in understanding and exploring the potential use of HGNs in drug delivery with a laser as a trigger for drug release.

To further our understanding, theoretical calculations have been carried out to gain insight into the optical absorption of the HGNs, especially in terms of how the extinction coefficient relates to the structure of the HGNs in comparison to solid AuNPs. One interesting finding is that HGNs with thinner shells not only absorb at redder wavelengths but also have higher extinction and absorption coefficients. The theoretical findings are supported by experimental results. The enhanced extinction coefficient is advantageous for applications such as photothermal ablation therapy (PTA) for cancer treatment, SPR, and SERS.

2.7 References

- (1) Sherry, L. J.; Chang, S. H.; Schatz, G. C.; Van Duyne, R. P.; Wiley, B. J.; Xia, Y. N. *Nano Lett.* **2005**, *5*, 2034.
- (2) Hicks, E. M.; Zhang, X. Y.; Zou, S. L.; Lyandres, O.; Spears, K. G.; Schatz, G. C.; Van Duyne, R. P. *J. Phys. Chem. B* **2005**, *109*, 22351.
- (3) Whitney, A. V.; Elam, J. W.; Zou, S. L.; Zinovev, A. V.; Stair, P. C.; Schatz, G. C.; Van Duyne, R. P. *J. Phys. Chem. B* **2005**, *109*, 20522.
- (4) Haes, A. J.; Hall, W. P.; Van Duyne, R. P. *Laser Focus World*, **2005**, *41*, 105.
- (5) Lahav, M.; Vaskevich, A.; Rubinstein, I. *Langmuir* **2004**, *20*, 7365.
- (6) He, L.; Smith, E. A.; Natan, M. J.; Keating, C. D. *J. Phys. Chem. B* **2004**, *108*, 10973.
- (7) Hutter, E.; Fendler, J. H.; Roy, D. *J. Phys. Chem. B* **2001**, *105*, 11159.
- (8) Jain, P. K.; Ei-Sayed, M. A. *J. Phys. Chem. C* **2007**, *111*, 17451.
- (9) Yonzon, C. R.; Stuart, D. A.; Zhang, X. Y.; McFarland, A. D.; Haynes, C. L.; Van Duyne, R. P. *Talanta* **2005**, *67*, 438.
- (10) Tian, Z. Q. *J. Raman Spectrosc.* **2005**, *36*, 466.
- (11) Haynes, C. L.; Yonzon, C. R.; Zhang, X. Y.; Van Duyne, R. P. *J. Raman Spectrosc.* **2005**, *36*, 471.
- (12) Otto, A. *J. Raman Spectrosc.* **2005**, *36*, 497.
- (13) Nie, S. M.; Emery, S. R. *Science* **1997**, *275*, 1102.
- (14) Hunyadi, S. E.; Murphy, C. J. *J. Mater. Chem.* **2006**, *16*, 3929.

- (15) Cotton, T. M.; Kim, J. H.; Chumanov, G. D. *J. Raman Spectrosc.* **1991**, *22*, 729.
- (16) Jana, N. R.; Gearheart, L.; Murphy, C. J. *J. Phys. Chem. B* **2001**, *105*, 4065.
- (17) Liu, M.; Guyot-Sionnest, P. *J. Phys. Chem. B* **2005**, *109*, 22192.
- (18) Jena, B. K.; Raj, C. R. *J. Phys. Chem. C* **2007**, *111*, 15146.
- (19) Pastoriza-Santos, I.; Liz-Marzan, L. M. *Nano Lett.* **2002**, *2*, 903.
- (20) Im, S. H.; Lee, Y. T.; Wiley, B.; Xia, Y. *Angew. Chem.* **2005**, *117*, 2192.
- (21) Kim, D.; Lee, N.; Park, M.; Kim, B. H.; An, K.; Hyeon, T. *J. Am. Chem. Soc.* **2009**, *131*, 454.
- (22) Haes, A. J.; Hall, W. P.; Chang, L.; Klein, W. L.; Van Duyne, R. P. *Nano Lett.* **2004**, *4*, 1029.
- (23) Arai, T.; Senda, S.-i.; Sato, Y.; Takahashi, H.; Shinoda, K.; Jeyadevan, B.; Tohji, K. *Chem. Mater.* **2008**, *20*, 1997.
- (24) Skrabalak, S. E.; Au, L.; Lu, X. M.; Li, X. D.; Xia, Y. N. *Nanomedicine* **2007**, *2*, 657.
- (25) Skrabalak, S. E.; Au, L.; Li, X. D.; Xia, Y. *Nat. Protocols* **2007**, *2*, 2182.
- (26) Qu, Y. Q.; Porter, R.; Shan, F.; Carter, J. D.; Guo, T. *Langmuir* **2006**, *22*, 6367.
- (27) Schwartzberg, A. M.; Olson, T. Y.; Talley, C. E.; Zhang, J. Z. *J. Phys. Chem. C* **2007**, *111*, 16080.
- (28) Norman, T. J.; Grant, C. D.; Magana, D.; Zhang, J. Z.; Liu, J.; Cao, D. L.;

- Bridges, F.; Van Buuren, A. *J. Phys. Chem. B* **2002**, *106*, 7005.
- (29) Tan, Y.; Jiang, L.; Li, Y.; Zhu, D. *J. Phys. Chem. B* **2002**, *106*, 3131.
- (30) Mahmoud, M. A.; El-Sayed, M. A. *Nano Lett.* **2009**, *9*, 3025.
- (31) Metraux, G. S.; Cao, Y. C.; Jin, R. C.; Mirkin, C. A. *Nano Lett.* **2003**, *3*, 519.
- (32) Kamat, P. V. *J. Phys. Chem. B* **2002**, *106*, 7729.
- (33) Cozzoli, P. D.; Fanizza, E.; Comparelli, R.; Curri, M. L.; Agostiano, A.; Laub, D. *J. Phys. Chem. B* **2004**, *108*, 9623.
- (34) Rand, B. P.; Peumans, P.; Forrest, S. R. *J. Appl. Phys.* **2004**, *96*, 7519.
- (35) Westphalen, M.; Kreibig, U.; Rostalski, J.; Luth, H.; Meissner, D. *Sol. Energy Mater. Sol. Cells* **2000**, *61*, 97.
- (36) Geddes, C. D.; Lakowicz, J. R. *J. Fluoresc.* **2002**, *12*, 121.
- (37) Aslan, K.; Malyn, S.; Geddes, C. *J. Fluoresc.* **2007**, *17*, 7.
- (38) Murphy, C. J.; Gole, A. M.; Hunyadi, S. E.; Stone, J. W.; Sisco, P. N.; Alkilany, A.; Kinard, B. E.; Hankins, P. *Chem. Commun.* **2008**, 544.
- (39) Boisselier, E.; Astruc, D. *Chem. Soc. ReV.* **2009**, *38*, 1759.
- (40) Kimling, J.; Maier, M.; Okenve, B.; Kotaidis, V.; Ballot, H.; Plech, A. *J. Phys. Chem. B* **2006**, *110*, 15700.
- (41) Liang, H. P.; Wan, L. J.; Bai, C. L.; Jiang, L. *J. Phys. Chem. B* **2005**, *109*, 7795.
- (42) Schwartzberg, A. M.; Olson, T. Y.; Talley, C. E.; Zhang, J. Z. *J. Phys. Chem. B* **2006**, *110*, 19935.

- (43) Melancon, M. P.; Lu, W.; Yang, Z.; Zhang, R.; Cheng, Z.; Elliot, A. M.; Stafford, J.; Olson, T.; Zhang, J. Z.; Li, C. *Mol. Cancer Ther.* **2008**, *7*, 1730.
- (44) Lu, W.; Xiong, C.; Zhang, G.; Huang, Q.; Zhang, R.; Zhang, J. Z.; Li, C. *Clin. Cancer Res.* **2009**, *15*, 876.
- (45) Weissleder, R. *Nat. Biotechnol.* **2001**, *19*, 316.
- (46) Zhang, J. Z. *J. Phys. Chem. Lett.* **2010**, *1*, 686.
- (47) Lu, W.; Zhang, G.; Zhang, R.; Flores, L. G., II; Huang, Q.; Gelovani, J. G.; Li, C. *Cancer Res.* **2010**, *70*, 3177.
- (48) Link, S.; Burda, C.; Mohamed, M. B.; Nikoobakht, B.; El-Sayed, M. A. *J. Phys. Chem. A* **1999**, *103*, 1165.
- (49) Kamat, P. V.; Flumiani, M.; Hartland, G. V. *J. Phys. Chem. B* **1998**, *102*, 3123.
- (50) Kurita, H.; Takami, A.; Koda, S. *Appl. Phys. Lett.* **1998**, *72*, 789.
- (51) Inasawa, S.; Sugiyama, M.; Yamaguchi, Y. *J. Phys. Chem. B* **2005**, *109*, 3104.
- (52) Plech, A.; Kotaidis, V.; Lorenc, M.; Boneberg, J. *Nat. Phys.* **2006**, *2*, 44.
- (53) Preciado-Flores, S.; Wang, D.; Wheeler, D. A.; Newhouse, R. J.; Hensel, J. K.; Schwartzberg, A. M.; Wang, L.; Zhu, J.; Barboza-Flores, M.; Zhang, J. Z. *Chem. Mater.*, submitted for publication, 2010.
- (54) Rasband, W. S. *ImageJ*; U. S. National Institutes of Health: Bethesda, MD, 2009; Vol. 1997-2009.
- (55) Mie, G. *Annalen der Physik* **1908**, *25*, 377.

(56) Zou, S. *Chem. Phys. Lett.* **2008**, 454, 289.

(57) Palik, E. D. *Handbook of Optical Constants of Solids*; Academic Press: New York, 1985.

(58) Coronado, E. A.; Schatz, G. C. *J. Chem. Phys.* **2003**, 119, 3926.

(59) Hao, E.; Li, S. Y.; Bailey, R. C.; Zou, S. L.; Schatz, G. C.; Hupp, J. T. *J. Phys. Chem. B* **2004**, 108, 1224.

(60) Schwartzberg, A. M.; Oshiro, T. Y.; Zhang, J. Z.; Huser, T.; Talley, C. E. *Anal. Chem.* **2006**, 78, 4732.

CHAPTER 3. Optical Properties and Coherent Vibrational Oscillations of Gold Nanostars

3.1 Abstract

Hot electron relaxation and coherent vibrational oscillations of gold nanostars (AuNS) were studied using femtosecond laser spectroscopy. Transient profiles feature a fast decay attributed to electron–phonon interaction and a slower decay due to phonon relaxation. Superimposed on the slow decay are oscillations attributed to coherent vibrations of the AuNS with a period dependent on probe wavelength, due to size variation of the AuNS. In addition, persistent spectral hole-burning studies indicate depletion of AuNS at the excitation wavelength and formation of redder-absorbing AuNS aggregates. In conjunction with experiments, theoretical calculations were carried out to gain insight into the coherent vibrational oscillations.

3.2 Introduction

Nanostructures consisting of noble metals have lately been the center of concentrated research due to their interesting optical properties, particularly the surface plasmon resonance (SPR) absorption due to the collective oscillation of conduction band electrons in response to light. Analytical methods based on SPR^{1,2} and surface enhanced Raman scattering (SERS)^{3,4} of metal nanoparticles have attracted much attention due to their potential application in chemical and biological analysis. A central factor to the properties of the SPR is the shape of the

nanoparticles. Advancements in synthetic methodology have resulted in a variety of shapes of nanoparticles, including: rods⁵, prisms⁶, cubes⁷, cages⁸, tubes⁹, aggregates¹⁰, and SPR-tunable hollow spheres¹¹.

Nanostars are another example of metallic nanostructures in which the SPR can be tuned. Recently, nanostars with extinction spectra between 550 and 1800nm have been synthesized^{12,13}. In Kumar's high-yield synthesis¹², it was demonstrated that the size and morphology of the AuNS could be controlled by adjusting the amount of initial Au seeds and the stability-inducing (poly)vinylpyrrolidone (PVP) concentration. Near infrared (NIR) tunability, high sensitivity to local changes in the dielectric environment, and enhancements of the localized electric field^{14,15} have been attributed to the presence of the sharp tips and edges.

The electron relaxation dynamics of metal nanostructures have been investigated in detail via ultrafast studies^{16,17}. An interesting feature observed is the coherent vibrational oscillations attributed to the excitation of the breathing vibrational modes of the nanoparticles due to energy transfer from the hot electrons into the lattice via electron-phonon coupling¹⁷⁻²⁰. This has been reported for gold and silver nanoparticles^{21,22}, gold nanoparticle aggregates²³, and hollow gold nanospheres (HGNs)²⁴.

In this Letter, we report the first study of hot electron relaxation and coherent vibrational oscillations of gold nanostars (AuNS) using ultrafast pump-probe spectroscopy, and found that the periodicity of the oscillations increases with increasing probe wavelength. Additionally, hole burning experiments were

conducted and the conversion from AuNS to laser-induced AuNS aggregates was observed. In conjunction with experiment, theoretical modeling was carried out to help explain the oscillatory behavior. The results are important for exploiting potential applications of AuNS in photothermal ablation (PTA) that rely on efficient photothermal conversion^{25,26}.

3.3 Methods and Materials

3.3.1 Synthesis of AuNP Seeds

Following Kumar's synthesis¹², gold nanoparticle seeds of 15 nm were synthesized by heating 100 mL of 5×10^{-4} M chlorauric acid (HAuCl₄, Aldrich) to boiling, to which was added 5 mL of a 1wt.% sodium citrate (Sigma) solution. After synthesis, the as-formed seeds were coated with poly(vinylpyrrolidone) (PVP, MW = 10000, Fluka) using an estimate of 60 molecules of PVP per nm², and dispersed in ethanol.

3.3.2 Synthesis of AuNS

A 10 mM solution (200 mL) of poly(vinylpyrrolidone) (PVP, MW = 10000, Fluka) in dimethylformamide (DMF, Fluka) was sonicated for 15 min. Subsequently, 1.09 mL of 50 mM HAuCl₄ (Aldrich) was added under continuous stirring at room temperature, followed by the addition of 143 μ L of the Au nanoparticle seeds (4.22 mM), resulting in the formation of AuNS.

3.3.3 UV-Vis and Electron Microscopy (EM)

Absorption measurements were conducted using an HP 8452A diode array spectrophotometer with spectral resolution set at 2 nm. Associated spectra were fit using the Igor 5.0 suite. Low-resolution transmission electron microscopy (TEM) and scanning electron microscopy (SEM) was carried out using an FEI Quanta 3D FEG Dualbeam microscope. Particle sizes were determined using the FEI Quanta's built-in sizing software.

3.3.4 Femtosecond Transient Absorption System

The ultrafast laser system used for the electron–phonon coupling experiments has been described before²⁴. The final output was <220 fs pulses with a power output of ≈ 400 nJ/pulse, centered at 390 nm which was attenuated with neutral density filters. The delay stage controlling the white light continuum (WLC) probe pulse propagation was operated by a motor-driven setup with 1 μ m resolution. The average power density of the laser was maintained at 400 nJ/pulse-cm² at a 0.75 kHz repetition rate. This power density should be considered against the power density of other systems in investigations of electron–phonon coupling times^{27,28}.

The measurements of the coherent vibrational oscillations of the AuNS were performed on a 1-kHz regeneratively amplified Ti:sapphire laser system that delivered 800 μ J pulse energies centered at 800 nm. The amplified pulse was characterized by frequency-resolved optical gating (FROG) pulse diagnostics. The amplified laser output was frequency doubled to generate 400 nm light (200 μ J/pulse), which was attenuated and used as the excitation pump pulse. Coherent

acoustic vibrations of gold nanostars were studied using excitation pulse energies of 500 nJ/pulse. A small portion (4%) of the fundamental laser output was passed through a 0.3-cm thick sapphire plate to generate the continuum probe pulse that typically extended from 450 nm to 850 nm. The pump–probe time delay was controlled using a retroreflecting mirror mounted on a motorized linear translation stage (Newport). Both pulses were spatially overlapped in the sample-laser interaction region. Differential absorption of the probe was measured as a function of the time delay between the pump and probe by mechanically chopping the pump pulse at 500 Hz. The visible probe was spectrally dispersed on a silicon diode array to generate a wavelength-resolved differential absorption spectrum that spanned from 450 to 850nm. The instrument response time (120fs) was determined from the non-resonant response of the pump and probe pulses in water. The full dynamic range of the measurements extended from 10 ps before to 3.3 ns after time zero. Data fitting used in this Letter was similar to previously published methods^{29–31}. Here, temporal integration of data at select wavelengths measured in the transient absorption spectrum provided electronic relaxation kinetic traces. The transient data were fit using an in-house program that uses an iterative least-squares approach. The best fits were obtained using the equation:

$$S(t) = g(t)[A_1 \exp(-t/\tau_1) + A_2 \exp(-t/\tau_2)] \quad (1)$$

where, $g(t)$ is a GAUSSIAN function, which deconvolutes the instrument response function to the GAUSSIAN pump and probe laser pulses, A_n is the amplitude coefficient of the n th component, and T_n is the time constant of the n th component.

At certain wavelengths, an oscillatory time-domain component was superimposed on the transient absorption data. The difference between the experimental data and the fit result obtained using Eq. (1) provided residual data that reflected the coherent vibrational dynamics. The vibrational frequencies of each gold nanostar sample studied were determined by Fourier transformation of the residual data.

Persistent spectral hole burning experiments were conducted by using the output from the optical parametric amplifier in which the pump wavelength was centered at 600 nm. The peak power in each case was varied by the usage of neutral density (ND) filters with values of 0.0, 0.3, and 0.5 (indicated as ND_{0.0}, ND_{0.3}, and ND_{0.5} respectively), while incident photon flux onto the sample was maintained at a constant value of 3×10^{18} photons/s by altering irradiation time. For the experiments, the average laser power was maintained at 820 mW when no ND filters were used.

3.4 Results

3.4.1 UV-Vis Spectra and Persistent Spectral Hole Burning

The UV-Vis spectrum of the as-prepared AuNSs shows an absorption band centered at 600 nm with a FWHM of 110 nm and an absorbance of 0.68 (Figure 1, black line). The SPR wavelength of the AuNS is red-shifted from the characteristic 520 nm peak position attributed to solid AuNPs³² and is attributed to the star-shaped structure of the AuNS as described in previous studies¹². There is a small, sharp peak in the spectra at 650 nm which is likely due to instrument response and is not treated

as a real feature of the spectra.

Figure 1. UV–Vis absorbance spectrum of AuNS with peak centered at 600 nm. The small, sharp peak in the spectra at \approx 650 nm is due to instrument response and is not treated as a real feature of the spectra.

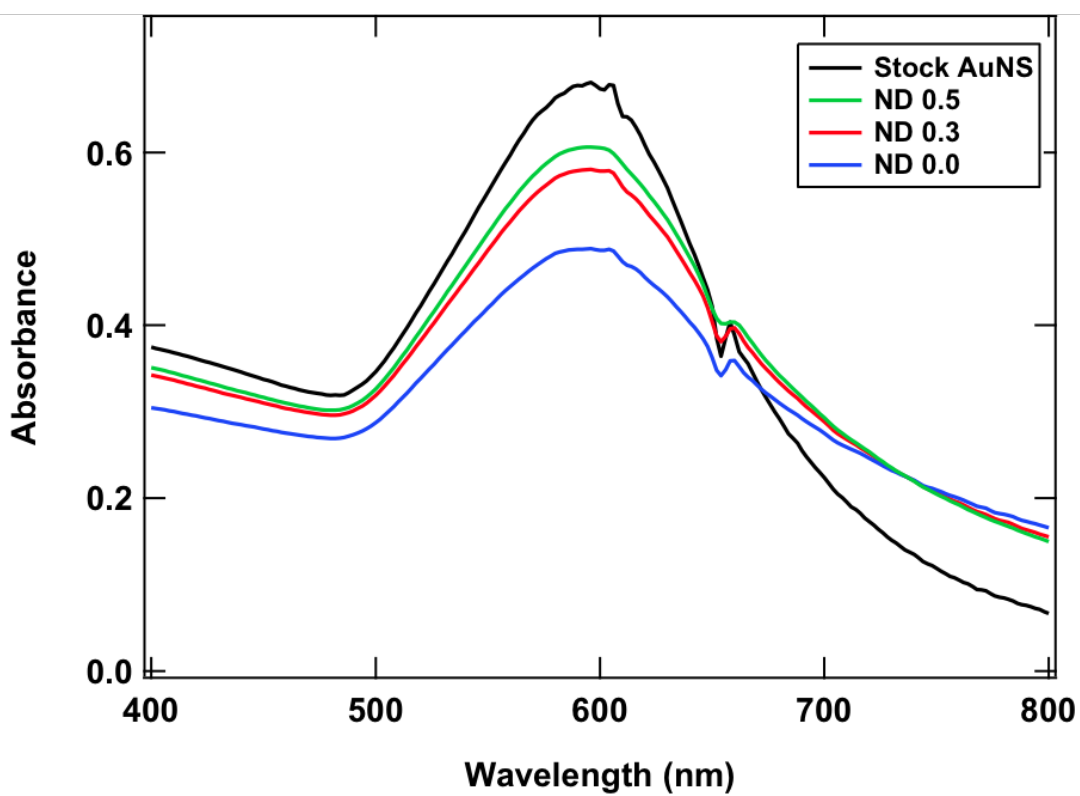


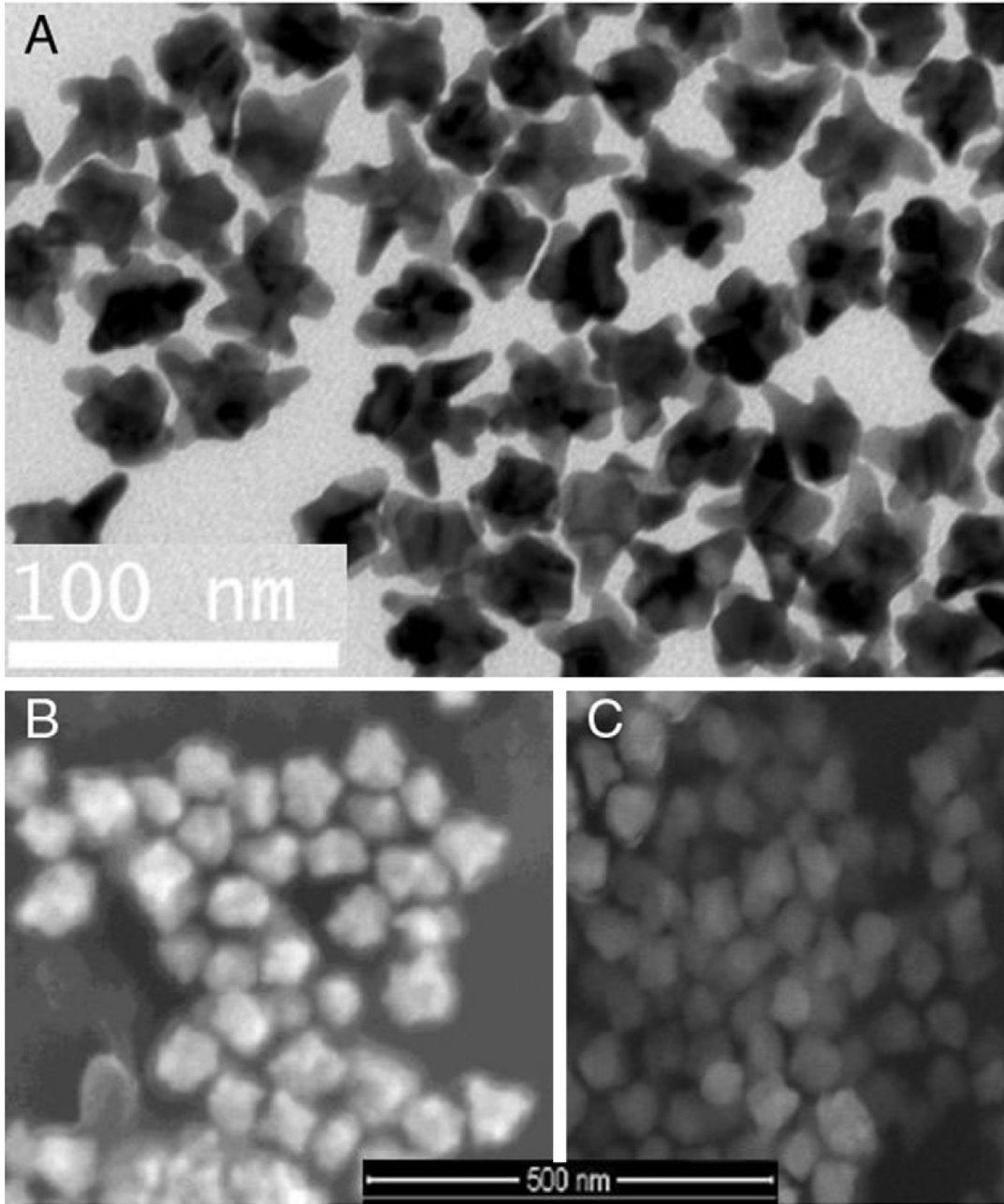
Figure 1 also shows UV–Vis spectra of AuNS after being exposed to 400 nJ/pulse fs laser pulses at 600 nm with varying ND filter in the beam to adjust the laser power at the sample. The spectrum changed appreciably after laser irradiation with the changes depending strongly on the amount of ND used in the laser beam as well as exposure time. After irradiation with ND0.5 in the laser beam the optical density (OD) of the SPR peak at 600 nm decreased by a value of 0.06, from 0.68 to 0.62, which indicates depletion of AuNS that absorb at the laser wavelength. Simultaneously, the OD at redder wavelengths increased, which indicates conversion of the depleted AuNS to another structure with NIR absorption. The redder-absorbing structure could be larger AuNS generated via photoreduction of excess Au³⁺ ions in solution³³ or the production of aggregates^{34,35}. For irradiation with ND_{0.3} in the laser beam, *e.g.*, increasing laser power, the optical density (OD) of the SPR peak decreased by a value of 0.1 from the stock solution, from 0.68 to 0.58. Additionally, there was a further increase in absorbance in the near-infrared (NIR), indicative of a further increase in population that absorbs at red wavelengths.

For irradiation with no ND in the beam, the absorbance of the SPR shows deepest depletion, decreasing by a value of 0.2, from 0.68 to 0.48. Additionally, red wavelengths show the more pronounced increase in absorbance, indicative of the largest increase in population that absorbs in the NIR. The results show that higher laser power resulted in more depletion of AuNS absorbing at the laser wavelength and formation of more of the species absorbing in the NIR might be responsible for an increased population of AuNS aggregates that absorb there.

3.4.2 SEM and TEM

Figure 2a is a TEM image of the as-prepared AuNS and shows star-like nanostructures incorporating a roughly spherical core and several pointed protrusions per nanostar. The average particle radius measured to be 35 ± 5 nm. The uncertainty in the measurement is due to the varied nature of the protrusions on the individual AuNS. The inset image is a close-up view of two AuNS, clearly displaying the pointed protrusions of the nanostructure. Figure 2b is an SEM image of the as-prepared AuNS, showing the high degree of surface roughness and star-like protrusions per particle. Also evident is the thin layer of protecting PVP that encapsulates the AuNS. Figure 2c is an SEM image of post-irradiated AuNS.

Figure 2. (a) Representative low-resolution TEM images of as-prepared AuNS. (b,c) SEM image of as-prepared AuNS, with the PVP-encapsulating and protecting layer visible.



3.4.3 Ultrafast Pump-probe Transient Absorption

Figure 3a shows the transient bleach recovery profile of the AuNS probed at 600 nm following excitation at 390 nm for two different excitation intensities of 100 and 400 nJ/pulse. The recovery following the initial pulse-width limited decay can be fit with a double exponential, similar to what has been observed in solid gold nanoparticles^{17,21,36}. At the higher power, the fast time constant is approximately 2.5 ps, while at the lower power the time constant decreased to \approx 1.5 ps. Experimental evidence of faster relaxation due to lower pump powers has been seen before^{17,23,37} and is similar to that of gold nanoparticle films³⁸. The inset of Figure 3a is a plot of the electron–phonon coupling time for several pump powers. The linear trend of the data indicates that the two-temperature model is correct and that we are pumping the samples in the linear regime, for which more will be discussed later.

Figure 3b shows the coherent portion of the transient absorption data, obtained from AuNS samples of varying size: 35, 59, and 188 nm. All samples were excited using a 400-nm pump wavelength (500 nJ/pulse), and monitored with temporally delayed probe wavelengths of 580, 590, and 705 nm for the 35, 59, and 188 nm diameter samples, respectively. As can be seen from the amplitude of the oscillations, the coherent data accounted for \approx 15–20% of the total signal. Note that the time axis of the 188 nm sample is 3 \times longer than that of the other two due to the low frequency of the acoustic mode. For the 35 nm AuNS sample probed at 580 nm, the oscillations have a period of 8 ps, while the 59 nm AuNS sample probed at 590 nm probe wavelength has a period of oscillation of 13 ps. Finally, for the 188 nm

AuNS sample probed at 705 nm, the oscillation period is 75 ps. At long time periods, the observed oscillations are seen to have damped out after the initial excitation pulse. From fast Fourier transform (FFT) presented in Figure 3c, the oscillation periods for the 35, 59, and 188 nm AuNS were calculated to be 4.0, 2.2, and 0.3 cm^{-1} , respectively. Performing FFT on the data also has the added benefit of accounting for group velocity dispersion (GVD), since the frequency of oscillation is not affected by the zero-time, which is obscured by GVD. Given the large signal-to-noise ratio, we attribute a nominal 5% error within these reported values. The physical process the oscillations represent is attributed to coherent vibrations following hot electronic relaxation, similar to what has been observed before for various gold nanoparticle systems including solid particles¹⁷, nanorods³⁷, hollow nanospheres²⁴, and nanoparticle aggregates²³.

Figure 3. (a) Ultrafast electronic relaxation dynamics of AuNS at two different pump powers, highlighting the power dependence of the fast component of the decay. Inset: plot of the electron–phonon coupling time as a function of pump power. (b) Probe wavelength-dependent transient bleach time traces of AuNS samples of varying size: 35, 59, and 188 nm following a 400 nm pump wavelength (500 nJ/pulse) for probe wavelengths of 580, 590, and 705 nm for the 35, 59, and 188 nm diameter samples, respectively. (c) Fast Fourier Transforms (FFT) of the data presented in Figure 3b. From FFT, the oscillation periods for the 35, 59, and 188 nm AuNS were calculated to be 4.0, 2.2, and 0.3 cm^{-1} , respectively.

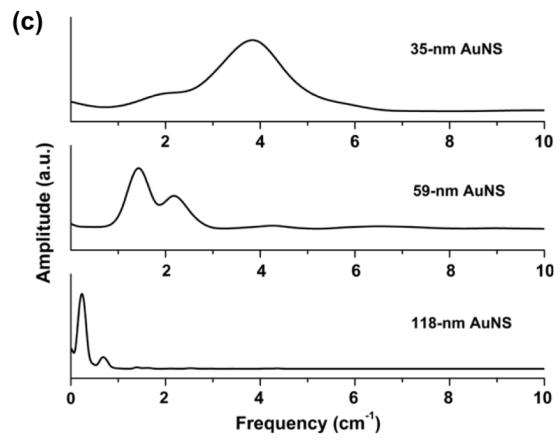
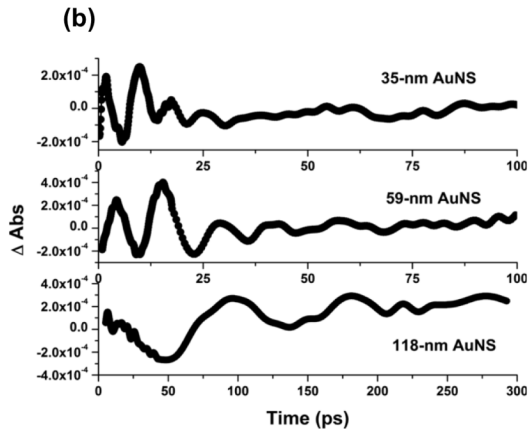
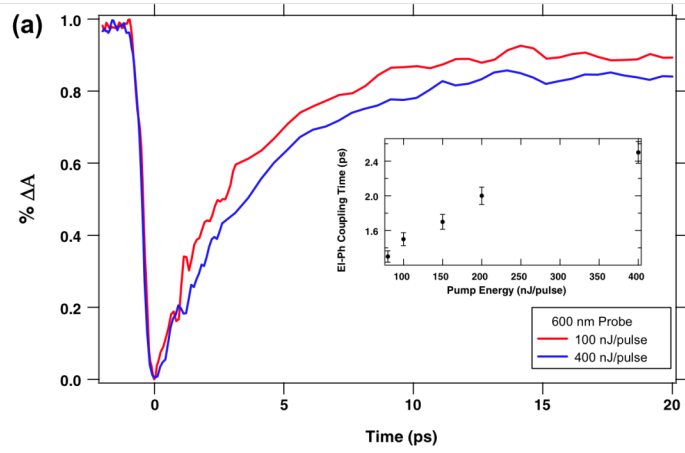
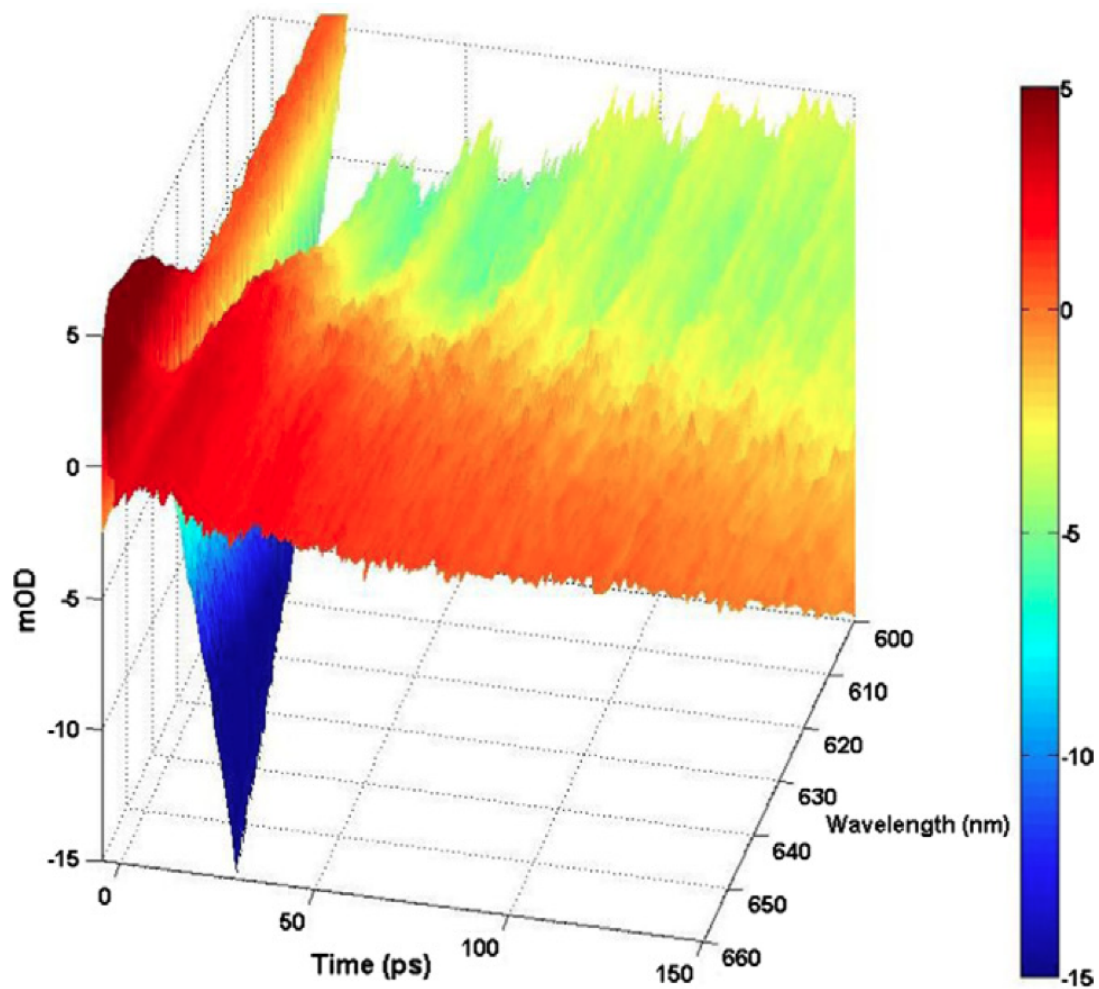


Figure 4 is a three-dimensional (3D) plot of the relaxation profile of the AuNS following the initial excitation pulse. A pulse-width limited bleach (<220 fs) is followed by an exponential fast recovery (1.5 ps) and the onset of periodic oscillations attributed to coherent vibrational modes of the AuNS. As will be discussed, the initial fast relaxation of the AuNS following irradiation is pump power-dependent and is explainable by the two-temperature model^{21,39}. To illustrate the validity of the two-temperature model, the electron-phonon coupling time as a function of pump pulse power should yield a linear plot, as is shown in the inset of Figure 3a.

Figure 4. Three-dimensional plot of the transient bleach followed by few ps recovery and coherent vibrational oscillations of the AuNS after a pump excitation of 400 nm which illustrates the coherent vibrational oscillations of the AuNS.



3.4.4 Theoretical Modeling and Calculation of Periodic Oscillations

We analyzed theoretically the vibrational modes of the AuNS. Since there is no available theory to model vibrational oscillations for particles of arbitrary shape (*e.g.*, AuNS), we treated the nanoparticle as a sphere of similar volume (AuNP). In a simulation, we used the same model as our previous letter for hollow gold nanospheres²⁴. The oscillation period, T_{osc} , should converge to the value for a solid AuNP with a 35 nm radius which was modeled to be 18.2 ps. We also utilized the elastic sphere model by Hodak *et al.*²¹, to gain further qualitative insight into the expected T_{osc} for an AuNP with a 35 nm radius. The elastic sphere model was predicted to be 22.9 ps for an AuNP with a 35 nm radius. In both cases, the modeled oscillation period is longer than the experimentally-derived result.

3.5 Discussion

3.5.1 Experimental and Calculated Oscillations

The initial fast relaxation of the AuNS (Figure 3a), which is attributed to electron–phonon coupling, is dependent upon the power of the pump pulses. This power dependence is similar to previous observations for solid gold or silver nanoparticles and can be explained by the two temperature model^{21,39} which states that higher pump powers will produce higher electronic temperatures, yielding longer relaxation times because of the temperature dependence of electronic heat capacity. The inset of Figure 3a illustrates the validity of the two-temperature model due to the overall linear nature of the electron–phonon coupling time as a function of pump

pulse power.

On longer time scales (Figure 3b) the transient decay profiles show oscillations, which are attributed to the coherent vibration of the breathing mode of the AuNS. There are two interesting features to note. First, the oscillation period becomes longer with redder probe wavelengths, as has been supported before in literature⁴⁰. Second, the onset of the first oscillation peak appeared later in time for redder probe wavelengths. Both features can be explained by the possibility that SPR spectrum of the AuNS is inhomogeneously broadened due to size or mass dispersion, similar to what has been found for Au nanoparticle aggregates²³. Due to the dependence of SPR on nanoparticle size⁴¹, larger or more massive particles have redder absorption. Thus, the redder probe wave- lengths interrogate redder-absorbing AuNS with larger size or more mass and thereby longer oscillation period^{21,42}. Likewise, the onset of the initial oscillation period will be delayed in time since larger or more massive particles will take longer to begin oscillating following hot electron relaxation. The effect of higher mass or large size effectively makes the oscillation slower or longer in period.

In comparison to AuNPs of the same average size (35 nm), the predicted oscillation period, τ , from the elastic sphere model²¹, can be calculated from:

$$\tau = \frac{2R\pi}{\eta c_i} \quad (2)$$

where R is the radius of the NPs, g is the vibrational eigenvalue taken to be 2.95 from experiment, and c_i is the longitudinal speed of sound in gold which is 3240 ms^{-1} ,²¹. From this, an oscillation periodicity of 23 ps is expected for AuNPs with 35 nm in

diameter. Clearly, as can be seen in [Figure 3b](#), this is not the case, indicating that the elastic sphere model does not hold for particles of arbitrary shape such as AuNS.

In both the simulated work, which yielded an oscillation period of 18.2 ps, and in the elastic sphere model, which yielded an oscillation period of 23 ps, the oscillation periodicity is notably longer than that of the experimentally-derived value of 13 ps. One potential reason for this involves the notion that the star-like protrusions, which overall have a lower mass, may contribute a faster oscillation period to the overall particle, yielding an overall oscillation period that is shorter than that of spherical particles. This would indicate also that the experimental oscillations have contributions from both the spherical core as well as the star-like protrusions. Ideally, this would be measured experimentally, however, having a precise control over the number and size of protrusions on the AuNS is experimentally difficult, if not impossible, to obtain.

3.5.2 Persistent Spectral Hole Burning

As shown in [Figure 1](#), after exposing the AuNS to fs laser pulses at 600 nm with an ND filter of 0.0, the optical density (OD) dropped by 0.2 with a concomitant increase at red wavelengths by 0.09 (at 800 nm). The simplest explanation is that AuNS populating the band centered at 600 nm have been induced to aggregate with each other, giving rise to the increased OD at red wavelengths. Laser-induced aggregation of metal nanoparticles has been seen before^{34,43}. It is seen from [Figure 1](#) that ND_{0.0} (higher peak power than ND_{0.3} and ND_{0.5}) results in a slightly increased

absorbance at 800 nm than ND0.3 does, indicating that the higher laser power irradiation will generate larger, *e.g.*, more red-shifted aggregates at that wavelength than the lower power laser irradiation. This is perhaps indicative that higher laser power is responsible for more aggregate growth at red wavelengths. The same trend of decreasing absorbance of SPR with increasing OD at red-wavelengths is true with ND0.3 and ND0.5 irradiation, but to a lesser extent. The band centered at 600 nm decreases by 0.1 with a concomitant increase in absorbance at wavelengths red of 660 nm.

When comparing the ND_{0.0}, ND_{0.3}, and ND_{0.5} results, an interesting trend emerges. At 675 nm, both ND_{0.3} and ND_{0.5} show a higher OD than ND_{0.0} (0.35 *vs.* 0.30), which indicates that the lower peak power irradiation generates more aggregates in that spectral region, *i.e.*, aggregates that are smaller. In other words, ND_{0.3} and ND_{0.5} indicate that while aggregation in the form of increased absorbance is produced, the aggregates that are produced are smaller (blue-shifted) than the aggregation produced from higher power experiments, ND_{0.0} (red-shifted). However, at wavelengths near 800 nm, the trend reverses, showing that ND_{0.0} absorbs more in that spectral region. This is indicative that the highest laser power will produce larger aggregates since a larger absorbance at a particular wavelength is indicative of a larger population. That is, because ND_{0.0} has a higher absorbance at 800 nm than ND_{0.3} and ND_{0.5}, there are larger and more massive aggregates forming at that spectral region.

A fundamental question arises when inspecting these hole burning data and is

related to what causes the aggregation. Although a modification of the dielectric environment around the AuNS could in principle be responsible for the observed spectral changes, we believe that the mechanism behind the aggregation is related to the protecting layer of PVP that is incorporated during AuNS synthesis. We believe that laser irradiation of the AuNS caused the protecting layer of PVP to melt off, thereby opening up the possibility for the unprotected AuNSs to aggregate. This type of phenomenon is similar to what has been seen before [44] Because an increase in absorbance was not seen at wavelengths blue of the AuNS' SPR in the UV-Vis spectra of Figure 1, we believe that the laser irradiation, while strong enough to melt the PVP layer off, was not strong enough to cause particle melting and reshaping, which has been seen before⁴⁵⁻⁴⁷. When comparing SEM images before and after laser irradiation, a clear change in the apparent aggregate or individual particle structure was not seen (Figure 2a and b). As mentioned previously, there were no melted particles that resulted in a spherical shape. It is possible that the AuNS represented in Figure 2a and b are part of a larger aggregated structure which tends to dominate the UV-Vis spectrum. Nevertheless, an aggregation of unprotected AuNS would lead to enhanced absorption in the NIR which explains the results in Figure 1. Because the NIR absorbance of ND_{0,0}-irradiated AuNS is higher than ND_{0,3} and ND_{0,5}, and because laser power is higher with ND_{0,0} than ND_{0,3} and ND_{0,5}, we believe that the higher laser powers are more effectively melting the PVP layer away, thereby resulting in a higher degree of aggregation.

3.6 Conclusion

The ultrafast electronic relaxation and coherent vibrational oscillations of AuNS have been studied using ultrafast pump–probe techniques. The fast component of the electronic relaxation is seen to have a power dependence, which becomes faster with decreasing pump powers. Also, coherent vibrational oscillations of AuNS are observed with the periodicity of the oscillations dependent on probe wavelengths: longer period at redder probe wavelengths. This is likely because AuNS with large size have SPR at longer wavelength and a longer oscillation period. The calculated results of oscillation period for AuNPs as a model system agree qualitatively with the experimental results of AuNS. Persistent spectral hole burning showed aggregation of the AuNS after exposure to fs laser pulses. The net result is that higher peak power generates larger and therefore more red-shifted aggregates than lower peak power does and is thought to be due to the ablation of the protecting layer of PVP. The results have implications for the exploitation of AuNS in photothermal ablation (PTA) which relies on efficient photothermal conversion.

3.7 References

- [1] E. Hutter, J.H. Fendler, D. Roy, *J. Phys. Chem. B* 105 (2001) 11159.
- [2] M. Lahav, A. Vaskevich, I. Rubinstein, *Langmuir* 20 (2004) 7365.
- [3] T.M. Cotton, J.H. Kim, G.D. Chumanov, *J. Raman Spectrosc.* 22 (1991) 729.
- [4] S.M. Nie, S.R. Emery, *Science* 275 (1997) 1102.

- [5] N.R. Jana, L. Gearheart, C.J. Murphy, *J. Phys. Chem. B* 105 (2001) 4065.
- [6] I. Pastoriza-Santos, L.M. Liz-Marzan, *Nano Lett.* 2 (2002) 903.
- [7] S.H. Im, Y.T. Lee, B. Wiley, Y. Xia, *Angew. Chem. Int. Ed.* 44 (2005) 2154.
- [8] S.E. Skrabalak, L. Au, X.M. Lu, X.D. Li, Y.N. Xia, *Nanomedicine* 2 (2007) 657.
- [9] Y. Qu, R. Porter, F. Shan, J.D. Carter, T. Guo, *Langmuir* 22 (2006) 6367.
- [10] T.J. Norman et al., *J. Phys. Chem. B* 106 (2002) 7005.
- [11] A.M. Schwartzberg, T.Y. Olson, C.E. Talley, J.Z. Zhang, *J. Phys. Chem. B* 110 (2006) 19935.
- [12] P.S. Kumar, I. Pastoriza-Santos, B. Rodríguez-González, F.J.G.d. Abajo, L.M. Liz-Marzán, *Nanotechnology* 19 (2008) 015606.
- [13] P. Sajanlal, T. Pradeep, *Nano Res.* 2 (2009) 306.
- [14] C. Burda, X. Chen, R. Narayanan, M.A. El-Sayed, *Chem. Rev.* 105 (2005) 1025.
- [15] F. Hao, C.L. Nehl, J.H. Hafner, P. Nordlander, *Nano Lett.* 7 (2007) 729.
- [16] S.L. Logunov, T.S. Ahmadi, M.A. El-Sayed, J.T. Khoury, R.L. Whetten, *J. Phys. Chem. B* 101 (1997) 3713.
- [17] J. Hodak, I. Martini, G.V. Hartland, *Chem. Phys. Lett.* 284 (1998) 135.
- [18] C. Voisin, N. Del Fatti, D. Christofilos, F. Vallée, *J. Phys. Chem. B* 105 (2001)

2264.

[19] A.L. Tchebotareva, P.V. Ruijgrok, P. Zijlstra, M. Orrit, *Laser Photonics Rev.* 4 (2010) 581.

[20] G.V. Hartland, *Annu. Rev. Phys. Chem.* 57 (2006) 403.

[21] J.H. Hodak, A. Henglein, G.V. Hartland, *J. Chem. Phys.* 111 (1999) 8613.

[22] N. Del Fatti, S. Tzortzakis, C. Voisin, C. Flytzanis, F. Vallée, *Phys. B Condens. Matter.* 263–264 (1999) 54.

[23] C.D. Grant, A.M. Schwartzberg, T.J. Norman, J.Z. Zhang, *J. Am. Chem. Soc.* 125 (2002) 549.

[24] R.J. Newhouse, H. Wang, J.K. Hensel, D.A. Wheeler, S. Zou, J.Z. Zhang, *J. Phys. Chem. Lett.* 2 (2011) 228.

[25] M.P. Melancon et al., *Mol. Cancer Ther.* 7 (2008) 1730.

[26] W. Lu, G. Zhang, R. Zhang, L.G. Flores, Q. Huang, J.G. Gelovani, C. Li, *Cancer Res.* 70 (2010) 3177.

[27] G.V. Hartland, *Int. J. Nanotechnol.* 2004 (1) (2004) 307.

[28] N. Del Fatti, A. Arbouet, F. Vallée, *Appl. Phys. B: Laser Opt.* 84 (2006)

175.

[29] K.L. Knappenberger, A.M. Schwartzberg, A.-M. Dowgiallo, C.A. Lowman, *J. Am. Chem. Soc.* 131 (2009) 13892.

[30] A.-M. Dowgiallo, A.M. Schwartzberg, K.L. Knappenberger, *Nano Lett.* 11 (2011)

3258.

[31] A.M. Dowgiallo, K.L. Knappenberger, *Phys. Chem. Chem. Phys.* 13 (2011)

21585.

[32] J. Kimling, M. Maier, B. Okenve, V. Kotaidis, H. Ballot, A. Plech, *J. Phys. Chem. B* 110 (2006) 15700.

[33] K. Kurihara, J. Kizling, P. Stenius, J.H. Fendler, *J. Am. Chem. Soc.* 105 (1983)

2574.

[34] F. Mafuné, J.-y. Kohno, Y. Takeda, T. Kondow, *J. Phys. Chem. B* 105 (2001) 9050.

[35] N. Matsuo, H. Muto, K. Miyajima, F. Mafune, *Phys. Chem. Chem. Phys.* 9 (2007)

6027.

[36] S. Link, A. Furube, M.B. Mohamed, T. Asahi, H. Masuhara, M.A. El-Sayed, *J. Phys. Chem. B* 106 (2002) 945.

- [37] S. Link, M.A. El-Sayed, *J. Phys. Chem. B* 103 (1999) 8410.
- [38] M.J. Feldstein, C.D. Keating, Y.-H. Liao, M.J. Natan, N.F. Scherer, *J. Am. Chem. Soc.* 119 (1997) 6638.
- [39] R.W. Schoenlein, W.Z. Lin, J.G. Fujimoto, G.L. Eesley, *Phys. Rev. Lett.* 58 (1987)1680.
- [40] M. Hu, X. Wang, G.V. Hartland, P. Mulvaney, J.P. Juste, J.E. Sader, *J. Am. Chem. Soc.* 125 (2003) 14925.
- [41] Y. Sun, Y. Xia, *Analyst* 128 (2003) 686.
- [42] J.H. Hodak, I. Martini, G.V. Hartland, *J. Phys. Chem. B* 102 (1998) 6958.
- [43] V.P. Drachev, S.V. Perminov, S.G. Rautian, *Opt. Express* 15 (2007) 8639.
- [44] A.M. Schwartzberg, C.D. Grant, T. van Buuren, J.Z. Zhang, *J. Phys. Chem. C* 111 (2007) 8892.
- [45] S. Link, C. Burda, M.B. Mohamed, B. Nikoobakht, M.A. El-Sayed, *J. Phys. Chem. A* 103 (1999) 1165.
- [46] P.V. Kamat, M. Flumiani, G.V. Hartland, *J. Phys. Chem. B* 102 (1998) 3123.
- [47] H. Kurita, A. Takami, S. Koda, *Appl. Phys. Lett.* 72 (1998) 789.

CHAPTER 4. Nanostructured Hematite: Synthesis, Characterization, Charge Carrier Dynamics, and Photoelectrochemical Properties

4.1 Abstract

As one of the most prevalent metal oxides on Earth, iron oxide, especially α -Fe₂O₃ or hematite, has been the subject of intense research for several decades. In particular, the combination of a relatively small bandgap and related visible light absorption, natural abundance, low cost, and stability under deleterious chemical conditions has made it ideal for many potential applications. However, the short charge carrier lifetime or diffusion length has limited its applicability. Nanostructures of hematite offer the possibility of overcoming some of the limitations through control of the structures and thereby its optical and electronic properties. In this review, we provide an overview of recent progress on the synthesis and characterization of nanostructured hematite, with an emphasis on the charge carrier dynamics and photoelectrochemical properties. Both current challenges and future opportunities are also discussed.

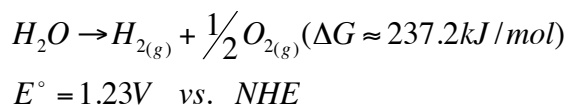
4.2 Introduction

The rapid increase in population has resulted in an ever-growing demand for energy. Over the years, we have met our energy needs by exploiting two main sources: natural gas and crude oil. However, this is not a recipe for the successful and continuous growth of the world. Because of this, seeking renewable and sustainable

energy sources is the defining problem of our time. Many varieties of sustainable energy sources exist, including solar, wind, hydropower, and geothermal. Efficient conversion of solar energy into useful forms is particularly important due to the huge amount of energy available. The solar energy flux reaching the Earth's surface each year is about 125 000 TW. The successful harvesting of merely 0.04% of the solar energy in order to produce 50 TW of energy would be sufficient to cover global energy needs.

Solar energy can be converted into electrical energy or provide access to chemical energy stored in fuels such as hydrogen. When compared to fossil fuels, hydrogen represents a potentially high- efficiency and environmentally benign fuel.¹⁻⁴ Owing to its low density ($\sim 0.089 \text{ g L}^{-1}$), the energy density of hydrogen is much higher than that of other fuel sources, such as gasoline. In fact, it is well-known that on a per-gram basis, hydrogen can produce approximately four times more energy than methane. Furthermore, hydrogen is a chemical fuel that can react with oxygen in a hydrogen fuel cell to produce electricity, with water as a side product. Therefore, production of hydrogen in an environment- friendly and effective way is highly desirable.

Photoelectrochemical (PEC) water splitting represents a promising and environmentally benign method for solar hydrogen generation, and has been studied for decades. More importantly, water splitting is a clean reaction that would not produce undesired carbon-based byproducts. Water splitting is known to be a thermodynamically uphill or endothermic process and is represented by:



A minimal potential of 1.23 V is needed for the reaction to proceed. In this regard, a PEC cell consisting of at least one semiconductor photoelectrode that can directly harvest solar energy for water splitting is necessary. A key challenge for PEC water splitting is identification of a suitable photoanode that can satisfy several key criteria, including favorable bandgap energy, band edge positions, chemical stability, raw material, and fabrication cost.

The utilization of metal oxide semiconductors as photoelectrode materials was borne out through the work of Fujishima and Honda in 1972.⁵ Since then, research has exploded, utilizing WO_3 ,⁶⁻¹⁰ ZnO ,¹¹⁻¹³ and TiO_2 ¹⁴⁻²⁰ as metal oxides of choice for PEC applications. Furthermore, the rapid development in the synthesis of nanomaterials and nanodevice fabrication has opened up new opportunities in the field. The use of nanomaterial-based photoelectrodes for water-splitting dates back to the work by Fitzmaurice et al., who used a nanostructured TiO_2 membrane sensitized with ruthenium-based complexes.²¹ Nanomaterials including zero-dimensional (0D) and one-dimensional (1D) nanostructures (e.g., nanoparticles, nanowires and nanotubes) with unique structural morphology and size-associated properties offer potential advantages over their bulk counterparts in several different manners. First, nanostructures provide a large semiconductor–electrolyte interface wherein the redox reactions can take place, which could facilitate the charge separation. Second, nanostructures provide a short diffusion length for minority carriers, compared to

planar structures. Third, the quantum size confinement in nanomaterials can be potentially used to manipulate the bandgap energy of the semiconductor, as compared to bulk materials.

Among the many metal oxide semiconductors that have been studied for usage as a PEC anode, hematite ($\alpha\text{-Fe}_2\text{O}_3$) has received considerable attention due to its abundance, low cost, excellent chemical stability, and favourable bandgap energy of 1.9–2.2 eV. However, hematite has a very short excited state lifetime (~ 1 ps)^{22–24} and a small hole diffusion length (~ 2 to 4 nm)²⁵ that significantly limits its efficiency in charge separation and collection as a PEC anode. In addition, the conduction band of hematite lies below the H₂ evolution potential, and therefore an external bias is required for PEC hydrogen generation at the cathode. These intrinsic material limitations of hematite result in a much lower solar-to-hydrogen (STH) efficiency compared to the theoretical value. Therefore, the utilization of hematite materials for efficient, cost-effective and sustainable PEC water splitting still represents significant challenges at both the conceptual and device levels.

Various strategies have been developed to overcome the aforementioned limitations of hematite photoanodes, two of which are the promising approaches of utilizing nanostructured materials and elemental doping to manipulate their structural, electronic and optical properties. In this review, we will focus primarily on the recent progress in the synthesis and characterization of nanostructured and element-doped hematite, as well as their implementation as PEC photoanodes with particular emphasis on their charge carrier dynamics and photoelectrochemical properties.

4.3 Synthesis

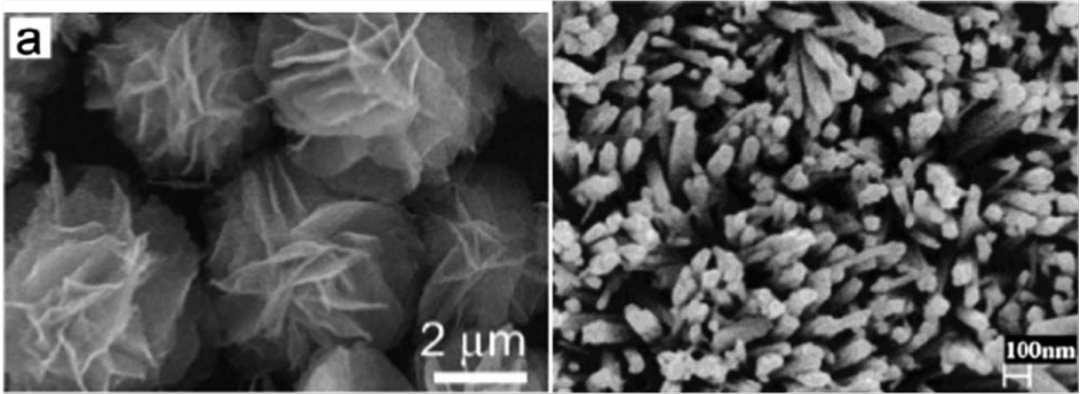
In the last few years, enormous efforts have been made to develop highly photoactive, nanostructured hematite photoanodes. Here we provide a brief overview of several recent synthetic methods for nanostructured hematite materials. This section is meant to provide a good overview of recent advances in synthetic methodology for hematite nanostructures and is not meant to be wholly thorough.

4.3.1 Solution-phase Synthetic Methods

The solution-based method is a facile and scalable method to fabricate nanostructures. α -Fe₂O₃, with different morphologies such as nanoparticles,²⁶ nanowires,²⁷⁻²⁹ nanotubes,³⁰⁻³⁴ hollow spheres,³⁵⁻³⁸ and nanoflowers,³⁹⁻⁴¹ has been fabricated *via* solution-based methods⁴²⁻⁴⁴ such as hydrothermal,^{27,45,46} solvothermal^{40,47,48} and sol-gel⁴⁹⁻⁵¹ routes. For example, Zhong *et al.* utilized a solvothermal method to synthesize 3D flower-like hematite nanostructures, as shown in Fig. 1a, by using an ethylene glycol-mediated self-assembly process.⁴⁰ Vayssieres *et al.* grew porous α -Fe₂O₃ nanorod arrays (Fig. 1b) on fluorine-doped tin oxide (FTO) conducting glass via a hydrothermal method.²⁸ These methods demonstrated that morphological control of α -Fe₂O₃ can be achieved by using different solvents. The sol-gel method is another simple and economical method to fabricate hematite nanostructures.^{50,51} Woo *et al.* reported the growth of α -Fe₂O₃ nanorods with a very small size of 7–24 nm⁵⁰ by the sol-gel method involving the sol-gel reaction in

reverse micelles followed by crystallization in reflux.

Fig. 1 (a) SEM image of 3D flower-like α -Fe₂O₃ nanostructure synthesized via a solvothermal method. Reproduced with permission from ref. 40. (b) SEM image of α -Fe₂O₃ nanorod arrays synthesized by a hydrothermal method. Reproduced with permission from ref. 28.



4.3.2 Vapor-phase Deposition Methods

Gas deposition synthesis includes physical vapor evaporation, chemical vapor deposition, atomic layer deposition, and reactive sputtering. Gas deposition methods have been extensively applied in various nanostructured and thin film fabrication, including hematite and others⁵²⁻⁵⁶. α -Fe₂O₃ with different morphologies such as nanowires, nanorod arrays, nano-dendritic structures and thin films have been achieved using gas phase deposition^{54,55,57-62}. For example, Wu *et al.* recently reported the growth of vertically aligned α -Fe₂O₃ nanorod arrays on a silicon substrate using metal organic chemical vapor deposition (MOCVD)⁵⁷. The as-prepared α -Fe₂O₃ nanorods were single-crystalline. Furthermore, Cesar *et al.* fabricated perpendicularly-oriented dendritic silicon-doped α -Fe₂O₃ nanostructures (Figure 2) using atmospheric pressure chemical vapor deposition (APCVD)⁵⁹. The as-prepared dendritic α -Fe₂O₃ nanostructure exhibit large surface area, and good contact between the α -Fe₂O₃ and the growth substrate, which is critical for charge carrier transfer. Moreover, atomic layer deposition is a unique method to fabricate tunable ultra-thin films with high crystal quality. Lin *et al.* used ALD to deposit a high-quality, ultra-thin α -Fe₂O₃ film on TiSi₂ nanonets (Figure 3)⁵⁵. The film thickness is comparable to the diffusion length of minority carriers. TiSi₂ nanonets were used as templates for the deposition of α -Fe₂O₃ film and serve as a conducting network to facilitate the charge transport.

Figure 2. Cross-sectional SEM images of 500 nm thick mesoporous Si-doped α - Fe_2O_3 films grown by APCVD on a FTO conducting glass. Reproduced with permission from Ref. 59.

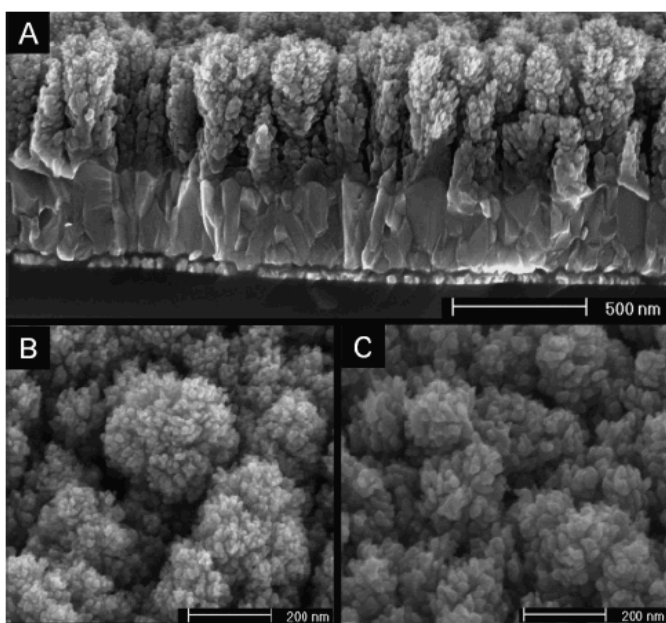
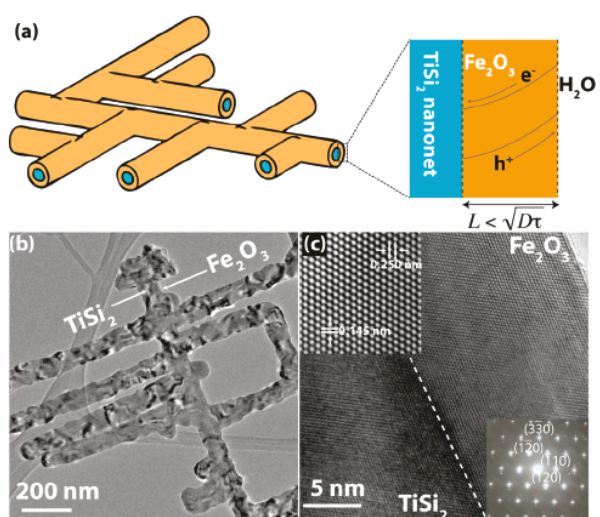


Figure 3. (a) Schematic illustration of the designed core-shell $\text{Fe}_2\text{O}_3\text{-TiSi}_2$ nanonets.
(b, c) TEM and HRTEM images of $\text{Fe}_2\text{O}_3\text{-TiSi}_2$ core@shell structure. Reproduced with permission from Ref. 55.



Reactive sputtering is another commonly used method for thin film materials. Hahn *et al.* used a reactive ballistic deposition method to fabricate α -Fe₂O₃ thin films. The film morphology can be tuned by deposition angles by taking advantage of ballistic shadowing⁶³. Gas-based methods can also be used to fabricate nanostructures in combination with templates. For example, hematite nanotube arrays were prepared by deposition of hematite onto ZnO nanowire arrays or on anodic aluminum oxide (AAO) templates, followed by the removal of ZnO or AAO⁶⁴.

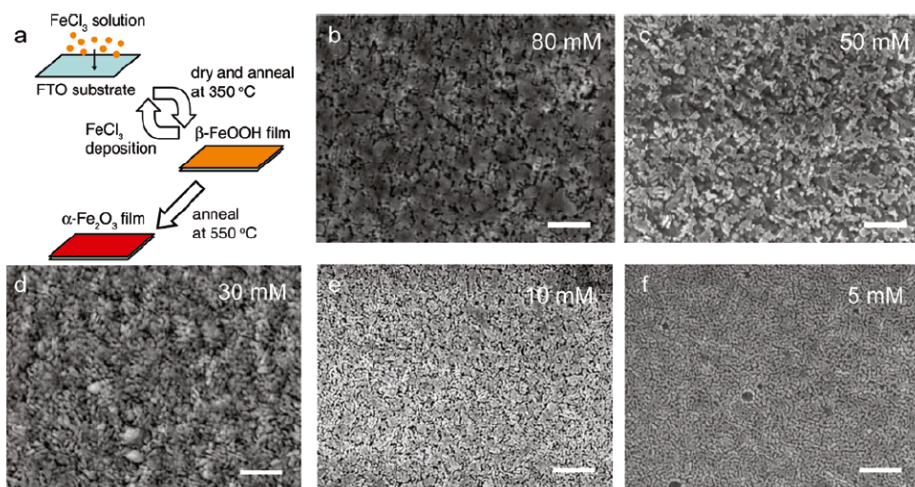
Although high quality nanostructured hematite films have been prepared by vapor phase deposition methods, each technique has its own drawbacks. For example, the iron precursors used in MOCVD and APCVD methods are typically flammable and highly toxic. While ALD is able to grow ultrathin single-crystal hematite film, it comes with a higher fabrication cost compared to solution-based methods.

4.3.3 Thermal oxidation and thermal pyrolysis

Thermal oxidation and pyrolysis are important approaches for the synthesis of nanostructured α -Fe₂O₃. Thermal oxidation of iron metal is the most direct approach to obtain α -Fe₂O₃⁶⁵⁻⁷³. By controlling the oxidation parameters, different morphologies of α -Fe₂O₃ have been synthesized, including nanoparticles, nanowires, and nanoflakes^{65,72}. For example, Rao *et al.* used a flame synthesis technique to fabricate densely aligned α -Fe₂O₃ nanoflake arrays⁶⁵. The morphologies of α -Fe₂O₃ can be manipulated with the end result being differences in nanoflake widths and

lengths by changing various synthetic parameters, such as annealing temperature and atmosphere. Furthermore, hematite thin films can be prepared by thermal pyrolysis. For example, spray pyrolysis is one of the most common methods to deposit thin films. By spraying an iron precursor solution such as FeCl_3 or iron organic precursors such as iron acetylacetonate on a heated substrate⁷⁴, the iron precursor decomposes during thermal treatment in air to form hematite. Duret *et al.* further extended this approach to fabricate mesoscopic $\alpha\text{-Fe}_2\text{O}_3$ leaflet films by using ultrasonic spray pyrolysis resulting in films with higher photoactivity relative to conventional spray pyrolysis techniques⁷¹. Wang *et al.* used a deposition-annealing process to deposit $\alpha\text{-Fe}_2\text{O}_3$ film onto FTO glass, as shown in Figure 4a⁷⁵. Particle sizes and thicknesses of the thin films can be tuned by controlling deposition cycle numbers and precursor concentrations in this process. While the preparations of $\alpha\text{-Fe}_2\text{O}_3$ nanostructures with different morphologies such as nanowires and nanorod arrays have been demonstrated by using vapor phase and solution-based methods, thermal pyrolysis methods have mainly been used for the growth of nanoparticle thin films.

Figure 4. (a) Schematic illustration of deposition-annealing method for α -Fe₂O₃. (b) SEM images of mesoporous α -Fe₂O₃ films prepared by using various FeCl₃ concentrations in a range of 5-80 mM; scale bars are 500 nm. Reproduced with permission from Ref. 75.

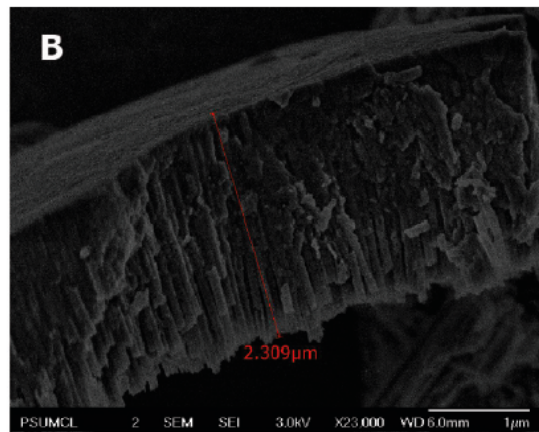
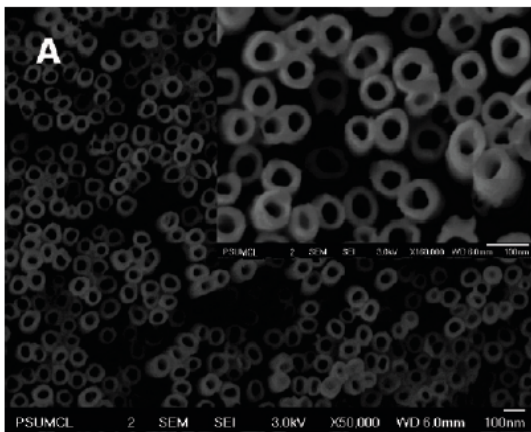


4.3.4 Electrochemical methods

Electrochemical methods have been extensively used to fabricate nanostructure by electrochemical deposition and electrochemical anodization. A typical example is electrochemical deposition of nanorod arrays into anodic aluminum oxide (AAO) templates. AAO templates exhibit ordered and vertically-aligned 1D channel structures after which the AAO template can be easily removed using acidic or basic solutions. Mao *et al.* has recently used electrochemical deposition method to deposit iron into AAO template channels and subsequently removed the AAO template using a NaOH solution, follow by thermal oxidation converting the as-prepared iron nanorod arrays into Fe_2O_3 ^{76,77}.

Without using AAO templates, electrochemical deposition has been used for forming hematite nanoparticle thin films⁷⁸⁻⁸¹. Additionally, electrochemical anodization has been used in the synthesis of hematite nanotube arrays⁸²⁻⁸⁴. $\alpha\text{-Fe}_2\text{O}_3$ nanotube arrays were prepared by anodization of iron foil in an ethylene glycol electrolyte solution containing NH_4F and deionized water at a voltage of 30-60 V⁸⁴. Figure 5 shows the as-prepared $\alpha\text{-Fe}_2\text{O}_3$ nanotube arrays fabricated by the electrochemical anodization⁸⁴. Anodization technique has also been employed for making nanoporous Ti-Fe-O materials from a Ti-Fe alloy foil⁸³. Although a variety of impressive hematite nanostructures can be obtained by electrochemical methods, they are typically polycrystalline materials.

Figure 5. (a,b) Top view and side view of α -Fe₂O₃ nanotube arrays synthesized by electrochemical anodization methods. Reproduced with permission from Ref. 84.

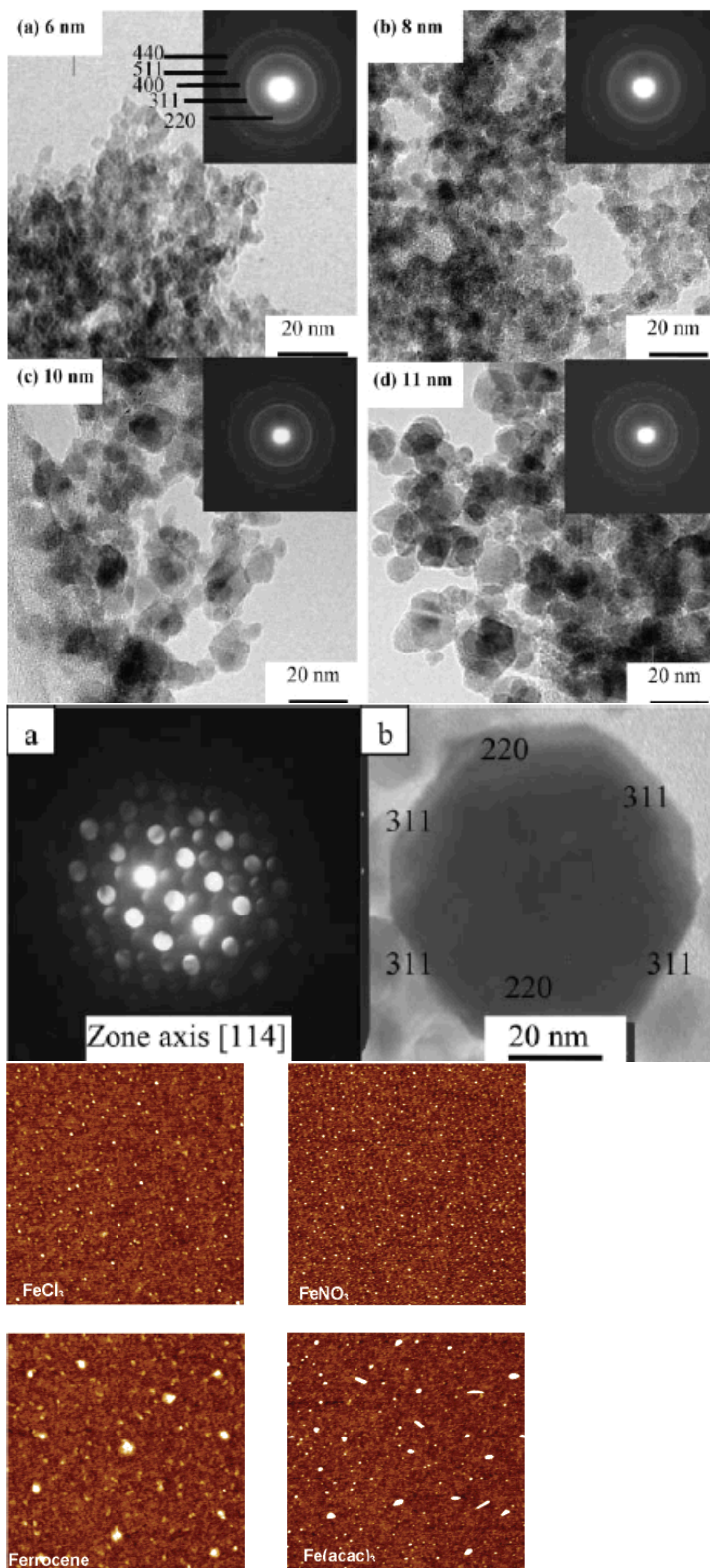


4.4. Structural and Morphological Properties

Owing to their small particle size, nanostructured iron oxides are typically examined by TEM and SEM. While SEM provides a 3D image and information regarding morphology and nanotopographical data, TEM provides a 2D image and is applied to very small crystals. High-resolution TEM (HRTEM) provides additional structural information and is used to follow phase transformations^{85,86}.

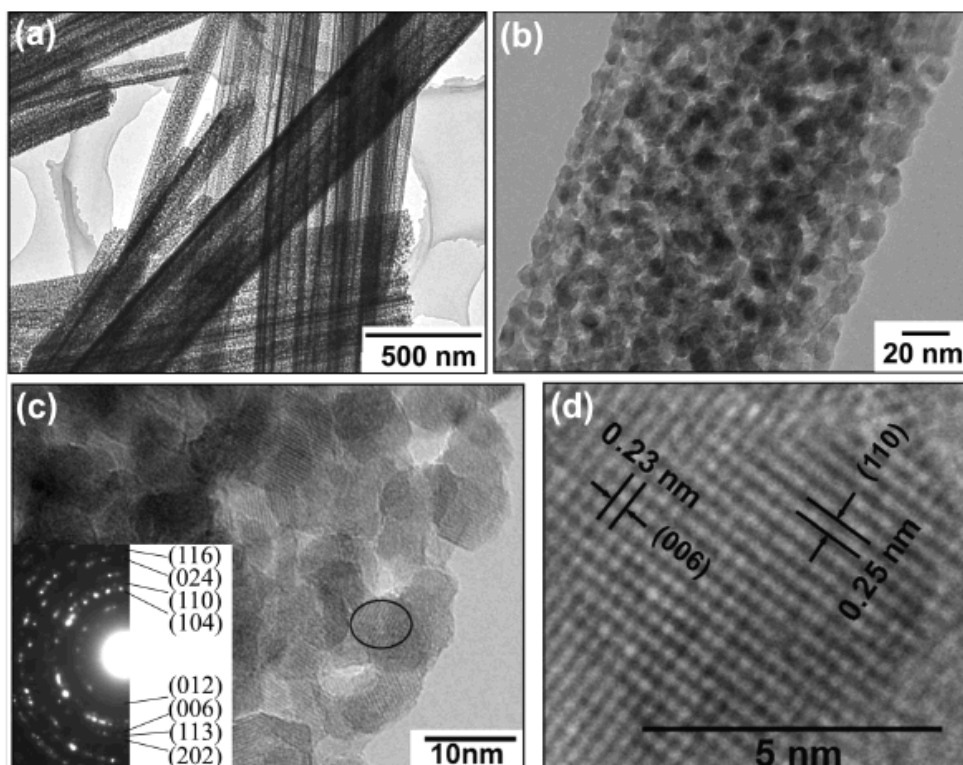
In relation to α - and γ -Fe₂O₃, EM shows that flame-spray pyrolysis-synthesized particles transformed from spherical (~7 nm particles) to irregularly edged particles (~10 nm) and finally to hexagonal and octagonal particle shapes (13-53 nm)⁸⁷. For smaller particles, the lack of well-defined crystal edges is a direct result of the minimization of surface energy. However, as the particle size increases, proper growth of lattice planes can occur and is governed by the tendency to assume minimal surface energy and growth kinetics of each plane. Selected area electron diffraction (SAED) patterning supports this by showing sharper and an increasing number of diffraction pattern rings with increasing particle size. Finally, EM shows that for particles of at least 53 nm, twinning occurs since bulk crystal defect sites grow in, suggesting an acute change in the direction of crystal growth. AFM can also bring forth interesting structural information in Fe₂O₃. For platelet growth, for example, the small axial ratio of tapping mode AFM can corroborate thin (4.5 nm) structures despite broad (57 nm) platelet diameters. More importantly, the homogenous thickness (ranging from 2-8 nm) suggests a 2D preferential growth of flame-spray pyrolysis particles. The EM and AFM images are shown below in Figure 6.

Figure 6. (a,b,c,d, top) Bright field TEM images of Fe₂O₃ particles of various sizes. The insets show electron diffraction patterns. (a,b, middle) Single-crystal selected area electron diffraction (SAED) patterns and their corresponding bright field HRTEM images for Fe₂O₃ of 53 nm size. Reproduced with permission from Ref. 87. Red images: AFM images of iron oxide sourced from various iron precursors. Reproduced with permission from Ref. 88.



High-resolution analysis of α -Fe₂O₃ nanowires in another study⁸⁹ shows two interesting findings. First, the effect on high-temperature sintering yields a previously unseen roughness in nanowires. The nanowires, before sintering, were seen to be dense and smooth. High-temperature treatment afforded an abrupt change to porous and polycrystalline. Second, high-temperature treatment decreases crystallite size to the 4-5 nm range. It is possible that this is toward the lower end of crystallite size, considering the relatively high temperature of 350°C. In addition to these findings, fundamental structural properties are noticed, including the lattice spacing of hematite: 2.3 Å for the (006) plane and 2.5 Å for the (110) plane. These images are shown below in Figure 7. Furthermore, recent HRTEM analyses of hematite nanowires show that the [110] direction is the preferred growth direction for hematite nanowires and corresponds to a thermal mechanism of growth arising from the compaction of precursor Fe powder⁹⁰.

Figure 7. Low resolution (a and b) and high resolution (c and d) TEM images of Fe_2O_3 nanowires. Note the porous nature of the nanowire as well as the high degree of polycrystallinity. Reproduced with permission from Ref. 89.



Besides phase identification, XRD provides information regarding crystal size, quality, structural parameters, and isomorphous substitution of Fe by other trivalent cations. Full accounts of the theory and practice of XRD is provided elsewhere^{91,92}. This section, therefore, will provide a brief account of features relevant for the characterization of iron oxides. The strongest XRD peaks for the different iron oxides are presented below in Table 1⁹³:

Mineral name/formula	Hematite $\alpha\text{-Fe}_2\text{O}_3$	Maghemite $\gamma\text{-Fe}_2\text{O}_3$	Goethite $\alpha\text{-FeOOH}$	Akaganeite $\beta\text{-FeOOH}$	Magnetite Fe_3O_4
Crystal System	Trigonal	Cubic or tetragonal	Orthorhombic	Monoclinic, $\beta = 90.24^\circ$	Cubic
Most intense XRD spacings, nm	0.270, 0.368, 0.252	0.252, 0.295	0.418, 0.245, 0.269	0.333, 0.255, 0.7467	0.253, 0.297

Table 1. Strongest XRD peaks for various iron oxides.

Deviations from the unit cell parameters obtained from an X-ray diffractogram of a pure phase may be used to quantify the extent of Fe substitution by other cations, provided the ionic radius of the foreign cations differs sufficiently from that of Fe^{3+} and the level of substitution is not too low. If, however, the crystals are small (typically below 100 nm) or show structural disorder, the broadening of the reflection becomes great. For example, the plate structure of small hematite crystals is reflected by broad *hkl* lines⁹⁴. Non-isodimensional structures (plates, rods) tend to show preferred orientation which changes the relative intensities of the peaks. From such changes, information regarding the shape of the iron oxide crystals may be gained⁹⁴.

Hematite structures studied using XRD have shown interesting results⁹⁴. Non-uniform broadening of peaks is suggested to be due to shape anisotropy of the particles. Another possible explanation is that, since the effect diminishes with increasing temperature, there is a correlation to some crystal imperfections, strains, or faults which occur at low temperatures. However, anisotropy of the material should lead to large differences in crystallite size, dependent upon the orientation of the diffracting planes. Additionally, in *hcp* structures, stacking faults are known to occur in the *c*-direction, such that line broadening occurs from fault domains. Therefore, non-uniform broadening can be related to stacking faults attributed to the packing of oxygen layers. Nevertheless, the good correlation between particle shape and non-uniform broadening in hematite suggests that – even at low temperature – the effect of particle shape anisotropy is predominant. Other studies have conducted XRD characterization on hematite nanowires and found peaks that can unambiguously be indexed to rhombohedral hematite with $a = 5.038 \text{ \AA}$ and $c = 13.772 \text{ \AA}$ ⁹⁰.

With respect to iron oxide, Raman spectra can also provide information regarding the sample quality, presence of any dopants, and crystallographic orientation. Typical Raman peaks for various iron oxides are presented below in Table 2, where the bold and underlined refer to the strongest and next strongest bands, respectively⁹⁵.

In particular, the spectra of the iron oxides are compatible with octahedrally-coordinated Fe^{3+} ,⁹⁵. Interestingly, this study showed that 2-line ferrihydrite and schwertmannite transform to hematite *via* a maghemite intermediate under heating

from a HeNe laser source yet 6-line ferrihydrite transforms directly to hematite with no intermediate formation. This suggests that the disordered component of the 2-line ferrihydrite transforms to maghemite. For the schwertmannite scenario, the loss on heating of the sulfate entails the simultaneous conversion of OH⁻ ions to O²⁻. It had been previously established that one end point of the crystallization of 2-line ferrihydrite is a cubic stacking of close packed oxide-hydroxide layers. From this, it is understandable that, upon heating, a transformation to maghemite since it is tetrahedrally coordinated.

Table 2. Typical Raman peaks for hematite iron oxide as well as some of its precursor iron oxides, ferrihydrite and δ -FeOOH. The bold and underlined values refer to the strongest and next strongest bands, respectively⁹³.

δ -FeOOH	297; 392 ; <u>666</u>
Ferrihydrite	<u>370</u> ; 510; 710
Hematite	<u>226</u> ; 245; 292 ; 411; 497; 612

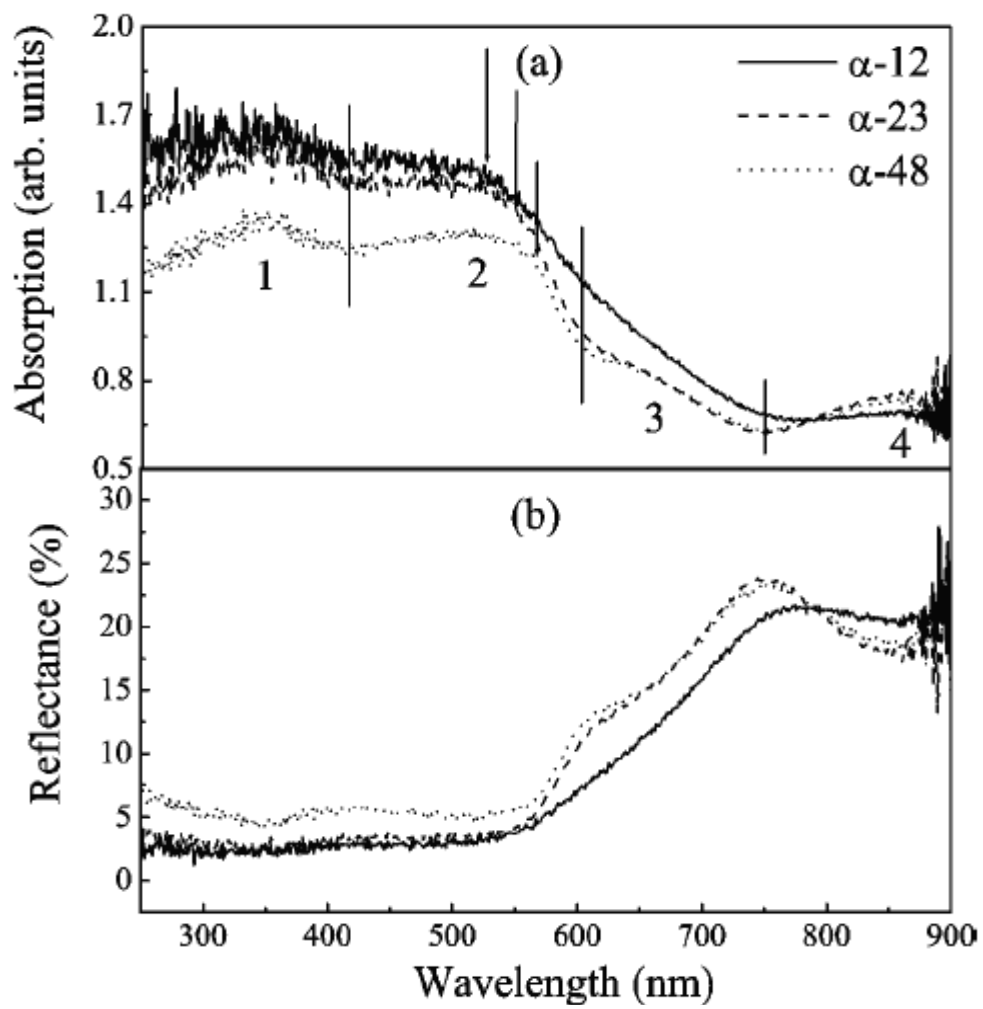
4.5. Optical and Electronic Properties

4.5.1. Optical absorption in near UV to near IR

The optical absorption properties of hematite have been well studied⁹⁶⁻¹⁰³. A typical optical absorption spectrum of α -Fe₂O₃ is shown in Figure 8. Four absorption regions can be classified as follows. The absorption bands in region 1 (250-400 nm) are due to the LMCT transitions (direct transitions) with combined contributions from

the Fe³⁺ ligand field transitions ${}^6A_1({}^6S)$ to ${}^4T_1({}^4P)$ at 290-310 nm, ${}^6A_1({}^6S)$ to ${}^4E({}^4D)$ and ${}^6A_1({}^6S)$ to ${}^4T_1({}^4D)$ at 360-380 nm¹⁰⁴. Region 2 (400-600 nm) is assigned to the pair excitation processes ${}^6A_1({}^6S) + {}^6A_1({}^6S)$ to ${}^4T_1({}^4G) + {}^4T_1({}^4G)$ at 485-550 nm, and is most likely overlapped by the contributions of ${}^6A_1({}^6S)$ to ${}^4E, {}^4A_1({}^4G)$ ligand field transitions at 430 and the LMCT transition band tail^{96,97}. Region 3 (600-780 nm) corresponds to the ${}^6A_1({}^6S)$ to ${}^4T_2({}^4G)$ ligand field transition at about 640 nm, while region 4 (750-900 nm) is the ${}^6A_1({}^6S)$ to ${}^4T_1({}^4G)$ ligand field transition at about 900 nm^{96,97}. Among these interband transitions, the double exciton process (${}^6A_1({}^6S) + {}^6A_1({}^6S)$ to ${}^4T_1({}^4G) + {}^4T_1({}^4G)$) yields the strongest absorption band at around 535 nm, thus it is primarily responsible for the red color of hematite.

Figure 8. (a) Absorption and (b) reflectance spectra of the α -Fe₂O₃ nanocrystals of different sizes, where α -12, α -23, and α -48 express particle size is 12 nm, 23 nm and 48 nm, respectively. Reproduced with permission from Ref. 97.



4.5.2. Size and shape effect on optical transition

The apparent color of hematite nanostructures depends significantly on the phase, size, and the shape of the structure¹⁰⁵⁻¹¹¹. Wang *et al.* found that polyhedral hematite particles with an approximate size of 0.3 μm had a maroon color, while platelet particles of 3 nm in diameter showed a purple color¹⁰⁵. Recently, Chen *et al.* performed a systemic investigation on apparent color change of a variety of hematite nanocrystals from bloody brown to dark brown¹⁰⁶. The intensity of reflectance was highly shape-dependent due to some specific surface planes that possess higher reflectance ability than other surface planes¹⁰⁶. The difference of intensity of reflection in a range of wavelengths will dominate the apparent color of hematite. The spectra show a very low reflectance of hematite particles from 400 to 550 nm, and a sharp increase at around 550 nm indicated that the bandgap was around 2.2 eV. Wang and co-workers also reported the optical properties of hydrothermally synthesized hematite particles studied using diffuse reflectance spectroscopy¹⁰⁵. In the near-infrared region (700-1200 nm), the band at ~ 850 nm was attributed to the 6A_1 to 4T_1 ligand field transition¹⁰⁵. The bands in the visible spectrum region from 400-700 nm were believed to result from spin-forbidden ligand field transition together with the spin-flip transition among the $2t_{2g}$ states¹⁰⁵. The weak absorption bands in the ultraviolet region from 200 to 400 nm were attributed to ligand-to-metal charge transfer between the O($2p$) orbitals to the Fe³⁺ $2t_{2g}$ and $3e_g$ orbitals¹¹².

Later, He *et al.* investigated the size-dependent optical absorption of α -Fe₂O₃ nanoparticles with crystal sizes of 5, 12, and 48 nm dispersed in SiO₂ powders⁹⁷. The result showed a blue-shift with a relative intensity reduction of absorption in the pair excitation processes region (400-600 nm) with reducing particle size: the absorption band shifted from 533 nm for 48 nm nanoparticles, 510 nm for 12 nm nanoparticles, to 488 nm for 5 nm nanoparticles. This blue-shift was in agreement with the earlier reports that the absorption edge blue-shifted with decreasing size for hematite nanoparticles^{113,114}.

The similar size-dependent blue-shift of this band (400-600 nm) was also observed in a recent work of shape-controlled single-crystalline hematite nanotubes⁹⁹. These hollow hematite nanocrystals exhibited two bands at ~450 nm and ~550 nm in the measured region (300-1,000 nm). The band at ~450 nm was blue-shifted to ~385 nm as the length of hollow nanocrystals was reduced with a morphology change from nanotube to nanoring⁹⁹. These results were attributed to the finite size effect¹¹⁵. Moreover, the blue-shift of the absorption band due to pair excitation is shape-dependent as well when the particle size is comparable with the incident wavelength. The shape-induced optical properties were also observed in the absorption of CuO shuttle-like nanoparticles⁹⁶, and in the polarized Raman spectroscopy and anisotropic electron-phonon coupling of CdS nanowires¹¹⁶. The absorption band shift of different-shaped hematite structures could be attributed to the anisotropic effects as the distribution of dipole and electric fields together with the finite size effect will be changed with the aspect ratio of hematite nanotubes⁹⁹.

4.5.3. Photoluminescence

It is well-known that bulk Fe₂O₃ does not show photoluminescence (PL) due to the local forbidden *d-d* transition, resonant energy transfer between cations, and efficient lattice and magnetic relaxations¹¹⁷. However, PL from the self-trapped states can be observed in hematite nanostructure due to their size-associated optical properties¹¹⁸. The quantum confinement effect results in the delocalization and quantization of the electronic state in the nanostructures, relax the forbidden rule for *d-d* transition¹¹⁹, and thus, the optical transition is partially allowed. The magnetic relaxations will also become much weaker within hematite nanoparticles due to more *3d-4sp* hybridization and quantization¹¹⁸, leading to long-lived-excited states. Finally, the hematite nanoparticle has a local collapse of the Fe magnetic moment and strong local lattice distortion in the strong antiferromagnetic background, which could generate luminescence after photoexcitation¹¹⁸.

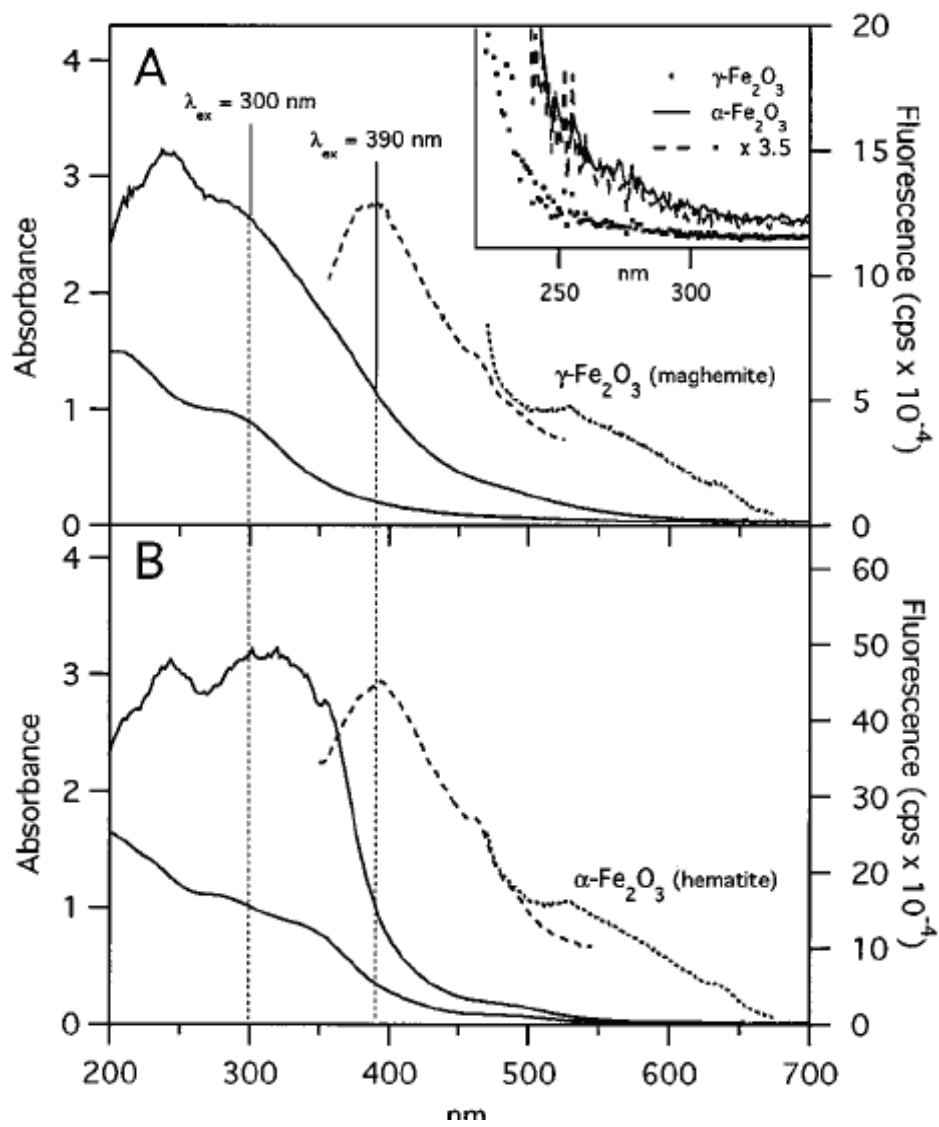
Zou and co-workers observed strong PL from hematite nanoparticles with sizes of < 20 nm either in the form of a hydrosol suspended in water, or in the form of organosol-capped nanoparticles with surfactants suspended in toluene^{118,120}. Hematite nanoparticles in water showed the dominant band-edge emission around 575 nm, while the capped nanoparticles exhibit broader Gaussian-fit emissions around 590 nm. The shift of emission wavelength was attributed to a stronger *3d-4sp* hybridization in capped nanoparticles in toluene than in nanoparticles in water¹¹⁷.

Additionally, Cherepy *et al.* observed an emission band at ~400 nm (excited at 300 nm) from spindle-shaped hematite nanostructures with a dimensionality of 1 × 5

nm¹¹³. It is intriguing because such an emission (400 nm) above the bandgap energy of hematite was rarely detected. The ~400 nm emission band was attributed to the ligand-to-metal charge-transfer (LMCT) transitions (direct transitions)¹¹³ since there was no measurable emission induced by the Fe³⁺ ligand field and exciton pair transitions (indirect transitions)⁹⁶ in the visible region.

The examples show that the absorption and emission properties of hematite are closely related to their size and morphology. The absorption bands in the UV to near IR of hematite are due to the Fe³⁺ ligand field transitions, pair exciton transitions, and the ligand-to-metal charge-transfer transitions (LMCT). The quantum size effect results in the delocalization and quantization of the electronic state in the nanostructures, resulting in change in the absorption and photoluminescence.

Figure 9. Absorption (s) and emission spectra excited at 300 nm (–) and excited at 390 nm (–) of (a) γ -Fe₂O₃ (maghemite) and (b) α -Fe₂O₃ (hematite). The pump wavelength of 390 nm used in the ultrafast measurements is also shown. Two absorption spectra are shown for each sample; the samples with OD ~1 were used in the pump-probe experiments, while the spectra for the dilute samples are used to show the absorption line shape. The inset shows the excitation spectrum for emission detected at 400 nm. Reproduced with permission from Ref. 23.



4.5.4. XPS and EXAFS

X-ray photoelectron spectroscopy (XPS) involves detection and analysis of the photoelectrons produced by interaction of X-rays with matter. The kinetic energy is measured by plotting the measured photoelectron intensity as a function of the binding energy. Each element has its own characteristic set of binding energies and therefore spectral lines. The iron oxides have characteristic Fe($2p_{3/2}$) and ($2p_{1/2}$) lines as well as the O($1s$) line are the most commonly scanned¹²¹⁻¹²³. For iron oxides, the main use of this technique is to provide information regarding the oxidation and structural state parameters and to determine the surface composition to a depth of ~10 nm. The spectra gave peak maxima for Fe($2p_{3/2}$) at 711.5 ± 0.1 eV and for O($1s$) at 530.0 ± 0.1 eV along with shoulders at 531.3 ± 0.1 eV. For iron oxides (other than FeOOH), the O($1s$) peaks do not vary and the Fe peaks are so closely spaced that unambiguous differentiation between oxides in a mixture is difficult. The technique, however, is useful for the investigation of adsorbed species on the oxide surfaces, having been used before for the identification of silicates¹²⁴, phosphates, sulfates, and selenites¹²⁵. Elemental investigations for zinc have also been conducted¹²⁶. XPS spectra have been used in combination with AFM to probe the growth of hematite on silica substrates, showing that the hematite grew in an island-formation manner, regardless of deposition temperature¹²⁷.

For extended X-ray absorption fine structure (EXAFS) measurements, synchrotron radiation is used to ionize the core electrons of a target atom. Absorption spectra are collected by continuously increasing the energy of the incident photons.

The outgoing electrons are backscattered by neighboring atoms; interference of these electrons with the outgoing ones produces a fine structure in the spectrum at energies greater than the absorption edge. EXAFS spectra reflect the local environment around the ionized atoms and provide information about the number and identity of nearest and next-to-nearest neighbors and their distances from each other.

Manceau *et al.* carried out much of the initial EXAFS work on iron oxides with focus on the identification and structural characterization as well as the transformation of ferrihydrite to more crystalline phases¹²⁸⁻¹³¹. In addition, EXAFS has been used recently to characterize adsorbates on iron oxide surfaces, in particular to adsorbed cations of toxic elements and to oxyanions of Se, Cr, and As¹³²⁻¹³⁵.

4.5.5. Theoretical studies of electronic band structure

Theoretical studies of the electronic band structure of hematite have been carried out before¹³⁶⁻¹⁴². For example, Thimsen studied pristine hematite which was modeled using a 30-atom unit cell (hexagonal: $a = 5.038 \text{ \AA}$, $c = 13.772 \text{ \AA}$; $R\text{-}3C$ symmetry group). Calculations were performed using a $5 \times 5 \times 1$ k -point set. For $\alpha\text{-Fe}_2\text{O}_3$, the calculated band gap was between the Fe $3d_L$ and Fe $3d_U$ levels with a value of 2.1 eV. The authors were careful to mention that the band gap values calculated by density functional theory (DFT) are systematically underestimated due to a failure for exchange correlation functionals to cancel out the electronic self-interaction energy. They mention that while other methods, such as DFT+U or the usage of exact Hartree

exchanges can overcome this, they tend to introduce additional complexities and difficulties in the computations relative to DFT calculations.

Periodic density functional theory calculations of bulk goethite have also been reported before using the Vienna *Ab Initio* Simulation Package (VASP)¹⁴³. In this study, calculations of the bulk material accurately reproduced the observed crystal structure and vibrational frequencies which lend credence to the usage of this computational methodology for modeling purposes. Energy-minimized structures of bare, hydrated, and solvated surfaces were modeled for unit cells. The calculated a , b , and c unit cell parameters were 9.95, 3.00, and 4.60 Å (as compared to 9.95, 3.01, and 4.62 Å, respectively, for experimental results) while vibrational frequencies spanning many various bond frequencies were calculated to be extremely accurate to experimentally observed energies. Because of this, the propensity for iron oxides to be accurately modeled is seen to be strong, which has positive implications for future endeavors with regard to calculation of band gaps, unit cell parameters, and vibrational frequencies.

4.6. Charge Carrier Dynamics in Hematite

4.6.1 Background on time-resolved studies of nanostructures

The study of charge carrier dynamics in nanomaterials allows for a deeper and more fundamental understanding of their properties. First, by being a dynamic measurement, it provides information that is complementary to that from static

measurements. Second, the dynamic information can guide the design, synthesis, and implementation of nanomaterials for a wide variety of applications, such as photocatalysis, photoelectrochemistry, and photovoltaics. Time-resolved laser spectroscopy has been established as a versatile and powerful technique for the investigation of charge carrier dynamics in nanomaterials¹⁴⁴⁻¹⁴⁸.

One commonly used technique in time-resolved studies is transient absorption (TA). In TA measurements, a short, usually femtosecond (fs) duration optical pulse (the “pump”) excites the sample and, after a temporal delay, a second short pulse (the “probe” pulse) is used to interrogate the excited population of charge carriers. Changes in the detected signal of the probe pulse, with the accompanying time delay, provides information of the dynamics of the excited carriers being probed¹⁴⁵. Since the assignment of the observed signal is complex, the determination of the origin of the TA signal is often accompanied by careful control experiments and other information, *e.g.* theoretical modeling and simulations. Because the time resolution is determined only by the cross-correlation of the pump and probe pulses, TA measurements provide valuable temporal resolution that few other techniques can afford.

Because of its versatility, TA has been used to study many various systems, including metal nanoparticles¹⁴⁹⁻¹⁵¹, semiconductors¹⁵²⁻¹⁵⁴, and metal oxide materials¹⁵⁵⁻¹⁵⁷. In particular, the interest in charge carrier dynamics in Fe₂O₃ nanostructures has gained significant attention recently.

4.6.2. Carrier dynamics of hematite nanostructures

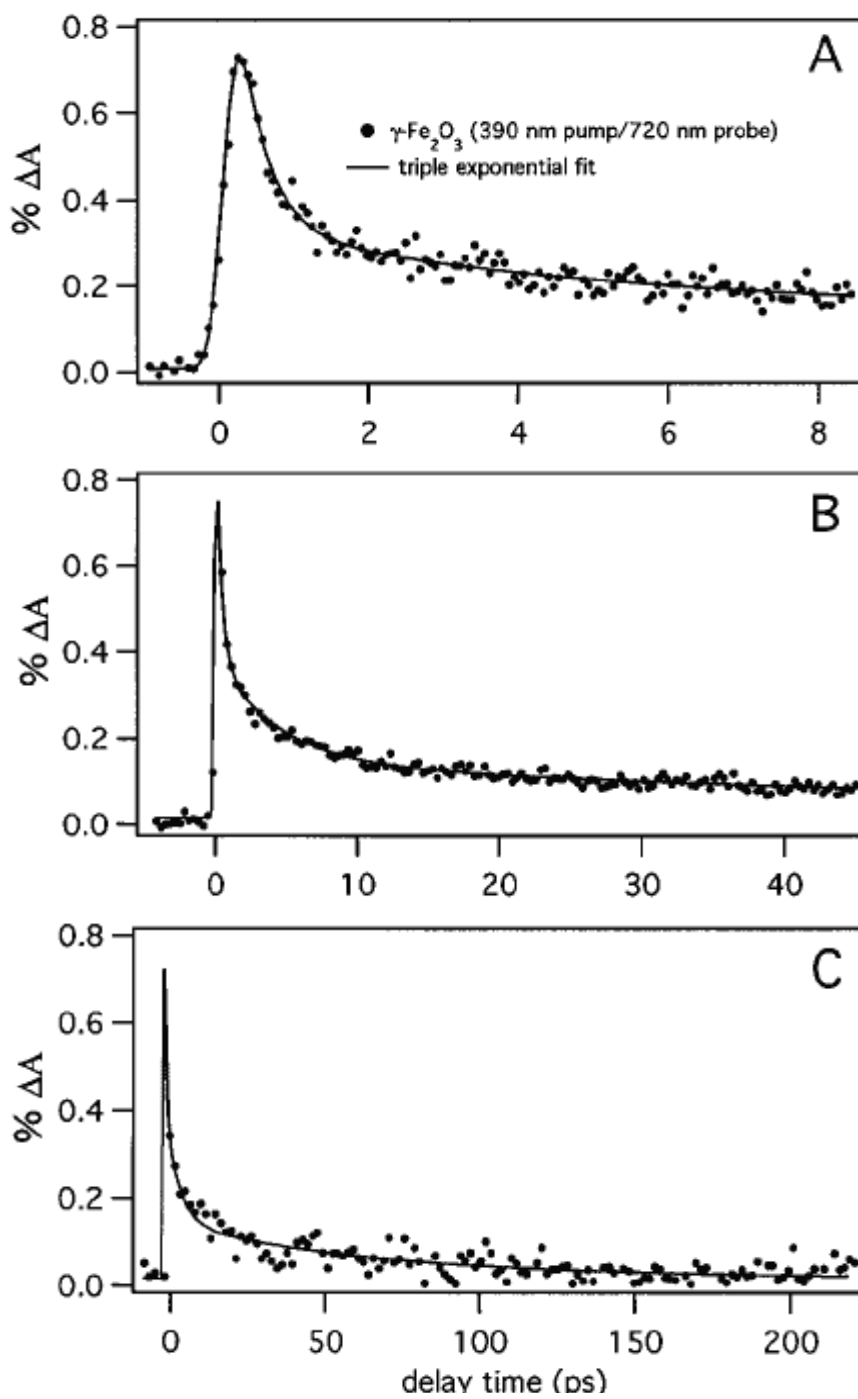
The first ultrafast study of Fe₂O₃ nanostructures was first reported in 1998, and the charge carrier relaxation was dominated by processes with lifetimes on the order of less than 1 ps to a few ps^{23,113,158,159}. Along with subsequent studies, these relaxation processes have been attributed to thermalization, trapping, and non-radiative recombination of the charge carriers.^{23,113,158,159} In comparison to other metal oxide nanomaterials, Fe₂O₃ seems to exhibit the shortest charge carrier lifetimes, indicative of a high density of trap states, which has significant implications in its utilization for applications.

4.6.3. Dependence of charge carrier dynamics on crystal structure and surface

Time-resolved studies of hematite with different morphologies, shapes, sizes, and dopants have been studied to gain insights into its fundamental charge carrier dynamics. Cherepy *et al.* conducted the first study of the ultrafast charge carrier dynamics of Fe₂O₃ using femtosecond (fs) pump-probe laser spectroscopy²³. Both the γ - and α -phases of Fe₂O₃ nanostructures were studied with a 390 nm pump and various probe wavelengths (660, 720, 790, and 850 nm). From this, several interesting findings were elucidated. First, both the α -Fe₂O₃ nanoparticles, which were spindle-shaped nanoparticles with a dimensionality of 1 × 5 nm, and the γ -Fe₂O₃, which were spherical nanoparticles with an average diameter of 1-2 nm, exhibited similar transient absorption decay profiles and were best fit with a triple exponential with time constants of 0.36, 4.2, and 67 picoseconds (ps). The fast overall

decay, in concert with weak fluorescent signals, suggest that extremely efficient non-radiative relaxation is related to the dense band structure, the high density of trap states, or strong coupling between trap states. Second, the decay dynamics were independent of pump power. The samples were pumped with 0.4, 0.6, and 1.2 mJ/pulse-cm², from which a linear correlation between pump powers was found; *i.e.*, there was no change in either the time constants or the relative amplitudes of the decay components regardless of peak power. Third, their transient absorption decay profiles did not change with varying probe wavelengths. The authors reasoned that the carriers were likely thermalized within the laser pulse (~150 fs) since no spectral shift was correlated with cooling. Similar findings have been reported later¹⁶⁰. The explanation was that the electron relaxation kinetics were the same over the entire probe spectrum *via* the capture of electrons by oxygen-deficient centers of Fe³⁺. Fourth, the role of surface species on the transient absorption profiles was investigated by altering the pH in the range of 3-6. The change in pH did not affect the transient absorption decay profile. Finally, the authors incorporated varying elemental dopant materials, including Zn, Co, Cr, and Cu, each at an amount of 10 mol% relative to the Fe. In each case, the transient absorption decay profile was unchanged.

Figure 10. Ultrafast transient absorption decay profiles of γ -Fe₂O₃ nanoparticles. (A) 0-8.3 ps, (B) 0-48 ps, and (C) 0-230 ps. Fitting incorporated a nonlinear least-squares algorithm to a triple exponential decay convolved with a Gaussian representing the cross-correlation of the 390 nm pump and the 720 nm probe pulses. Time constants τ_1 , τ_2 , and τ_3 were calculated to be 0.36, 4.2, and 67 ps, respectively. Reproduced with permission from Ref. 23.



4.6.4. Size dependence

Later, Fu *et al.* conducted an intensive investigation into the size-dependent relaxation times for hematite¹⁶¹ with particle sizes of 4 and 10 nm using pump-probe laser spectroscopy with 355 nm pump and varying probe wavelengths. Smaller (4 nm) hematite hydrosol particles were found to have longer time constants than larger particles (10 nm). The results were fit well with a biexponential decay and showed a drastic change in decay profiles for a given size of an hematite particle. The lifetime derived for a 4 nm hematite hydrosol was 0.12 ps and 4.6 ps for the short and long component, respectively, while a 10 nm hematite hydrosol had time constants of 0.054 ps and 1.7 ps. The difference in time constants was ascribed to itinerant carriers in the extended band that contain Fe 4*sp* and O 2*p* orbitals that show strong steady state absorption with a strong size dependence. They could, in principle, combine to the *d-d* transition through hybridization of the 3*d*-4*sp* orbitals, which is reflected in the femtosecond scale with the long-lived component.

4.6.5. Nanoparticle shape dependence

As discussed in Section 2, Fe₂O₃ nanomaterials can be synthesized with different shapes that allows study of possible shape dependence of the charge carrier dynamics⁹⁹. Fan *et al.* successfully synthesized three different hematite-based samples: nanotubes (98 nm outer diameter) and nanorings (74 and 150 nm outer diameters), and measured their femtosecond spectra. In all three cases, the lifetimes were fit to a triple exponential decay. This fastest decay component was ultimately

attributed to the relaxation of hot electrons at the bottom of the conduction band *via* three different paths: (i) direct recombination, both radiative and non-radiative, (ii) trapping into intrinsic low-lying electronic states through *d-d* “hopping,” and (iii) trapping into surface defect states. In all, the first and third paths are relatively small contributions due to the overall high efficiency of *d-d* hopping. Thus, the fast decay component is attributed to the relaxation of hot carriers at the bottom of the conduction band through trapping into a high density of trap states (Fe^{3+} ligand states) within the band gap. On the scale of tens to hundreds of ps, the slow decay was also essentially the same for all samples and is due to the slower relaxation of trapping electrons. Likewise, in all three cases, the lifetime components were essentially unchanged regardless of morphology of the sample.

4.6.6. Effect of crystallinity

A notorious difficulty in the synthesis of nanostructured particles has been obtaining single crystalline materials. Joly *et al.* successfully synthesized and obtained the transient reflective femtosecond laser dynamics of epitaxially grown single-crystalline $\alpha\text{-Fe}_2\text{O}_3$ ¹⁵⁹. Following an excitation pulse of 407 nm, a white light continuum-derived probe beam monitored the reflective transient absorption of the single-crystalline Fe_2O_3 . Their time constant results are in general agreement with the other studies presented here, with a triple exponential fit containing time constants of 0.300 ps, 2.5 ps, and a slow component of hundreds of ps. The slow component, which extends to hundreds of picoseconds, differs from Cherepy’s result. Joly *et al.*

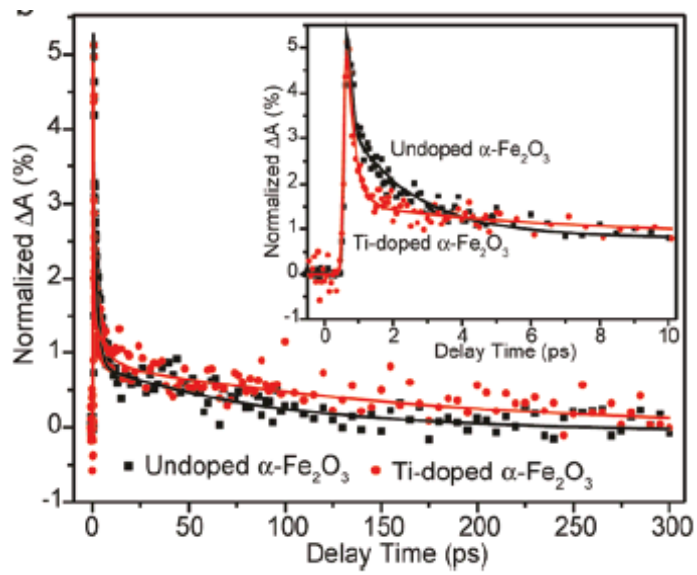
attribute this mainly due to the weaker electron-phonon coupling of the thin films, as compared to the solution-based samples that Cherepy *et al.* measured. Nevertheless, Joly *et al.* noticed that single-crystalline Fe₂O₃ materials have a comparatively shorter lifetime than polycrystalline materials. They attributed the differences to the different nature of the defect states within the single crystal. These trap states may have much stronger absorptions in long wavelength regions of the spectrum, and thus will show up strongly in the transient response. Most interestingly, Joly *et al.* found that at longer lifetimes, the single-crystalline Fe₂O₃ displayed low-frequency oscillations at all probe wavelengths at or below the bandgap¹⁵⁹. The frequency of the oscillation, 68 GHz, was believed to be due to the optical excitation of longitudinal acoustic phonons, the generation of which is due in part to the elastic deformation caused by local heating following strong absorption of ultrafast laser pulses^{162,163}.

4.6.7. Effect of doping

Various doping of hematite has been the focus of recent research. It is hoped that the doping of hematite would extend the lifetime of the excited state of hematite beyond its fastest component of approximately a third of a ps. It is this fast component that has been one of the major obstacles in the implementation of hematite in applications such as solar technology. As previously mentioned, Cherepy *et al.* attempted the implementation of various elemental dopants, including Zn, Co, Cr, and Cu, each at an amount of 10 mol% relative to the Fe²³. The doping did not yield any noticeable increase in excited state lifetimes.

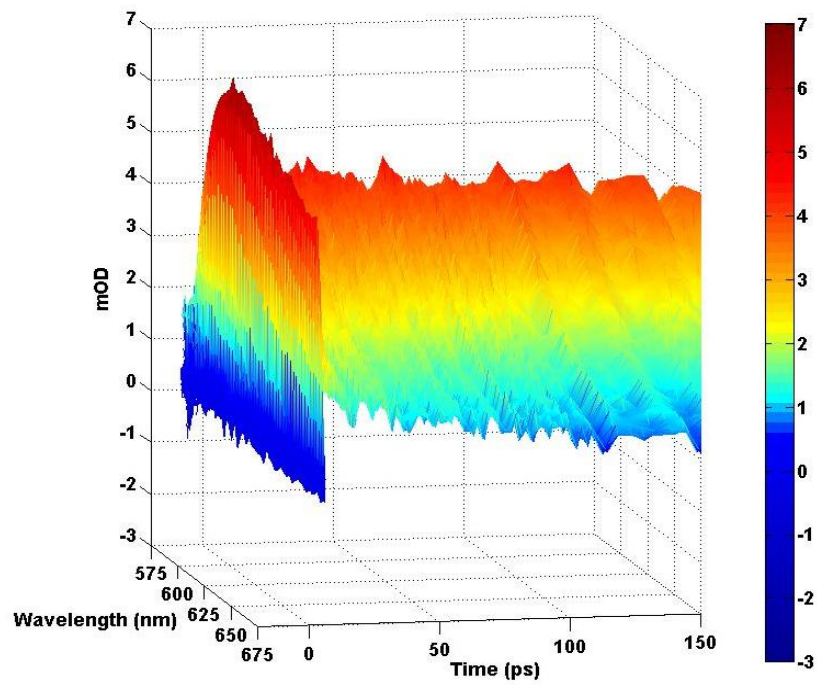
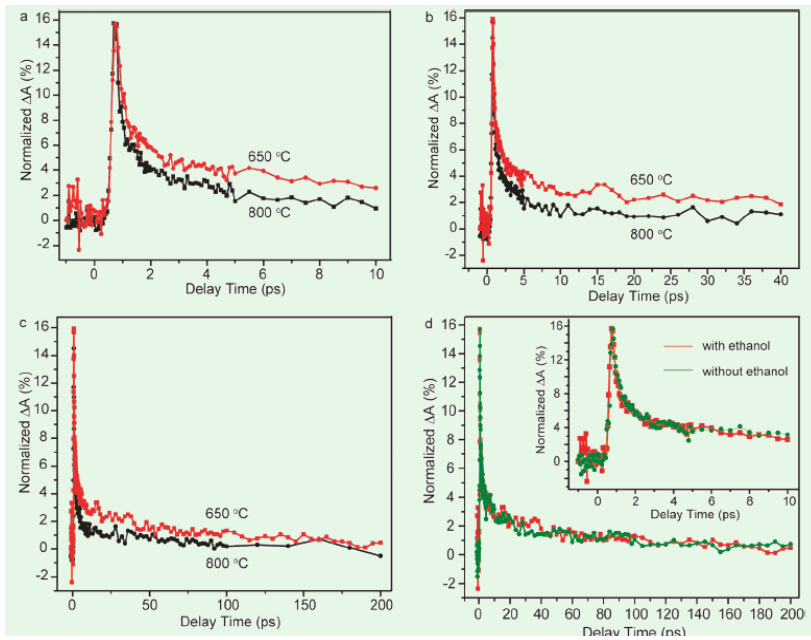
Other dopants have been attempted later, including Ti-doped hematite in which Ti^{4+} substitution occurred at Fe^{3+} sites in $\alpha\text{-Fe}_2\text{O}_3$. The overall charge carrier dynamics were very fast, being fitted to a triple exponential with time constants of 0.34, 2.3, and 71 ps compared to 0.33, 2.2, and 71 ps for undoped $\alpha\text{-Fe}_2\text{O}_3$. The very fast decay was attributed to a high density of electronic states in the bandgap caused by both internal and surface defects, indicating that the early time dynamics are dominated by intrinsic properties of the $\alpha\text{-Fe}_2\text{O}_3$. Although the time constants between the Ti-doped and undoped samples were essentially the same, the absorption decay profile of the Ti-doped sample had a slightly higher amplitude than that of the undoped sample and is indicative of reduced electron-hole recombination on the time scale measured.

Figure 11. Normalized ultrafast transient absorption decay profiles of undoped and Ti-doped Fe_2O_3 films in 0-10 ps (inset) and 0-300 ps windows. They were fit simultaneously using a nonlinear least squares fitting algorithm to a triple exponential decay convolved with a Gaussian, representing the cross-correlation of the 440 nm pump and 620 nm probe pulses. The solid lines are fitted curves. Reproduced with permission from Ref. 164.



Sn-doping¹⁵⁸ in which Sn⁴⁺ substitution at Fe³⁺ sites occurred¹⁶⁴ has also had its charge carrier dynamics measured experimentally. As with the Ti-doping and the doping reported by Cherepy *et al.*²³, the reported lifetime of the Sn-doped material did not significantly differ from pristine α -Fe₂O₃, with reported decay constants of 0.36, 2.45, and 73 ps. The similar dynamics of Sn-doped α -Fe₂O₃ with pristine α -Fe₂O₃ indicates that the presence of Sn does very little, if anything, to alter the photoexcited electron dynamics of α -Fe₂O₃ on the picosecond time scale. Despite that the Sn-doped α -Fe₂O₃ has a different morphology from that of pristine α -Fe₂O₃, the decay profiles of the two samples were essentially the same in both 0-10 and 0-200 ps windows, indicating that morphological changes and Sn-doping have a negligible effect on charge carrier dynamics. Clearly, further study of doping of Fe₂O₃ with different dopants is needed to determine if the charge carrier dynamics can be affected, ideally lengthened, by the appropriate dopant.

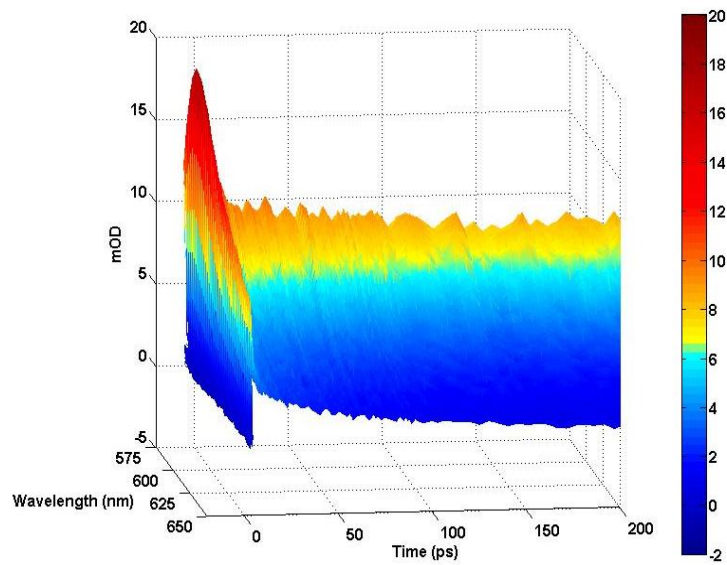
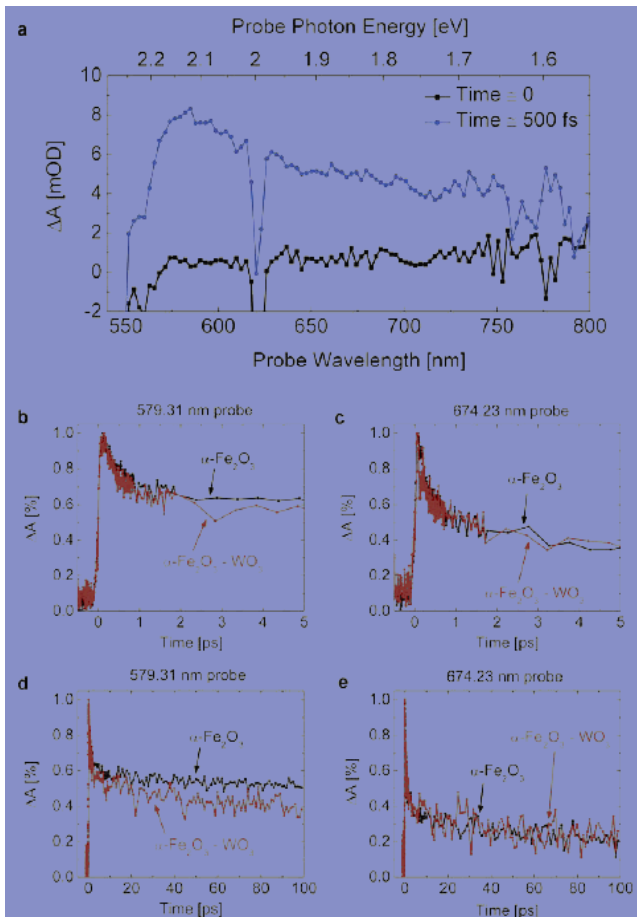
Figure 12. Ultrafast transient absorption decay profiles of hematite nanowires: (a) the 0-10 ps, (b) the 0-40 ps, and (c) the 0-200 ps windows are fit simultaneously using a nonlinear least-squares fitting algorithm to a triple exponential decay convolved with a Gaussian representing the cross-correlation of the 540 nm pump (100 nJ/(pulse cm²), attenuated with neutral density filters) and 620 nm probe pulses. The transient absorption has a pulse width limited rise time and is best fit to a triple exponential with 0.362, 2.451, and 73.37 ps and 0.351, 2.304, and 67.4 ps time constants for 650 and 800°C samples, respectively. (d) Normalized ultrafast transient absorption decay profiles (0-200 ps) of hematite nanowires sintered at 650°C, prepared in the solution with (red line) and without (green line) ethanol. Inset: the same decay profiles in 0-10 ps window. The 3D plot is a plot of the Sn-doped Fe₂O₃. A pulse-width-limited (< 130 fs) rise is followed by a triple exponential fast decay and illustrates the probe wavelength-dependence of the transient absorption kinetic decay processes across part of the visible spectrum. Reproduced with permission from Ref. 158.



The effect of compositing Fe₂O₃ with other metal oxides has also been recently examined. Kronawitter *et al.*¹⁶⁵ examined the effect that WO₃ compositing would have on the early time dynamics of Fe₂O₃. It was found that a fast (~1 ps) and slower (~10 ps) decay occurred over the entire white light probe spectrum, indicating that a common physical process was occurring; namely, the capture of electrons by oxygen-deficient centers of Fe³⁺. The same results were found with samples that had been doped with the WO₃, indicating that the ultrafast physical processes occur irrespective of the presence of dopant. On longer time scales, it was observed that WO₃-composited Fe₂O₃ decayed at a faster rate than for pristine Fe₂O₃ at a probe wavelength of 580 nm. It was furthermore observed that that same trend was not noticeable for redder probe wavelengths (*e.g.*, 675 nm). From this, it was thought that the introduction of the WO₃ enhanced the trapping rate of electrons within a particular wavelength band. Because trapped electrons have a low extinction coefficient, the observed signal will have a smaller absorbance. This is corroborated when considering that Fe₂O₃ has many mid-band gap trap states which can explain the relaxation of conduction band electrons to both shallow and deep traps. The fact that redder probe wavelengths did not display an absorbance-dependent decay profile is explainable by the fact that associated recombination events evolve over the probe spectrum. In fact, it was observed that as the probe energies approached the band gap energy, an increasingly large signal difference between WO₃-composited Fe₂O₃ and pristine Fe₂O₃ was seen. Based on a previous study indicating that the removal of surface-trapped holes from Fe₂O₃ equates to a decay in 580 nm absorption after

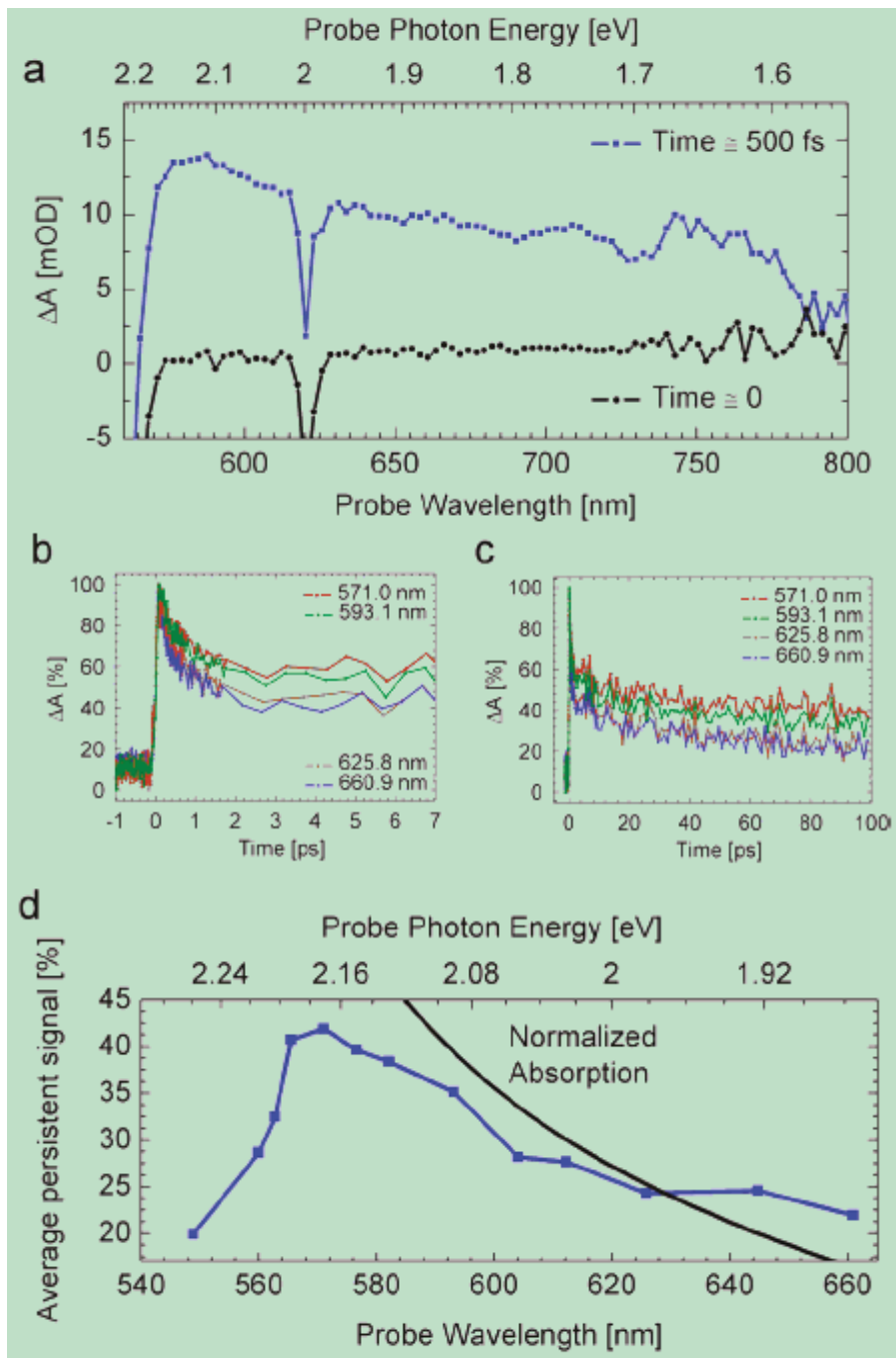
excitation, this suggests that modification of Fe_2O_3 with WO_3 promotes the extraction of surface-trapped holes on picosecond time scales.

Figure 13. Ultrafast transient absorption spectroscopy for hetero-nanostructure electrodes: (a) Transient difference absorbance spectra for α -Fe₂O₃-WO₃ before excitation (black squares) and 500 fs after excitation (blue circles). Transient absorption signals for α -Fe₂O₃ (black) and α -Fe₂O₃-WO₃ (red) at the picosecond time scale for 579.31 nm probe (b) and 674.23 nm probe (c) and the sub-nanosecond time scale for 579.31 nm probe (d) and 674.23 nm probe (e). The 3D plot is a plot of the WO₃-doped Fe₂O₃. A pulse-width-limited (< 130 fs) rise is followed by a triple exponential fast decay and illustrates the strong probe wavelength-dependence of the transient absorption kinetic decay processes across part of the visible spectrum. Reproduced with permission from Ref. 165.



Another study investigated charge carrier dynamics in Ti_xO_y -doped Fe_2O_3 ¹⁶⁶. A biexponential decay was observed with time constants of ~ 2 ps and a slower event persisting to 100 ps and beyond. As with WO_3 -composited Fe_2O_3 ¹⁶⁵, the magnitude of the decay processes depended largely on the probe wavelength used. Over the temporal range investigated, the maximum TA signal was seen for a probe wavelength of 570 nm, very near the bandgap of Fe_2O_3 as well as near the bandedge of the heteronanostructure array. The TA signals were attributed primarily to absorption from trapped electrons. The decay from these trap states is known to be primarily nonradiative²³ and is mediated by further, lower-lying midgap states. However, the signal nearer to the bandgap of Fe_2O_3 (e.g. 580 nm) is thought to be dominated by contributions from surface-trapped holes¹⁶⁷. Despite these claims, a confident assignment of TA signal is challenging. In particular, the high density of localized *d*-levels which are associated with numerous optical transitions, a high density of intrinsic and surface-defect-induced trap states, as well as the known quantum confinement effect in Fe_2O_3 ¹⁶⁸ can all influence and contribute to the signal observed.

Figure 14. (a). Normalized transient absorption signals for four representative probe wavelengths at ~ 1 ps (b) and ~ 10 ps (c) time regimes. (d) Transient absorption (averages of signals from 70 to 100 ps) after ultrafast excitation of $\text{Ti}_x\text{O}_y\text{-Fe}_2\text{O}_3$ array at various probe wavelengths (blue squares). Also included is the normalized steady-state absorption (black solid line), indicating the correlation of the transient data with the band edge. Reproduced with permission from Ref. 166.



A particularly interesting point arises when considering the decay profiles of the variously-doped or composited iron oxides in relation to size and quantum confinement effects. Extensive doping in hematite nanostructures has yielded no discernible difference in charge carrier lifetimes. Additionally, reported lifetimes do not seem to be effected to any large degree by morphological changes. For example, in both the Sn-doped nanocorals, with a large surface-to-volume ratio, and the WO₃-composited nanorods, charge carrier lifetimes were dominated by a fast, ~1 ps feature independent of dopant. This is interesting because the two systems are seemingly entirely different – both in shape and in chemical constituency. Yet despite the similar charge carrier lifetimes, regardless of doping and morphology in the two hematite systems, the decay profiles of the transient absorption in the two systems were different and are related to the size differences. Investigation of the Sn-doped material showed an average particle size of ~60 nm, in direct comparison to that of the WO₃-composited nanostructures which were 3-5 nm single crystals. Inspection of the data shows that, in general, the larger particles (*e.g.*, the Sn-doped hematite) tend to have a fast component that dominates the signal. Along the same line, the smaller particles (*e.g.*, the WO₃-composited hematite) have an amplitude of the fast component that comprises a smaller proportion of the overall signal relative to the larger particles. Quantitatively, in the WO₃-composited material, the amplitude of the fast component comprises ~50% of the overall signal intensity across the probed wavelengths. Meanwhile, the Sn-doped Fe₂O₃ material had a fast component of a larger amplitude, with the fast component being ~80% of the overall signal intensity.

A possibility is that the contribution to the signal intensity by the fast component may be related to quantum confinement or surface-to-volume ratio, both of which are expected to be more significant for smaller particle or feature sizes.

4.6.8. Charge Carrier Kinetics of α -Fe₂O₃ for Water Oxidation

Recently, transient absorption spectroscopy has been applied to study kinetics of photogenerated holes in nanocrystalline hematite photoanodes under applied bias. For hematite in PEC applications, a positive electrical bias is required for water oxidation to occur efficiently, which has the effect of facilitating proton reduction. A recent work by Pendlebury *et al.*¹⁶⁷ probed the transient absorption decay profiles of α -Fe₂O₃ films on the μ s-s timescale, thought to be the temporal domain in which water oxidation occurs. More specifically, they investigated the dynamics of photogenerated holes under positive bias conditions. Following UV excitation, and at an applied bias of -0.1 V, or approximately an open-circuit condition, the transient absorption profile displayed relaxation on the μ s timescale. However, upon the application of a positive bias of 0.4 V, the decay profile greatly increased with a decay that was fit with a stretched exponential of 3 ± 1 s, which decreased to 400 ± 100 ms in the presence of methanol. Their data suggest that the application of a positive, small bias results in long-lived holes which do not undergo the characteristically fast recombination. Usage of methanol as a hole scavenger decreased the lifetime of the decay process, which further indicates that surface oxidation kinetics play a large role in the long lifetime seen, indicating that holes at

the surface of the film are the primary species being probed. Two possible explanations can be given for the long lifetimes seen under bias. The first is that a positive bias can have the effect of increasing the width of the depletion layer and facilitating removal of electrons, thereby decreasing the possibility for electron-hole recombination. The second explanation is that a positive bias decreases electron density throughout the film. Either way, the net result is that a positive bias can significantly increase the lifetime of the photogenerated holes. This is clearly important for a material such as α -Fe₂O₃ since it has a fairly high electron donor density.

The factors underlying the observation of long-lived holes were further explored¹⁶⁹. It was noted that the slow decay (on the μ s-s timescale) has an amplitude dependence upon the applied bias; that an increasingly positive bias will increase the amplitude of the transient signal. As the positive bias increases, the width of the space charge layer increases, thereby generating more holes within the space charge layer. It should also be noted that the particle size also plays a role in these studies. For very small particles, where charge carrier transport relies on diffusion primarily, a positive bias can effectively lower the Fermi level, which can decrease the electron donor density. As mentioned previously, this can have the effect of diminishing the electron-hole recombination, thereby resulting in longer lifetimes.

The charge carrier dynamics studies have yielded some interesting results as well as useful information to guide the design of new hematite nanostructures with improved properties. Hematite itself has been shown to have a fast electron-hole

recombination time of ~ 1 ps. This fast recombination limits the efficiency of charge transfer desired for applications such as solar hydrogen generation. This fast recombination is dominant in hematite systems, largely independent of doping, morphology, crystallinity, shape, surface, and phase. One potentially important factor to manipulate is the physical size of the nanostructure. By reaching the quantum confined regime, one may be able to enhance electron-hole separation or reduce recombination by taking advantage of the short diffusion distance and low density of states. The short diffusion distance can facilitate electron-hole separation but may also increase trapping of charge carriers. A lower density of electronic and phonon states usually results in weaker overlap of carrier and phonon wave functions or spectra, leading to slower electron and hole relaxation and recombination¹⁷⁰.

4.7. Photoelectrochemistry of Fe_2O_3

Hematite as a photoanode material for PEC water oxidation has attracted significant attention due to its suitable bandgap for light absorption, excellent chemical stability, natural abundance, and environmental compatibility¹⁷¹⁻¹⁷⁹. In this article, we will briefly review the recent advancement, limitations and challenges of hematite photoanodes. The working mechanism of a PEC cell using $\alpha\text{-Fe}_2\text{O}_3$ photoanode is illustrated in Figure 15¹⁸⁰. *n*-type hematite is used as the photoanode where water oxidation occurs; simultaneously, water reduction occurs on the cathode. At the semiconductor-electrolyte interface, a space charge layer (depletion layer) is formed due to ion absorption. Upon irradiance, photoexcited electrons (e^-) are

separated at the space charge layer and further transferred to a counter electrode to reduce water, resulting in hydrogen evolution. Simultaneously, photoexcited holes (h^+) travel to the photoanode surface which are driven by a space charge field to oxidize water, thereby resulting in oxygen evolution¹⁸⁰.

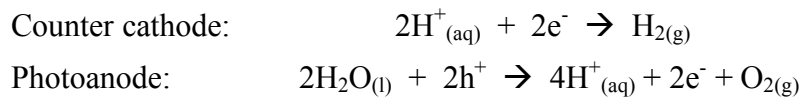
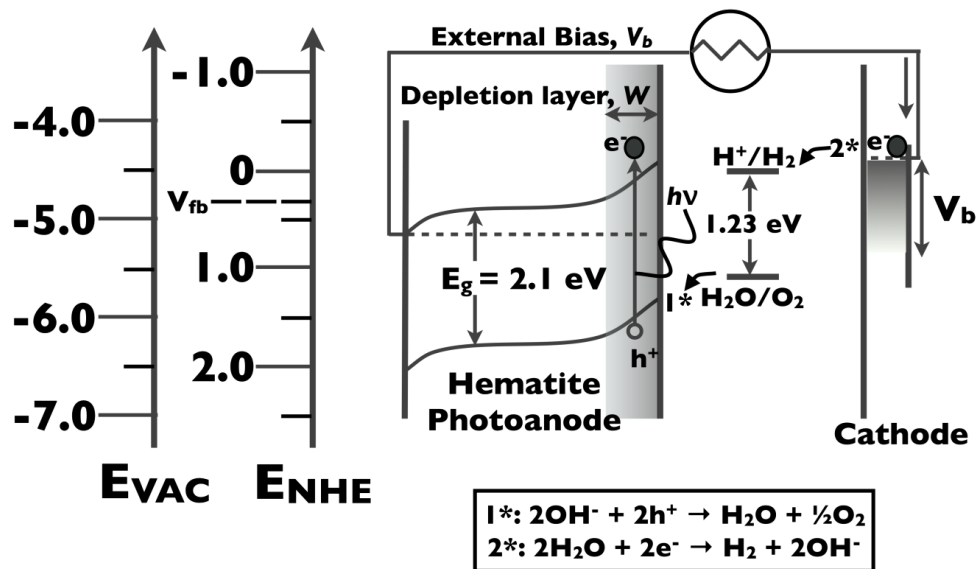


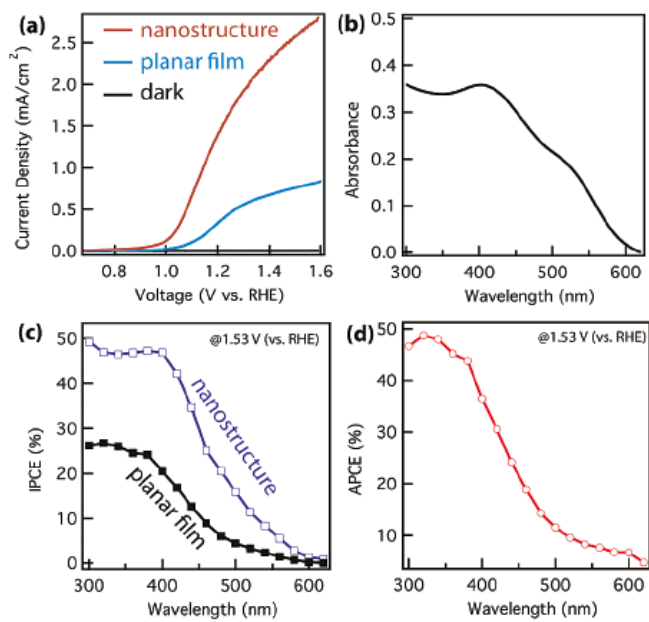
Figure 15. Energy diagram of *n*-type hematite photoanode and schematic illustration of photoelectrochemical water splitting on photoanode and cathode.



α -Fe₂O₃ has a bandgap of 2.0-2.2 eV^{56,181}, with a maximum solar energy conversion efficiency of 14-16.8%¹⁸². However, the reported solar-to-hydrogen efficiency of α -Fe₂O₃ is notoriously lower than the predicted value, mainly due to its very short excited state lifetime (<10 ps)^{183,184} and short hole diffusion length (~2-4 nm)¹⁸⁵⁻¹⁸⁷. The majority of photoexcited electrons in α -Fe₂O₃ are typically lost *via* different electron-hole recombination processes within the first few picoseconds, and only holes created close enough to the semiconductor/electrolyte interface can be used for water oxidation. In this regard, very thin α -Fe₂O₃ films are required to be used for facilitating transport/collection of electrons and holes. Nanostructures with small grain sizes provide large surface areas and short hole diffusion distances, which can potentially address short hole diffusion limitations. For instance, Lin *et al.* used ALD method to obtain ultra-thin single crystal α -Fe₂O₃ (~25 nm) on TiSi₂ nanonets, as shown in Figure 3⁵⁵. This core-shell structure has two primary advantages over the bulk structures: (i) α -Fe₂O₃/TiSi₂ nanonets have larger surface areas and TiSi₂ acts a high conductive net which is beneficial for charge transport to the back contact; (ii) single crystal and shorter hole diffusion distances could reduce charge carrier lost through electron-hole recombination. As expected, the α -Fe₂O₃/TiSi₂ core shell nanostructures exhibit much better PEC performance than the planar structures. Figure 16 shows the comparative PEC studies of α -Fe₂O₃/TiSi₂ heterostructures and α -Fe₂O₃ planar films in 1.0 M NaOH aqueous electrolyte⁵⁵. α -Fe₂O₃/TiSi₂ nanonets show a three-fold enhanced photocurrent density compared to the planar films. Additionally, the nanonets achieved 2.7 mA/cm² at 1.53 V *vs.* RHE as well as 1.6

mA/cm² at 1.23V vs. RHE, which are currently the best values for undoped pristine α -Fe₂O₃. Incident photon-to-electron conversion efficiency (IPCE) shows that the photoactivity has been enhanced in the entire absorption range. Importantly, absorbed photon conversion efficiency (APCE) is almost the same as IPCE, indicating the excellent efficiency of charge separation and collection (quantum yield). It proves the advantage of using ultra-thin α -Fe₂O₃ film for water oxidation.

Figure 16. (a) Comparison of photocurrent-potential curves of planar Fe_2O_3 and $\text{Fe}_2\text{O}_3/\text{TiSi}_2$ heterostructures. (b) UV-Vis absorption of Fe_2O_3 films. (c) IPCE comparison of planar and heterostructures at 1.53 V vs. RHE. (d) APCE of heterostructured $\text{Fe}_2\text{O}_3/\text{TiSi}_2$. Reproduced with permission from Ref. 55.



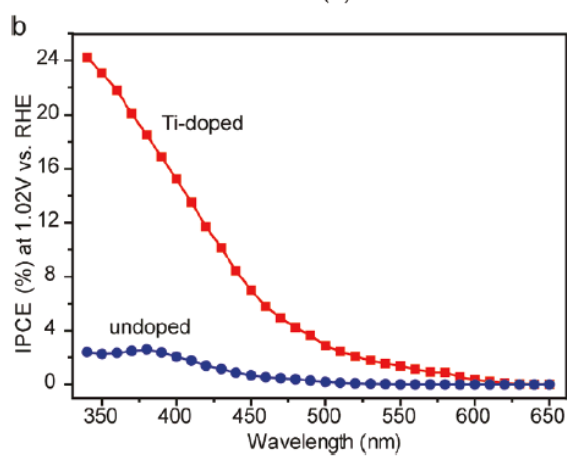
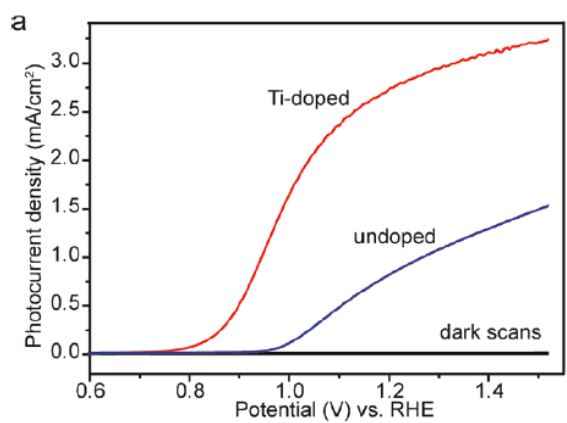
Although ultrathin films are beneficial for charge collection, $\alpha\text{-Fe}_2\text{O}_3$ is an indirect bandgap semiconductor and thus requires a relatively thick layer of active material for the complete absorption of solar light. However, thicker films will result in severe electron-hole recombination and lower conversion efficiencies due to the short hole diffusion length.

Poor electrical conductivity is another major hurdle for hematite to be used as photoanode, as it will limit the charge transport^{188,189}. Elemental doping is a promising method to potentially address this limitation^{58-60,68,190-192}. Various elemental doping methods have been developed for hematite. Elemental doping with electron donors such as Si, Sn, and Ti can significantly enhance hematite's conductivity by increasing its donor density^{58-60,75,191,193}. For example, Ling *et al.* recently report the preparation of Sn-doped hematite nanostructures *via* a hydrothermal method²⁷. Sn doping can be achieved through Sn diffusion from FTO substrate induced by thermal treatment or intentionally mixing the iron with Sn precursor during hydrothermal growth^{27,192,194,195}. Si-doping has been developed by spray pyrolysis and APCVD techniques^{58,59,61,62,71,191} in which the best PEC performance was achieved^{59,61}. At 1.23 V *vs.* Ag/AgCl, the photocurrent density reached a maximum value of 2.3 mA/cm² without catalyst. The enhanced PEC properties observed in these doped $\alpha\text{-Fe}_2\text{O}_3$ are believed to be due to the increased conductivity^{59,60,75,191}.

Wang *et al.* doped Ti into $\alpha\text{-Fe}_2\text{O}_3$ mesoporous films *via* a deposition-annealing method⁷⁵. The PEC performance of $\alpha\text{-Fe}_2\text{O}_3$ has been enhanced by doping of

different elements. Figure 17 shows Ti-doped α -Fe₂O₃ by deposition-annealing exhibits a two-fold enhancement and approximately 0.2 V negative shift of onset of photocurrent⁷⁵. The IPCE spectrum shows significant enhancement in the whole absorption range. Another important example is Si-doped dendritic α -Fe₂O₃ nanostructures synthesized by APCVD. For example, Ti-doping was reported to increase the conductivity of α -Fe₂O₃ by several orders of magnitude¹⁹⁶. The increase of conductivity can be characterized by donor densities derived from electrochemical impedance measurements. Wang *et al.* found that Ti-doped α -Fe₂O₃ has a nearly two-order-magnitude enhancement in donor density as compared to undoped Fe₂O₃ mesoporous films⁷⁵.

Figure 17. (a) Comparison of photocurrent densities of undoped and Ti-doped α - Fe_2O_3 films. (b) IPCE spectra collected at 1.02 V vs. RHE. Reproduced with permission from Ref. 75.

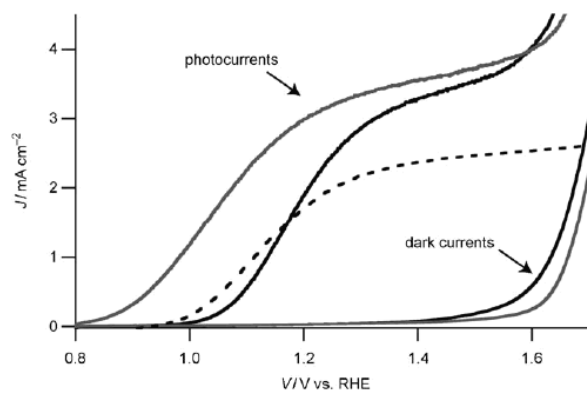


In addition to improve $\alpha\text{-Fe}_2\text{O}_3$ PEC performance through controlled manipulation of morphology and elemental doping, research efforts have also been focus on addressing the slow kinetics of water oxidation on $\alpha\text{-Fe}_2\text{O}_3$ surface, which result in a large overpotential and a low conversion efficiency⁶¹. The solar-to-hydrogen (STH) conversion efficiency is defined by the equation:

$$\eta = \frac{I(1.23 - V)}{J_{light}} \quad (1)$$

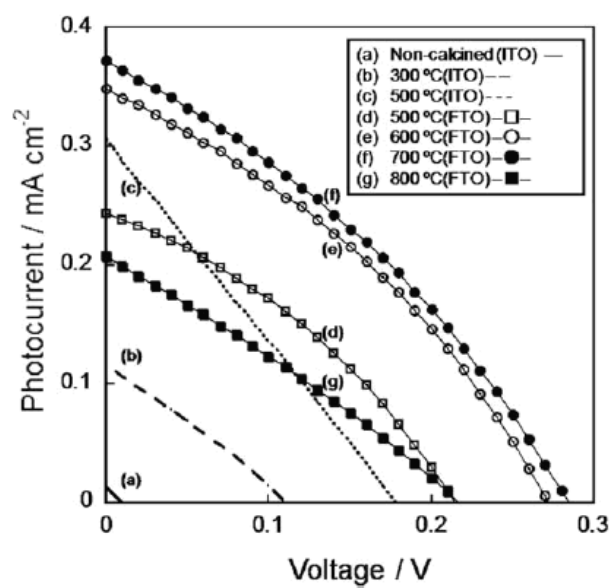
where V is the applied bias vs. RHE, I is the photocurrent density at the measured bias, and J_{light} is the irradiance intensity of 100 mW/cm^2 (AM 1.5G). A large overpotential will result in a large applied bias and thereby a low STH conversion efficiency. Modification of the $\alpha\text{-Fe}_2\text{O}_3$ surface with oxygen evolution catalysts could reduce surface overpotential and negatively shift photocurrent onset potential¹⁹⁷. Figure 18 shows the effect IrO_2 catalyst on the PEC performance of Si-doped $\alpha\text{-Fe}_2\text{O}_3$. The photocurrent onset potential negatively shifted. Other oxygen evolution catalysts such as cobalt ions and cobalt phosphate have also been developed and used to modify $\alpha\text{-Fe}_2\text{O}_3$ anodes for PEC water oxidation^{59,197,198}. Zhong *et al.* reported different methods such as photoassisted electrodeposition and electrochemical deposition to modify $\alpha\text{-Fe}_2\text{O}_3$ with cobalt phosphate based catalysts^{197,198}.

Figure 18. Photoelectrochemical performance of an unmodified hematite photoanode (solid black trace) and the same photoanode modified with IrO₂ nanoparticles (solid gray trace). Reproduced with permission from Ref. 61. The dashed trace was the previously reported best PEC data for Fe₂O₃ without usage of a catalyst. Reproduced with permission from Ref. 59.



α -Fe₂O₃ has also been used for other PEC applications such as hydrogen evolution with a hole scavenger and photoelectrochemical solar cells¹⁹⁹⁻²⁰². The most common hole scavengers used in the reactions are H₂O₂, CH₃OH, I⁻, and Na₂S. Instead of water oxidation, hole scavengers will be oxidized on the photoanode surface. PEC solar cells use regenerated redox couple such as I⁻/I₃⁻ and K₃Fe(CN)₆/K₄Fe(CN)₆ in the electrolyte^{201,202}. For example, Somekawa *et al.* used α -Fe₂O₃ films prepared by laser ablation for solar cells application²⁰². Figure 19 shows the *I-V* curves obtained from α -Fe₂O₃ electrode prepared at different calcination temperatures. Although α -Fe₂O₃ can be used as photoelectrode for solar cell, the efficiency is relative low (~0.03%)²⁰². Similar solar conversion efficiency was obtained for α -Fe₂O₃ electrode by using K₃Fe(CN)₆/K₄Fe(CN)₆ redox pair as electrolyte²⁰¹. The low efficiency of α -Fe₂O₃ based solar cell is due to its shorter lifetime of excited carriers and short hole diffusion distance.

Figure 19. Calcination-temperature dependence of I - V curves collected for α - Fe_2O_3 based solar cells. Reproduced with permission from Ref. 202.



4.8. Conclusion

This review has covered several interesting and important aspects of nanostructured iron oxide, specifically hematite. Specifically, its synthesis and optical characterization has been discussed, with particular emphasis on the charge carrier dynamics and photoelectrochemical properties. Hematite is a unique material due to its small bandgap for visible light absorption, extreme abundance, low cost, and chemical stability. However, due to its intrinsic short charge carrier lifetime or short carrier diffusion length, its photoelectrochemical performance has been limited. Several different strategies, *e.g.* doping, reducing physical size, and using heterostructures, have been explored to overcome some of the limitations. While there is some encouraging progress, further research is clearly needed to both better understand the fundamental properties and exploit various technological applications of nanostructured iron oxide. The complex nature of the system requires combined experimental and theoretical studies at the advanced level.

Acknowledgement

We are grateful to the BES Division of the U.S. DOE (DE-FG02-ER46232) (JZZ) and NSF (DMR-0847786) (YL) for financial support.

4.9. References

(1) Ogden, J. M. *Annual Review of Energy and the Environment* Prospects for Building a Hydrogen Energy Infrastructure. **1999**, *24*, 227-279.

- (2) Bak, T.; Nowotny, J.; Rekas, M.; Sorrell, C. C. *International Journal of Hydrogen Energy* Photo-electrochemical hydrogen generation from water using solar energy. Materials-related aspects. **2002**, *27*, 991-1022.
- (3) M.S. Dresselhaus, G. W. C., M.V. Buchanan (Eds.). *DoE Office of Basic Energy Sciences Basic Research Needs for the Hydrogen Economy*. **2003**, 178.
- (4) C.A. Grimes, O. K. V., S. Ranjan *Light, Water, Hydrogen: The Solar Generation of Hydrogen by Water Photoelectrolysis*; Springer: New York, 2008.
- (5) Fujishima, A.; Honda, K. *Nature* Electrochemical Photolysis of Water at a Semiconductor Electrode. **1972**, *238*, 37-38.
- (6) Bedja, I.; Hotchandani, S.; Kamat, P. V. *The Journal of Physical Chemistry* Photoelectrochemistry of quantized tungsten trioxide colloids: electron storage, electrochromic, and photoelectrochromic effects. **1993**, *97*, 11064-11070.
- (7) Bedja, I.; Hotchandani, S.; Carpentier, R.; Vinodgopal, K.; Kamat, P. V. *Thin Solid Films* Electrochromic and photoelectrochemical behavior of thin WO₃ films prepared from quantized colloidal particles. **1994**, *247*, 195-200.
- (8) Saeki, I.; Okushi, N.; Konno, H.; Furuichi, R. *Journal of The Electrochemical Society* The Photoelectrochemical Response of TiO₂-WO₃ Mixed Oxide Films Prepared by Thermal Oxidation of Titanium Coated with Tungsten. **1996**, *143*, 2226-2230.
- (9) Wang, H.; Lindgren, T.; He, J.; Hagfeldt, A.; Lindquist, S.-E. *The Journal of Physical Chemistry B* Photoelectrochemistry of Nanostructured WO₃ Thin

Film Electrodes for Water Oxidation: Mechanism of Electron Transport. **2000**, *104*, 5686-5696.

(10) Wolcott, A.; Kuykendall, T. R.; Chen, W.; Chen, S.; Zhang, J. Z. *The Journal of Physical Chemistry B* Synthesis and Characterization of Ultrathin WO₃ Nanodisks Utilizing Long-Chain Poly(ethylene glycol)†. **2006**, *110*, 25288-25296.

(11) Ahn, K.-S.; Yan, Y.; Lee, S.-H.; Deutsch, T.; Turner, J.; Tracy, C. E.; Perkins, C. L.; Al-Jassim, M. *Journal of The Electrochemical Society* Photoelectrochemical Properties of N-Incorporated ZnO Films Deposited by Reactive RF Magnetron Sputtering. **2007**, *154*, B956-B959.

(12) Ahn, K.-S.; Shet, S.; Deutsch, T.; Jiang, C.-S.; Yan, Y.; Al-Jassim, M.; Turner, J. *Journal of Power Sources* Enhancement of photoelectrochemical response by aligned nanorods in ZnO thin films. **2008**, *176*, 387-392.

(13) Y. Yan, K. S. A., S. Shet, T. Deutsch, M. Huda, S.H. Wei, J. Turner, M.M. Al-Jassim. *SPIE Proc.* Band gap reduction of ZnO for photoelectrochemical splitting of water. **2007**, *6650*, 66500H.

(14) Ni, M.; Leung, M. K. H.; Leung, D. Y. C.; Sumathy, K. *Renewable and Sustainable Energy Reviews* A review and recent developments in photocatalytic water-splitting using for hydrogen production. **2007**, *11*, 401-425.

(15) Cao, F.; Oskam, G.; Meyer, G. J.; Searson, P. C. *The Journal of Physical Chemistry* Electron Transport in Porous Nanocrystalline TiO₂ Photoelectrochemical Cells. **1996**, *100*, 17021-17027.

- (16) Stergiopoulos, T.; Arabatzis, I. M.; Katsaros, G.; Falaras, P. *Nano Letters* Binary Polyethylene Oxide/Titania Solid-State Redox Electrolyte for Highly Efficient Nanocrystalline TiO₂ Photoelectrochemical Cells. **2002**, *2*, 1259-1261.
- (17) Zhao, H.; Jiang, D.; Zhang, S.; Wen, W. *Journal of Catalysis* Photoelectrocatalytic oxidation of organic compounds at nanoporous TiO₂ electrodes in a thin-layer photoelectrochemical cell. **2007**, *250*, 102-109.
- (18) Hwang, Y. J.; Boukai, A.; Yang, P. *Nano Letters* High Density n-Si/n-TiO₂ Core/Shell Nanowire Arrays with Enhanced Photoactivity. **2008**, *9*, 410-415.
- (19) Wolcott, A.; Smith, W. A.; Kuykendall, T. R.; Zhao, Y.; Zhang, J. Z. *Small* Photoelectrochemical Water Splitting Using Dense and Aligned TiO₂ Nanorod Arrays. **2009**, *5*, 104-111.
- (20) Park, J. H.; Kim, S.; Bard, A. J. *Nano Letters* Novel Carbon-Doped TiO₂ Nanotube Arrays with High Aspect Ratios for Efficient Solar Water Splitting. **2005**, *6*, 24-28.
- (21) Hoyle, R.; Sotomayor, J.; Will, G.; Fitzmaurice, D. *The Journal of Physical Chemistry B* Visible-Light-Induced and Long-Lived Charge Separation in a Transparent Nanostructured Semiconductor Membrane Modified by an Adsorbed Electron Donor and Electron Acceptor. **1997**, *101*, 10791-10800.
- (22) Bjoerksten, U.; Moser, J.; Graetzel, M. *Chemistry of Materials* Photoelectrochemical Studies on Nanocrystalline Hematite Films. **1994**, *6*, 858-863.

- (23) Cherepy, N. J.; Liston, D. B.; Lovejoy, J. A.; Deng, H.; Zhang, J. Z. *The Journal of Physical Chemistry B* Ultrafast Studies of Photoexcited Electron Dynamics in γ - and α -Fe₂O₃ Semiconductor Nanoparticles. **1998**, *102*, 770-776.
- (24) Joly, A. G.; Williams, J. R.; Chambers, S. A.; Xiong, G.; Hess, W. P.; Laman, D. M. *Journal of Applied Physics* Carrier dynamics in α -Fe₂O₃ (0001) thin films and single crystals probed by femtosecond transient absorption and reflectivity. **2006**, *99*, 053521.
- (25) Kennedy, J. H.; Frese, J. K. W. *Journal of The Electrochemical Society* Photooxidation of Water at α -Fe₂O₃ Electrodes. **1978**, *125*, 709-714.
- (26) Yang, Y.; Ma, H. X.; Zhuang, J.; Wang, X. *Inorganic Chemistry* Morphology-Controlled Synthesis of Hematite Nanocrystals and Their Facet Effects on Gas-Sensing Properties. **2011**, *50*, 10143-10151.
- (27) Ling, Y. C.; Wang, G. M.; Wheeler, D. A.; Zhang, J. Z.; Li, Y. *Nano Letters* Sn-Doped Hematite Nanostructures for Photoelectrochemical Water Splitting. **2011**, *11*, 2119-2125.
- (28) Vayssieres, L.; Beermann, N.; Lindquist, S. E.; Hagfeldt, A. *Chemistry of Materials* Controlled aqueous chemical growth of oriented three-dimensional crystalline nanorod arrays: Application to iron(III) oxides. **2001**, *13*, 233-235.
- (29) Wang, R.; Chen, Y.; Fu, Y.; Zhang, H.; Kisielowski, C. *The Journal of Physical Chemistry B* Bicrystalline Hematite Nanowires. **2005**, *109*, 12245-12249.

(30) Jia, C. J.; Sun, L. D.; Yan, Z. G.; You, L. P.; Luo, F.; Han, X. D.; Pang, Y. C.; Zhang, Z.; Yan, C. H. *Angewandte Chemie-International Edition* Iron oxide nanotubes - Single-crystalline iron oxide nanotubes. **2005**, *44*, 4328-4333.

(31) Mao, A.; Shin, K.; Kim, J. K.; Wang, D. H.; Han, G. Y.; Park, J. H. *ACS Applied Materials & Interfaces* Controlled Synthesis of Vertically Aligned Hematite on Conducting Substrate for Photoelectrochemical Cells: Nanorods versus Nanotubes. **2011**, *3*, 1852-1858.

(32) Wu, W.; Xiao, X.; Zhang, S.; Zhou, J.; Fan, L.; Ren, F.; Jiang, C. *The Journal of Physical Chemistry C* Large-Scale and Controlled Synthesis of Iron Oxide Magnetic Short Nanotubes: Shape Evolution, Growth Mechanism, and Magnetic Properties. **2010**, *114*, 16092-16103.

(33) Zhang, Z.; Hossain, M. F.; Takahashi, T. *Applied Catalysis B: Environmental* Self-assembled hematite (α -Fe₂O₃) nanotube arrays for photoelectrocatalytic degradation of azo dye under simulated solar light irradiation. **2010**, *95*, 423-429.

(34) Liu, J.; Li, Y.; Fan, H.; Zhu, Z.; Jiang, J.; Ding, R.; Hu, Y.; Huang, X. *Chemistry of Materials* Iron Oxide-Based Nanotube Arrays Derived from Sacrificial Template-Accelerated Hydrolysis: Large-Area Design and Reversible Lithium Storage. **2009**, *22*, 212-217.

(35) Cavalieri, A. L.; Muller, N.; Uphues, T.; Yakovlev, V. S.; Baltuska, A.; Horvath, B.; Schmidt, B.; Blumel, L.; Holzwarth, R.; Hendel, S.; Drescher, M.;

Kleineberg, U.; Echenique, P. M.; Kienberger, R.; Krausz, F.; Heinzmann, U. *Nature* Attosecond spectroscopy in condensed matter. **2007**, *449*, 1029.

(36) Fan, H. M.; You, G. J.; Li, Y.; Zheng, Z.; Tan, H. R.; Shen, Z. X.; Tang, S. H.; Feng, Y. P. *Journal of Physical Chemistry C* Shape-Controlled Synthesis of Single-Crystalline Fe₂O₃ Hollow Nanocrystals and Their Tunable Optical Properties. **2009**, *113*, 9928-9935.

(37) Wu, Z.; Yu, K.; Zhang, S.; Xie, Y. *The Journal of Physical Chemistry C* Hematite Hollow Spheres with a Mesoporous Shell: Controlled Synthesis and Applications in Gas Sensor and Lithium Ion Batteries. **2008**, *112*, 11307-11313.

(38) Hu, C.; Gao, Z.; Yang, X. *Chemistry Letters* Hematite Hollow Spheres with Excellent Catalytic Performance for Removal of Carbon Monoxide. **2006**, *35*, 1288-1289.

(39) Zeng, S. Y.; Tang, K. B.; Li, T. W.; Liang, Z. H.; Wang, D.; Wang, Y. K.; Qi, Y. X.; Zhou, W. W. *Journal of Physical Chemistry C* Facile route for the fabrication of porous hematite nanoflowers: Its synthesis, growth mechanism, application in the lithium ion battery, and magnetic and photocatalytic properties. **2008**, *112*, 4836-4843.

(40) Zhong, L. S.; Hu, J. S.; Liang, H. P.; Cao, A. M.; Song, W. G.; Wan, L. J. *Advanced Materials* Self-assembled 3D flowerlike iron oxide nanostructures and their application in water treatment. **2006**, *18*, 2426-+.

(41) Zeng, S.; Tang, K.; Li, T.; Liang, Z.; Wang, D.; Wang, Y.; Qi, Y.; Zhou, W. *The Journal of Physical Chemistry C* Facile Route for the Fabrication of

Porous Hematite Nanoflowers: Its Synthesis, Growth Mechanism, Application in the Lithium Ion Battery, and Magnetic and Photocatalytic Properties. **2008**, *112*, 4836-4843.

(42) Li, S. Z.; Zhang, H.; Wu, J. B.; Ma, X. Y.; Yang, D. R. *Crystal Growth & Design* Shape-control fabrication and characterization of the airplane-like FeO(OH) and Fe₂O₃ nanostructures. **2006**, *6*, 351-353.

(43) Zhu, L. P.; Xiao, H. M.; Fu, S. Y. *Crystal Growth & Design* Template-free synthesis of monodispersed and single-crystalline cantaloupe-like Fe₂O₃ superstructures. **2007**, *7*, 177-182.

(44) Ramchandra, S. K.; Min-Seung, C.; Kwi-Sub, Y.; Tae-Sin, K.; Chan-Jin, P. *Nanotechnology* Catalytic characteristics of MnO₂ nanostructures for the O₂ reduction process. **2011**, *22*, 395402.

(45) Zhenmin, L.; Xiaoyong, L.; Hong, W.; Dan, M.; Chaojian, X.; Dan, W. *Nanotechnology* Direct hydrothermal synthesis of single-crystalline hematite nanorods assisted by 1,2-propanediamine. **2009**, *20*, 245603.

(46) Golden, D. C.; Ming, D. W.; Morris, R. V.; Graff, T. G. *American Mineralogist* Hydrothermal synthesis of hematite spherules and jarosite: Implications for diagenesis and hematite spherule formation in sulfate outcrops at Meridiani Planum, Mars. **2008**, *93*, 1201-1214.

(47) Kim, H.-J.; Choi, K.-I.; Pan, A.; Kim, I.-D.; Kim, H.-R.; Kim, K.-M.; Na, C. W.; Cao, G.; Lee, J.-H. *Journal of Materials Chemistry* Template-free

solvothermal synthesis of hollow hematite spheres and their applications in gas sensors and Li-ion batteries. **2011**, *21*.

(48) Li, J.; Lai, X.; Xing, C.; Wang, D. *Journal of Nanoscience and Nanotechnology* One-Pot Synthesis of Porous Hematite Hollow Microspheres and Their Application in Water Treatment. **2010**, *10*, 7707-7710.

(49) Armelao, L.; Granozzi, G.; Tondello, E.; Colombo, P.; Principi, G.; Lottici, P. P.; Antonioli, G. *Journal of Non-Crystalline Solids* Nanocrystalline α -Fe₂O₃ sol-gel thin films: a microstructural study. **1995**, *192–193*, 435-438.

(50) Woo, K.; Lee, H. J.; Ahn, J. P.; Park, Y. S. *Advanced Materials* Sol-gel mediated synthesis of Fe₂O₃ nanorods. **2003**, *15*, 1761-+.

(51) Watanabe, A.; Kozuka, H. *Journal of Physical Chemistry B* Photoanodic properties of sol-gel-derived Fe₂O₃ thin films containing dispersed gold and silver particles. **2003**, *107*, 12713-12720.

(52) Li, Y.; Xiang, J.; Qian, F.; Gradecak, S.; Wu, Y.; Yan, H.; Yan, H.; Blom, D. A.; Lieber, C. M. *Nano Letters* Dopant-free GaN/AlN/AlGaIn radial nanowire heterostructures as high electron mobility transistors. **2006**, *6*, 1468-1473.

(53) Qian, F.; Gradecak, S.; Li, Y.; Wen, C. Y.; Lieber, C. M. *Nano Letters* Core/multishell nanowire heterostructures as multicolor, high-efficiency light-emitting diodes. **2005**, *5*, 2287-2291.

(54) Glasscock, J. A.; Barnes, P. R. F.; Plumb, I. C.; Savvides, N. *Journal of Physical Chemistry C* Enhancement of photoelectrochemical hydrogen production from hematite thin films by the introduction of Ti and Si. **2007**, *111*, 16477-16488.

- (55) Lin, Y.; Zhou, S.; Sheehan, S. W.; Wang, D. *Journal of the American Chemical Society* Nanonet-Based Hematite Heteronanostructures for Efficient Solar Water Splitting. **2011**, *133*, 2398-2401.
- (56) Lin, Y.; Zhou, S.; Liu, X.; Sheehan, S. W.; Wang, D. *Journal of the American Chemical Society* TiO₂/TiSi₂ Heterostructures for High-Efficiency Photoelectrochemical H₂O Splitting. **2009**, *131*, 2772-2773.
- (57) Wu, J. J.; Lee, Y. L.; Chiang, H. H.; Wong, D. K. P. *Journal of Physical Chemistry B* Growth and magnetic properties of oriented α -Fe₂O₃ nanorods. **2006**, *110*, 18108-18111.
- (58) Zhang, M. L.; Luo, W. J.; Li, Z. S.; Yu, T.; Zou, Z. G. *Applied Physics Letters* Improved photoelectrochemical responses of Si and Ti codoped α -Fe₂O₃ photoanode films. **2010**, *97*, 3.
- (59) Kay, A.; Cesar, I.; Gratzel, M. *Journal of the American Chemical Society* New benchmark for water photooxidation by nanostructured α -Fe₂O₃ films. **2006**, *128*, 15714-15721.
- (60) Cesar, I.; Sivula, K.; Kay, A.; Zboril, R.; Graetzel, M. *Journal of Physical Chemistry C* Influence of Feature Size, Film Thickness, and Silicon Doping on the Performance of Nanostructured Hematite Photoanodes for Solar Water Splitting. **2009**, *113*, 772-782.
- (61) Tilley, S. D.; Cornuz, M.; Sivula, K.; Gratzel, M. *Angewandte Chemie-International Edition* Light-Induced Water Splitting with Hematite: Improved Nanostructure and Iridium Oxide Catalysis. **2010**, *49*, 6405-6408.

- (62) Sivula, K.; Le Formal, F.; Gratzel, M. *Chemistry of Materials* WO₃-Fe₂O₃ Photoanodes for Water Splitting: A Host Scaffold, Guest Absorber Approach. **2009**, *21*, 2862-2867.
- (63) Hahn, N. T.; Ye, H. C.; Flaherty, D. W.; Bard, A. J.; Mullins, C. B. *ACS Nano* Reactive Ballistic Deposition of α -Fe₂O₃ Thin Films for Photoelectrochemical Water Oxidation. **2010**, *4*, 1977-1986.
- (64) Liang, Y.; Wang, C. C.; Kei, C. C.; Hsueh, Y. C.; Cho, W. H.; Perng, T. P. *Journal of physical Chemistry C* Photocatalysis of Ag-Loaded TiO₂ Nanotube Arrays Formed by Atomic Layer Deposition. **2011**, *115*, 9498-9502.
- (65) Rao, P. M.; Zheng, X. L. *Nano Letters* Rapid Catalyst-Free Flame Synthesis of Dense, Aligned α -Fe₂O₃ Nanoflake and CuO Nanoneedle Arrays. **2009**, *9*, 3001-3006.
- (66) Wang, H. L.; Turner, J. A. *Journal of the Electrochemical Society* Characterization of Hematite Thin Films for Photoelectrochemical Water Splitting in a Dual Photoelectrode Device. **2010**, *157*, F173-F178.
- (67) Sartoretti, C. J.; Alexander, B. D.; Solarska, R.; Rutkowska, W. A.; Augustynski, J.; Cerny, R. *Journal of Physical Chemistry B* Photoelectrochemical oxidation of water at transparent ferric oxide film electrodes. **2005**, *109*, 13685-13692.
- (68) Saremi-Yarahmadi, S.; Wijayantha, K. G. U.; Tahir, A. A.; Vaidhyanathan, B. *Journal of Physical Chemistry C* Nanostructured α -Fe₂O₃

Electrodes for Solar Driven Water Splitting: Effect of Doping Agents on Preparation and Performance. **2009**, *113*, 4768-4778.

(69) Perednis, D.; Gauckler, L. J. *Journal of Electroceramics* Thin film deposition using spray pyrolysis. **2005**, *14*, 103-111.

(70) Ingler, W. B.; Khan, S. U. M. *International Journal of Hydrogen Energy* Photoresponse of spray pyrolytically synthesized copper-doped p-Fe₂O₃ thin film electrodes in water splitting. **2005**, *30*, 821-827.

(71) Duret, A.; Gratzel, M. *Journal of Physical Chemistry B* Visible light-induced water oxidation on mesoscopic α -Fe₂O₃ films made by ultrasonic spray pyrolysis. **2005**, *109*, 17184-17191.

(72) Nasibulin, A. G.; Rackauskas, S.; Jiang, H.; Tian, Y.; Mudimela, P. R.; Shandakov, S. D.; Nasibulina, L. I.; Sainio, J.; Kauppinen, E. I. *Nano Research* Simple and Rapid Synthesis of α -Fe₂O₃ Nanowires Under Ambient Conditions. **2009**, *2*, 373-379.

(73) Dong, Z.; Kashkarov, P.; Zhang, H. *Nanoscale* Monte Carlo study for the growth of α -Fe₂O₃ nanowires synthesized by thermal oxidation of iron. **2010**, *2*, 524-528.

(74) Mooney, J. B.; Radding, S. B. *Annual Review of Materials Science* Spray Pyrolysis Processing. **1982**, *12*, 81-101.

(75) Wang, G. M.; Ling, Y. C.; Wheeler, D. A.; George, K. E. N.; Horsley, K.; Heske, C.; Zhang, J. Z.; Li, Y. *Nano Letters* Facile Synthesis of Highly Photoactive α -Fe₂O₃-Based Films for Water Oxidation. **2011**, *11*, 3503-3509.

- (76) Mao, A.; Han, G. Y.; Park, J. H. *Journal of Materials Chemistry* Synthesis and photoelectrochemical cell properties of vertically grown α -Fe₂O₃ nanorod arrays on a gold nanorod substrate. **2010**, *20*, 2247-2250.
- (77) Aiming, M.; Nam-Gyu, P.; Gui Young, H.; Jong Hyeok, P. *Nanotechnology* Controlled Growth of Vertically Oriented Hematite/Pt Composite Nanorod Arrays: use for Photoelectrochemical Water Splitting. **2011**, *22*, 175703-175707.
- (78) Kleiman-Shwarscstein, A.; Huda, M. N.; Walsh, A.; Yan, Y. F.; Stucky, G. D.; Hu, Y. S.; Al-Jassim, M. M.; McFarland, E. W. *Chemistry of Materials* Electrodeposited Aluminum-Doped α -Fe₂O₃ Photoelectrodes: Experiment and Theory. **2010**, *22*, 510-517.
- (79) Spray, R. L.; Choi, K. S. *Chemistry of Materials* Photoactivity of Transparent Nanocrystalline Fe₂O₃ Electrodes Prepared via Anodic Electrodeposition. **2009**, *21*, 3701-3709.
- (80) Hu, Y. S.; Kleiman-Shwarscstein, A.; Forman, A. J.; Hazen, D.; Park, J. N.; McFarland, E. W. *Chemistry of Materials* Pt-doped α -Fe₂O₃ thin films active for photoelectrochemical water splitting. **2008**, *20*, 3803-3805.
- (81) Kleiman-Shwarscstein, A.; Hu, Y. S.; Forman, A. J.; Stucky, G. D.; McFarland, E. W. *Journal of Physical Chemistry C* Electrodeposition of α -Fe₂O₃ doped with Mo or Cr as photoanodes for photocatalytic water splitting. **2008**, *112*, 15900-15907.

- (82) Prakasam, H. E.; Varghese, O. K.; Paulose, M.; Mor, G. K.; Grimes, C. A. *Nanotechnology* Synthesis and photoelectrochemical properties of nanoporous iron (III) oxide by potentiostatic anodization. **2006**, *17*, 4285-4291.
- (83) Mor, G. K.; Prakasam, H. E.; Varghese, O. K.; Shankar, K.; Grimes, C. A. *Nano Letters* Vertically oriented Ti-Fe-O nanotube array films: Toward a useful material architecture for solar spectrum water photoelectrolysis. **2007**, *7*, 2356-2364.
- (84) LaTempa, T. J.; Feng, X. J.; Paulose, M.; Grimes, C. A. *Journal of Physical Chemistry C* Temperature-Dependent Growth of Self-Assembled Hematite (α -Fe₂O₃) Nanotube Arrays: Rapid Electrochemical Synthesis and Photoelectrochemical Properties. **2009**, *113*, 16293-16298.
- (85) Giovanoli, R.; Brüttsch, R. *Thermochimica Acta* Kinetics and mechanism of the dehydration of γ -FeOOH. **1975**, *13*, 15-36.
- (86) Watari, F.; Van Landuyt, J.; Delavignette, P.; Amelinckx, S. *Journal of Solid State Chemistry* Electron microscopic study of dehydration transformations. I. Twin formation and mosaic structure in hematite derived from goethite. **1979**, *29*, 137-150.
- (87) Li, D.; Teoh, W. Y.; Selomulya, C.; Woodward, R. C.; Munroe, P.; Amal, R. *Journal of Materials Chemistry* Insight into microstructural and magnetic properties of flame-made γ -Fe₂O₃ nanoparticles. **2007**, *17*, 4876-4884.
- (88) Lu, J. Q.; Moll, N.; Fu, Q.; Liu, J. *Chemistry of Materials* Iron Nanoparticles Derived from Iron-Complexed Polymethylglutarimide To Produce

High-Quality Lithographically Defined Single-Walled Carbon Nanotubes. **2005**, *17*, 2237-2240.

(89) Wang, G.; Gou, X.; Horvat, J.; Park, J. *The Journal of Physical Chemistry C* Facile Synthesis and Characterization of Iron Oxide Semiconductor Nanowires for Gas Sensing Application. **2008**, *112*, 15220-15225.

(90) Diaz-Guerra, C.; Perez, L.; Piqueras, J.; Chioncel, M. F. *Journal of Applied Physics* Magnetic transitions in α -Fe₂O₃ nanowires. **2009**, *106*, 104302-104304.

(91) H.P. Klug, L. E. A. *X-ray Diffraction Procedures*; J. Wiley and Sons Inc: New York, 1974.

(92) G.W. Brindley, G. B. *Crystal structures of clay minerals and their X-ray diffraction*; Min. Soc.: London, 1980.

(93) U. Schwertmann, R. M. C. *Iron Oxides in the Laboratory: Preparation and Characterization* 2ed.; Wiley VCH: Weinheim, 2000.

(94) Duvigneaud, P. H.; Derie, R. *Journal of Solid State Chemistry* Shape effects on crystallite size distributions in synthetic hematites from X-ray line-profile analysis. **1980**, *34*, 323-333.

(95) Mazzetti, L.; Thistlethwaite, P. J. *Journal of Raman Spectroscopy* Raman spectra and thermal transformations of ferrihydrite and schwertmannite. **2002**, *33*, 104-111.

- (96) Sherman, D. M.; Waite, T. D. *American Mineralogist* Electronic Spectra of Iron(III) Oxides and Oxide Hydroxides in the Near IR to Near UV. **1985**, *70*, 11-12.
- (97) He, Y. P.; Miao, Y. M.; Li, C. R.; Wang, S. Q.; Cao, L.; Xie, S. S.; Yang, G. Z.; Zou, B. S.; Burda, C. *Physical Review B* Size and Structure Effect on Optical Transitions of Iron Oxide Nanocrystals. **2005**, *71*, 125411.
- (98) Hashimoto, T.; Yamada, T.; Yoko, T. *Journal of Applied Physics* Third-Order Nonlinear Optical Properties of Sol-Gel Derived α -Fe₂O₃, γ -Fe₂O₃, and Fe₃O₄ Thin Films. **1996**, *80*, 3184-3190.
- (99) Fan, H. M.; You, G. J.; Li, Y.; Zheng, Z.; Tan, H. R.; Shen, Z. X.; Tang, S. H.; Feng, Y. P. *The Journal of Physical Chemistry C* Shape-Controlled Synthesis of Single-Crystalline Fe₂O₃ Hollow Nanocrystals and Their Tunable Optical Properties. **2009**, *113*, 9928.
- (100) Zhu, W.; Cui, X.; Wang, L.; Liu, T.; Zhang, Q. *Materials Letters* Monodisperse porous pod-like hematite: Hydrothermal formation, optical absorbance, and magnetic properties. **2011**, *65*, 1003-1006.
- (101) Galuza, A. I.; Beznosov, A. B.; Eremenko, V. V. *Low Temperature Physics* Optical absorption edge in α -Fe₂O₃: The exciton--magnon structure. **1998**, *24*, 726-729.
- (102) Marra, A. C.; Blanco, A.; Fonti, S.; Jurewicz, A.; Orofino, V. *Journal of Physics: Conference Series* Fine hematite particles of Martian interest: absorption spectra and optical constants. **2005**, *6*, 132.

(103) Shi, J.-B.; Lee, C.-W.; Guo, J.-W.; Cheng, M.-J.; Wu, C.; Chen, C.-J.; Chen, Y.-C.; Lin, Y.-T.; Chang, C.-C. *Materials Letters* Optical and magnetic properties of elliptical hematite (α -Fe₂O₃) nanoparticles coated with uniform continuous layers of silica of different thickness. **2007**, *61*, 5268-5270.

(104) Jorand Sartoretti, C.; Alexander, B. D.; Solarska, R.; Rutkowska, I. A.; Augustynski, J.; Cerny, R. *The Journal of Physical Chemistry B* Photoelectrochemical Oxidation of Water at Transparent Ferric Oxide Film Electrodes. **2005**, *109*, 13685-13692.

(105) Wang, J.; White, W. B.; Adair, J. H. *Journal of the American Ceramic Society* Optical Properties of Hydrothermally Synthesized Hematite Particulate Pigments. **2005**, *88*, 3449-3454.

(106) Chen, L.; Yang, X.; Chen, J.; Liu, J.; Wu, H.; Zhan, H.; Liang, C.; Wu, M. *Inorganic Chemistry* Continuous Shape- and Spectroscopy-Tuning of Hematite Nanocrystals. **2010**, *49*, 8411-8420.

(107) Hund, F. *Angewandte Chemie International Edition in English* Inorganic Pigments: Bases for Colored, Uncolored, and Transparent Products. **1981**, *20*, 723-730.

(108) Ryde, N. P.; Matijevic, E. *Applied Optics* Color Effects of Uniform Colloidal Particles of Different Morphologies Packed into Films. **1994**, *33*, 7275-7281.

- (109) Yamanoi, Y.; Nakashima, S.; Katsura, M. *American Mineralogist* Temperature dependence of reflectance spectra and color values of hematite by in situ, high-temperature visible micro-spectroscopy. **2009**, *94*, 90-97.
- (110) Torrent, J.; Barrón, V. *Clays and Clay Minerals* The Visible Diffuse Reflectance Spectrum in Relation to the Color and Crystal Properties of Hematite. **2003**, *51*, 309-317.
- (111) Galvez, N.; Barron, V.; Torrent, J. *Clays and Clay Minerals* Preparation and properties of hematite with structural phosphorus. **1999**, *47*, 375-385.
- (112) Marusak, L. A.; Messier, R.; White, W. B. *Journal of Physics and Chemistry of Solids* Optical Absorption Spectrum of Hematite, α -Fe₂O₃ near IR to UV. **1980**, *41*, 981-984.
- (113) Cherepy, N. J.; Liston, D. B.; Lovejoy, J. A.; Deng, H.; Zhang, J. Z. *The Journal of Physical Chemistry B* Ultrafast Studies of Photoexcited Electron Dynamics in γ - and α -Fe₂O₃ Semiconductor Nanoparticles. **1998**, *102*, 770.
- (114) Chatterjee, S.; Sarkar, S.; Bhattacharyya, S. N. *Journal of Photochemistry and Photobiology A: Chemistry* Size Effect in the Photochemical Generation of Hydrogen from Water by Colloidal Fe₂O₃ Particles. **1993**, *72*, 183-187.
- (115) Lu, L.; Li, L.; Wang, X.; Li, G. *The Journal of Physical Chemistry B* Understanding of the Finite Size Effects on Lattice Vibrations and Electronic Transitions of Nano α -Fe₂O₃. **2005**, *109*, 17151-17156.

- (116) Fan, H. M.; Fan, X. F.; Ni, Z. H.; Shen, Z. X.; Feng, Y. P.; Zou, B. S. *The Journal of Physical Chemistry C* Orientation-Dependent Raman Spectroscopy of Single Wurtzite CdS Nanowires. **2008**, *112*, 1865-1870.
- (117) Tsuda, N.; Nasu, K.; Yanase, A.; Siratori, K. *Electronic Conduction in Oxide (Springer Series in Solid State Science 94)*; Springer-Vedag: Berlin, 1991.
- (118) Zou, B.; Huang, W.; Han, M. Y.; Li, S. F. Y.; Xiaochun, W.; Zhang, Y.; Zhang, J.; Pengfei, W.; Wang, R. *Journal of Physics and Chemistry of Solids* Anomalous Optical Properties and Electron-Phonon Coupling Enhancement in Fe₂O₃ Nanoparticles Coated with a Layer of Stearates. **1997**, *58*, 1315-1320.
- (119) Tolbert, S. H.; Alivisatos, A. P. *Science* Size Dependence of a First Order Solid-Solid Phase Transition: The Wurtzite to Rock Salt Transformation in CdSe Nanocrystals. **1994**, *265*, 373-376.
- (120) Zou, B. S.; Volkov, V. *Journal of Physics and Chemistry of Solids* Surface Modification on Time-Resolved Fluorescences of Fe₂O₃ Nanocrystals. **2000**, *61*, 757-764.
- (121) Brundle, C. R.; Chuang, T. J.; Wandelt, K. *Surface Science* Core and valence level photoemission studies of iron oxide surfaces and the oxidation of iron. **1977**, *68*, 459-468.
- (122) Harvey, D. T.; Linton, R. W. *Analytical Chemistry* Chemical characterization of hydrous ferric oxides by x-ray photoelectron spectroscopy. **1981**, *53*, 1684-1688.

- (123) Wandelt, K. *Surface Science Reports* Photoemission studies of adsorbed oxygen and oxide layers. **1982**, 2, 1-121.
- (124) Vempati, R. K.; Loeppert, R. H.; Dufner, D. C.; Cocke, D. L. *Soil Sci. Soc. Am. J. X-ray Photoelectron Spectroscopy as a Tool to Differentiate Silicon-Bonding State in Amorphous Iron Oxides*. *54*, 695-698.
- (125) Martin, R. R.; Smart, R. S. C. *Soil Sci. Soc. Am. J. X-ray Photoelectron Studies of Anion Adsorption on Goethite*. **1987**, 51, 54-56.
- (126) Harvey, D. T.; Linton, R. W. *Colloids and Surfaces* X-ray photoelectron spectroscopy (XPS) of adsorbed zinc on amorphous hydrous ferric oxide. **1984**, 11, 81-96.
- (127) Yubero, F.; González-Elipe, A. R.; Tougaard, S. *Surface Science* Determination of growth mechanisms by X-ray photoemission and ion scattering spectroscopies: application to thin iron oxide films deposited on SiO₂. **2000**, 457, 24-36.
- (128) Manceau, A.; Combes, J. M. *Phys. Chem. Miner* **1988**, 15, 283.
- (129) Manceau, A.; Drits, V. A. *Clay Minerals* Local structure of ferrihydrite and ferroxihite by EXAFS spectroscopy. **1993**, 28, 165-184.
- (130) Combes, J. M.; Manceau, A.; Calas, G.; Bottero, J. Y. *Geochimica et Cosmochimica Acta* Formation of ferric oxides from aqueous solutions: A polyhedral approach by X-ray absorption spectroscopy: I. Hydrolysis and formation of ferric gels. **1989**, 53, 583-594.

(131) Combes, J. M.; Manceau, A.; Calas, G. *Geochimica et Cosmochimica Acta* Formation of ferric oxides from aqueous solutions: A polyhedral approach by X-ray Absorption Spectroscopy: II. Hematite formation from ferric gels. **1990**, *54*, 1083-1091.

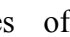
(132) Charlet, L.; Manceau, A. A. *Journal of Colloid and Interface Science* X-ray absorption spectroscopic study of the sorption of Cr(III) at the oxide-water interface: II. Adsorption, coprecipitation, and surface precipitation on hydrous ferric oxide. **1992**, *148*, 443-458.

(133) Manceau, A.; Charlet, L.; Boisset, M. C.; Didier, B.; Spadini, L. *Applied Clay Science* Sorption and speciation of heavy metals on hydrous Fe and Mn oxides. From microscopic to macroscopic. **1992**, *7*, 201-223.

(134) O'Day, P. A.; Newville, M.; Neuhoff, P. S.; Sahai, N.; Carroll, S. A. *Journal of Colloid and Interface Science* X-Ray Absorption Spectroscopy of Strontium(II) Coordination: I. Static and Thermal Disorder in Crystalline, Hydrated, and Precipitated Solids and in Aqueous Solution. **2000**, *222*, 184-197.

(135) Sahai, N.; Carroll, S. A.; Roberts, S.; O'Day, P. A. *Journal of Colloid and Interface Science* X-Ray Absorption Spectroscopy of Strontium(II) Coordination: II. Sorption and Precipitation at Kaolinite, Amorphous Silica, and Goethite Surfaces. **2000**, *222*, 198-212.

(136) Thimsen, E.; Biswas, S.; Lo, C. S.; Biswas, P. *The Journal of Physical Chemistry C* Predicting the Band Structure of Mixed Transition Metal Oxides: Theory and Experiment. **2009**, *113*, 2014-2021.

- (137) Sandratskii, L. M.; Uhl, M.; Kübler, J. *Journal of Physics: Condensed Matter* Band theory for electronic and magnetic properties of  [http://ej.iop.org/images/0953-8984/8/8/009/toc_img1.gif]. **1996**, *8*, 983.
- (138) Rollmann, G.; Rohrbach, A.; Entel, P.; Hafner, J. *Physical Review B* First-principles calculation of the structure and magnetic phases of hematite. **2004**, *69*, 165107.
- (139) Droubay, T.; Rosso, K. M.; Heald, S. M.; McCready, D. E.; Wang, C. M.; Chambers, S. A. *Physical Review B* Structure, magnetism, and conductivity in epitaxial Ti-doped α -Fe₂O₃ hematite: Experiment and density functional theory calculations. **2007**, *75*, 104412.
- (140) Rollmann, G.; Entel, P.; Rohrbach, A.; Hafner, J. *Phase Transitions* High-pressure characteristics of α -Fe₂O₃ using DFT+U. **2005**, *78*, 251-258.
- (141) Alvarez-Ramírez, F.; Martínez-Magadán, J. M.; Gomes, J. R. B.; Illas, F. *Surface Science* On the geometric structure of the (0001) hematite surface. **2004**, *558*, 4-14.
- (142) Blanchard, M.; Lazzeri, M.; Mauri, F.; Balan, E. *American Mineralogist* First-principles calculation of the infrared spectrum of hematite. **2008**, *93*, 1019-1027.
- (143) Kubicki, J.; Paul, K.; Sparks, D. *Geochemical Transactions* Periodic density functional theory calculations of bulk and the (010) surface of goethite. **2008**, *9*, 4.

- (144) Zhang, J. Z. *Acc. Chem. Res.* Ultrafast studies of Electron Dynamics in Semiconductor and Metal Colloidal Nano-Particles: Effects of Size and Surface. **1997**, *30*, 423-429.
- (145) Zhang, J. Z. *J. Phys. Chem. B* Interfacial Charge Carrier Dynamics of Colloidal Semiconductor Nanoparticles. **2000**, *104*, 7239-7253.
- (146) Klimov, V. I.; McBranch, D. W. *Opt. Lett.* Femtosecond High-Sensitivity, Chirp-Free Transient Absorption Spectroscopy Using Kilohertz Lasers. **1998**, *23*, 277-279
- (147) Kaiser, K. *Ultrashort Laser Pulses: Generation and Applications*; Springer-Verlag: Berlin, 1993.
- (148) Backus, S.; Durfee III, C. G.; Kapteyn, H. C.; M.M. Murnane, M. M. *Rev. Sci. Instr.* High Power Ultrafast Lasers. **1998**, *69*, 1207-1223.
- (149) Roberti, T. W.; Smith, B. A.; Zhang, J. Z. *J. Chem. Phys.* Ultrafast Electron Dynamics at the Liquid-Metal Interface: Femtosecond Studies Using Surface Plasmons in Aqueous Silver Colloid. **1995**, *102*, 3860-3866.
- (150) Link, S.; Burda, C.; Nikoobakht, B.; El-Sayed, M. A. *Chem. Phys. Lett.* How Long Does It Take to Melt a Gold Nanorod? A Femtosecond Pump-Probe Absorption Spectroscopic Study. **1999**, *315*, 12-18.
- (151) Link, S.; El-Sayed, M. A. *Ann. Rev. Phys. Chem.* Optical Properties and Ultrafast Dynamics in Metallic Nanocrystals. **2003**, *54*, 331-366.
- (152) Zhang, J. Z.; O'Neil, R. H.; Roberti, T. W.; McGowen, J. L.; Evans, J. E. *Springer Ser. Chem. Phys.* Femtosecond Studies of Photoinduced Electron

Dynamics at the Liquid-Solid Interface of Semiconductor Nano-Particles in Water. **1994**, *60*, 316-317.

(153) Lupo, M. G.; Della Sala, F.; Carbone, L.; Zavelani-Rossi, M.; Fiore, A.; Luer, L.; Polli, D.; Cingolani, R.; Manna, L.; Lanzani, G. *Nano Letters* Ultrafast Electron-Hole Dynamics in Core/Shell CdSe/CdS Dot/Rod Nanocrystals. **2008**, *8*, 4582-4587.

(154) Peng, P.; Milliron, D. J.; Hughes, S. M.; Johnson, J. C.; Alivisatos, A. P.; Saykally, R. J. *Nano Letters* Femtosecond Spectroscopy of Carrier Relaxation Dynamics in Type II CdSe/CdTe Tetrapod Heteronanostructures. **2005**, *5*, 1809-1813.

(155) Sun, C.-K.; Sun, S.-Z.; Lin, K.-H.; Zhang, K. Y.-J.; Liu, H.-L.; Liu, S.-C.; Wu, J.-J. *Appl. Phys. Lett.* Ultrafast Carrier Dynamics in ZnO Nanorods. **2005**, *87*, 023106-023103.

(156) Rehm, J. M.; McLendon, G. L.; Nagasawa, Y.; Yoshihara, K.; Moser, J.; Grätzel, M. *The Journal of Physical Chemistry* Femtosecond Electron-Transfer Dynamics at a Sensitizing Dye-Semiconductor (TiO₂) Interface. **1996**, *100*, 9577-9578.

(157) Heimer, T. A.; Heilweil, E. J.; Bignozzi, C. A.; Meyer, G. J. *J. Phys. Chem. A* Electron Injection, Recombination and Halide Oxidation Dynamics at Dye-sensitized TiO₂ Interfaces. **2000**, *104*, 4256-4262.

(158) Ling, Y.; Wang, G.; Wheeler, D. A.; Zhang, J. Z.; Li, Y. *Nano Letters* Sn-Doped Hematite Nanostructures for Photoelectrochemical Water Splitting. **2011**, null.

(159) Joly, A. G.; Williams, J. R.; Chambers, S. A.; Xiong, G.; Hess, W. P.; Laman, D. M. *Journal of Applied Physics* Carrier Dynamics in α -Fe₂O₃ (0001) Thin Films and Single Crystals Probed by Femtosecond Transient Absorption and Reflectivity. **2006**, *99*, 053521.

(160) Nadochenko, V. A.; Denisov, N. N.; Gak, V. Y.; Gostev, F. E.; Titov, A. A.; Sarkisov, O. M.; Nikandrov, V. V. *Russian Chemical Bulletin* Femtosecond Relaxation of Photoexcited States in Nanosized Semiconductor Particles of Iron Oxides. **2002**, *51*, 457.

(161) Fu, L.; Wu, Z.; Ai, X.; Zhang, J.; Nie, Y.; Xie, S.; Yang, G.; Zou, B. *The Journal of Chemical Physics* Time-Resolved Spectroscopic Behavior of Fe₂O₃ and ZnFe₂O₄ Nanocrystals. **2004**, *120*, 3406.

(162) Thomsen, C.; Grahn, H. T.; Maris, H. J.; Tauc, J. *Physical Review B* Surface Generation and Detection of Phonons by Picosecond Light Pulses. **1986**, *34*, 4129.

(163) Grahn, H. T.; Maris, H. J.; Tauc, J. *Quantum Electronics, IEEE Journal of Picosecond Ultrasonics*. **1989**, *25*, 2562.

(164) Wang, G.; Ling, Y.; Wheeler, D. A.; George, K. E. N.; Horsley, K.; Heske, C.; Zhang, J. Z.; Li, Y. *Nano Letters* Facile Synthesis of Highly Photoactive α -Fe₂O₃-Based Films for Water Oxidation. **2011**, *11*, 3503-3509.

(165) Kronawitter, C. X.; Vayssieres, L.; Shen, S.; Guo, L.; Wheeler, D. A.; Zhang, J. Z.; Antoun, B. R.; Mao, S. S. *Energy & Environmental Science A*

perspective on solar-driven water splitting with all-oxide hetero-nanostructures. **2011**, *4*, 3889-3899.

(166) Kronawitter, C. X.; Bakke, J. R.; Wheeler, D. A.; Wang, W.-C.; Chang, C.; Antoun, B. R.; Zhang, J. Z.; Guo, J.; Bent, S. F.; Mao, S. S.; Vayssieres, L. *Nano Letters* Electron Enrichment in 3d Transition Metal Oxide Hetero-Nanostructures. **2011**, *11*, 3855-3861.

(167) Pendlebury, S. R.; Barroso, M.; Cowan, A. J.; Sivula, K.; Tang, J.; Gratzel, M.; Klug, D.; Durrant, J. R. *Chemical Communications* Dynamics of photogenerated holes in nanocrystalline α -Fe₂O₃ electrodes for water oxidation probed by transient absorption spectroscopy. **2011**, *47*, 716-718.

(168) Vayssieres, L.; Sathe, C.; Butorin, S. M.; Shuh, D. K.; Nordgren, J.; Guo, J. *Advanced Materials* One-Dimensional Quantum-Confinement Effect in α -Fe₂O₃ Ultrafine Nanorod Arrays. **2005**, *17*, 2320-2323.

(169) Pendlebury, S. R.; Cowan, A. J.; Barroso, M.; Sivula, K.; Ye, J.; Gratzel, M.; Klug, D. R.; Tang, J.; Durrant, J. R. *Energy & Environmental Science* Correlating long-lived photogenerated hole populations with photocurrent densities in hematite water oxidation photoanodes. **2012**.

(170) Zhang, J. Z. *Optical properties and spectroscopy of nanomaterials*; World Scientific Publishing Co.: Hackensack, NJ, 2009.

(171) Beermann, N.; Vayssieres, L.; Lindquist, S.-E.; Hagfeldt, A. *Journal of The Electrochemical Society* Photoelectrochemical Studies of Oriented Nanorod Thin Films of Hematite. **2000**, *147*, 2456-2461.

- (172) Desai, J. D.; Pathan, H. M.; Min, S.-K.; Jung, K.-D.; Joo, O. S. *Applied Surface Science* FT-IR, XPS and PEC characterization of spray deposited hematite thin films. **2005**, *252*, 1870-1875.
- (173) Satsangi, V. R.; Kumari, S.; Singh, A. P.; Shrivastav, R.; Dass, S. *International Journal of Hydrogen Energy* Nanostructured hematite for photoelectrochemical generation of hydrogen. **2008**, *33*, 312-318.
- (174) Boumaza, S.; Boudjemaa, A.; Omeiri, S.; Bouarab, R.; Bouguelia, A.; Trari, M. *Solar Energy* Physical and photoelectrochemical characterizations of hematite α -Fe₂O₃: Application to photocatalytic oxygen evolution. **2010**, *84*, 715-721.
- (175) Wang, H.; Turner, J. A. *Journal of The Electrochemical Society* Characterization of Hematite Thin Films for Photoelectrochemical Water Splitting in a Dual Photoelectrode Device. **2010**, *157*, F173-F178.
- (176) Ahmed, S. M.; Leduc, J.; Haller, S. F. *The Journal of Physical Chemistry* Photoelectrochemical and impedance characteristics of specular hematite. 1. Photoelectrochemical parallel conductance, and trap rate studies. **1988**, *92*, 6655-6660.
- (177) Hisatomi, T.; Le Formal, F.; Cornuz, M.; Brillet, J.; Tetreault, N.; Sivula, K.; Gratzel, M. *Energy & Environmental Science* Cathodic shift in onset potential of solar oxygen evolution on hematite by 13-group oxide overlayers. **2011**, *4*.

(178) Hiralal, P.; Saremi-Yarahmadi, S.; Bayer, B. C.; Wang, H.; Hofmann, S.; Upul Wijayantha, K. G.; Amaratunga, G. A. J. *Solar Energy Materials and Solar Cells* Nanostructured hematite photoelectrochemical electrodes prepared by the low temperature thermal oxidation of iron. **2011**, *95*, 1819-1825.

(179) Morrish, R.; Rahman, M.; MacElroy, J. M. D.; Wolden, C. A. *ChemSusChem* Activation of Hematite Nanorod Arrays for Photoelectrochemical Water Splitting. **2011**, *4*, 474-479.

(180) Sivula, K.; Le Formal, F.; Gratzel, M. *Chemsuschem* Solar Water Splitting: Progress Using Hematite α -Fe₂O₃ Photoelectrodes. **2011**, *4*, 432-449.

(181) Le Formal, F.; Gratzel, M.; Sivula, K. *Advanced Functional Materials* Controlling Photoactivity in Ultrathin Hematite Films for Solar Water-Splitting. **2010**, *20*, 1099-1107.

(182) Murphy, A. B.; Barnes, P. R. F.; Randeniya, L. K.; Plumb, I. C.; Grey, I. E.; Horne, M. D.; Glasscock, J. A. *International Journal of Hydrogen Energy* Efficiency of solar water splitting using semiconductor electrodes. **2006**, *31*, 1999-2017.

(183) Joly, A. G.; Williams, J. R.; Chambers, S. A.; Xiong, G.; Hess, W. P.; Laman, D. M. *Journal of Applied Physics* Carrier dynamics in α -Fe₂O₃ (0001) thin films and single crystals probed by femtosecond transient absorption and reflectivity. **2006**, *99*, 6.

- (184) Cherepy, N. J.; Liston, D. B.; Lovejoy, J. A.; Deng, H. M.; Zhang, J. *Z. Journal of Physical Chemistry B* Ultrafast studies of photoexcited electron dynamics in gamma- and α -Fe₂O₃ semiconductor nanoparticles. **1998**, *102*, 770-776.
- (185) Stojic, D. L.; Marceta, M. P.; Sovilj, S. P.; Miljanic, S. S. *Journal of Power Sources* Hydrogen generation from water electrolysis - possibilities of energy saving. **2003**, *118*, 315-319.
- (186) Khaselev, O.; Turner, J. A. *Science* A monolithic photovoltaic-photoelectrochemical device for hydrogen production via water splitting. **1998**, *280*, 425-427.
- (187) Kennedy, J. H.; Frese, K. W. *Journal of the Electrochemical Society* Photooxidation of Water at α -Fe₂O₃ Electrodes. **1977**, *124*, C130-C130.
- (188) Goodlet, G.; Faty, S.; Cardoso, S.; Freitas, P. P.; Simoes, A. M. P.; Ferreira, M. G. S.; Belo, M. D. *Corrosion Science* The electronic properties of sputtered chromium and iron oxide films. **2004**, *46*, 1479-1499.
- (189) Glasscock, J. A.; Barnes, P. R. F.; Plumb, I. C.; Bendavid, A.; Martin, P. J. *Thin Solid Films* Structural, optical and electrical properties of undoped polycrystalline hematite thin films produced using filtered arc deposition. **2008**, *516*, 1716-1724.
- (190) Kennedy, J. H.; Shinar, R.; Ziegler, J. P. *Journal of the Electrochemical Society* α -Fe₂O₃Photoanodes Doped with Silicon. **1980**, *127*, 2307-2309.

(191) Cesar, I.; Kay, A.; Martinez, J. A. G.; Gratzel, M. *Journal of the American Chemical Society* Translucent thin film Fe₂O₃ photoanodes for efficient water splitting by sunlight: Nanostructure-directing effect of Si-doping. **2006**, *128*, 4582-4583.

(192) Brillet, J.; Gratzel, M.; Sivula, K. *Nano Letters* Decoupling Feature Size and Functionality in Solution-Processed, Porous Hematite Electrodes for Solar Water Splitting. **2010**, *10*, 4155-4160.

(193) Zhang, P.; Kleiman-Shwarscstein, A.; Hu, Y. S.; Lefton, J.; Sharma, S.; Forman, A. J.; McFarland, E. *Energy & Environmental Science* Oriented Ti doped hematite thin film as active photoanodes synthesized by facile APCVD. **2011**, *4*, 1020-1028.

(194) Sivula, K.; Zboril, R.; Le Formal, F.; Robert, R.; Weidenkaff, A.; Tucek, J.; Frydrych, J.; Gratzel, M. *Journal of the American Chemical Society* Photoelectrochemical Water Splitting with Mesoporous Hematite Prepared by a Solution-Based Colloidal Approach. **2010**, *132*, 7436-7444.

(195) Lukowski, M. A.; Jin, S. *Journal of Physical Chemistry C* Improved Synthesis and Electrical Properties of Si-Doped α -Fe₂O₃ Nanowires. **2011**, *115*, 12388-12395.

(196) Morin, F. J. *Physical Review* Electrical Properties of α -Fe₂O₃ and α -Fe₂O₃ Containing Titanium. **1951**, *83*, 1005-1010.

(197) Zhong, D. K.; Cornuz, M.; Sivula, K.; Graetzel, M.; Gamelin, D. R. *Energy & Environmental Science* Photo-assisted electrodeposition of cobalt-

phosphate (Co-Pi) catalyst on hematite photoanodes for solar water oxidation. **2011**, *4*, 1759-1764.

(198) Zhong, D. K.; Sun, J. W.; Inumaru, H.; Gamelin, D. R. *Journal of the American Chemical Society* Solar Water Oxidation by Composite Catalyst/ α -Fe₂O₃ Photoanodes. **2009**, *131*, 6086-+.

(199) Pendlebury, S.; Barroso, M.; Cowan, A.; Sivula, K.; Tang, J.; Gratzel, M.; Klug, D.; Durrant, J. *Chemical Communications* Dynamics of photogenerated holes in nanocrystalline α -Fe₂O₃ electrodes for water oxidation probed by transient absorption spectroscopy. **2011**, *47*, 716-718.

(200) Dotan, H.; Sivula, K.; Gratzel, M.; Rothschild, A.; Warren, S. *Energy Environmental & Science* Probing the photoelectrochemical properties of hematite (α -Fe₂O₃) electrodes using hydrogen peroxide as a hole scavenger. **2011**, *4*, 958-964.

(201) Klahr, B. M.; Martinson, A. B. F.; Hamann, T. W. *Langmuir* Photoelectrochemical Investigation of Ultrathin Film Iron Oxide Solar Cells Prepared by Atomic Layer Deposition. **2011**, *27*, 461-468.

(202) Somekawa, S.; Kusumoto, Y.; Abdulla-Al-Mamun, M.; Muruganandham, M.; Horie, Y. *Electrochemistry Communications* Wet-type Fe₂O₃ solar cells based on Fe₂O₃ films prepared by laser ablation: Drastic temperature effect. **2009**, *11*, 2150-2152.

CHAPTER 5. Ultrafast Charge Carrier Dynamics and Photoelectrochemical Properties of Hydrogen-Treated TiO₂ Nanowire Arrays

5.1 Abstract

Here we report studies of photoelectrochemical (PEC) properties and ultrafast charge carrier relaxation dynamics of hydrogen-treated TiO₂ (H:TiO₂) nanowire arrays. PEC measurements showed the photocurrent density of the H:TiO₂ was approximately double that of TiO₂, attributed to increased donor density due to the formation of oxygen vacancies in H:TiO₂ due to hydrogen treatment. Charge carrier dynamics of H:TiO₂, measured using fs transient absorption spectroscopy, showed a fast decay of ~20 ps followed by slower decay persisting to tens of picoseconds. The fast decay is attributed to bandedge electron-hole recombination and the slower decay is attributed to recombination from trap states. Visible absorption is attributed to either electronic transitions from the valence band to oxygen vacancy states or from oxygen vacancy states to the conduction band of the TiO₂, which is supported by incident photon to current conversion efficiency (IPCE) data. H:TiO₂ represents a unique material with improved photoelectrochemical properties for applications including PEC water splitting, solar cells, and photocatalysis.

5.2 Introduction

Photoelectrochemical (PEC) water splitting is an attractive addition to our current energy sources because it uses abundant source materials, sunlight and water,

to produce hydrogen which burns without producing any CO₂. Since the inception of PEC water splitting¹ TiO₂ has been the cornerstone of PEC research because it is stable in aqueous electrolyte, has high carrier mobility and it has valence and conduction bands which straddle the reduction potentials for hydrogen and oxygen². The drawback of TiO₂ as a photoanode for PEC water splitting is its wide band gap that prevents it from absorbing the majority of the solar spectrum. Many studies have attempted to remedy this issue by sensitizing TiO₂ to visible light by combining it with narrow band gap semiconductors³ or by doping TiO₂ with other elements such as nitrogen³ or chromium⁴ to add additional states within the band gap.

One of the latest strategies for improving the photoactivity of TiO₂ involves treating the TiO₂ films with hydrogen gas at elevated temperature rendering the TiO₂ black^{5,6}. The H-treated TiO₂ (H:TiO₂) prepared in this way exhibited solar to hydrogen (STH) efficiency of 1.1%, the highest reported for a TiO₂ photoanode. Interestingly, although the performance was greatly enhanced due to the hydrogen treatment, incident photon to current efficiency (IPCE) measurements taken as a function of incident wavelength showed that the majority of the increase in photocurrent occurs in the UV with performance decreasing for wavelengths longer than about 450 nm. In spite of this decrease beyond 450 nm the efficiency for H:TiO₂ is still greater than that of TiO₂ at visible wavelengths.

In the current study we studied the PEC performance and ultrafast charge carrier relaxation dynamics of H:TiO₂ pumped with visible light to gain a better understanding of the nature of the states involved in the visible light absorption of

hydrogen treated TiO₂ films. Probing these states using transient absorption spectroscopy provided insights into the nature of these states and helped us understand why hydrogen treatment is so effective for improving the PEC properties of TiO₂. Overall, the visible absorption in the H:TiO₂ is attributed to electronic transitions from oxygen vacancy states to the conduction band of the TiO₂.

5.3 Experiment

5.3.1 TiO₂ nanowire array synthesis

TiO₂ nanowire arrays were grown on FTO glass using a previously reported hydrothermal method⁷. Briefly, 15 mL of DI water was mixed with 15 mL of concentrated HCl (37.2%) in a 100 mL beaker with continuous stirring. Subsequently, 0.5mL of titanium *n*-butoxide was added to the diluted HCl solution. The prepared solution and a piece of FTO glass were transferred into a Teflon-lined stainless steel autoclave. The sealed autoclave was placed in a 150°C oven for 5 hours and allowed to cool naturally down to room temperature. A uniform white film was coated onto FTO glass. The sample was then washed with ethanol and water, respectively. Finally, the sample was annealed in air at 550°C for 3 hours before hydrogen treatment.

5.3.2 Hydrogen treatment:

TiO₂ nanowire arrays were annealed in a hydrogen atmosphere at various temperatures; in a range of 200-550°C, for 30 minutes. The hydrogen treatment was

performed in a home-built CVD system in which the CVD tube was filled with ultrahigh purity hydrogen gas (Praxair).

5.3.3 Electron Microscopy (EM) and Raman Measurements:

Scanning electron microscopy (SEM) images were collected with a field-emission SEM (Hitachi S-4800 II) with an acceleration voltage of 30 kV. Raman scattering measurements were conducted using a Renishaw InVia Raman Microscope System, utilizing a HeNe (632.8 nm excitation) laser at a power of ~0.2 mW. A 20× objective lens was used to focus the laser light onto the nanowire sample. Sample integration times were set to 10 seconds.

5.3.4 Photoelectrochemical Measurements:

TiO₂ and H:TiO₂ nanowire arrays were fabricated into photoanodes by soldering a copper wire onto a bare part of the FTO substrate. The substrate edges and the metal contact region were sealed with insulating epoxy resin. The working electrode area is in the range of 0.2-0.25 cm². A 1 M NaOH aqueous solution (pH = 13.6) was used as the electrolyte for PEC measurements. Linear sweeps and *I-t* scans were measured by a CHI 660D electrochemical station, with Ag/AgCl as the reference and a Pt wire as the counter electrode, under simulated sunlight with a 150 W xenon lamp (Newport 6255) coupled with an AM 1.5 global filter (Newport 81094). All measurements were carried out with front side illumination.

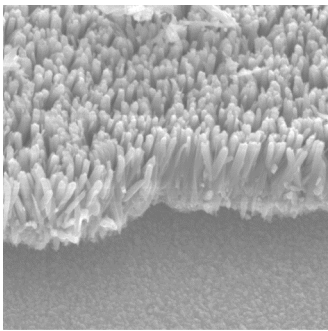
5.3.5 Femtosecond Transient Absorption System:

Ultrafast transient bleach measurements were conducted using an amplified femtosecond Ti-sapphire laser system described previously⁸. In all experiments, a pump wavelength of 470 nm was selected from an optical parametric amplifier and used. The final output was ~180 fs pulses with a power output of ~200 nJ/pulse which was attenuated with neutral density filters. A white light continuum (WLC) generated from a sapphire crystal was used as the probe pulse that was detected using a CCD detector. The delay stage controlling the WLC propagation was operated by a motor-driven setup with 1 μm resolution.

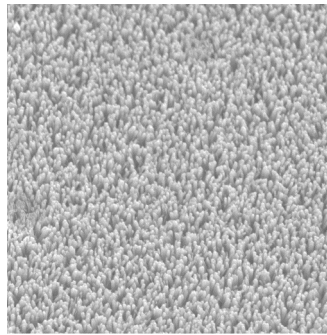
5.4 Discussion

Figure 1 shows representative SEM images of fairly uniform TiO₂ nanowire arrays prepared on an FTO substrate. The TiO₂ nanowires have typical diameters of 100-200 nm with corresponding lengths of 2-3 μm . As shown in the images, the nanowire arrays are vertically-aligned and have rectangular cross-sections.

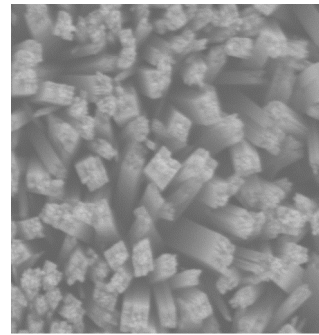
Figure 1: SEM image of vertically aligned H:TiO₂ nanowire arrays prepared on an FTO substrate with an average diameter of 100-200 nm and an average length of 2-3 μm. The right panel shows the rectangular cross-sectional shape of the H:TiO₂ nanowires.



2 μ m 10000X



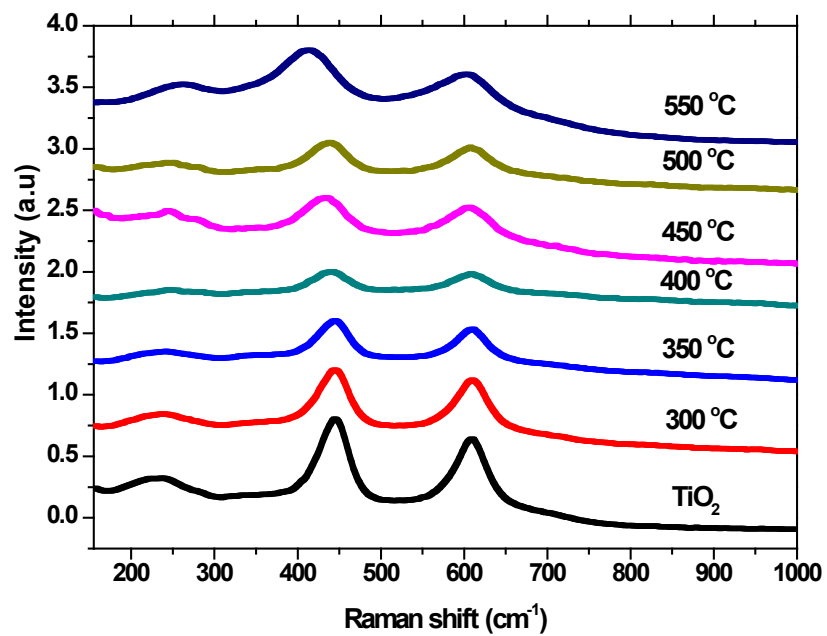
4 μ m 5000X



1 μ m 20000X

Figure 2 is a plot of the Raman spectra of the H:TiO₂ nanowires following annealing in a hydrogen environment at various temperatures. Also plotted is the Raman spectrum of non-hydrogen-treated TiO₂. Most notable is the presence of two distinct modes at 450 (E_g) and 610 (A_{1g}) cm⁻¹, which are attributed to the rutile phase of the TiO₂⁹. The TiO₂ curve, represented in black in Figure 2, also shows rutile modes.

Figure 2: Raman spectra of TiO_2 and H:TiO_2 annealed in a hydrogen atmosphere at various temperatures (300°C-550°C).



We investigated the effect that hydrogen treatment on the PEC performance of TiO₂ (Figure 3) by comparing the linear sweeps of pristine TiO₂ (red) with a H:TiO₂ nanowire sample prepared at 350°C (green) in a window with a potential range of -1.0 to 0.5 V *vs.* Ag/AgCl. After analyzing the data, we arrived at two interesting conclusions. First, the photocurrent density of the H:TiO₂ nanowire sample was approximately two times higher relative to the pristine TiO₂ nanowires throughout the potential window. This confirms the fact that hydrogen treatment is a simple and effective method for enhancing the PEC performance of TiO₂. Second, the photocurrent density of the pristine TiO₂ sample increases gradually with the applied potential and reaches a saturated current of 0.95 mA/cm² at ~0 V *vs.* Ag/AgCl. In contrast, the H:TiO₂ sample showed a drastic increase in photocurrent density at an onset potential of -0.9 V *vs.* Ag/AgCl, and the photocurrent saturated at a substantially lower potential of approximately -0.4 V *vs.* Ag/AgCl (0.6 V *vs.* RHE) at ~2.88 mA/cm². The negative shift of saturation potential indicates that the charge separation and transport in the H:TiO₂ samples are more efficient, compared to the pristine TiO₂ nanowires.

Figure 3: Linear sweep voltammogram collected from non-hydrogen-treated TiO₂ nanowires (red) and H:TiO₂ nanowires annealed at a temperature of 350°C (green).

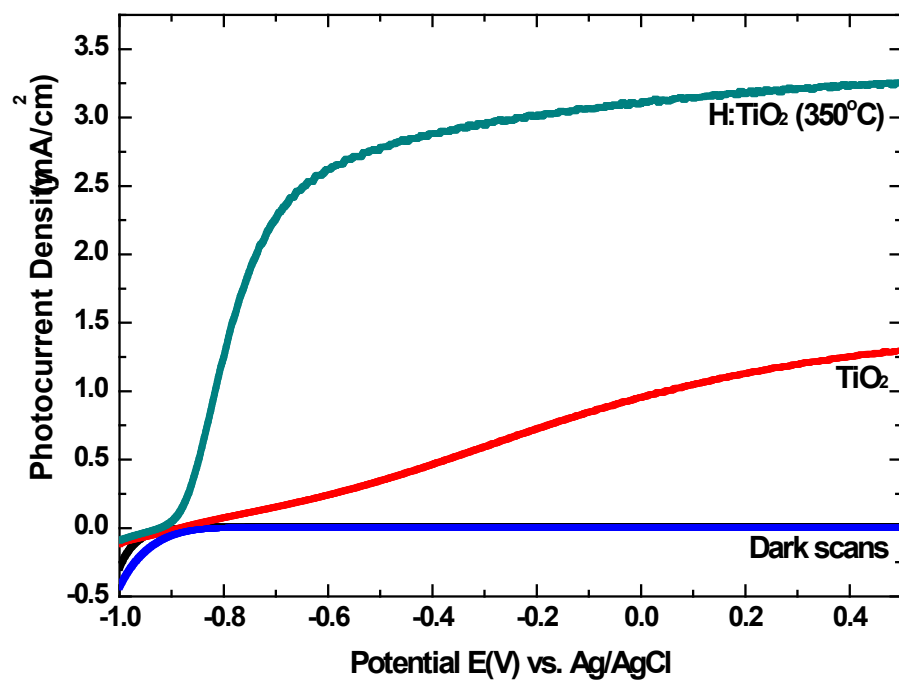


Figure 4a is a 3D plot of the transient time decay profile (in ps) for the H:TiO₂ following excitation at 470 nm (maintained at a pulse energy of 200 nJ/pulse) at probe wavelengths of 500-650 nm. Figure 4b is a plot of signal vs. time following a 470 nm pump taken at a probe wavelength of 550 nm. A pulse-width-limited (<180 fs) transient bleach is followed by a small amplitude fast decay with a lifetime of ~20 ps and was followed by another exponential recovery of several tens of picoseconds. The 470 nm pump pulse excites electrons from either the interband states arising from oxygen vacancies to the conduction band of TiO₂, or from the valence band to the interband states (Figure 5). The recovery of the bleach represents the recombination of these excited electrons with the holes in the oxygen vacancy states. The fast and slow components of the bleach recovery represent different pathways by which the electron and hole recombine, with the fast component correlating with recombination between the conduction band and the oxygen vacancy states and the slow component representing recombination from deep, mid-band gap traps.

These results compare interestingly to dynamics studies conducted previously on pristine TiO₂. In those studies, band-edge recombination of TiO₂ was seen to happen on timescales of approximately 30 ps¹⁰⁻¹³. Furthermore, the presence of a long-lived decay process in our sample suggests slower recombination from trap states which would help explain the overall better PEC performance (Figure 3) since long-lived charge carriers promote efficient photocurrent generation. The effect of hydrogen treatment on the early time dynamics is significant, suggesting that hydrogen treatment has an important effect on trap states within the bandgap. Even

though there is significant electron-hole recombination based on the dynamics data, strong photocurrent was still observed (Figure 3), which is partly due to the improved donor density as a result of H₂ treatment and 1-D structures that facilitate charge transfer and transport.

The origin of the visible signal in the H:TiO₂ becomes a fascinating point of discussion and is tied closely with the PEC plot presented in Figure 3. It was previously reported that oxygen vacancies play a critical role in determining both the surface and electronic properties of TiO₂¹⁴⁻¹⁶. Previously reported⁶ XPS data showed that the H:TiO₂ nanowires do not contain dopants from other elements. The defect states are attributed to the formation of oxygen vacancies and surface hydroxyl groups on TiO₂. The O 2*p* energy levels for Ti-OH-Ti and Ti-OH were reported to be positioned 2.6 and 0.7 eV below the valence band of the rutile phase of TiO₂, respectively. Furthermore, it was reported that these states are energetically stable and are not oxidized by the valence band holes *via* electron transfer^{17,18}. The presence of these Ti-OH energy states below the valence band of TiO₂ should not lead to visible light absorption. We therefore believe that the oxygen vacancies in the TiO₂ structure created during hydrogenation play a critical role in the visible light absorption and therefore the dark color of TiO₂. The oxygen vacancy energy levels have been determined to be ~0.75 and 1.18 eV below the conduction band (CB) of hydrogen-reduced rutile plates^{14,15}. Although a direct and unambiguous discernment of the visible absorption probed in this study is difficult, these calculated energies have led us to assign the visible absorption to either electronic transitions from the

valence band of TiO_2 to oxygen vacancy states below the conduction band or from the oxygen vacancy states to the conduction band.

Figure 6 shows the IPCE spectra of TiO_2 and H:TiO_2 nanowires. A significantly enhanced IPCE in the UV region was observed after hydrogen treatment. In addition, we also observed a small amount visible light photoactivity at longer wavelengths. Based on an energy diagram reported by Wang⁶, it was determined that the strong UV absorption of TiO_2 is due to the electronic transition from the valence band to the conduction band. However, subsequent high-temperature treatment in a hydrogen-rich environment has the effect of creating oxygen vacancies within the band gap of TiO_2 . The visible and near-infrared absorption was proposed to be due to transitions from the valence band to mid-band gap oxygen vacancies or from mid-band gap oxygen vacancies to the TiO_2 conduction band.

Figure 4: (Left) Transient absorption decay profile of H₂-treated TiO₂ nanowires following a 470 nm pump excitation with a white-light continuum monitoring probe. (Right) Transient absorption plot of signal vs. time for a pump wavelength of 470 nm and a probe of 550 nm. Following the initial 180 fs excitation pulse, electron-hole recombination as well as electron trapping into trap states occur quickly (~20 ps), which is followed by slower trapping/recombination events persisting to tens of picoseconds.

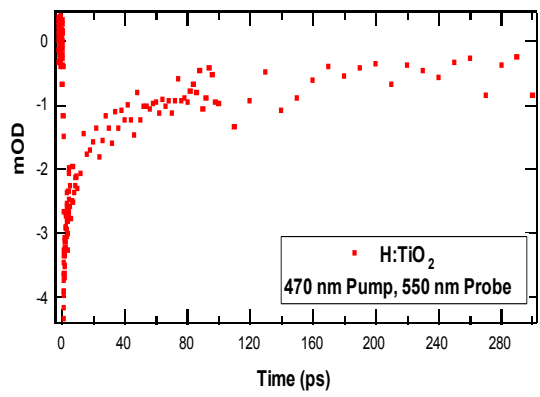
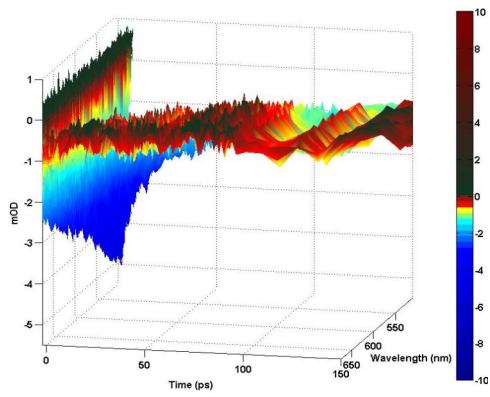


Figure 5: Proposed band diagram model illustrating the dynamics of UV-pumped pristine TiO_2 (left) with a bandgap of 3.0 eV as compared to the visible light-pumped $\text{H}:\text{TiO}_2$ (right) with CB and VB being the conduction band and valence band, respectively, and V_o are the oxygen vacancies, positioned 0.75 and 1.18 eV below the CB. The red lines in the $\text{H}:\text{TiO}_2$ diagram are intended to represent two possible processes: either excitation from the VB to the V_o or excitation from the V_o to the CB.

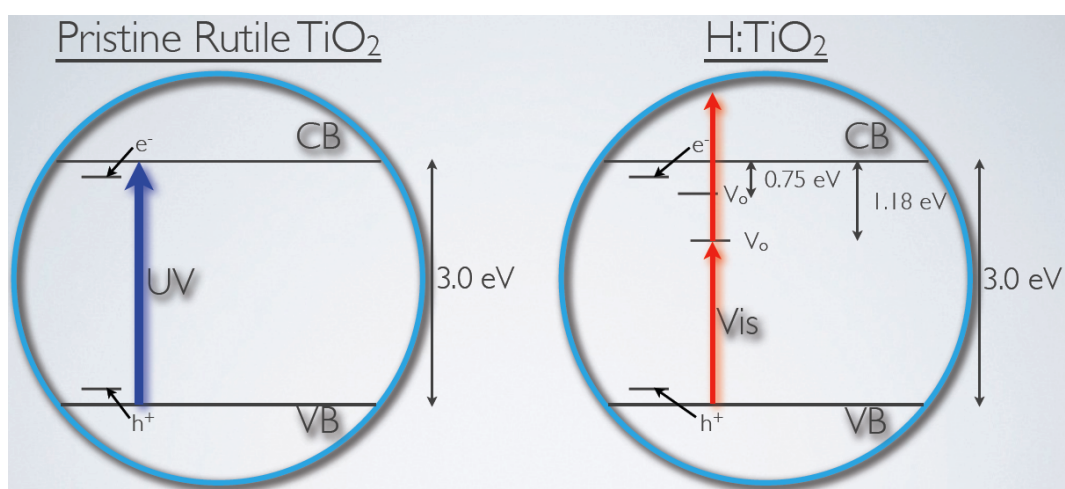
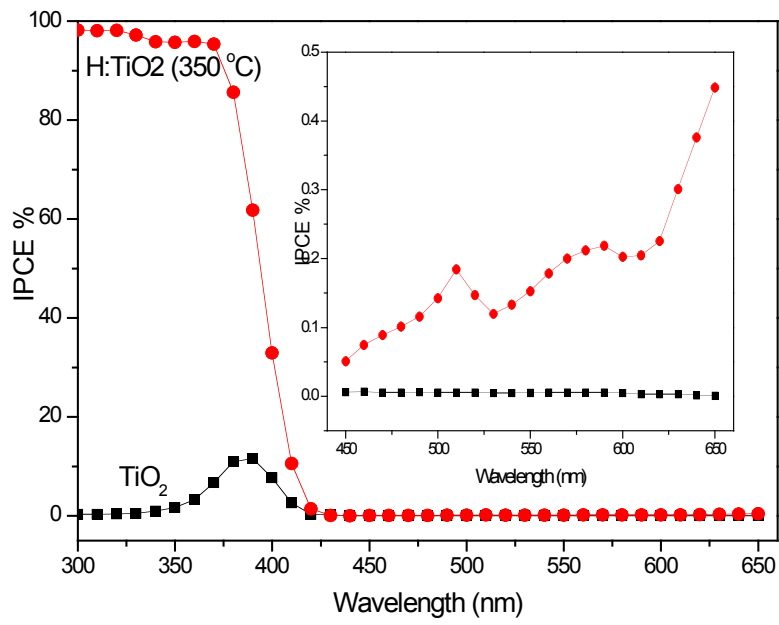


Figure 6: IPCE spectra of pristine TiO₂ and H:TiO₂ nanowires prepared at 350°C and collected at an incident wavelength range from 300-650 nm at a potential of -0.6V vs. Ag/AgCl. Inset: magnified IPCE spectra in the range of 450-650 nm.



5.5 Conclusion

In this work, we report the PEC properties and ultrafast charge carrier dynamics of H:TiO₂. In particular, the PEC performance of H:TiO₂ was drastically improved relative to TiO₂ which was mostly attributed to improved photoactivity in the UV region. IPCE measurements for H:TiO₂ showed a small amount of photocurrent under visible light irradiation where pristine TiO₂ does not absorb. Additionally, with probing these visible light transitions using ultrafast transient absorption spectroscopy it was determined that the bleach recovers with exponential decays of ~20 ps and a slower decay of several tens of ps which is faster than previous reports for band edge recombination in TiO₂. We have assigned the improved photoactivity of the H:TiO₂ in the visible spectrum to the introduction of oxygen vacancy states below the conduction band. Furthermore, the visible absorption of the H:TiO₂ is assigned to transitions from the valence band to the oxygen vacancy states or from the oxygen vacancy states to the conduction band. This finding has a direct application to solar energy harvesting *via* water splitting.

5.6 References

- (1) Fujishima, A.; Honda, K. *Nature* **1972**, *238*, 37-38.
- (2) Alexander, B. D.; Kulesza, P. J.; Rutkowska, L.; Solarska, R.; Augustynski, J. *Journal Of Materials Chemistry* **2008**, *18*, 2298-2303.

- (3) Hensel, J.; Wang, G.; Li, Y.; Zhang, J. Z. *Nano letters* **2010**, *10*, 478-483.
- (4) Larsen, G.; Fitzmorris, R. C.; Zhang, J. Z.; Zhao, Y. *The Journal of Physical Chemistry C*.
- (5) Chen, X.; Liu, L.; Yu, P. Y.; Mao, S. S. *Science* **2011**, *331*, 746-750.
- (6) Wang, G.; Wang, H.; Ling, Y.; Tang, Y.; Yang, X.; Fitzmorris, R. C.; Wang, C.; Zhang, J. Z.; Li, Y. *Nano Letters* **2011**, *11*, 3026-3033.
- (7) Liu, B.; Aydil, E. S. *Journal of the American Chemical Society* **2009**, *131*, 3985-3990.
- (8) Newhouse, R. J.; Wang, H.; Hensel, J. K.; Wheeler, D. A.; Zou, S.; Zhang, J. Z. *The Journal of Physical Chemistry Letters* **2011**, *2*, 228.
- (9) Chen, C.; Huang, Y.; Chung, W.; Tsai, D.; Tiong, K. *Journal of Materials Science: Materials in Electronics* **2009**, *20*, 303-306.
- (10) Colombo, D. P.; Bowman, R. M. *The Journal of Physical Chemistry* **1996**, *100*, 18445-18449.
- (11) Rothenberger, G.; Moser, J.; Graetzel, M.; Serpone, N.; Sharma, D. K. *Journal of the American Chemical Society* **1985**, *107*, 8054-8059.
- (12) Serpone, N.; Lawless, D.; Khairutdinov, R.; Pelizzetti, E. *The Journal of Physical Chemistry* **1995**, *99*, 16655-16661.
- (13) Zhou, W.-c.; Li, Z.-c.; Zhang, Z.-j.; Onda, K.; Ogihara, S.; Okimoto, Y.; Koshihara, S.-y. *Frontiers of Materials Science in China* **2009**, *3*, 403-408.
- (14) Cronmeyer, D. C. *Physical Review* **1959**, *113*, 1222-1226.

- (15) Cronmeyer, D. C.; Gilleo, M. A. *Physical Review* **1951**, *82*, 975-976.
- (16) Kim, W.-T.; Kim, C.-D.; Choi, Q. W. *Physical Review B* **1984**, *30*, 3625-3628.
- (17) Nakamura, R.; Nakato, Y. *Journal of the American Chemical Society* **2004**, *126*, 1290-1298.
- (18) Imanishi, A.; Okamura, T.; Ohashi, N.; Nakamura, R.; Nakato, Y. *Journal of the American Chemical Society* **2007**, *129*, 11569-11578.

CHAPTER 6: Probing the Nature of Bandgap States in Hydrogen-Treated TiO₂ Nanowires

6.1 Abstract

Hydrogen treatment of TiO₂ has been demonstrated to significantly alter its optical properties, including substantially enhanced visible light absorption that has important implications for various applications. The chemical nature of the bandgap states responsible for the increased visible absorption is not yet well understood. This work reports a detailed study of the structural, optical, electronic, and ultrafast properties of hydrogen-treated TiO₂ (H:TiO₂) nanowires (NWs) using a combination of experimental techniques including high-resolution transmission electron microscopy (HRTEM), electron paramagnetic resonance spectroscopy (ESR), time-resolved fluorescence (TRF), and femtosecond transient absorption (TA) spectroscopy in order to explain what constitutes the strong visible absorption. The initial combined ESR, TRF, and TA data suggest that the presence of a localized mid-bandgap oxygen vacancy (V_O) occupied by a lone electron is responsible for the visible absorption of the material. The data further indicate that, while untreated TiO₂ NWs are fluorescent, the hydrogen treatment leads to quenching of the fluorescence and highly efficient charge carrier recombination from the V_O state following excitation with visible light. With ultraviolet excitation, however, the charge carrier recombination of the H:TiO₂ NWs exhibits a larger component of a slow decay

compared to untreated TiO₂, which is correlated with enhanced photoelectrochemical performance. The results have provided deeper insight into the chemical nature and related properties of bandgap states in chemically-modified TiO₂ nanomaterials.

6.2 Introduction

In 1972, Fujishima and Honda discovered that titanium dioxide (TiO₂) was a promising material as a photoanode for photoelectrochemical (PEC) water splitting.¹ In the intervening four decades, research on the material has exploded. Much effort has been devoted to providing a fundamental understanding of its photocatalytic properties as well as enhancing its overall efficiency and performance as a PEC material. In particular, research on TiO₂ has gained significant traction due to the advantageous characteristics of the material, including its strong optical absorption, favorable band alignment, resistance to chemical degradation and photobleaching, abundance, low toxicity, and low cost.²⁻⁷

One of the limitations to TiO₂ has been its wide bandgap that prevents it from absorbing the majority of the solar spectrum. This is shown by its low photoconversion efficiency (2.2%) under 1W, 1.5 AM global solar irradiation.⁸ Because of this, an emphasis is being placed on improving the visible absorption characteristics of TiO₂ since ~45% of the solar spectrum is composed of visible-wavelength photons. To that end, an extensive amount of research has been performed on improving and gauging the efficiency of TiO₂ in various architectures. Varying platforms have been explored, including TiO₂-quantum dot (QD)

heterostructures,⁹⁻¹¹ and elemental doping by elements such as nitrogen,¹¹⁻¹³ chromium,¹⁴ and other transition metals.¹⁵⁻¹⁷

One recently developed strategy for improving the photoelectrochemical properties of TiO₂ involves the treatment of the TiO₂ with molecular hydrogen at elevated temperatures which renders the TiO₂ a black color.¹⁸⁻²⁰ It has been proposed that the dark coloration of H:TiO₂ is due to the formation of either H or H₂ impurities in the bandgap from the hydrogen treatment.^{21, 22} It is also suggested that the black color is caused by the existence of a lone electron occupying a Ti3*d* state within the bandgap of the TiO₂.¹⁹ Because the hydrogen gas used to treat the sample has a strong reductive ability and generates a high density of electron donors, this Ti3*d* state has been termed an “oxygen vacancy” (V_O).^{19, 23} Electronically, this V_O serves as a potential gateway for optical transitions, which contribute to the strong optical absorption, thereby contributing to the black color of the H:TiO₂.

Because of the hydrogen treatment, the solar-to-hydrogen efficiency was reported by Wang *et al.* as 1.1%, the highest ever reported for a hydrogen-treated TiO₂ photoanode.¹⁹ The improvement was attributed to elevated charge transport due to increased donor density from the V_O. The increased donor density, ascribed to the hydrogen-treatment, thereby increased the conductivity as explained by accompanying Mott-Schottky plots. In all, this finally resulted in a five-fold enhancement of the incident-photon-to-current-conversion efficiency (IPCE) in the UV region.

Despite the promising results that have been obtained by using H:TiO₂ as a photoanode, there is still some dissension with regard to the chemical nature of the black color: whether or not if the photons absorbed can be utilized for PEC water splitting. Because H:TiO₂ samples display consistently improved PEC performance relative to pristine TiO₂, a fundamental understanding of the separation of electron-hole pairs as well as their recombination is of great interest. In other words, while the existence of the V_O has been proven unambiguously,^{18, 19, 23-25} the maximal exploitation of its properties can only be accomplished with the elucidation of its chemical nature, energetic position within the bandgap, and overall charge carrier dynamics. Furthermore, the exposition of the physical construct that contributes to the black coloration, a marked difference from the normally pure white color of untreated TiO₂, is of great import. Gaining an intimate knowledge of this would require a complete description of the physical origin of the optical transitions involved.

In this work, we carried out structural, optical, electronic, and ultrafast transient absorption characterizations of the mid-bandgap states by systematically investigating hydrogen-treated and pristine TiO₂ NWs using transmission electron microscopy (TEM), electron spin resonance (ESR), time resolved fluorescence (TRF), and transient absorption pump-probe spectroscopy (TA). The TEM indicated that the smooth, dense, and untreated NWs gave yield to the presence of a highly roughened surface structure upon hydrogen treatment. ESR analyses indicated the presence of a lone electron localized at a Ti3*d* state, characterized by an axial *g*-tensor

at $g_{\perp} = 1.99$ and $g_{\parallel} = 1.96$, typical of less than half-full d orbital metal ions. Meanwhile, TRF and TA studies were used to probe the dynamics of the charge carrier in the V_O and related states which provide insight into the constitution of the mid-bandgap state and how it gives rise to improved PEC performance. From all of these results in conjunction, we obtained a more complete picture about the electronic states that give rise to the color of and the overall improved PEC response of the H:TiO₂ relative to the untreated TiO₂.

6.3 Experimental

6.3.1 TiO₂ Nanowire Synthesis

The TiO₂ NW arrays were synthesized based on a previously reported hydrothermal method.²⁶ Briefly, 15 mL of deionized water was mixed with 15 mL of concentrated (37%) HCl in a 100 mL beaker with continuous stirring. Subsequently, 0.5 mL of titanium *n*-butoxide was added to the dilute HCl solution. The prepared solution and a piece of fluorine-doped tin oxide (FTO) glass substrate were transferred to a 40 mL Teflon-lined stainless steel autoclave with the FTO being fully submerged in the solution. The sealed autoclave was heated for five hours in an oven set at 150°C and allowed to cool naturally to room temperature. A uniform white film composed of TiO₂ was found coated on the FTO glass. The sample was then washed sequentially with ethanol and water. Finally, the sample was annealed in air at 550°C for three hours in order to increase the crystallinity of the NWs and increase their contact with the FTO substrate.

6.3.2 Hydrogen Treatment of TiO₂ Nanowires

The as-prepared TiO₂ NWs were annealed in a hydrogen-rich atmosphere at a temperature range from 350°C to 550°C for 30 minutes. The hydrogen treatment was performed in a home-built chemical vapor deposition (CVD) system in which the CVD tube was filled with ultrahigh purity hydrogen gas (Praxair).

6.3.3 UV-Vis, Electron Microscopy, and Electron Spin Resonance

Absorption measurements were performed on an HP 8452A diode array spectrophotometer with spectral resolution set to 2 nm. High-resolution transmission electron microscopy (HRTEM) was carried out on a Philips CM300-FEG at the National Center for Electron Microscopy at Lawrence Berkeley National Laboratory with the accelerating voltage set to 300 kV. ESR analysis was conducted at 9.44 GHz using a Bruker X-band EleXsys spectrometer with an SHQ (Bruker) cavity. All samples were loaded into a quartz ESR tube under ambient conditions; no special precautions were taken in their handling. Samples were analyzed at 298 K with power in the range of 0.6-5 mW, modulation amplitude of 1 G, and sweep width of 280 G. An external frequency counter was employed to reference the applied frequency.

6.3.4 Time-resolved Fluorescence

Time-resolved fluorescence experiments were performed on a regeneratively amplified Spectra Physics Spitfire laser system with a repetition rate of 40 kHz. The

400 nm pump beam was generated by frequency doubling the 800 nm fundamental with a barium borate (BBO) crystal. Residual fundamental was removed with a hot-mirror and a Schott Glass BG39 filter. Pump power-dependence study was conducted by setting the per-pulse fluence to 0.4 and 1.3 $\mu\text{J}/\text{cm}^2$. The samples were kept under vacuum in a Janus ST100 cryostat and excited in the front-face geometry. Pump scatter was filtered from the signal using a 400 nm long-wave-pass filter and two Schott Glass OG420 filters. The signal was detected with a Hamamatsu C4334 Streakscope.

6.3.5 Femtosecond Transient Absorption System

The transient absorption (TA) system utilized in this study has been described previously.²⁷ 2.5 mW and 110 fs seed pulses with a repetition rate of 33 MHz were obtained from a frequency-doubled Er-doped fiber oscillator and amplified in a Ti-sapphire regenerative amplifier using chirped-pulse (multipass) amplification. The seed pulse from the oscillator was stretched temporally to ~ 200 ps using a grating stretcher, regeneratively amplified at a repetition rate of 752 Hz by an intracavity-doubled, Q-switched Nd:YLF laser, and recompressed by a grating compressor. The final output pulses that were obtained were typically 150 fs with a pulse energy of 1 mJ and centered at 795 ± 10 nm. The amplified output was beam split such that 90% of the light was directed into an optical parametric amplifier (OPA) while the remaining 10% was passed through a sapphire crystal to generate a white light continuum (WLC) probe pulse with a spectral range from 450 to 750 nm. The pump

pulse repetition rate was halved by an optical chopper which was monitored by a CCD and used to produce a differential absorption spectrum. The delay between the pump and probe pulses was managed by a motor-controlled optical delay stage with a temporal resolution of 10 fs. The pump and probe pulses were focused on a 5 cm focal length curved mirror to overlap spatially and temporally on the surface of the sample. For UV-pumped experiments, a 380 nm pump pulse was selected from two phase-matched bismuth borate (BiBO) crystals in the OPA, while for visible-pumped experiments a 450 nm excitation was chosen. Pump fluences were maintained at ~200 nJ/pulse.

6.4 Results

Figure 1 are representative UV-Vis spectra of the TiO₂ and H:TiO₂ samples. As can be seen, the absorbance maxima are centered at ~330 nm with a persistent tail at red wavelengths. This indicates a strong contribution from scattering.

Figure 1. UV-Vis spectra of TiO₂ and H:TiO₂ NWs annealed at various temperatures

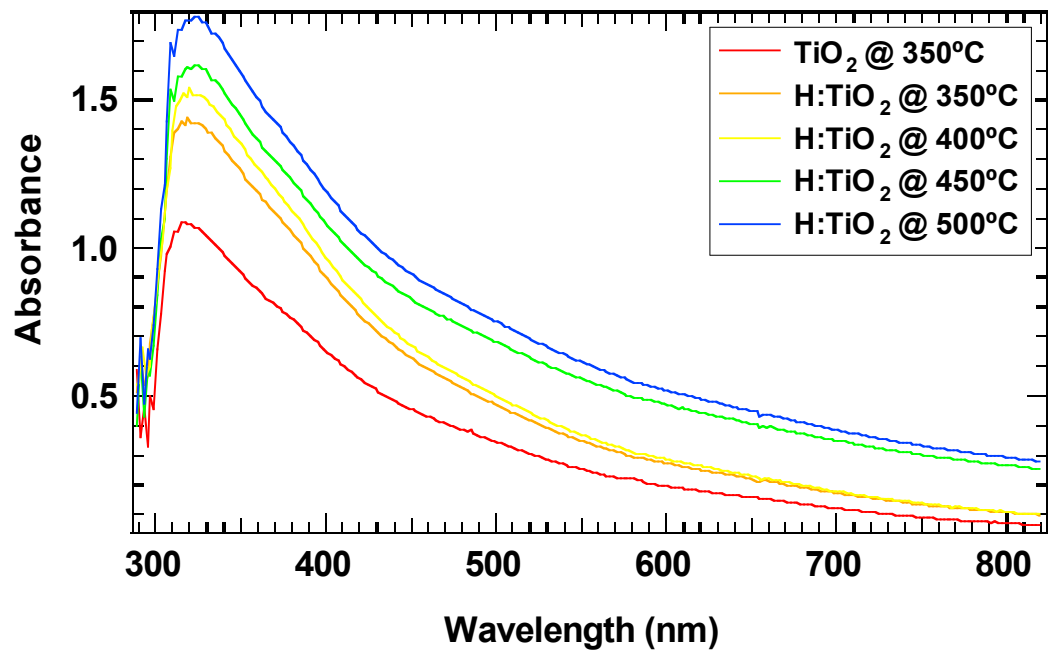
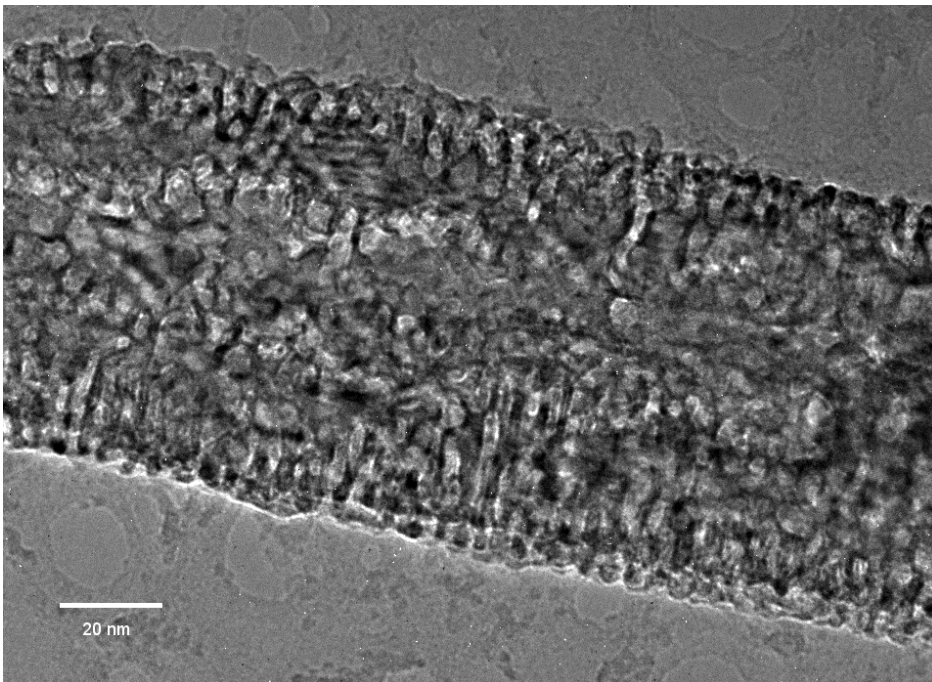
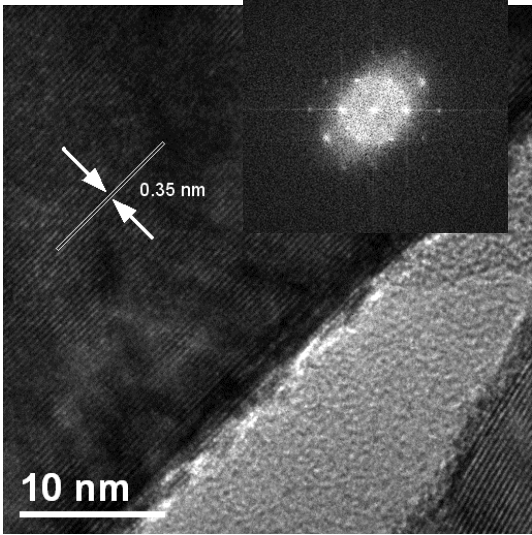


Figure 2 are a series of HRTEM images which show the crystal lattices of the untreated TiO₂ sample. A lattice spacing of 3.5 Å, indicative of the *d*-spacing of the (001) plane of rutile-phase TiO₂, has been highlighted. Also shown in Figure 2a (inset) is the electron diffraction pattern of the samples. Additionally, the H:TiO₂ samples show an increased polycrystallinity when compared to the untreated TiO₂ (Fig. 2b). While the TiO₂ NWs are relatively dense and smooth, the hydrogen treatment rendered the NWs more polycrystalline with grains on the order of ~4-5 × 15 nm in size. The image in Fig. 2b was a sample annealed at 450°C, but is representative of all H:TiO₂ samples in terms of surface roughness. In considering both the change in stoichiometry associated with V_O states as well as the increased polycrystallinity and, particularly, smaller grain sizes, this potentially accounts for the formation of the highly roughened morphology which has been seen before in reduced TiO_{1.9965}.²⁸ The smaller size of the grain boundaries are thus likely tied into the “corn-on-the-cob” patterning. As the annealing temperature of the H:TiO₂ samples increased, the observed density of the point defects likewise increased. These point defects are notably absent in the untreated TiO₂ samples.

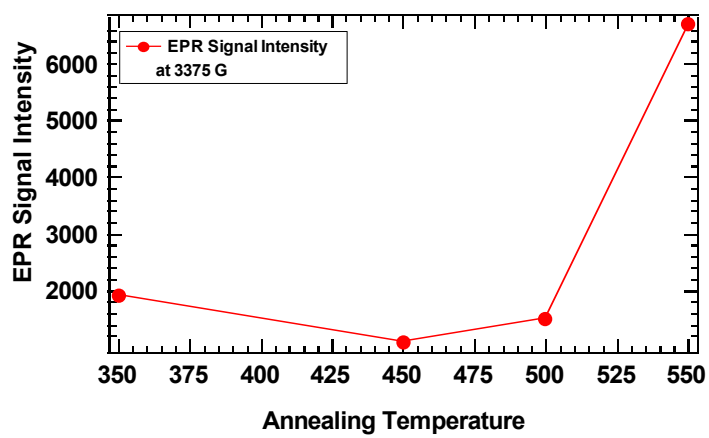
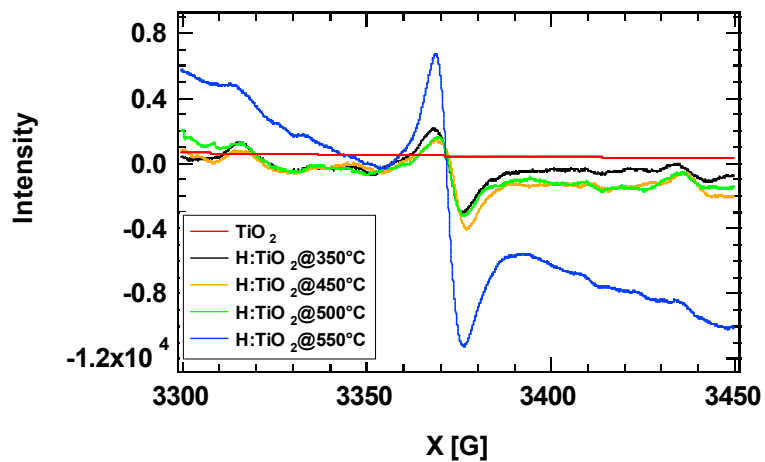
Figure 2. Representative HRTEM images of (a) TiO₂ NWs, showing a dense and smooth architecture, and (b) H:TiO₂ NWs, with the previously dense and smooth architecture converted to a roughened “corn on the cob” morphology with grain sizes of 4 × 15 nm



ESR was performed in order to validate the notion that the V_O was composed of a lone electron in the localized^{21, 29} $Ti3d$ state of the $H:TiO_2$. In Figure 3, we present the ESR spectra of the untreated TiO_2 and $H:TiO_2$. No noticeable signal was obtained for the TiO_2 . This is indicative of the lack of any paramagnetic state within the sample (red curve in Figure 3). Upon hydrogen treatment, however, the signal consists of one strong band consisting of two peaks: a narrow peak centered at 3362 G and a second, slightly asymmetric signal centered at 3369 G, corresponding to axial g -tensors of $g_{\perp} = 1.99$ and $g_{\parallel} = 1.96$. No noticeable hyperfine splitting was seen in the $H:TiO_2$ sample. This is in very good agreement with previous ESR studies on reduced TiO_2 .^{30, 31} One other interesting and potent application of ESR is its potential to detect not only paramagnetic species, but also to provide a measure for the density of the V_O . To that end, we synthesized $H:TiO_2$ powder samples (annealed at varying temperatures) and measured the resulting ESR spectrum in order to investigate the correlation between defect density and annealing temperature. Intriguingly, we found that the intensity of the ESR signal, which is correspondent to defect density, centered at ~ 3370 G was independent of the annealing temperature for the 350, 450, and 500°C samples. For the 350-500°C samples, the intensity of the ESR signal was relatively constant; however, the intensity of the ESR signal increased dramatically, by a factor of $\sim 8\times$ at 550°C. This is represented by the jump from the green curve to the blue curve in Figure 3, which indicates that the relative density of the Ti^{3+} states increased at that treatment temperature. Care was taken to ensure that the exact same amount, by mass, of $H:TiO_2$ sample was used for each of the different annealing

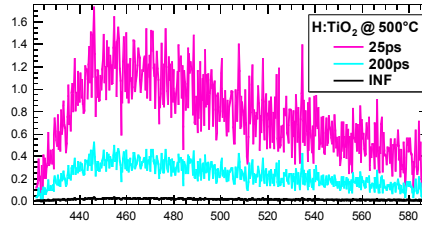
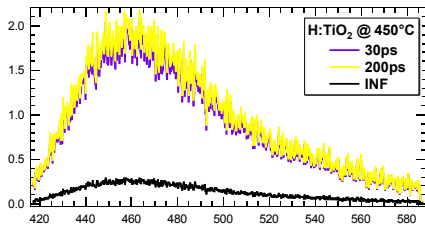
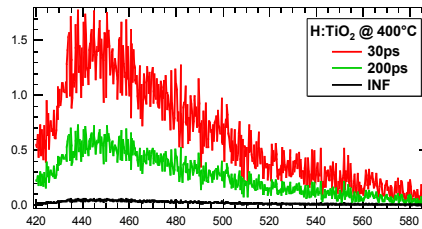
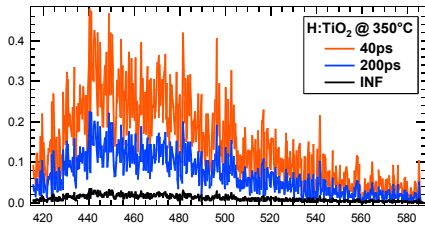
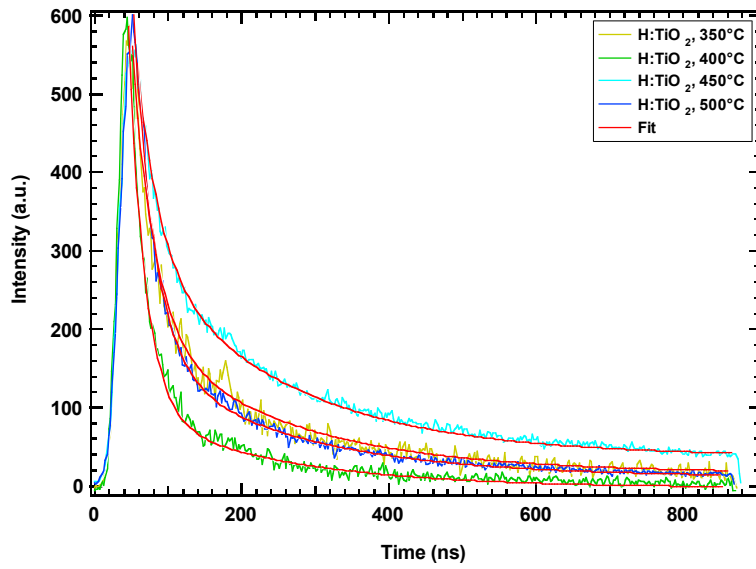
temperatures so that the measured ESR intensity was not affected by differences in sample mass.

Figure 3. ESR of (a) untreated (red curve) and hydrogen-treated TiO₂ NWs. The untreated sample shows no overt signal, while the hydrogen-treated samples have a splitting centered at 3370 G. (b) plot of ESR intensity as a function of treatment temperature, showing that 550C H:TiO₂ NWs have a signal intensity of ~8× higher than the lower temperatures.



Time-resolved fluorescence (TRF) was collected on the TiO₂ and H:TiO₂ NW samples following a 400 nm excitation from a frequency-doubled 800 nm fundamental. Figure 4 represents the time-resolved fluorescence (TRF) of the TiO₂ and H:TiO₂ NWs annealed at various temperatures. A global fitting algorithm was employed to determine a single set of time constants that would fit the kinetic traces across all probe wavelengths for a given sample with a minimal number of exponentials.^{32, 33} For both treated and untreated samples, all decays were fit well with a triple exponential. The TiO₂ sample had a decay that was fit to time constants of 35 ps, 120 ps, and > 1 ns regardless of pump fluence. For the 0.4 μJ/cm² fluence runs, the H:TiO₂ samples displayed a faster decay for the fast component with increasing annealing temperature with lifetimes of 30 ps for the samples. The middle component fit well to a 200 ps lifetime, and the long component had a lifetime of > 1 ns for all samples. For the 1.3 μJ/cm² fluence runs, the fast component lifetime fit well to a triple exponential of 25 ps for the samples. Again, the middle component fit to a 200 ps lifetime and a slow component of > 1 ns for all samples. These rate constants are summarized in Table 1. Additionally, as seen in Figure 4b, the global fitting revealed that the relative intensity of the fast component of the decays increased from 68-77% as the annealing temperature increased from 350-550°C. Despite that, the integrated intensity of the fast component remained at 30% for all treatment temperatures.

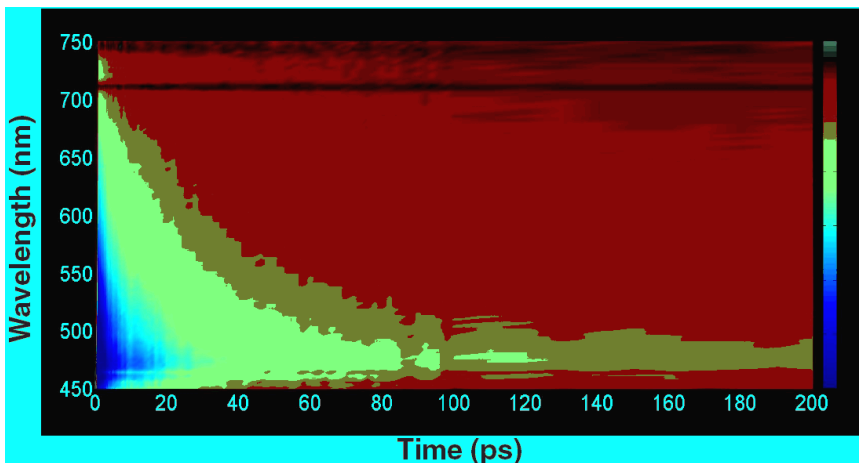
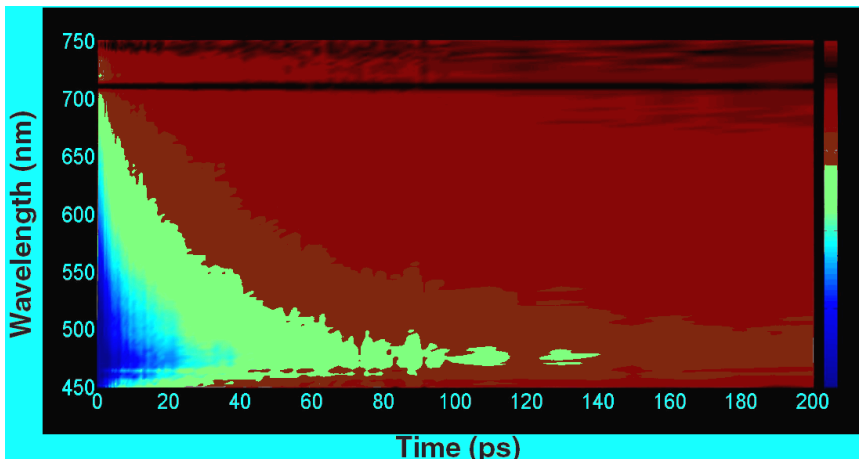
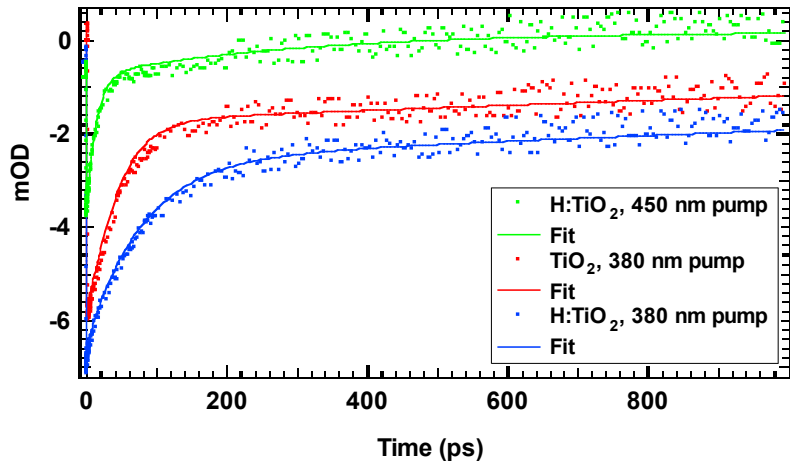
Figure 4. (a) Intensity vs. time (ps) of TiO₂ and H:TiO₂ NWs along with fitting curves and (b) Global fitting results of the PL lifetime of H:TiO₂, annealed at 350, 400, 450, and 500°C, showing the contribution from each lifetime component to the overall integrated spectrum at each wavelength. The H:TiO₂ samples required triple exponential functions to fit their decays.



Ultrafast TA data were collected of the TiO₂ and H:TiO₂ NWs at UV pump (380 nm, 475 nm probe) and visible pump (450 nm, 505 nm probe) wavelengths and is shown in Figure 5. It should be noted that great care was taken to ensure consistency and reproducibility in each of the datasets from the samples. For the untreated TiO₂ sample, visible wavelength excitation produced no noticeable signal; thus data could not be collected on that sample at that pump wavelength. However, for the UV pump, the TiO₂ exhibited a fast initial decay followed by a medium decay and a long-lived slow decay manifesting as a persistent y-offset. The data were fit to a triple exponential with time constants of 30 ps, 100 ps, and > 1 ns. The UV-pumped H:TiO₂ displayed a slower medium decay than the UV-pumped TiO₂; yet, as with the untreated TiO₂ NW sample, the H:TiO₂ also retained the persistent offset. This is indicative of long-lived electron-hole pairs. All of the data of the UV-pumped H:TiO₂ samples were fit well to a triple exponential with time constants of 60, 200 ps and > 1 ns. For the 450 nm-pumped H:TiO₂, a fast initial decay was noticed, followed by a nearly complete relaxation to baseline, indicative of very efficient electron-hole recombination. Those data, essentially independent of annealing temperature, were fit to a double exponential with time constants of 30 ps and ~125 ps. For all of the samples studied, no power dependence was observed. These rate constants are summarized in Table 1. Figures 5b and 5c are three-dimensional false-colored plots of the H:TiO₂ and TiO₂ TA data with UV excitation which indicates the spectral location of the maximum transient bleach feature. Noticeably, the transient bleach is seen to extend for a longer time period for H:TiO₂ (Fig. 5b) than for pristine

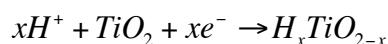
TiO₂ (Fig. 5c). Additionally, it is apparent from Figures 5b and 5c that there is no overt spectral evolution of TA signals over time, and the maximum bleach feature for both is consistently situated at probe wavelengths of 475 nm.

Figure 5. (a) Transient bleach relaxation traces of TiO_2 and $\text{H}:\text{TiO}_2$ NWs following 450 nm excitation (red curve) and 380 nm excitation (blue and green curves). No noticeable differences in the bleach relaxation traces were evident based upon annealing temperature. (b, c) 3D plot of $\text{H}:\text{TiO}_2$ and TiO_2 NWs, respectively, with optical density plotted as a function of wavelength (nm) and time (ps).



6.5 Discussion

Fully oxidized and defect-free TiO₂ is composed of O anions and Ti cations in the native 4+ state with a five-fold coordination to oxygen atoms.²³ It is known that heating the sample at elevated temperatures in excess of 350°C results in desorption of surface-adsorbed oxygen atoms, which results in oxygen vacancies, or V_O.^{19, 34, 35} In terms of structure, an absent oxygen atom at a bridging oxygen site renders two subsurface Ti³⁺ ions exposed. As has been established previously,^{18, 19} the inclusion of Ti³⁺-based disorder into the lattice of pristine, rutile-phase TiO₂ during the high-temperature treatment with atomic hydrogen has the effect of reducing Ti⁴⁺ to Ti³⁺ through the occupation of vacant Ti3*d* orbitals of TiO₂ that are otherwise empty. The generation of Ti³⁺ states is therefore believed to follow a stoichiometric equation of:



These isolated and localized states are known to exist ~0.75 eV below the CB of TiO₂ that is composed of 3*d* Ti³⁺.^{21, 29, 36}

Structurally, it is the TiO₂ (110) plane that has been thought to have defect stoichiometry leading to a photocatalytically active Ti³⁺ state.^{23, 37, 38} There also exists a number of defects in the lattice. The formation process of the defects likely follows that of a traditional interstitial defect, *i.e.*, generation of additional Ti³⁺ cations as point defects. Because point defects are energetically unfavored by the crystal, they become reordered into fault lines, concentrating at or around grain boundaries.³⁹ This follows the notion that the defects are effectively a displacement vector associated with a stacking fault which can alter the chemical composition or

stoichiometry along the fault line.^{40, 41} The extension of the fault lines from the surface into the core of the NWs appear to take on a similar grain structure of surface grain features present in the native TiO₂ NWs. The resulting structures appear as corn-on-the-cob features along the long axis of the NWs. Because of this, we believe the line defects, which manifest in the H:TiO₂ NW samples but are notably absent from the TiO₂ NW sample, are composed primarily of conducting Ti³⁺ ions or V_O states. One other interesting feature of the H:TiO₂ NWs, relative to the TiO₂ NWs, is that the high-temperature annealing yields a previously unseen roughness in the nanowires. Prior to annealing, the nanowires were largely smooth and dense. The high-temperature annealing afforded an abrupt change to a much more polycrystalline form. The result was that the crystallite size decreased to $\sim 4\text{-}5 \times 15$ nm in size. This has been seen before in other inorganic systems, notably hematite,⁴² phosphorus-doped silicon,⁴³ and metallic alloys.⁴⁴

Fully oxidized TiO₂, which should contain no unpaired electrons indicative of the V_O, displayed no ESR signal. However, upon treatment with the hydrogen and subsequent generation of the V_O state, a strong signal was noticeable. The spectral position of the signal is in accordance with previously reported ESR signatures from Ti³⁺.^{30, 31} However, upon temperature increase to 550°C, the ESR intensity increased by a factor of $\sim 8\times$. Although obtaining an exact stoichiometric formula for the H:TiO₂ NWs was not possible, these data indicate – qualitatively – an overall increased density of V_O states for the 550°C sample relative to lower temperatures. Nevertheless, the ESR results may suggest one possible mechanism of interaction

between H_2 and TiO_2 during the hydrogen treatment. At temperatures above $350^\circ C$, electrons are transferred from H atoms to O atoms in the lattice of TiO_2 . The formation of the V_O is suggestive that an O atom chemically binds to an H atom in the form of a surface-bound hydroxyl. Electronically, the interaction between the H_2 and TiO_2 , in which electrons are transferred to Ti^{4+} thereby forming Ti^{3+} , proceeds drastically. According to the ESR data shown in Figure 3a, the process appears to be significant at temperatures above $550^\circ C$ where the ESR signal intensity is seen to jump dramatically relative to that at $500^\circ C$. This suggests that the thermodynamically-driven mechanism of the formation of V_O sites is substantially increased at $550^\circ C$. In terms of the generation of V_O , it would appear that the optimal temperature for the hydrogen treatment falls at temperatures of at least $550^\circ C$. This notion that temperatures of $550^\circ C$ results in a higher density of V_O states, relative to lower temperatures, is supported by literature,^{25, 45} wherein the ESR signal due to V_O sites was seen to peak at the $550^\circ C$ temperature range.

Traditionally, the PL from rutile is considered to be weak, and is likely mediated by a high density of defect states.^{46, 47} Interestingly, the weak PL was reduced further upon hydrogen treatment. This suggests that hydrogen treatment fundamentally alters the quantity and energetic position or depth of trap states within the bandgap since a higher density of states within the bandgap can have the effect of not only quenching PL but also rendering the PL lifetime shorter. The latter is evidenced in the increasingly fast PL lifetime for TiO_2 vs. $H:TiO_2$ NWs in which the fast component lifetime decreased from 35 ps for the TiO_2 NWs to ~ 30 ps for the

H:TiO₂ for low pump power and 25 ps for the higher pump power. Interestingly, there is little dependence on lifetime with increasing temperature for the H:TiO₂ NW samples. This may be due, in part, to the notion that the noise in the TRF data renders any differences to be meaningless. That is, no overt trend, *e.g.*, decrease in PL lifetimes of the fast, medium, or slow components, was noticeable when the annealing temperature was increased. This indicates that the effect of hydrogen treatment itself has a greater effect on the introduction of PL-quenching mid-bandgap states than the annealing temperature does. A decrease in the fast component of the PL decay for the H:TiO₂ vs. the TiO₂ NWs suggests that the initial decay is quickened from the presence of a manifold of PL-quenching defect sites which can also speed up recombination. This is in-line with the HRTEM results indicating an increase in defect density in the crystalline lattice of the samples upon hydrogen treatment. However, the fact that the medium component becomes slower progressing from TiO₂ (120 ps) to H:TiO₂ (200 ps) indicates that the PL decay process is retarded due to some long-lived trap state. As mentioned earlier, the relative intensity of the fast component was seen to rise from 68% to 77% as the annealing temperature rose from 350°C to 550°C despite the fact that the integrated intensity of the fast component remained at 30% for all treatment temperatures. These results are attributable to the increased surface disorder contributing to nonradiative decay pathways upon hydrogen-treatment of the pristine TiO₂.

The lack of a fast component in the H:TiO₂ sample with UV excitation as compared to the untreated sample indicates that there is a fluorescent trap state near

the bottom of the CB in the TiO₂ which is absent from the bandgap of the H:TiO₂ material. Based on the PL peak position (~460 nm, or 2.7 eV), the fluorescent trap state is estimated to be ~0.3 eV below the CB since the bandgap of rutile is known to be 3.0 eV. With the electron relaxing to the bottom of the CB upon photoexcitation, the initial decay into the fluorescent trap should be quick, which it is with a 30 ps initial relaxation time. However, upon hydrogen-treatment the UV-pump relaxation is significantly slowed to ~160 ps, indicating that there is no fast relaxation into the fluorescent trap state. This potentially indicates that the fluorescent trap state was removed in the hydrogen-treatment process. Conversely, it is possible that the hydrogen treatment afforded more surface trap states which leads to a greater amount of non-radiative recombination. Effectively then, the first relaxation into the bandgap would be from the CB to the V_O, which lies ~0.75 eV below the CB.¹⁹ Relative to the ~0.3 eV relaxation process as for the TiO₂, this longer 0.75 eV relaxation would most certainly be a slower transition, which is indeed the case given that the H:TiO₂ has a fast component of 60 ps, which is twice that of the pristine TiO₂ of 30 ps.. In other words, while the initial relaxation for the TiO₂ is represented by the CB-to-fluorescent state transition of ~0.3 eV (corresponding to a 30 ps initial relaxation), the initial relaxation for the H:TiO₂ is represented by the CB-to-V_O transition of ~0.75 eV (corresponding to a 60 ps initial relaxation). Additionally, the V_O state is believed to be highly localized.^{21, 29} Because of its localization, relaxation/recombination of the exciton is likely to become slower for that particular transition. Because the localization, which results in slower recombination times, arises from hydrogen

treatment, the recombination of the exciton for H:TiO₂ should be slower at that pump wavelength; which it is. There are other states in the bandgap which have been recently identified which may also contribute to the decay timescales. For example, interstitial hydrogen, introduced during the hydrogen treatment, is shown to locate in positions close to surface oxide ions.⁴⁸⁻⁵⁰ These hydrogen-oxygen species, which take the form of –OH functionalities, are known to have to primary energetic locations: 0.6 eV below the CB and 0.82 eV below the CB.⁵¹ As with the V_O, these bands are also greatly localized⁴⁹ which will aid in the slower recombination time subsequent to UV pumping.

For visibly-pumped H:TiO₂, there is once again a fast initial decay (~30 ps). This is because the visible pump will excite energetically only to the V_O. The concept that pumping occurs from the V_O to within the CB is possible; however, the subsequent intraband recombination which would take place would likely have a temporal signature that is much faster than what is being seen in our data. Further, there is likely a dense manifold of states under the V_O, formed during the annealing process which not only act to quench the PL, as seen in the TRF, but also to provide fast and efficient exciton recombination. This is represented graphically in Figure 7. The complete return to baseline for the kinetic trace of the visibly-pumped H:TiO₂ provides some evidence that the exciton recombination is efficient; in effect, there are no long-lived trap states which impede the recombination.

In relating the ultrafast studies with the structural data of the H:TiO₂ presented in the HRTEM, we conclude that while electrons and holes are generated in the initial

UV photoillumination, the surface defects, *e.g.*, the highly polycrystalline grains of the surface of the NWs, can suppress the electron-hole recombination and thus extend their lifetime. This is because the surface defects act as localized electron traps² while surface hydroxyl groups are known to act as hole traps.⁵² Ultimately, these traps for the electron and hole combine to compete with recombination and leads to a product whose charge carrier recombination rate is slow.⁵² This is reflected in all three components of the lifetime of the H:TiO₂ in comparison with the untreated TiO₂. With regard to the visible-pumped H:TiO₂, the fast decay indicates quick recombination of charge carriers from the V_O state. This is likely due to a high density of trap states between V_O and the VB of TiO₂. The origin of the visible signal in the H:TiO₂ becomes a fascinating point of discussion and is tied closely between the ultrafast studies (Fig. 6) and the PEC data from Wang *et al.*¹⁹ It was previously reported that oxygen vacancies play a critical role in determining both the surface and electronic properties of H:TiO₂.^{21, 53, 54} Previously reported¹⁹ XPS data showed that the H:TiO₂ nanowires do not contain dopants from other elements. The defect states are therefore attributed to the generation of V_Os and surface hydroxyl (-OH) groups on TiO₂. It should be noted here that the ESR measurements were unfortunately unable to detect unambiguously the presence of any hydroxyl groups, despite the fact that such a determination has been made prior.⁵⁵ The presence of these Ti-OH energy states below the VB of TiO₂ should not lead to visible light absorption since previous XPS data¹⁹ showed that the energy levels for the Ti-OH-Ti and Ti-OH species were reported to be positioned 2.6 and 0.7 eV below the VB.

Additionally, it was reported that these states are energetically stable and are not oxidized by the valence band holes *via* electron transfer.^{56, 57} Because of this, the visible absorption characteristics of the H:TiO₂ NW samples has to arise from optical transitions associated with the V_O states. The oxygen vacancy energy level has been determined to be ~0.75 eV below the (CB) of hydrogen-reduced rutile.^{19, 20}

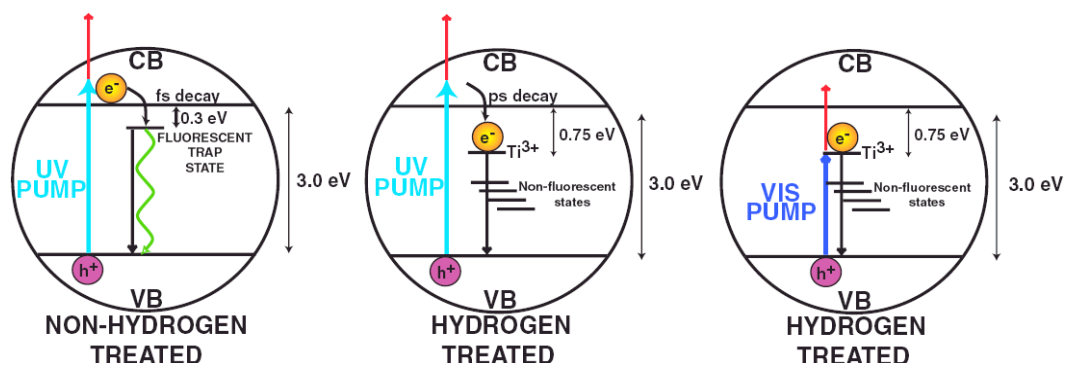
To gain further insight into the energy relaxation mechanism of the H:TiO₂, we utilized a four-state kinetic scheme to model the observed dynamics, as shown in Figure 5 and explained in more detail in the Supplemental Information. The proposed scheme includes the valence band (VB), conduction band (CB), fluorescent state (FTS), and V_O. After combining the contributions of each of the states at varying percentages with a set of rate constants, we were able to closely model our experimental data. The rate constants were chosen based on the experimental results in this study as well as other experiments²⁰. In modeling the data for the H:TiO₂, the VB needs to be explicitly included since it is probed by the probe pulse and is reflected as a transient bleach signal. By combining 30% contribution from the VB, 30% from the CB, and 20% from both the FTS and V_O, a curve could be generated which modeled closely our observed data.

In terms of the mechanism of the modeled decay, and from the final rate constants determined by comparing the modeled data with the experimental data, we are able to unambiguously assign rate constants to the key physical processes shown in Figure 5. In particular, the time constant from the CB to the FTS was modeled to be 0.5 ps, while the decay from the FTS to the V_O is 4 ps and the V_O to VB was 500

ps. Although the time constants may not be unique due to several assumptions made in the modeling scheme, we believe they are indicative of key physical processes that are occurring during the transient absorption decay profile.

In providing a preliminary model to the system, we suggest that the high-temperature annealing of the H:TiO₂ has the net effect of increasing crystallite grain sizes as shown in the HRTEM images and increasing the surface disorder of the NWs. Figure 6 presents a model to illustrate the relevant energy levels including the bandgap states of TiO₂ and H:TiO₂ and associated charge carrier relaxation process following UV or visible excitation. In doing so, an increasing number of defects are introduced into the system, thereby serving to quench the PL – both in intensity as well as PL lifetime. Additionally, the treatment of the TiO₂ with molecular hydrogen has the ability to donate electrons, thereby reducing some Ti⁴⁺ ions into Ti³⁺ ions and creating a V_O, the energetic location of which is within the bandgap, approximately 0.75 eV below the CB. Upon probing the state with UV-pumped transient absorption, an electron-hole pair is photogenerated, the electron of which relaxes down 0.75 eV into the V_O. Compared to untreated TiO₂, the relaxation is relatively slow since the TiO₂ has a fluorescent state located ~0.3 eV below the CB, making the initial electronic relaxation into that state relatively fast. In order to probe the V_O directly, visible-wavelength pumping photoexcites an electron to the V_O. Again, due to the high-temperature treatment and thereby the generation of a dense manifold of PL-quenching states below the V_O, the recombination of the visibly-pumped electron and hole is fast and efficient. This is shown schematically in Figure 6.

Figure 6. Proposed model for energy levels related to the optical properties and dynamics studies. CB and VB represent the conduction band and valence band, respectively. For H:TiO₂ NWs, visible pumping excites an electron to the V_O state which is followed by non-radiative exciton decay mediated by a manifold of trap states. UV pumping for the same sample excites an electron across the bandgap which is followed by relaxation to the V_O state and subsequent relaxation through the manifold of trap states. For TiO₂ NWs, UV pumping (visible pumping not possible) likewise excited an electron across the bandgap which was followed by relaxation into a fluorescent trap state situated ~0.3 eV below the CB. Subsequent recombination was fast due to trap states oriented throughout the bandgap.



6.6 Conclusion

We have carried out a systematic study in order to gain fundamental insight into the chemical nature of the bandgap states in hydrogen treated TiO₂ NWs that results in visible light absorption. Pristine, rutile-phase TiO₂ strongly absorbs UV light due to its bandgap of 3.0 eV. Hydrogen-treatment, however, introduces mid-bandgap states, attributed to oxygen vacancies or V_O, as well as non-fluorescent trap states situated below the localized V_O state. This V_O state is partly responsible for the visible absorption of the hydrogen-treated TiO₂. Moreover, the manifold of states below the V_O leads to fast recombination of charge carriers following visible excitation. ESR data indicate that a lone, unpaired electron occupies an electronic state situated within the bandgap of the rutile H:TiO₂ NW. Ultrafast TA measurements suggest the charge carrier relaxation to the V_O state with above-bandgap excitation using UV light is relatively slower, 160 ps, as compared to untreated TiO₂ NWs. Upon excitation with visible light, however, the recombination of the electron-hole pair is very fast, 30 ps, due to the manifold of trap states that lie below the V_O. The new bandgap states introduced from hydrogen treatment led to PL quenching due to increased non-radiative decay. These results have afforded a deeper insight into the chemical nature and related properties of bandgap states in hydrogen-treated TiO₂ nanowires.

6.7 References

1. Fujishima, A.; Honda, K., Electrochemical Photolysis of Water at a Semiconductor Electrode. *Nature* 1972, 238, (5358), 37-38.
2. Linsebigler, A. L.; Lu, G.; Yates, J. T., Photocatalysis on TiO₂ Surfaces: Principles, Mechanisms, and Selected Results. *Chemical Reviews* 1995, 95, (3), 735-758.
3. Bak, T.; Nowotny, J.; Rekas, M.; Sorrell, C., Photo-electrochemical hydrogen generation from water using solar energy. Materials-related aspects. *International Journal of Hydrogen Energy* 2002, 27, (10), 991-1022.
4. Fujishima, A.; Zhang, X.; Tryk, D. A., TiO₂ photocatalysis and related surface phenomena. *Surface Science Reports* 2008, 63, (12), 515-582.
5. Lin, Y.; Zhou, S.; Liu, X.; Sheehan, S.; Wang, D., TiO₂/TiSi₂ Heterostructures for High-Efficiency Photoelectrochemical H₂O Splitting. *Journal of the American Chemical Society* 2009, 131, (8), 2772-2773.
6. Leary, R.; Westwood, A., Carbonaceous nanomaterials for the enhancement of TiO₂ photocatalysis. *Carbon* 2011, 49, (3), 741-772.
7. Liu, M.; de Leon Snapp, N.; Park, H., Water photolysis with a cross-linked titanium dioxide nanowire anode. *Chemical Science* 2011, 2, (1), 80-87.
8. Murphy, A. B.; Barnes, P. R. F.; Randeniya, L. K.; Plumb, I. C.; Grey, I. E.; Horne, M. D.; Glasscock, J. A., Efficiency of solar water splitting using semiconductor electrodes. *International Journal of Hydrogen Energy* 2006, 31, (14), 1999-2017.

9. Fitzmorris, B. C.; Larsen, G. K.; Wheeler, D. A.; Zhao, Y.; Zhang, J. Z., Ultrafast Charge Transfer Dynamics in Polycrystalline CdSe/TiO₂ Nanorods Prepared by Oblique Angle Codeposition. *The Journal of Physical Chemistry C* 2012, 116, (8), 5033-5041.
10. Baker, D. R.; Kamat, P. V., Photosensitization of TiO₂ nanostructures with CdS quantum dots: particulate versus tubular support architectures. *Advanced Functional Materials* 2009, 19, (5), 805-811.
11. Hensel, J.; Wang, G.; Li, Y.; Zhang, J. Z., Synergistic effect of CdSe quantum dot sensitization and nitrogen doping of TiO₂ nanostructures for photoelectrochemical solar hydrogen generation. *Nano Letters* 2010, 10, (2), 478-483.
12. Asahi, R.; Morikawa, T.; Ohwaki, T.; Aoki, K.; Taga, Y., Visible-light photocatalysis in nitrogen-doped titanium oxides. *Science* 2001, 293, (5528), 269-271.
13. Liu, G.; Yang, H. G.; Wang, X.; Cheng, L.; Pan, J.; Lu, G. Q.; Cheng, H. M., Visible light responsive nitrogen doped anatase TiO₂ sheets with dominant {001} facets derived from TiN. *Journal of the American Chemical Society* 2009, 131, (36), 12868-12869.
14. Li, Y.; Wang, W.; Qiu, X.; Song, L.; Meyer III, H. M.; Paranthaman, M. P.; Eres, G.; Zhang, Z.; Gu, B., Comparing Cr, and N only doping with (Cr, N)-codoping for enhancing visible light reactivity of TiO₂. *Applied Catalysis B: Environmental* 2011.

15. Doan, N. M.; Estrellan, C. R.; Purnomo, A.; Gallardo, S.; Salim, C.; Hinode, H., Characterization and Photocatalytic Activity of Nano-TiO₂ Doped with Iron and Niobium for Turquoise Blue Dye Removal. *ASEAN Journal of Chemical Engineering* 2012, 1, 34-41.
16. Zhang, L. K.; Wu, B.; Wang, M.; Chen, L.; Ye, G. X.; Chen, T.; Liu, H. L.; Huang, C. R.; Li, J. L., Crystal, Electronic and Magnetic Structure of Co and Ag Doped Rutile TiO₂ from First-Principles Calculations. *Advanced Materials Research* 2012, 399, 1789-1792.
17. Zhong, X. C.; Pan, Z. C.; Wei, Z. G.; Xie, S. G.; Cheng, Z. J.; Xiao, C. M., Experimental and Theoretical Study on Transition Metal Ion Doped TiO₂. *Advanced Materials Research* 2011, 233, 2219-2222.
18. Chen, X.; Liu, L.; Yu, P. Y.; Mao, S. S., Increasing Solar Absorption for Photocatalysis with Black Hydrogenated Titanium Dioxide Nanocrystals. *Science* 2011, 331, (6018), 746-750.
19. Wang, G.; Wang, H.; Ling, Y.; Tang, Y.; Yang, X.; Fitzmorris, R. C.; Wang, C.; Zhang, J. Z.; Li, Y., Hydrogen-Treated TiO₂ Nanowire Arrays for Photoelectrochemical Water Splitting. *Nano Letters* 2011, 11, (7), 3026-3033.
20. Wheeler, D. A.; Wang, G.; Fitzmorris, B. C.; Adams, S. A.; Li, Y.; Zhang, J. Z., Ultrafast Charge Carrier Dynamics and Photoelectrochemical Properties of Hydrogen-treated TiO₂ Nanowire Arrays. *MRS Proc.* 2012, 1387, e04-e07.
21. Cronmeyer, D. C., Infrared Absorption of Reduced Rutile TiO₂ Single Crystals. *Physical Review* 1959, 113, (5), 1222-1226.

22. Fabregat-Santiago, F.; Barea, E. M.; Bisquert, J.; Mor, G. K.; Shankar, K.; Grimes, C. A., High Carrier Density and Capacitance in TiO₂ Nanotube Arrays Induced by Electrochemical Doping. *Journal of the American Chemical Society* 2008, 130, (34), 11312-11316.
23. Lu, G.; Linsebigler, A.; Yates Jr, J. T., Ti³⁺ defect sites on TiO₂ (110): Production and chemical detection of active sites. *The Journal of Physical Chemistry* 1994, 98, (45), 11733-11738.
24. Wang, H.; Wang, G.; Ling, Y.; Lepert, M.; Wang, C.; Zhang, J. Z.; Li, Y., Photoelectrochemical study of oxygen deficient TiO₂ nanowire arrays with CdS quantum dot sensitization. *Nanoscale* 2012, 4, (5), 1463-1466.
25. Liu, H.; Ma, H.; Li, X.; Li, W.; Wu, M.; Bao, X., The enhancement of TiO₂ photocatalytic activity by hydrogen thermal treatment. *Chemosphere* 2003, 50, (1), 39-46.
26. Liu, B.; Aydil, E. S., Growth of Oriented Single-Crystalline Rutile TiO₂ Nanorods on Transparent Conducting Substrates for Dye-Sensitized Solar Cells. *Journal of the American Chemical Society* 2009, 131, (11), 3985-3990.
27. Newhouse, R. J.; Wang, H.; Hensel, J. K.; Wheeler, D. A.; Zou, S.; Zhang, J. Z., Coherent Vibrational Oscillations of Hollow Gold Nanospheres. *The Journal of Physical Chemistry Letters* 2011, 2, (3), 228.
28. Bursill, L.; Blanchin, M., Structure of cation interstitial defects in nonstoichiometric rutile. *Journal de Physique Lettres* 1983, 44, (4), 165-170.

29. Zuo, F.; Wang, L.; Wu, T.; Zhang, Z.; Borchardt, D.; Feng, P., Self-Doped Ti³⁺ Enhanced Photocatalyst for Hydrogen Production under Visible Light. *Journal of the American Chemical Society* 2010, 132, (34), 11856-11857.
30. Howe, R. F.; Gratzel, M., EPR observation of trapped electrons in colloidal titanium dioxide. *The Journal of Physical Chemistry* 1985, 89, (21), 4495-4499.
31. Ookubo, A.; Kanezaki, E.; Ooi, K., ESR, XRD, and DRS studies of paramagnetic titanium(3+) ions in a colloidal solid of titanium oxide prepared by the hydrolysis of titanium trichloride. *Langmuir* 1990, 6, (1), 206-209.
32. Gul, S.; Cooper, J. K.; Corrado, C.; Vollbrecht, B.; Bridges, F.; Guo, J.; Zhang, J. Z., Synthesis, Optical and Structural Properties, and Charge Carrier Dynamics of Cu-Doped ZnSe Nanocrystals. *The Journal of Physical Chemistry C* 2011.
33. Hug, S. J.; Lewis, J. W.; Einterz, C. M.; Thorgeirsson, T. E.; Kliger, D. S., Nanosecond photolysis of rhodopsin: evidence for a new blue-shifted intermediate. *Biochemistry* 1990, 29, (6), 1475-1485.
34. Bowker, M.; Bennett, R. A., The role of Ti³⁺ interstitials in TiO₂ (110) reduction and oxidation. *Journal of Physics: Condensed Matter* 2009, 21, (47), 474224.
35. Diebold, U.; Lehman, J.; Mahmoud, T.; Kuhn, M.; Leonardelli, G.; Hebenstreit, W.; Schmid, M.; Varga, P., Intrinsic defects on a TiO₂(110)(1 × 1) surface and their reaction with oxygen: a scanning tunneling microscopy study. *Surface Science* 1998, 411, (1), 137-153.

36. Lisachenko, A.; Kuznetsov, V.; Zakharov, M.; Mikhailov, R., The interaction of O₂, NO, and N₂O with surface defects of dispersed titanium dioxide. *Kinetics and catalysis* 2004, 45, (2), 189-197.
37. Shklover, V.; Nazeeruddin, M. K.; Zakeeruddin, S. M.; Barbé, C.; Kay, A.; Haibach, T.; Steurer, W.; Hermann, R.; Nissen, H. U.; Grätzel, M., Structure of Nanocrystalline TiO₂ Powders and Precursor to Their Highly Efficient Photosensitizer. *Chemistry of Materials* 1997, 9, (2), 430-439.
38. Kumar, P. M.; Badrinarayanan, S.; Sastry, M., Nanocrystalline TiO₂ studied by optical, FTIR and X-ray photoelectron spectroscopy: correlation to presence of surface states. *Thin Solid Films* 2000, 358, (1–2), 122-130.
39. Uberuaga, B. P.; Bai, X. M., Defects in rutile and anatase polymorphs of TiO₂: kinetics and thermodynamics near grain boundaries. *Journal of Physics: Condensed Matter* 2011, 23, (43), 435004.
40. Buseck, P.; Cowley, J. M.; Eyring, L. R., *High-resolution transmission electron microscopy and associated techniques*. Oxford University Press, USA: 1988.
41. Putnis, A., *Introduction to mineral sciences*. Cambridge Univ Pr: 1992.
42. Wang, G.; Gou, X.; Horvat, J.; Park, J., Facile Synthesis and Characterization of Iron Oxide Semiconductor Nanowires for Gas Sensing Application. *The Journal of Physical Chemistry C* 2008, 112, (39), 15220-15225.
43. Learn, A. J.; Foster, D. W., Deposition and electrical properties of in situ phosphorus-doped silicon films formed by low-pressure chemical vapor deposition. *Journal of Applied Physics* 1987, 61, (5), 1898-1904.

44. Harandi, S. E.; Idris, M. H.; Jafari, H., Effect of forging process on microstructure, mechanical and corrosion properties of biodegradable Mg-1Ca alloy. *Materials & Design* 2011.
45. Okamoto, K.; Yamamoto, Y.; Tanaka, H.; Tanaka, M.; Itaya, A., Heterogeneous photocatalytic decomposition of phenol over TiO₂ powder. *Bulletin of the Chemical Society of Japan* 1985, 58, (7), 2015-2022.
46. Ghosh, A. K.; Wakim, F.; Addiss Jr, R., Photoelectronic processes in rutile. *Physical Review* 1969, 184, (3), 979.
47. Hachiya, K.; Kondoh, J., Photoluminescence from localized states in rutile by Ar⁺-ion laser excitation. *Physica B: Condensed Matter* 2003, 334, (1-2), 130-134.
48. Bjorheim, T. S.; Stolen, S.; Norby, T., Ab initio studies of hydrogen and acceptor defects in rutile TiO₂. *Physical Chemistry Chemical Physics* 2010, 12, (25), 6817-6825.
49. Bjørheim, T. S.; Kuwabara, A.; Norby, T., Defect Chemistry of Rutile TiO₂ from First Principles Calculations. *The Journal of Physical Chemistry C* 2013.
50. Koudriachova, M. V.; de Leeuw, S. W.; Harrison, N. M., First-principles study of H intercalation in rutile TiO₂. *Physical Review B* 2004, 70, (16), 165421.
51. Deák, P.; Aradi, B.; Frauenheim, T., Polaronic effects in TiO₂ calculated by the HSE06 hybrid functional: Dopant passivation by carrier self-trapping. *Physical Review B* 2011, 83, (15), 155207.

52. Rothenberger, G.; Moser, J.; Graetzel, M.; Serpone, N.; Sharma, D. K., Charge carrier trapping and recombination dynamics in small semiconductor particles. *Journal of the American Chemical Society* 1985, 107, (26), 8054-8059.
53. Cronemeyer, D. C.; Gilleo, M. A., The Optical Absorption and Photoconductivity of Rutile. *Physical Review* 1951, 82, (6), 975-976.
54. Kim, W.-T.; Kim, C.-D.; Choi, Q. W., Sub-band-gap photoresponse of TiO_{2-x} thin-film—electrolyte interface. *Physical Review B* 1984, 30, (7), 3625-3628.
55. Harris, L.; Schumacher, R., The influence of preparation on semiconducting rutile (TiO₂). *Journal of The Electrochemical Society* 1980, 127, (5), 1186-1188.
56. Imanishi, A.; Okamura, T.; Ohashi, N.; Nakamura, R.; Nakato, Y., Mechanism of Water Photooxidation Reaction at Atomically Flat TiO₂ (Rutile) (110) and (100) Surfaces: □ Dependence on Solution pH. *Journal of the American Chemical Society* 2007, 129, (37), 11569-11578.
57. Nakamura, R.; Nakato, Y., Primary Intermediates of Oxygen Photoevolution Reaction on TiO₂ (Rutile) Particles, Revealed by in Situ FTIR Absorption and Photoluminescence Measurements. *Journal of the American Chemical Society* 2004, 126, (4), 1290-1298.

CHAPTER 7. Magnetic Fe₃O₄-Au Core-Shell Nanostructures for Surface Enhanced Raman Scattering

7.1 Abstract

The synthesis, structural and optical characterization, and application of superparamagnetic and water-dispersed Fe₃O₄-Au core-shell nanoparticles for surface enhanced Raman scattering (SERS) is reported. The structure of the nanoparticles was determined by scanning transmission electron microscopy (STEM) and high-resolution transmission electron microscopy (HRTEM). STEM images of the Fe₃O₄-Au core-shell nanoparticles reveal an average diameter of 120 nm and a high degree of surface roughness. The nanoparticles, which display superparamagnetic properties due to the core Fe₃O₄ material, exhibit a visible surface plasmon resonance (SPR) peaked at 580 nm due to the outer gold shell. The nanoparticles are used as a substrate for surface enhanced Raman scattering (SERS) with rhodamine 6G (R6G) as a Raman reporter molecule. The SERS enhancement factor is estimated to be on the order of 10⁶, which is ~2 times larger than that of conventional gold nanoparticles (AuNPs) under similar conditions. Significantly, magnetically-induced aggregation of the Fe₃O₄-Au core-shell nanoparticles substantially enhanced SERS activity compared to non-magnetically-aggregated Fe₃O₄-Au nanoparticles. This is attributed to both increased scattering from the aggregates as well as “hot spots” due to more junction sites in the magnetically-induced aggregates. The magnetic properties of the Fe₃O₄ core, coupled with the optical properties of the Au shell, make the Fe₃O₄-Au

nanoparticles unique for various potential applications including biological sensing and therapy.

7.2 Introduction

In recent years, the development of novel plasmonic nanostructures has been an active area of research. Of these nanostructures, gold nanoparticles have been the focus of intense research, mainly due to their fascinating optical properties, particularly surface plasmon resonance (SPR) absorption¹⁻⁷ and surface enhanced Raman scattering (SERS)⁸⁻¹⁴. Due to its advantage of molecular specificity¹⁵⁻¹⁷, SERS is highly adequate for the detection of a wide variety of analytes, including biomolecules¹⁸⁻²¹, chemical agents²²⁻²⁴, explosives²⁵⁻²⁷

Two conditions central to SERS are the aforementioned SPR excitation of the metal substrate and close proximity of analyte molecules to the metal substrate surface. The electromagnetic (EM) field has been shown to diminish exponentially from the metal surface and will induce strong Raman scattering within an optimal spatial zone of 0-4 nm²⁸. Studies have demonstrated that at dislocations or sharp discontinuities on a metal surface, the electromagnetic (EM) field will be greatly enhanced^{29,30}. Enormous SERS enhancements are often present at the junction of two or more silver nanoparticles, as Brus and co-workers have demonstrated³¹. As the amount of aggregation of the nanoparticles used in that study increased, so did the SERS enhancement due to what is believed to be the generation of multiple “hot spots” at the junction sites. When two metal nanoparticles are brought together to

form a larger aggregated structure, their transition dipoles couple to each other and the enhanced fields of each particle coherently interfere at the junction site between the particles. Calculations have shown that, at a 1 nm separation distance between two nanospheres, an EM enhancement of 10^{10} may be expected³². These results strongly suggest that nanoparticle aggregates are better substrates for SERS than individual nanoparticles due to the coherent interference experienced at the junction sites. Several studies have been conducted and seemed to support this notion for gold and silver nanoparticle aggregates³³⁻³⁷.

Several methods exist to induce aggregation, including chemical^{38,39} and photoinduced aggregation⁴⁰⁻⁴². One novel method that is gradually gaining popularity is the careful control of magnetic properties⁴³⁻⁴⁵ involving the implementation of a paramagnetic or superparamagnetic core being encapsulated by a metallic shell. Utilization of the magnetic properties of the core material allows for controlled aggregation and thereby generation of a favorable density of hot spots for subsequent SERS enhancement.

Although aggregates may indeed provide enormous SERS enhancements, the surface of the aggregate must still be amenable to the analyte or no SERS will be observed. Because of that, the surface chemistry of the substrate is crucial since the analyte molecule must lie within the optimal 0-4 nm spatial zone in order to experience SERS enhancement. Essentially then, the analyte molecule must bind to the surface of the substrate to achieve SERS enhancement. Unfortunately, this is a nontrivial problem for many various analytes. As an example, Rhodamine 6G (R6G),

which characteristically is used in silver-based SERS studies, typically does not display any preferential binding to gold surfaces. Such selective binding characteristics renders engineering of a generic substrate nearly impossible. Because of this, one potentially suitable solution would be to use aggregated nanoparticles as the metallic substrate of choice since these aggregated nanostructures could simultaneously afford an increase in the number of junction sites between aggregates which is crucial for SERS, as well as increased light scattering. Additionally, the aggregates could be further improved should they have increased surface roughness as well as an increase in the number of “hot spots.”

In this work, we report the synthesis, structural and optical characterization, and SERS performance of a novel paramagnetic Fe₃O₄-Au core-shell nanoparticle system for the fingerprint detection of R6G. For the SERS detection of R6G, a concentration of $\sim 1 \times 10^{-5}$ M was easily achieved using the Fe₃O₄-Au core-shell nanoparticles as the SERS substrate. Furthermore, the Fe₃O₄-Au core-shell nanoparticles displayed a 2× SERS intensity enhancement over conventional spherical AuNPs. Magnetically-induced aggregation of the Fe₃O₄-Au core-shell nanoparticles served to increase the SERS signal a further 7× over the non-aggregated Fe₃O₄-Au core-shell nanoparticles. The overall performance enhancement of the Fe₃O₄-Au core-shell nanoparticles relative to AuNPs is due to the increased surface roughness as well as a higher density of SERS hotspots due to magnetic aggregation.

7.3 Experimental

7.3.1 Gold Nanoparticles (AuNPs)

Chlorauric acid trihydrate ($\text{HAuCl}_4 \cdot 3\text{H}_2\text{O}$, Acros), sodium citrate trihydrate ($\text{Na}_3\text{C}_6\text{H}_5\text{O}_7 \cdot 3\text{H}_2\text{O}$, Fisher), and sodium borohydride (NaBH_4 , Acros) were used as-received. The water that was used in all subsequent syntheses was 18 M Ω ultrapure water.

AuNPs were synthesized following the protocol established by Jana *et al.*⁴⁶ Briefly, a 20 mL aqueous solution of 2.5×10^{-4} M $\text{HAuCl}_4 \cdot 3\text{H}_2\text{O}$ and 2.5×10^{-4} M $\text{Na}_3\text{C}_6\text{H}_5\text{O}_7 \cdot 3\text{H}_2\text{O}$ was prepared in a two-necked round-bottom flask. Next, 0.6 mL of ice-cold, freshly prepared 0.1 M NaBH_4 solution was added while vigorously stirring. The solution turned pink immediately, indicating particle formation. The final concentration of the nanoparticles was estimated to be 5×10^9 particles per mL based on previous calculations.⁴⁷

7.3.2 Fe_3O_4 Synthesis

$\text{FeCl}_3 \cdot 6\text{H}_2\text{O}$, sodium acetate, ethylene glycol and polyethylene glycol were used as-received and were obtained from Fisher Scientific.

The Fe_3O_4 nanoparticles were synthesized according to the method established by Liu *et al.*⁴⁸ Briefly, 1.35 g of $\text{FeCl}_3 \cdot 6\text{H}_2\text{O}$ was first dissolved in 40 mL of ethylene glycol to form a clear yellow solution. Additions of 3.60 g of sodium acetate and 0.10 g of polyethylene glycol were then incorporated into the solution. After stirring for ~30 minutes, the solution was transferred to a Teflon-lined stainless steel autoclave. The autoclave was sealed and heated at 200 °C for 10 hours and

allowed to cool to room temperature. A black precipitate was collected and washed, sequentially, six times with water and ethanol, respectively. The resulting Fe₃O₄ nanoparticles were dispersed in an aqueous solution of ethanol (20 mg/mL) and had a concentration of $\sim 5.1 \times 10^{11}$ particles per mL.

7.3.3 Fe₃O₄-Au Synthesis

Sodium hydroxide (Fisher), HAuCl₄·3H₂O (Acros), hydroxylamine hydrochloride (NH₂·HCl, Thermo Scientific) and 3-aminopropyltrimethoxysilane (APTMS, Aldrich) were used as-received.

Gold-shell encapsulation was achieved by following and appropriately modifying the method established by Du *et al*⁴⁹ who achieved Ag-shell encapsulation. In order to encapsulate the Fe₃O₄ nanoparticles with a gold shell, proper surface modification with APTMS was necessary. To bind with APTMS, 0.25 g of as-prepared Fe₃O₄ nanoparticles were added into 100 mL of ethanol and sonicated for 30 minutes. After the addition of 1 mL of APTMS, the solution was vigorously mixed for 6 hours. To encapsulate the nanoparticles in a gold shell, the APTMS-bound Fe₃O₄ nanoparticles were mixed in a 100 mL aqueous solution of 0.15% HAuCl₄·3H₂O and sonicated for 30 minutes. Freshly-prepared reductant, which was a mixture of 50 mL of 0.1 M NaOH and 45 mL of 0.06 M NH₂·HCl, was added and mixed for a further 45 minutes. Upon the addition of the reductants, the solution immediately turned a deep blue-purple. Final particle concentration was estimated to

be $\sim 3.5 \times 10^{11}$ particles per mL. The final particles were obtained using a magnetic field.

The procedure to introduce R6G to the surfaces of the AuNPs and Fe₃O₄-Au nanospheres involved mixing of as-prepared nanoparticles in a 9:1 volume ratio with solutions of R6G of varying concentrations. R6G solutions were prepared in 1 mL of water.

7.3.4 UV-Vis, Electron Microscopy, and Raman Systems

Absorption measurements were conducted on an HP 8452A UV-visible spectrophotometer with spectral resolution set to 2 nm. The morphology and size of the Fe₃O₄ and Fe₃O₄-Au nanospheres were characterized by scanning transmission electron microscopy (STEM) using an FEI Quanta 3D FEG Dualbeam at 30 keV. For improved contrast between the gold and Fe₃O₄, another SEM (FEI Nanosem 200) using STEM (scanning transmission electron microscopy) mode was used. Additionally, the Au coating was confirmed by chemical analysis of the sample by energy dispersive X-ray (EDX). High-resolution transmission electron microscopy (HRTEM) was performed using an FEI Titan 80-300 with accelerating voltage set to 300 keV. The Raman system is a Renishaw Raman System (Renishaw Inc., Model RM2000) with a 20× objective lens configured for backscattering geometry. The excitation laser operated at 632.8 nm with a power of ~ 2 mW with a beam size on the order of $1 \mu\text{m}^2$. The integration time for each measurement was 10 seconds. For the bulk detection, the laser excitation light was directly focused onto the surface of the

sample solution (300 μL) with the same laser power and integration time. For subsequent magnetic field experiments, a 0.25 cm^3 strong neodymium magnet was utilized to magnetically induce aggregation at the focal point of the microscope, ensuring that the aggregate would be illuminated with the laser for subsequent SERS measurements. SERS spectra were collected within seconds of magnetic aggregation of the nanoparticles.

7.4 Results

7.4.1 Optical Properties and EM Characterization

Figure 1 displays UV-Vis spectra of Fe_3O_4 , Au, Fe_3O_4 -Au nanoparticles, and magnetically-induced aggregates of Fe_3O_4 -Au nanoparticles. For the Fe_3O_4 nanoparticles, a broad absorption spectrum which spans the visible wavelengths with a center at 645 nm is noticeable. This is expected for two reasons: (i) the Fe_3O_4 nanoparticles are black, indicating that they will absorb at all wavelengths, and (ii) there is a slight particle size distribution, as will soon be discussed. The AuNPs show a characteristic SPR centered at 520 nm^{50} with an accompanying full width at half max (FWHM) of 70 nm. The small FWHM is indicative of a narrow size dispersion. For the Fe_3O_4 -Au nanoparticles, an SPR manifested at a band peaked around 580 nm with a FWHM of 144 nm; here, the SPR is due to the presence of the gold shell atop the core Fe_3O_4 material. The 580 nm SPR, red-shifted from the normal 520 nm absorbance of solid Au nanoparticles⁵⁰, is indicative of the shell-like nature of the encapsulating gold material⁵¹. The slightly large FWHM is indicative of a particle

size inhomogeneity likely due to both the deposition of the gold shell on the Fe_3O_4 nanoparticles as well as the inherent particle size distribution of the parent Fe_3O_4 nanoparticles. The small shoulder which is seen at 355 nm is due to uncapped Fe_3O_4 nanoparticles⁵². It should be noted that the Fe_3O_4 -Au nanoparticles have decreased absorbance compared to the parent Fe_3O_4 nanoparticles at wavelengths beyond ~ 700 nm. We believe this phenomenon is due to the fact that there is less overall aggregation in the Fe_3O_4 -Au nanoparticle system compared to the Fe_3O_4 since it is likely the Fe_3O_4 -Au nanoparticles are less magnetic than the Fe_3O_4 nanoparticles (due to the gold shell overlayer) which would induce less aggregation and therefore less optical density at red-shifted wavelengths. This decreased density of naturally-occurring aggregates would account for the diminished absorption at red wavelengths. Meanwhile, the magnetically-induced aggregates of the Fe_3O_4 -Au nanoparticles shows substantially increased absorbance at wavelengths red-shifted of ~ 650 nm, which is attributed to an extended plasmon band of the aggregate system.

Figure 1. UV-Vis absorption spectra of Fe₃O₄ (blue line), Au (black line), Fe₃O₄-Au nanoparticles (red line), and magnetically-induced aggregates of the Fe₃O₄-Au nanoparticles (green line).

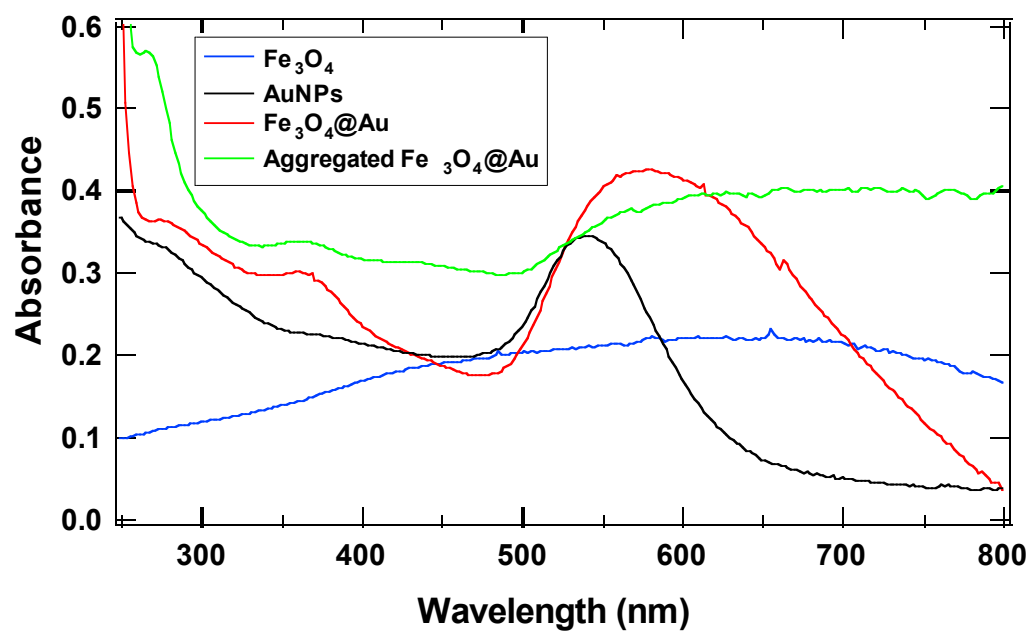
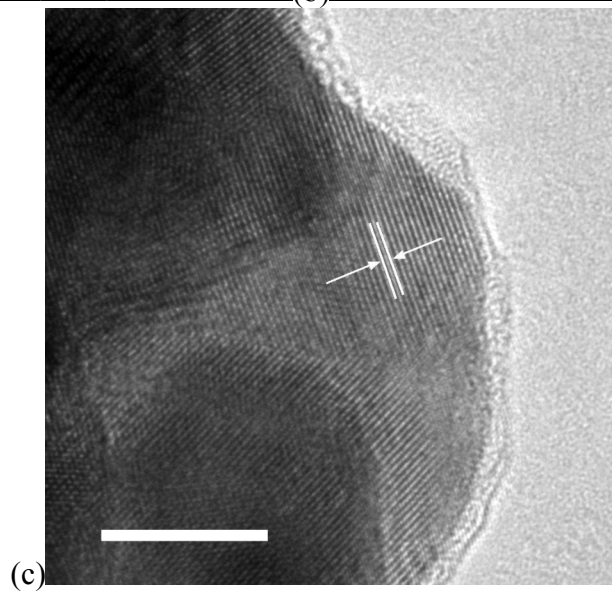
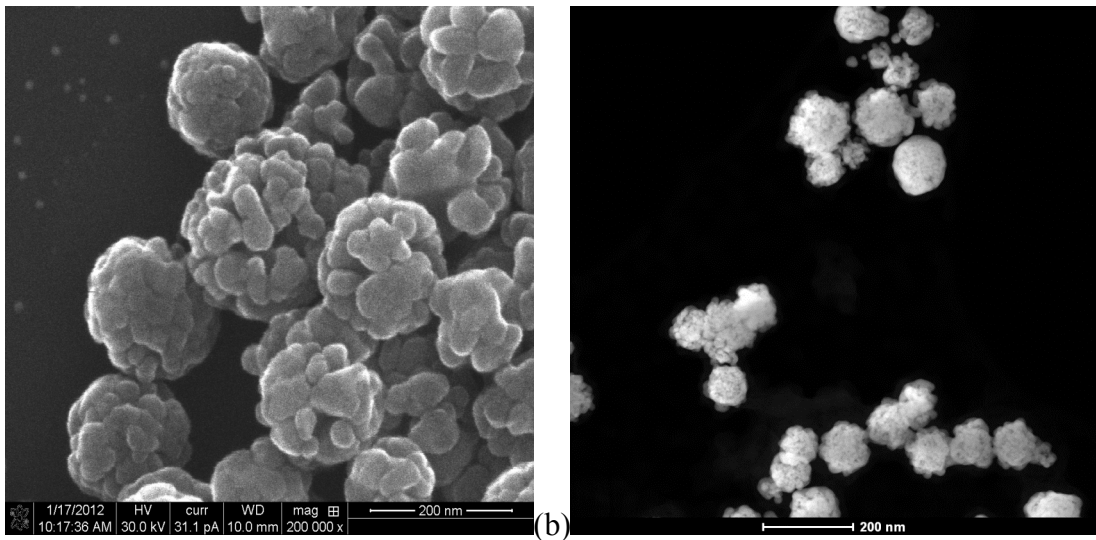


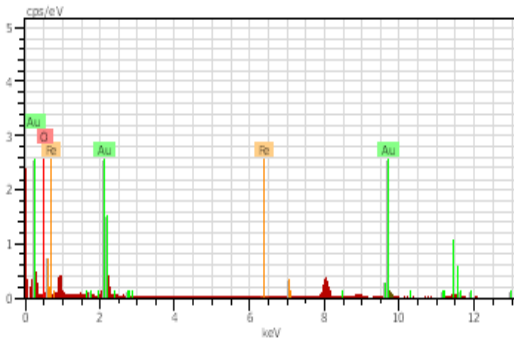
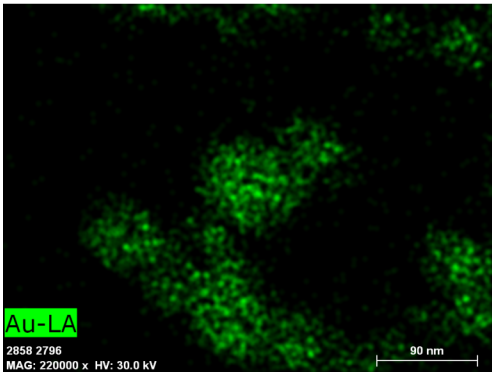
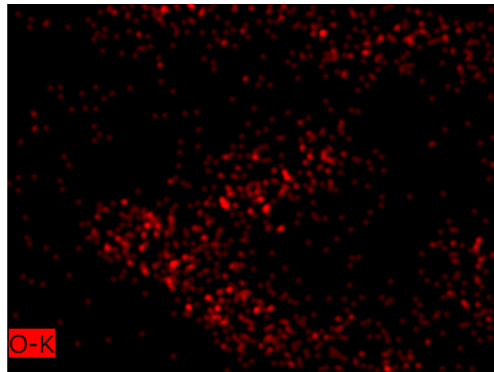
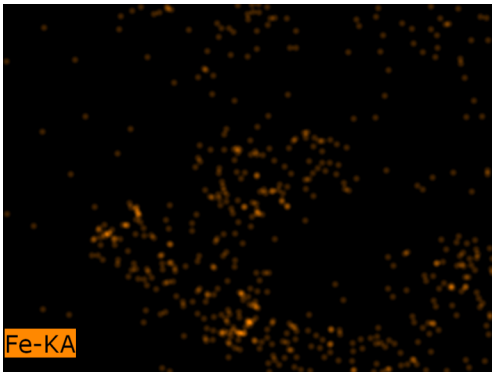
Figure 2 shows representative STEM and HRTEM images of the Fe_3O_4 and Fe_3O_4 -Au nanoparticles. The preparation of the Fe_3O_4 yielded nanoparticles with an average overall diameter of ~ 165 nm, characterized by a high degree of surface roughness. Image analysis of 100 different Fe_3O_4 nanoparticles indicated a particle size distribution of 18.4%. Upon the gold shell deposition, a cation exchange occurred, whereby some of the $\text{Fe}^{2+/3+}$ cations donated electrons to solvated Au^{3+} cations, simultaneously solvating and oxidizing the iron while reducing the gold. The concept of cation exchange in producing a core-shell nanostructure has been studied before.^{53,54} The net result was a smaller overall particle of ~ 120 nm diameter complete with a gold shell. As with the Fe_3O_4 nanoparticles, EM image analysis of 100 different nanoparticles was conducted and yielded a particle size distribution of 15.5%. Upon inspection with HRTEM, the Fe_3O_4 -Au nanoparticles showed a lattice spacing of 0.219 nm, indicative of the [111] planes of Au which also illustrated the polycrystallinity of the nanoparticle⁵¹. Noticeable in all EM images is the high degree of surface roughness.

Figure 2. (a) STEM image of as-prepared Fe_3O_4 nanoparticles with an average diameter of 165 nm. (b) STEM image of as-prepared Fe_3O_4 -Au nanoparticles with an average diameter of 120 nm. (c) HRTEM image of Fe_3O_4 -Au nanoparticles with a lattice constant of 0.219 nm, indicative of gold. The scale bar is 5 nm.



To confirm the presence of the gold shell on the Fe_3O_4 nanoparticles, EDX spectra were collected and are shown below in Figure 3. In the images, the relative distributions of oxygen, iron, and gold may be seen. Please note that due to the low accelerating voltage, and therefore the low penetration depth, the relative abundance of gold appears to be higher than that of iron since it is bound to the surface of the nanoparticle. From this, however, a uniform distribution of gold along the underlying iron is evident, suggesting the Au atoms were deposited around the iron oxide lattice. The corresponding spectrum, plotted as a function of keV, shows that the presence of gold predominates while iron and oxygen also play a role in the chemical constituency of the nanoparticles.

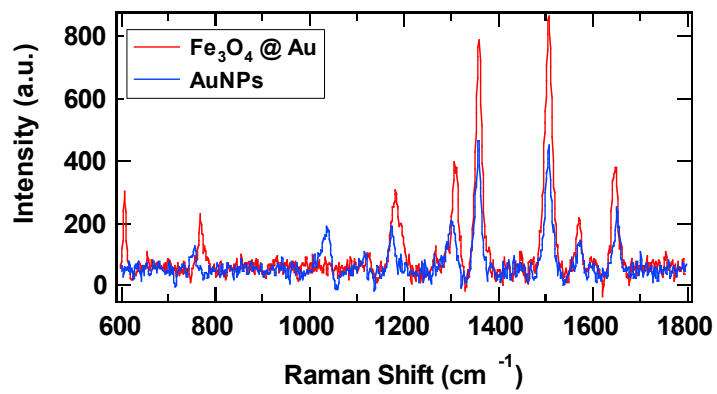
Figure 3. EDX mapping and associated spectrum of Fe₃O₄-Au nanoparticles. Shown are the iron (top left), oxygen (top right), and gold (bottom left) abundances. In the bottom right is the actual EDX spectrum, showing the presence of iron, oxygen, and gold within the nanoparticle.



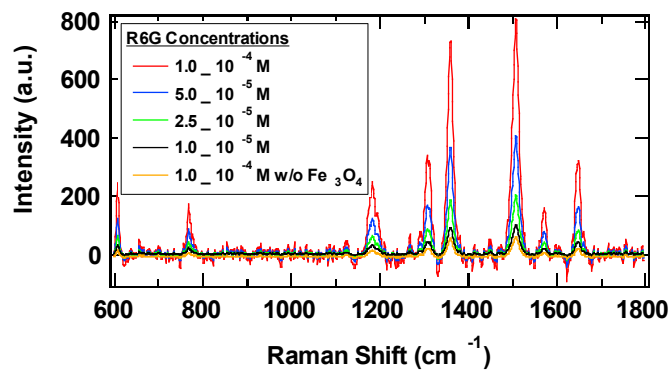
7.4.2 SERS Spectra

Figure 4a shows the SERS spectra of 1×10^{-4} M R6G adsorbed onto the surfaces of the as-prepared AuNP and Fe₃O₄-Au nanoparticles. Characteristic Raman signals⁵⁵ of R6G at 775, 953, 1132, 1278, 1455 and 1646 cm⁻¹ are shown, where it is observed that spectral positions and widths do not change noticeably with the presence of the superparamagnetic core. The signal increases $\sim 2\times$ when the Fe₃O₄-Au nanoparticles were used instead of the AuNPs, indicating that the Fe₃O₄-Au nanoparticles have a higher SERS efficiency than the AuNPs as a substrate material; this is most likely due to the increased amount of surface roughness of the Fe₃O₄-Au nanoparticles. In order to have a quantitative and comparative study, Figure 4b shows the intensity of the SERS spectra of R6G, at varying R6G concentrations, utilizing the Fe₃O₄-Au nanoparticles as the SERS substrate.

Figure 4a. SERS spectra of R6G adsorbed onto AuNPs (blue line) and Fe₃O₄-Au nanoparticles (red line), showing that the Fe₃O₄-Au nanoparticles have increased SERS efficiency relative to AuNPs. Figure 4b. SERS spectra of R6G utilizing the Fe₃O₄-Au nanoparticles as the SERS substrate.



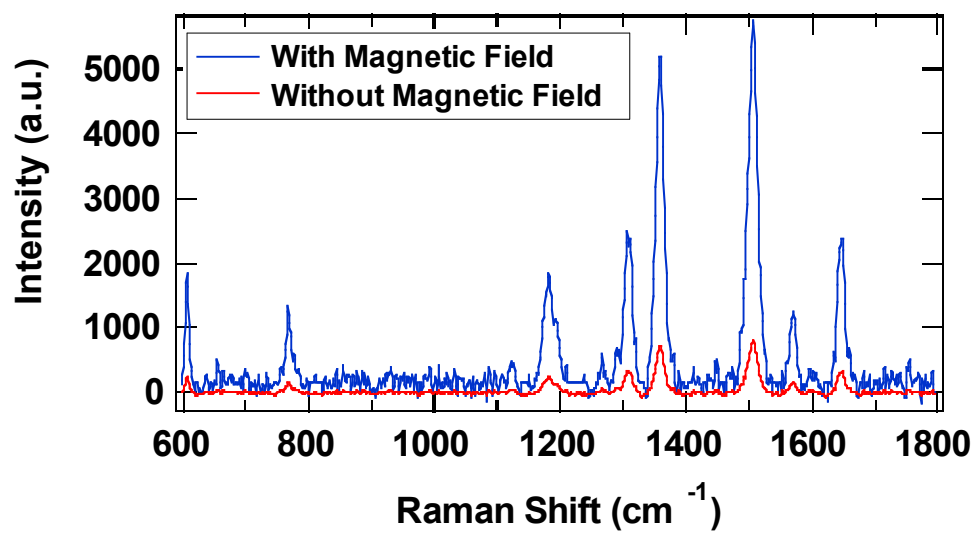
(a)



(b)

Figure 5, meanwhile, shows the effect of magnetically-induced aggregation on the intensity of the SERS spectra for the Fe_3O_4 -Au nanoparticles, where the magnetically aggregated Fe_3O_4 -Au nanoparticles have a $\sim 7\times$ enhancement over the as-prepared, non-magnetically-aggregated Fe_3O_4 -Au nanoparticles. This large increase in SERS intensity likely arises from increased scattering brought about by the magnetic aggregation of the Fe_3O_4 -Au nanoparticles. This enhancement factor is similar to what has been seen before in literature⁴³. Again, the spectral positions and bandwidths are not seen to change with magnetic aggregation.

Figure 5. SERS spectra of R6G adsorbed onto the Fe₃O₄-Au nanoparticles in the absence and presence of an applied magnetic field.



7.5 Discussion

7.5.1 SPR Properties of Gold-coated Fe₃O₄

It is known that the spectral position of the SPR absorption from gold, due to the collective oscillation of conduction band electrons, not only lies in visible wavelengths, but also is sensitive to morphology and size of the nanoparticles being studied^{51,56-58} in addition to the solvent and its dielectric constant. While solid gold nanoparticles have a characteristic SPR at 520 nm⁵⁰, alterations to the spherical nature of the nanoparticle can induce massive spectral changes. In particular, the spectral position of the SPR of hollow gold nanospheres has shown great sensitivity to its aspect ratio (the quotient of its core diameter by its shell thickness)^{51,57,59,60}. TEM images (not shown) indicate an overall aspect ratio of ~5:1 which corresponds to a strong SPR at ~570 nm, as has been shown elsewhere⁵⁷. Our results however, from Figure 1, indicate an SPR at 580 nm. The discrepancy is likely due to the incorporation of the superparamagnetic core and silane ligand coverage which undoubtedly altered the dielectric constant and thereby shifted the band position. Additionally, the particle size distribution likely contributed to the slight red-shift.^{61,62} Finally, since the Fe₃O₄-Au nanoparticles are naturally superparamagnetic, a slight amount of spontaneous magnetic aggregation occurs, thereby generating small aggregated structures which can red-shift the absorption characteristics.

For the Fe₃O₄-Au nanoparticles, a very weak band centered at 355 nm may be seen in Figure 1, which may be due to an electronic excitation of an oxygen lone pair or due to some *d-d* "hopping." Further attempts were made to increase the gold shell

thickness by introducing more Au^{3+} into solution and subsequently reducing and depositing it onto the already-formed gold shells, however this resulted in aggregation of nanoparticles.

7.5.2 Mechanism of Enhanced SERS of Magnetically-Induced Fe_3O_4 -Au Nanoparticle Aggregates

Detailed studies of the combined effects of plasmonic and magnetic properties of Fe_3O_4 -Au core-shell nanoparticles and their application to SERS is limited⁴³. However, work has been done on SERS detection utilizing silver-coated Fe_3O_4 ⁶³, composited Au/Ag/Fe nanocrescents⁴⁴, and Ag- and Au-coated $\gamma\text{-Fe}_2\text{O}_3$ nanoparticles⁴³. In each of these studies, the application of an external magnetic field induced strong aggregation or alignment of the nanoparticles in order to provide strong SERS performance with spectral intensities increasing greatly due to the magnetic field. Another study, based on Fe_3O_4 -Ag core-shell nanoparticles, utilized the superparamagnetic properties of the nanoparticles to render the substrate separable from the bulk analyte solution⁴⁵. Our results are comparable to, if not better, than these. Our improved performance likely arises from the increased overall surface roughness as well as properties arising from the magnetic aggregation, *e.g.*, number of junction sites or “hot spots,” additional “sandwich effect” properties, *etc.*, of which more will be discussed below.

Nevertheless, since the Fe_3O_4 -Au nanoparticles show a strong plasmon band in the visible, they are expected to show good SERS properties as with other gold

nanoparticle systems⁶⁴⁻⁶⁶ for which our results are consistent with those systems. From Figure 4, it is interesting to note that the relative intensities of the SERS peaks from R6G hardly change, if at all, from the normal Raman peaks arising from R6G without any enhancement. Most usually, spectral intensity changes may be expected due to the complex interplay between the analyte molecule and the SERS substrate. In this case, the insignificant spectral change may be due to an overall weak chemical interaction between the R6G and the SERS substrate. This observation is similar to results previously reported wherein small spectral intensity changes were seen^{38,67}.

It should be noted that, historically, fewer studies on the SERS of R6G from gold have been published than silver, simply because R6G usually does not interact strongly with gold^{68,69}. However, gold affords some advantages over silver. First, gold is chemically more inert, resisting oxidation and being more stable over long periods of time. Additionally, aggregates of gold can have absorption bands red-shifted into the near-infrared (NIR) which is beyond that of silver. This greater flexibility of gold allows for greater tunability in the selection of excitation wavelengths. Core-shell structures can provide similar tunability; however they do not typically exhibit strong SERS enhancement factors due to their general lack of aggregation and thereby lack of hot spot junctions at the surface of the nanoparticles. Because of this, incorporation of a magnetic core into the center of the core-shell system is attractive due to the possibility of careful manipulation of the extent of aggregation. Magnetically-induced aggregation, as shown in Figure 5, indeed can be

responsible for increased overall SERS signal relative to the non-magnetically-induced system. This point bears further explanation.

There are two principle explanations for the increased SERS signal due to magnetic aggregation, both of which are related to the utilization of hot spots at junction sites. First, as can be seen in the STEM images of Figure 2b, the Fe₃O₄-Au nanoparticles show a relatively high degree of surface roughness. Surface roughness has been proven to play a vital role in the SERS efficiency of metallic substrates⁷⁰⁻⁷² since it has the singular capacity to increase the density of SERS hot spots along the surface of the nanoparticle which can have dramatic effects on SERS intensity. This is important when considering future applications for these nanoparticles. Second, the aggregation itself can contribute to the increased SERS signal. When the individual nanoparticles aggregate together, a constructive “sandwich” effect becomes possible. In the “sandwich” effect, an analyte molecule can become trapped between two metallic SERS substrate nanoparticles. Should the nanoparticles sandwich together within the optimal zone of electromagnetic field enhancement, and should the analyte molecule be ensconced within the sandwich, the resulting enhancement factor is immense. This has been demonstrated with bioanalytes that are notoriously difficult to detect *via* SERS²⁹. Moreover, clusters of aggregated solid will have the propensity to scatter light more which may contribute to an overall increased signal. In concert with one another, both the surface morphology as well as the aggregation becomes vital for the SERS enhancement factor for magnetically-aggregated nanoparticles.

While this is not the first SERS detection of R6G utilizing gold as the SERS substrate, this is, we believe, the first to report the SERS detection of R6G with Fe₃O₄-Au nanoparticles as the SERS substrate. As mentioned previously, gold substrates have several key advantages over silver, and with an enhanced surface *via* surface roughness and increased aggregation due to its superparamagnetic properties, both of which contribute to the generation of SERS hot spots, these Fe₃O₄-Au nanoparticles have a distinct advantage over other gold-based SERS substrates. In order to provide a semi-quantitative comparison, we can provide an estimate of the enhancement factor afforded to the Fe₃O₄-Au nanoparticles. Comparing the intensities of the 1362 cm⁻¹ peak of the Raman spectra of the 0.1 mM R6G alone and the 30 μL volume in the presence of the Fe₃O₄-Au nanoparticle aggregates, and including concentration differences, we obtain a 10⁶ enhancement of the Raman signal (Figure 4). This enhancement factor is excellent for ensemble-averaged, non-resonant SERS in comparison to previous enhancement factors⁷³.

There are two possibilities that can account for this large enhancement. First, the aggregates have an increased number of SERS active sites due to the large number of junctions present, as has been discussed. Because the R6G concentration in this study is greater than the concentration of the Fe₃O₄-Au nanoparticle aggregates, it is possible to have more than one molecule per aggregate become enhanced. This also increases the probability that the analyte molecule will adsorb onto a hot spot as opposed to an adsorption site with no enhancement. Second, the unique surface properties of the Fe₃O₄-Au nanoparticle aggregates may facilitate

efficient adsorption or binding of the R6G molecules to the surface of the aggregate. This bears further study and, in conjunction with biomolecules that are traditionally more difficult to detect, will be the subject of future work.

7.6 Conclusion

In summary, we have demonstrated that core-shell Fe_3O_4 -Au and magnetically-aggregated Fe_3O_4 -Au nanoparticles are highly SERS-active substrates for quantitative R6G detection with an enhancement factor of 10^6 . Compared to solid spherical AuNPs, the SERS signal of R6G using Fe_3O_4 -Au is enhanced by a factor of $2\times$, attributable to the high degree of surface roughness. Upon magnetic aggregation of the Fe_3O_4 -Au nanoparticles, the SERS signal of R6G was seen to increase a further $7\times$. The further increase in SERS signal is the result of an increased amount of “hot spots” or junction sites for concomitant electromagnetic field enhancement as well as increased scattering that occurs upon the coalescence of aggregated structures. The Fe_3O_4 -Au nanoparticles display superparamagnetic properties due to the core Fe_3O_4 material as well as an SPR arising from the Au overlayer. The magnetic properties of the Fe_3O_4 core, coupled with the optical properties of the Au shell, make the Fe_3O_4 -Au nanoparticles unique for various potential applications including sensing and therapy.

7.7 References

- [1] L. J. Sherry; S. H. Chang; G. C. Schatz; R. P. Van Duyne; B. J. Wiley; Y. N. Xia, "Localized surface plasmon resonance spectroscopy of single silver nanocubes," *Nano Letters*, **2005**, *5*, 2034-2038.
- [2] E. M. Hicks; X. Y. Zhang; S. L. Zou; O. Lyandres; K. G. Spears; G. C. Schatz; R. P. Van Duyne, "Plasmonic properties of film over nanowell surfaces fabricated by nanosphere lithography," *Journal Of Physical Chemistry B*, **2005**, *109*, 22351-22358.
- [3] A. V. Whitney; J. W. Elam; S. L. Zou; A. V. Zinovev; P. C. Stair; G. C. Schatz; R. P. Van Duyne, "Localized surface plasmon resonance nanosensor: A high-resolution distance-dependence study using atomic layer deposition," *Journal Of Physical Chemistry B*, **2005**, *109*, 20522-20528.
- [4] A. J. Haes; W. P. Hall; R. P. Van Duyne, "Nanoscale plasmonics begins to unravel Alzheimer's disease," *Laser Focus World*, **2005**, *41*, 105-+.
- [5] L. He; E. A. Smith; M. J. Natan; C. D. Keating, "The distance-dependence of colloidal Au-amplified surface plasmon resonance," *Journal Of Physical Chemistry B*, **2004**, *108*, 10973-10980.
- [6] E. Hutter; J. H. Fendler; D. Roy, "Surface plasmon resonance studies of gold and silver nanoparticles linked to gold and silver substrates by 2-aminoethanethiol and 1,6-hexanedithiol," *Journal Of Physical Chemistry B*, **2001**, *105*, 11159-11168.

- [7] P. K. Jain; M. A. Ei-Sayed, "Surface plasmon resonance sensitivity of metal nanostructures: Physical basis and universal scaling in metal nanoshells," *Journal Of Physical Chemistry C*, **2007**, *111*, 17451-17454.
- [8] C. R. Yonzon; D. A. Stuart; X. Y. Zhang; A. D. McFarland; C. L. Haynes; R. P. Van Duyne, "Towards advanced chemical and biological nanosensors - An overview," *Talanta*, **2005**, *67*, 438-448.
- [9] Z. Q. Tian, "Surface-enhanced Raman spectroscopy: advancements and applications," *Journal Of Raman Spectroscopy*, **2005**, *36*, 466-470.
- [10] C. L. Haynes; C. R. Yonzon; X. Y. Zhang; R. P. Van Duyne, "Surface-enhanced Raman sensors: early history and the development of sensors for quantitative biowarfare agent and glucose detection," *Journal Of Raman Spectroscopy*, **2005**, *36*, 471-484.
- [11] A. Otto, "The 'chemical' (electronic) contribution to surface-enhanced Raman scattering," *Journal Of Raman Spectroscopy*, **2005**, *36*, 497-509.
- [12] S. M. Nie; S. R. Emery, "Probing single molecules and single nanoparticles by surface-enhanced Raman scattering," *Science*, **1997**, *275*, 1102-1106.
- [13] T. M. Cotton; J. H. Kim; G. D. Chumanov, "Application of surface-enhanced Raman spectroscopy to biological systems," *Journal of Raman Spectroscopy*, **1991**, *22*, 729.

- [14] S. E. Hunyadi; C. J. Murphy, "Bimetallic silver-gold nanowires: fabrication and use in surface-enhanced Raman scattering," *Journal Of Materials Chemistry*, **2006**, *16*, 3929-3935.
- [15] L. Zeiri; B. V. Bronk; Y. Shabtai; J. Eichler; S. Efrima, "Surface-Enhanced Raman Spectroscopy as a Tool for Probing Specific Biochemical Components in Bacteria," *Applied Spectroscopy*, **2004**, *58*, 33-40.
- [16] A. Sengupta; M. Mujacic; E. Davis, "Detection of bacteria by surface-enhanced Raman spectroscopy," *Analytical and Bioanalytical Chemistry*, **2006**, *386*, 1379.
- [17] H. Wei; J. Li; Y. Wang; E. Wang, "Silver nanoparticles coated with adenine: preparation, self-assembly and application in surface-enhanced Raman scattering," *Nanotechnology*, **2007**, *18*, 175610.
- [18] Y. Cui; B. Ren; J.-L. Yao; R.-A. Gu; Z.-Q. Tian, "Synthesis of AgcoreAushell Bimetallic Nanoparticles for Immunoassay Based on Surface-Enhanced Raman Spectroscopy," *The Journal of Physical Chemistry B*, **2006**, *110*, 4002-4006.
- [19] K. E. Shafer-Peltier; C. L. Haynes; M. R. Glucksberg; R. P. Van Duyne, "Toward a Glucose Biosensor Based on Surface-Enhanced Raman Scattering," *Journal of the American Chemical Society*, **2002**, *125*, 588.
- [20] C. R. Yonzon; C. L. Haynes; X. Zhang; J. T. Walsh; R. P. Van Duyne, "A Glucose Biosensor Based on Surface-Enhanced Raman Scattering:â€% Improved

Partition Layer, Temporal Stability, Reversibility, and Resistance to Serum Protein Interference," *Analytical Chemistry*, **2003**, 76, 78.

[21] L. F. Cheow; S. H. Ko; S. J. Kim; K. H. Kang; J. Han, "Increasing the Sensitivity of Enzyme-Linked Immunosorbent Assay Using Multiplexed Electrokinetic Concentrator," *Analytical Chemistry*, **2010**, 82, 3383.

[22] M. G. Albrecht; J. A. Creighton, "Anomalously intense Raman spectra of pyridine at a silver electrode," *Journal of the American Chemical Society*, **1977**, 99, 5215.

[23] S. Farquharson; A. Gift; P. Maksymiuk; F. Inscore, "Surface-enhanced Raman spectra of VX and its hydrolysis products," *Applied Spectroscopy*, **2005**, 59, 654-660.

[24] P. Kao; N. A. Malvadkar; M. Cetinkaya; H. Wang; D. L. Allara; M. C. Demirel, "Surface-Enhanced Raman Detection on Metalized Nanostructured Poly(p-xylylene) Films," *Advanced Materials*, **2008**, 20, 3562.

[25] H. Wackerbarth; C. Salb; L. Gundrum; M. Niederkrüger; K. Christou; V. Beushausen; W. Viöl, "Detection of explosives based on surface-enhanced Raman spectroscopy," *Applied optics*, **2010**, 49, 4362-4366.

[26] F. Calzzani; R. Sileshi; A. Kassu; J. Taguenang; A. Chowdhury; A. Sharma; P. Ruffin; C. Brantley; E. Edwards. "Detection of residual traces of explosives by surface enhance Raman scattering using gold coated substrates produced by nanospheres imprint technique", 2008.

- [27] H. Wackerbarth; L. Gundrum; C. Salb; K. Christou; W. Viöl, "Challenge of false alarms in nitroaromatic explosive detection—a detection device based on surface-enhanced Raman spectroscopy," *Applied optics*, **2010**, *49*, 4367-4371.
- [28] G. C. Schatz; R. P. Van Duyne, "Electromagnetic Mechanism of Surface-Enhanced Spectroscopy," *Handbook of vibrational spectroscopy*, **2002**,
- [29] S. Preciado-Flores; D. A. Wheeler; T. M. Tran; Z. Tanaka; C. Jiang; M. Barboza-Flores; F. Qian; Y. Li; B. Chen; J. Z. Zhang, "SERS spectroscopy and SERS imaging of *Shewanella oneidensis* using silver nanoparticles and nanowires," *Chemical Communications*, **2011**, *47*, 4129.
- [30] M. Quinten, "Evanescent wave scattering by aggregates of clusters—application to optical near-field microscopy," *Applied Physics B: Lasers and Optics*, **2000**, *70*, 579-586.
- [31] A. M. Michaels; J. Jiang; L. Brus, "Ag nanocrystal junctions as the site for surface-enhanced Raman scattering of single rhodamine 6G molecules," *The Journal of Physical Chemistry B*, **2000**, *104*, 11965-11971.
- [32] H. Xu; E. J. Bjerneld; M. Käll; L. Börjesson, "Spectroscopy of Single Hemoglobin Molecules by Surface Enhanced Raman Scattering," *Physical Review Letters*, **1999**, *83*, 4357-4360.
- [33] C. Blatchford; J. Campbell; J. Creighton, "Plasma resonance-enhanced raman scattering by absorbates on gold colloids: The effects of aggregation," *Surface Science*, **1982**, *120*, 435-455.

[34] B. Vlckova; X. Gu; M. Moskovits, "SERS excitation profiles of phthalazine adsorbed on single colloidal silver aggregates as a function of cluster size," *The Journal of Physical Chemistry B*, **1997**, *101*, 1588-1593.

[35] L. Sun; Y. Song; L. Wang; C. Guo; Y. Sun; Z. Liu; Z. Li, "Ethanol-induced formation of silver nanoparticle aggregates for highly active SERS substrates and application in DNA detection," *The Journal of Physical Chemistry C*, **2008**, *112*, 1415-1422.

[36] A. P. Budnyk; A. Damin; G. Agostini; A. Zecchina, "Gold nanoparticle aggregates immobilized on high surface area silica substrate for efficient and clean SERS applications," *The Journal of Physical Chemistry C*, **2010**, *114*, 3857-3862.

[37] N. T. B. Thuy; R. Yokogawa; Y. Yoshimura; K. Fujimoto; M. Koyano; S. Maenosono, "Surface-enhanced Raman spectroscopy for facile DNA detection using gold nanoparticle aggregates formed via photoligation," *Analyst*, **2010**, *135*, 595-602.

[38] A. M. Schwartzberg; C. D. Grant; A. Wolcott; C. E. Talley; T. R. Huser; R. Bogomolni; J. Z. Zhang, "Unique Gold Nanoparticle Aggregates as a Highly Active Surface-Enhanced Raman Scattering Substrate," *The Journal of Physical Chemistry B*, **2004**, *108*, 19191-19197.

[39] E. Messina; E. Cavallaro; A. Cacciola; M. A. Iatì; P. G. Gucciardi; F. Borghese; P. Denti; R. Saija; G. Compagnini; M. Meneghetti; V. Amendola; O. M.

Maragò, "Plasmon-Enhanced Optical Trapping of Gold Nanoaggregates with Selected Optical Properties," *ACS Nano*, **2011**, *5*, 905-913.

[40] Y. Zhang; C. Gu; A. M. Schwartzberg; S. Chen; J. Z. Zhang, "Optical trapping and light-induced agglomeration of gold nanoparticle aggregates," *Physical Review B*, **2006**, *73*, 165405.

[41] R. Jin; Y. Cao; C. A. Mirkin; K. L. Kelly; G. C. Schatz; J. G. Zheng, "Photoinduced Conversion of Silver Nanospheres to Nanoprisms," *Science*, **2001**, *294*, 1901-1903.

[42] A. Pyatenko; M. Yamaguchi; M. Suzuki, "Synthesis of Spherical Silver Nanoparticles with Controllable Sizes in Aqueous Solutions," *The Journal of Physical Chemistry C*, **2007**, *111*, 7910-7917.

[43] G. V. P. Kumar; N. Rangarajan; B. Sonia; P. Deepika; N. Rohman; C. Narayana, "Metal-coated magnetic nanoparticles for surface enhanced Raman scattering studies," *Bulletin of Materials Science*, **2011**, *34*, 207.

[44] G. L. Liu; Y. Lu; J. Kim; J. C. Doll; L. P. Lee, "Magnetic Nanocrescents as Controllable Surface-Enhanced Raman Scattering Nanoprobes for Biomolecular Imaging," *Advanced Materials*, **2005**, *17*, 2683-2688.

[45] J. Du; C. Jing, "Preparation of Thiol Modified Fe₃O₄@ Ag Magnetic SERS Probe for PAHs Detection and Identification," *The Journal of Physical Chemistry C*, **2011**,

[46] N. R. Jana; L. Gearheart; C. J. Murphy, "Seeding Growth for Size Control of 5–40 nm Diameter Gold Nanoparticles," *Langmuir*, **2001**, *17*, 6782-6786.

- [47] W. Haiss; N. T. K. Thanh; J. Aveyard; D. G. Fernig, "Determination of Size and Concentration of Gold Nanoparticles from UV–Vis Spectra," *Analytical Chemistry*, **2007**, *79*, 4215-4221.
- [48] B. Liu; M. Han; G. Guan; S. Wang; R. Liu; Z. Zhang, "Highly-Controllable Molecular Imprinting at Superparamagnetic Iron Oxide Nanoparticles for Ultrafast Enrichment and Separation," *The Journal of Physical Chemistry C*, **2011**, *115*, 17320-17327.
- [49] J. Du; C. Jing, "Preparation of Fe₃O₄@ Ag SERS substrate and its application in environmental Cr (VI) analysis," *Journal of Colloid and Interface Science*, **2011**,
- [50] J. Kimling; M. Maier; B. Okenve; V. Kotaidis; H. Ballot; A. Plech, "Turkevich method for gold nanoparticle synthesis revisited," *Journal Of Physical Chemistry B*, **2006**, *110*, 15700-15707.
- [51] D. A. Wheeler; R. J. Newhouse; H. Wang; S. Zou; J. Z. Zhang, "Optical Properties and Persistent Spectral Hole Burning of Near Infrared-Absorbing Hollow Gold Nanospheres," *The Journal of Physical Chemistry C*, **2010**, *114*, 18126.
- [52] Z. Xu; Y. Hou; S. Sun, "Magnetic Core/Shell Fe₃O₄/Au and Fe₃O₄/Au/Ag Nanoparticles with Tunable Plasmonic Properties," *Journal of the American Chemical Society*, **2007**, *129*, 8698-8699.
- [53] M. Ethayaraja; R. Bandyopadhyaya, "Model for Core–Shell Nanoparticle Formation by Ion-Exchange Mechanism," *Industrial & Engineering Chemistry Research*, **2008**, *47*, 5982-5985.

- [54] K. Lambert; B. D. Geyter; I. Moreels; Z. Hens, "PbTe| CdTe core| shell particles by cation exchange, a HR-TEM study," *Chemistry of Materials*, **2009**, *21*, 778-780.
- [55] W. E. Doering; S. Nie, "Single-Molecule and Single-Nanoparticle SERS: Examining the Roles of Surface Active Sites and Chemical Enhancement," *The Journal of Physical Chemistry B*, **2001**, *106*, 311-317.
- [56] A. M. Schwartzberg; C. D. Grant; T. van Buuren; J. Z. Zhang, "Reduction of H₂AuCl₄ by Na₂S Revisited: The Case for Au Nanoparticle Aggregates and Against Au₂S/Au Core/Shell Particles" *The Journal of Physical Chemistry C*, **2007**, *111*, 8892.
- [57] A. M. Schwartzberg; T. Y. Olson; C. E. Talley; J. Z. Zhang, "Synthesis, characterization, and tunable optical properties of hollow gold nanospheres," *Journal Of Physical Chemistry B*, **2006**, *110*, 19935-19944.
- [58] S. E. Skrabalak; L. Au; X. M. Lu; X. D. Li; Y. N. Xia, "Gold nanocages for cancer detection and treatment," *Nanomedicine*, **2007**, *2*, 657-668.
- [59] S. Preciado-Flores; D. Wang; D. A. Wheeler; R. Newhouse; J. K. Hensel; A. Schwartzberg; L. Wang; J. Zhu; M. Barboza-Flores; J. Z. Zhang, "Highly reproducible synthesis of hollow gold nanospheres with near infrared surface plasmon absorption using PVP as stabilizing agent," *Journal of Materials Chemistry*, **2010**, *21*, 2344.

[60] R. J. Newhouse; H. Wang; J. K. Hensel; D. A. Wheeler; S. Zou; J. Z. Zhang, "Coherent Vibrational Oscillations of Hollow Gold Nanospheres," *The Journal of Physical Chemistry Letters*, **2011**, *2*, 228.

[61] W. Cai; H. Hofmeister; T. Rainer, "Surface effect on the size evolution of surface plasmon resonances of Ag and Au nanoparticles dispersed within mesoporous silica," *Physica E: Low-dimensional Systems and Nanostructures*, **2001**, *11*, 339-344.

[62] T. J. Norman; C. D. Grant; D. Magana; J. Z. Zhang; J. Liu; D. L. Cao; F. Bridges; A. Van Buuren, "Near infrared optical absorption of gold nanoparticle aggregates," *Journal Of Physical Chemistry B*, **2002**, *106*, 7005-7012.

[63] B. H. Jun; M. S. Noh; J. Kim; G. Kim; H. Kang; M. S. Kim; Y. T. Seo; J. Baek; J. H. Kim; J. Park, "Multifunctional Silver-Embedded Magnetic Nanoparticles as SERS Nanoprobes and Their Applications," *Small*, **2010**, *6*, 119-125.

[64] G. Goncalves; P. A. A. P. Marques; C. M. Granadeiro; H. I. S. Nogueira; M. Singh; J. Gracio, "Surface modification of graphene nanosheets with gold nanoparticles: the role of oxygen moieties at graphene surface on gold nucleation and growth," *Chemistry of Materials*, **2009**, *21*, 4796-4802.

[65] M. Suzuki; Y. Niidome; N. Terasaki; K. Inoue; Y. Kuwahara; S. Yamada, "Surface-enhanced nonresonance Raman scattering of rhodamine 6G molecules adsorbed on gold nanorod films," *Japanese Journal of Applied Physics*, **2004**, *43*, 554.

- [66] Q. Su; X. Ma; J. Dong; C. Jiang; W. Qian, "A reproducible SERS substrate based on electrostatically assisted APTES-functionalized surface-assembly of gold nanostars," *ACS Applied Materials & Interfaces*, **2011**,
- [67] P. Hildebrandt; M. Stockburger, "Surface-enhanced resonance Raman spectroscopy of Rhodamine 6G adsorbed on colloidal silver," *The Journal of Physical Chemistry*, **1984**, 88, 5935-5944.
- [68] R. Gupta; W. Weimer, "High enhancement factor gold films for surface enhanced Raman spectroscopy," *Chemical Physics Letters*, **2003**, 374, 302-306.
- [69] L. Maya; C. Vallet; Y. Lee, "Sputtered gold films for surface-enhanced Raman scattering," *Journal of Vacuum Science & Technology A: Vacuum, Surfaces, and Films*, **1997**, 15, 238-242.
- [70] J. I. Gersten, "The effect of surface roughness on surface enhanced Raman scattering," *The Journal of Chemical Physics*, **1980**, 72, 5779.
- [71] L. Vigderman; E. R. Zubarev, "Starfruit-Shaped Gold Nanorods and Nanowires: Synthesis and SERS Characterization," *Langmuir: the ACS journal of surfaces and colloids*, **2012**,
- [72] J. C. Tinguely; I. Sow; C. Leiner; J. Grand; A. Hohenau; N. Felidj; J. Aubard; J. R. Krenn, "Gold Nanoparticles for Plasmonic Biosensing: The Role of Metal Crystallinity and Nanoscale Roughness," *BioNanoScience*, **2011**, 1-8.

[73] K. Kneipp; H. Kneipp; I. Itzkan; R. R. Dasari; M. S. Feld,
"Ultrasensitive chemical analysis by Raman spectroscopy," *Chemical Reviews*, **1999**,
99, 2957-2976.

CHAPTER 8. Exciton Dynamics in Semiconductor Nanocrystals

8.1 Abstract

This review article provides an overview of recent advances in the study and understanding of dynamics of excitons in semiconductor nanocrystals (NCs) or quantum dots (QDs). Emphasis is placed on the relationship between exciton dynamics and optical properties, both linear and non-linear. We also focus on the unique aspects of exciton dynamics in semiconductor NCs as compared to those in bulk crystals. Various experimental techniques for probing exciton dynamics, particularly time-resolved laser methods, are reviewed. Relevant models and computational studies are also briefly presented. By comparing different materials systems, a unifying picture is proposed to account for the major dynamic features of excitons in semiconductor QDs. While the specific dynamic processes involved are material-dependent, key processes can be identified for all the materials that include electronic dephasing, intraband relaxation, trapping, and interband recombination of free and trapped charge carriers (electron and hole). Exciton dynamics play a critical role in the fundamental properties and functionalities of nanomaterials of interest for a variety of applications including optical detectors, solar energy conversion, lasers, and sensors. A better understanding of exciton dynamics in nanomaterials is thus important both fundamentally and technologically.

8.2 Introduction

Nanomaterials are the cornerstones of nanoscience and nanotechnology and are considered central to the future of research and development across many different scientific and engineering-based disciplines. What makes nanomaterials fundamentally fascinating is their unique physical and chemical properties and functionalities that can differ significantly from their corresponding bulk counterparts. Furthermore, semiconductor nanocrystals (NCs), also referred to as quantum dots (QDs), with spatial features on the order of a few nanometers exhibit a profound size-dependence of their optical and electronic properties due to quantum confinement effect.^[1-5] Additionally, due to the enormous surface-to-volume ratio, properties of nanomaterials are extremely sensitive to surface characteristics.^[6-9] Because of this, successful manipulation or modification of the surface of nanomaterials can aid in control of their properties. Therefore, having fine control over the size, shape, and surface characteristics of the nanomaterials is crucial for exploitation of their basic properties and various applications such as energy conversion,^[10-19] nanoelectronics,^[20-28] photonics,^[29-37] biological and chemical sensing,^[38-47] communication,^[48-53] catalysis,^[54-62] and environmental protection and remediation.^[63-68]

One of the most interesting and useful aspects of nanomaterials is their optical properties, including linear and nonlinear absorption and light scattering. The optical properties also have a strong dependence on shape and interparticle interactions.^[69-73] Measurement of the structural and optical properties of nanomaterials typically employs static techniques, *e.g.*, microscopy, UV-Vis, Raman, and several various X-

ray based techniques. These studies can provide important information regarding structure, size, shape, and surface. Complementary to static studies are dynamic studies of charge carriers that afford additional information about the fundamental properties of nanomaterials.^[74] Dynamic studies become especially useful in helping determine the lifetime of charge carriers or excitons and their associated relaxation pathways. For instance, dynamic information can help to gain fundamental insights into the effects of bandgap trap states due to both internal and surface characteristics.

Because the main focus of this article is on exciton dynamics and related optical properties of semiconductor nanomaterials, we will not provide any discussion on synthesis and structural characterization of nanomaterials that can be found in many excellent reviews and books.^[75-84]

In this review, we present an overview of recent research efforts on optical and dynamic properties of semiconductor NCs with a focus on exciton dynamics. Based on experimental results and modeling or situational data, we attempt to provide a consistent picture about the behavior of excitons and related charge carrier dynamics, which include electronic dephasing, intraband relaxation, charge carrier trapping, and interband recombination. Even though the time scale for the different dynamic processes are dependent on the specific semiconductor and quality of the sample due to variations on defects and surface characteristics, a general unifying model is proposed to account for the key processes involve with time scales identified for a number of materials that have been well investigated.

8.3 Optical Properties

8.3.1 Linear Optical Absorption and Emission

Upon the absorption of a photon of light by a semiconductor, an exciton is first created instantaneously. The excitonic properties are thus intimately related to optical properties. The optical absorption of semiconductors, determined by their electronic structure, is often used as a way to probe their optical and electronic properties. In particular, the aforementioned size-dependence has great effects on both the electronic absorption and photoluminescence (PL), especially when the particle size is smaller or comparable to the exciton Bohr radius. A decrease in particle size manifests itself as a blue-shift of the electronic absorption and PL spectra. This can be accounted for using the particle-in-a-sphere model for a spherical particle with radius R .^[85,86]

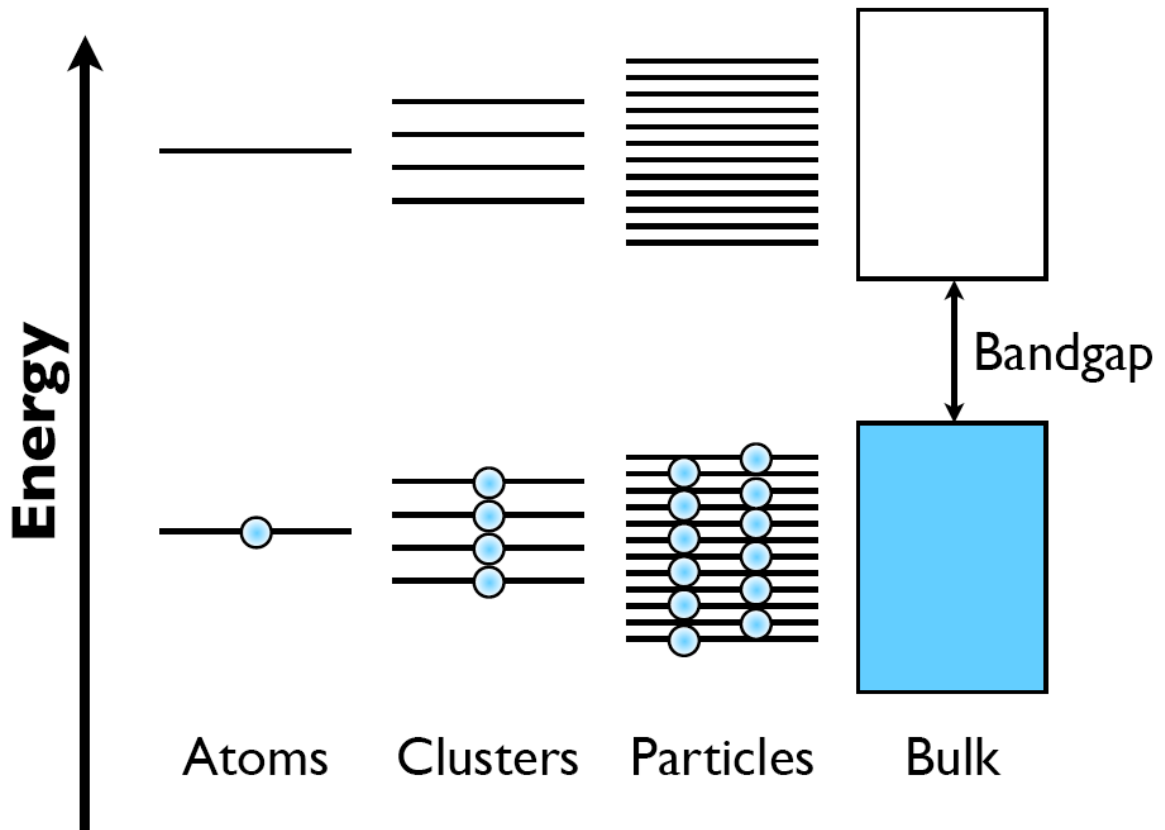
$$E_{g, effective}(R) = E_g(\infty) + \frac{\hbar^2 \pi^2}{2R^2} \left(\frac{1}{m_e} + \frac{1}{m_h} \right) - \frac{1.8e^2}{\epsilon R}; \quad (\text{Eq. 1})$$

where $E_g(\infty)$ is the bulk bandgap, m_e and m_h are the effective masses of the electron and hole, and ϵ is the bulk dielectric constant, also known as the relative permittivity. The second term on the right hand side shows the effective bandgap is inversely proportional to the square of the particle's radius and thus increases as the size decreases, while the third term on the right, due to Columbic attraction between the electron and hole, results in a decrease in the bandgap with increasing particle radius. However, the second term dominates for small R and thereby the effective bandgap increases with decreasing R . This is illustrated schematically in Figure 1, where the

effective bandgap is seen to increase with progressively larger structures, going from atoms to clusters to nanoparticles (or QDs), finally to bulk.

Quantum confinement results not only in an increase of the bandgap with a concomitant blue-shift of the absorption edge, but also alters the density of states (DOS) toward a more discrete distribution. The DOS variation with size can explain many phenomena including the size-dependence of electron-phonon coupling^[87] and carrier relaxation^[88,89] in nanostructured materials. This will be covered in greater detail in Section 3.

Figure 1. Illustration of the quantum confinement effect in different systems ranging from atoms to clusters to particles and finally to bulk materials.

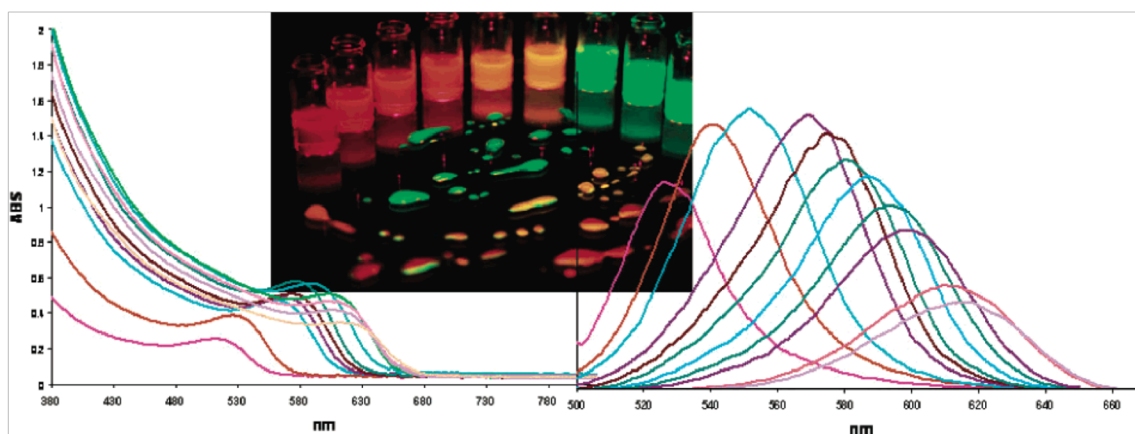


As mentioned, the quantum size confinement effect is most pronounced especially when the particle size becomes comparable to or smaller than the Bohr exciton radius, α_B , which is given by:

$$\alpha_B = \frac{\varepsilon_0 \varepsilon h^2}{\pi \mu e^2}; \quad (\text{Eq. 2})$$

where ε and ε_0 are the relative permittivity of the semiconductor and the permittivity of the free vacuum, respectively, μ is the reduced mass of the electron and hole, given as $m_e m_h / (m_e + m_h)$, and e is the electron charge. As an example, the Bohr radius of CdS is approximately 3.0 nm.^[90] For CdS particles that are smaller than 2.4 nm, noticeable blue-shifts in their optical absorption and PL spectra manifest relative to bulk.^[91] The same is true for other semiconductor QD systems when they approach sizes smaller than their respective Bohr radii, such as CdSe,^[92] CdTe,^[93] ZnS,^[94] ZnSe,^[95] and Si^[96]. Figure 2 shows the UV-Vis electronic absorption (left) and PL (right) spectra of differently-sized CdTe QDs.^[97] From left to right, the particle size increases and both the excitonic absorption peak and emission peak red shift. Such behavior holds true for nearly all semiconductor QDs.

Figure 2. UV-Vis (left) and PL spectra (right) of CdTe QDs capped with thioglycolic acid in aqueous solution. The spectra were taken from aliquots after 1 to 42 hours of refluxing. The photograph captures images of the QDs with sizes ranging from ~6 nm (left, red) to ~2.5 nm (right, green). Reproduced with permission from Ref. 97.



The UV-Vis absorption, plotted as absorption as a function of wavelength (left side of Figure 2), is a reflection of the strength of the electronic transition between the VB and the CB. For direct bandgap transitions, a strong excitonic peak is observable at slightly red-shifted wavelengths, or the low-energy area of the spectrum. This is due to electronic transitions from the VB to the excitonic state that is located just below the bottom of the CB. The energy difference between the bottom of the CB and the excitonic state is referred to as the electron-hole or exciton binding energy. Typically, this value is on the meV level and may be represented by the simple analytical equation:^[98]

$$E_b = \left[\frac{2}{\alpha - 1} \right]^2 E_0; \quad (\text{Eq. 3})$$

where α is an integer parameter that describes the degree of anisotropy of the interaction of the electron and hole, and E_0 is the effective Rydberg constant which is dependent upon the permittivities of both the QD and free space, the free electron mass, and the exciton reduced mass. Strictly speaking, this equation works for bulk materials. For example, the binding energy of bulk CdS is 28 meV.^[99]

The position of the exciton provides a reasonable estimate of the bandgap of the nanoparticle because of these steady state absorption considerations. For a direct bandgap transition, the absorption coefficient, α , is related to the incident illumination frequency by:^[100]

$$\alpha = A^* \sqrt{h\nu - E_g}; \quad (\text{Eq. 4})$$

where

$$A^* = \frac{q^2 x_{vc}^2 (2m_r)^{3/2}}{\lambda_0 \epsilon_0 \hbar^3 n}; \quad (\text{Eq. 5})$$

where ν is the light frequency, $h\nu$ is the photon energy, h is the Planck constant, E_g is the bandgap energy, A^* is a frequency-independent constant, m_r is the reduced mass of the electron and hole, q is the elementary charge, n is the index of refraction, ϵ_0 is the vacuum permittivity, and x_{vc} is a matrix element with units of length with values similar to the lattice constant. This equation is important since it is valid for light with a photon energy slightly larger than the bandgap and ignores other sources of absorption other than the VB-to-CB absorption, thereby providing a clear estimation of the size of the bandgap.

For indirect bandgap transitions, which require phonon assistance or change in the crystal momentum (k -vector), no noticeable excitonic peak appears in the spectrum. Rather, a smooth and monotonically increasing absorption with decreasing wavelength is usually observed. A well-known example of a material with an indirect bandgap is silicon.^[101]

Because no excitonic peak is overtly noticeable for indirect bandgap materials, any quantum confinement effects are less observable due to the lack of sharp or well-defined spectral peaks, making a reliable determination of the size of the QD difficult. Nevertheless, the intensity of the absorbance for QDs is known to follow Beer's law.^[102,103] Because normal QDs contain a few hundred or few thousand atoms, the absorption oscillator strength for one QD is proportional to the number of atoms in each QD.^[104,105] This has been verified with experiments that

have determined the molar absorptivity of various semiconductor QDs as a function of size.^[106,107]

Complementary to absorption spectroscopy, photoluminescence (PL) spectroscopy detects light emitted from an excited state to a lower energy state, *e.g.* from the CB to the VB, as a function of wavelength following excitation of the sample with incident light. In PL measurement of QDs, bandgap states can substantially affect the PL spectrum. As a result, PL spectrum can be used as a sensitive probe of bandgap states. For a typical nanoparticle sample, PL is often composed of both bandedge emission and trap state emission.^[74] For QD samples with a narrow size distribution, bandedge PL is often accompanied by a small Stokes shift from the excitonic spectral peak along with a narrow bandwidth, indicative that there is a narrow energy distribution of emitting states.^[108,109] In contrast, trap states, which are typically located within the bandgap, have a red-shifted emission relative to bandedge emission since the energy difference between the trap states and the VB is small.^[110-112] The bandwidth is also typically large, representative of the broad and varied nature of trap states within the bandgap.

It is possible to prepare high-quality samples that have mostly bandedge emission when the surface is well capped or passivated. For example, tri-*n*-octylphosphine oxide-(TOPO) capped CdSe show mostly bandedge emission and weak trap state emission, which is an indication of a high quality sample.^[112-114] Luminescence may also be enhanced by surface modification techniques^[115-119] or using core/shell structures.^[120-123] Nanoparticles that have been found to show strong

PL include CdSe, CdS, and ZnS.^[124-126] Other particles have generally been found to be weakly luminescent or even non-luminescent at room temperature, *e.g.*, PbS,^[127,128] PbI₂,^[129] CuS,^[130] Ag₂S,^[131] and silica-passivated Si nanowires.^[132] Two reasons account for the weak luminescence: an indirect nature of the semiconductor bandgap,^[133] which entails nonradiative recombination, or a high density of internal and/or surface trap states which act to quench the luminescence.^[132] Controlling the surface by removal of surface trap states can lead to significant enhancement of luminescence as well as the ratio of band-edge-over-trap state emission.^[134-139] This is an important consideration in using semiconductor NCs for applications that require a high luminescence yield, *e.g.*, lasers, light emitting diodes (LEDs), fluorescence imaging, and optical sensing. Additionally, PL usually increases with decreasing temperature, from both band-edge and trap states,^[140,141] due to a suppression of electron-phonon interactions which thereby increases the excited state lifetime of the electron.

Compared to zero-dimensional (0D) NCs or QDs, one dimensional (1D) nanostructures such as nanorods/nanowires typically show less dramatic changes in their optical properties due to weaker overall quantum confinement. The detailed changes depend on the chemical nature of the material and the exact dimensionality involved. For example, GaN nanorods have shown to have excellent band-edge PL efficiency with little trap state emission despite the nanorods being an average of 200 nm in diameter and several microns in length, which is much larger than the Bohr exciton radius of 11 nm.^[142] This likely had to do with the nanorods being hosted in

an aluminum matrix which helped increase the oscillator strength, thereby making the fluorescence peak associated with exciton recombination more intense than that associated with free carrier recombination.

8.3.2 Nonlinear Optical Absorption and Emission

Upon absorption of photons, excitons are formed. When the intensity of the incident light is strong enough, significant nonlinear effects manifest, which can have profound implications on exciton dynamics. We briefly discuss these nonlinear processes with respect to excitonic properties here.

Semiconductor NCs exhibit nonlinear optical properties at high excitation light intensities, including nonlinear absorption and saturation, shift of transient features, higher harmonic generation, and upconversion luminescence. Of these, the two most commonly observed nonlinear effects are absorption saturation and transient bleach shift at high intensities.^[143-147] For instance, nonlinear absorption events have been observed for nanowires of GaAs^[148] and porous Si.^[149] These nonlinear optical properties have been considered potentially useful for optical limiting and switching applications.^[150] The mechanism behind this is that the initially-absorbed photons bleach the absorption associated with one-phonon transitions and, subsequently absorbed photons can no longer be absorbed as the initial photons, resulting in overall less absorption when normalized to the number of photons or laser power as compared to linear absorption.

Harmonic generation is a nonlinear optical phenomenon in which photons with a multiple of the incident photon frequency can be generated. This is caused by nonlinear interaction of light with a material. While second harmonic generation (SHG) is common for materials with non-central symmetry, it is weak for NCs due to their near-central symmetry. For semiconductor NCs, third-order nonlinear optical properties are more easily observed.^[151-153] Not many studies have been performed on second-order nonlinearities since it is believed that the centrosymmetry or near-centrosymmetry of spherical nanoparticles reduces their first-order hyperpolarizability (β) to zero or near-zero. Using hyper-Rayleigh scattering, second harmonic generation in CdSe nanocrystals has been observed.^[154] The first-order hyperpolarizability per NC was found to have a particle size dependence, decreasing with radius size to 1.3 nm and increasing with further size reduction thereafter. The results are explained in terms of surface and bulk-like contributions. Comparable procedures have been employed for CdS nanoparticles for which the hyperpolarizability per particle (~ 4 nm mean diameter) was found to be on the order of 10^{-27} esu, which is large for solution species.^[155]

Third-order nonlinear optical properties are also accountable for phenomena including the Kerr effect and degenerate four wave mixing (DFWM).^[156] As an example, the third-order nonlinear susceptibility, $\chi^{(3)}$, ($\sim 5.6 \times 10^{-12}$ esu) for PbS nanoparticles has been established by means of time-resolved optical Kerr effect spectroscopy, from which it was found to be dependent upon surface modification.^[157] In addition, the third-order nonlinear behavior of porous silicon has

been determined by utilizing the Z-scan technique and found to be considerably augmented over crystalline silicon.^[150] DFWM analyses of thin films comprised of CdS nanoparticles found a substantial $\chi^{(3)}$ value ($\sim 10^{-7}$ esu) around the excitonic resonance at room temperature.^[158]

Anti-Stokes PL or PL upconversion is a different and intriguing nonlinear optical phenomenon concerning excitonic transitions. In contrast to Stokes emission, the energy of the emitted light is higher than that of the excitation light. This phenomenon has been observed for both doped^[159,160] and high-purity semiconductors.^[161,162] With regard to bulk, energy upconversion is characteristically accomplished by one of three processes: (i) Auger recombination, (ii) anti-Stokes Raman scattering mediated by thermally-populated phonons, or (iii) two-photon absorption.^[163,164] Such upconversion has been noticed in heterostructures and quantum wells^[165-171] and has been described as being based on either Auger recombination^[172] or two-photon absorption.^[173] Persistent intermediate levels are thought to be crucial for luminescence upconversion in heterostructures such as GaAs/Al_xGa_{1-x}As.^[174] Surface states have been proposed to play an important role in the upconversion in nanoparticles such as CdS and CdSe.^[175] For semiconductor QDs with three-dimensional (3D) quantum confinement, upconversion has recently been reported for CdS,^[176] InP,^[177] CdSe,^[175] InAs/GaAs,^[178] InGaN/GaN multiple quantum wells,^[179] ZnSe^[180], CdSeS,^[172] Er-doped CdS^[181] and lanthanide-doped NaYF₄.^[182]

Upconversion has also been studied in doped semiconductor NCs such as NaGdF₄ nanoparticles doped with any of trivalent Tb, Eu, Dy, or Sm ions.^[183] By doping the host material precisely at several different layers, efficient upconversion emission was observed through Gd-mediated energy migration. This was believed to be true due to one of the ions acting as a “migratory” ion which acted to extract the excitation energy from high-lying energy states, followed by random energy hopping through the migrator’s sublattice and trapping of the migrating energy by an activator ion (one of the trivalent ions). Furthermore, by generating a core-shell NaGdF₄-NaGdF₄ structure, the elimination of quenching cross-relaxation was achieved. This was because the ⁶P_{7/2} excited state of Gd³⁺ and the ground state of Gd³⁺ are separated by a large energy gap, leading to a minimized energy loss caused by multiphonon emission, which had been observed elsewhere.^[184]

8.4 Charge Carrier Dynamics

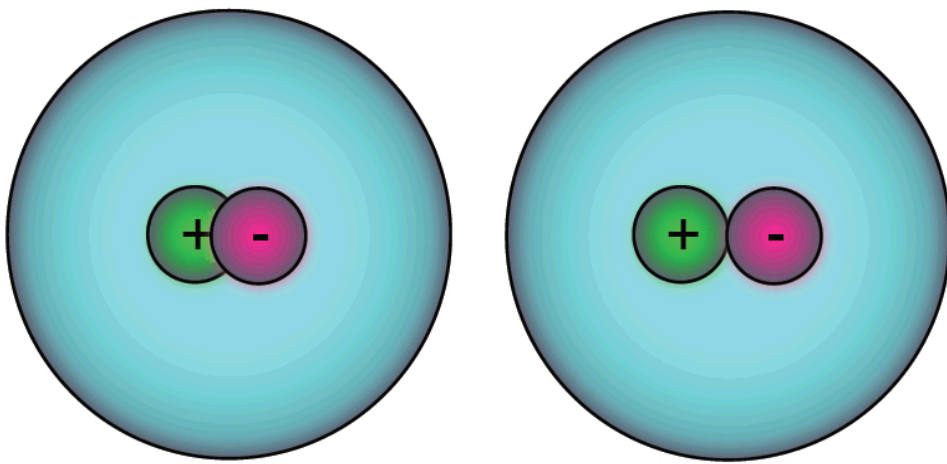
8.4.1 Basic Properties of Excitons

An exciton in a semiconductor is an electron and hole pair with associated Coulombic attraction. When treated quantum mechanically in a manner similar to that of the hydrogen atom, the exciton binding energy is given by:

$$E_{ex} = -\frac{13.6 \mu / m_e}{\left(\frac{\epsilon}{\epsilon_0}\right)^2 n^2} eV; \quad (\text{Eq. 6})$$

where μ is the reduced effective mass of the exciton, m_e is the free electron mass, $\varepsilon/\varepsilon_0$ is the relative dielectric constant of the material with ε being the dielectric constant of the material and ε_0 being the permittivity of free space, n is the quantum number with $n = 1$ being the ground state. When $n = \infty$, E_{ex} will be zero, and the exciton dissociates or is unbound and therefore the electron and hole are free. It should be noted that the treatment surrounding Eq. 6 applies to Mott-Wannier excitons, as opposed to Frenkel excitons, since the Mott-Wannier type are the most encountered type in semiconductors and nanomaterials while Frenkel excitons typically have much larger binding energies, on the order of 0.1 to 1 eV. An illustration of strongly and weakly bound excitons in a semiconductor nanocrystal is shown below in Figure 3:

Figure 3. Schematic illustration of a strongly-bound (left) and weakly-bound (right) photogenerated exciton in a semiconductor NC.



The exciton binding energy for most bulk semiconductors is in the range of a few to a few tens of meV for Mott-Wanier excitons. As examples, E_{ex} for GaAs is 4.6 meV for the ground state^[185] and 28 meV for CdS.^[186] As a point of comparison, the ground state of the hydrogen atom lies 13.6 eV below the energy for the free electron and proton. Therefore, the exciton binding energy is usually small and is comparable to the thermal energy, kT , at room temperature, which is approximately 25 meV. This thermal energy has to be counterweighed against the Coulombic attraction, given as:^[187]

$$E_c = \frac{e^2}{4\pi\epsilon_r\epsilon_0 r}; \quad (\text{Eq. 7})$$

where e is the elementary charge, ϵ_r is the relative dielectric constant of the surrounding medium, ϵ_0 is the permittivity of free space, and r is the electron-hole separation. As can be seen, the Coulombic attraction energy becomes larger for smaller dielectric constant. The general rule of thumb is that E_{ex} is a few tens of meV for inorganic semiconductors. As a result, most excitons easily dissociate at room temperature. Therefore, the excitonic state is often considered the same as the CB edge at room temperature. Should the thermal energy be lower than the binding energy of the photogenerated excitons, the excitons should be bound. One way to gain fundamental insight into the exciton dynamics is to probe its lifetime directly with time-resolved laser techniques.

8.4.2 Ultrafast Times-Resolved Laser Techniques

The study of exciton dynamics in semiconductor NCs allows for a deeper understanding of their fundamental properties by providing information that is complementary to that from static measurements. This can in turn guide the design, synthesis, and implementation of nanomaterials for a wide variety of applications, such as photocatalysis, photoelectrochemistry, and photovoltaics.

Due to the relatively short lifetime of excitons, it is necessary to use ultrafast laser techniques in order to probe or monitor directly their lifetime and associated relaxation or recombination processes. Advancements in ultrafast laser technology and different monitoring methods based on transient absorption or time-resolved fluorescence over the last two decades has made it relatively easy to study exciton dynamics.^[88,188-190] Due to the complex nature of NCs, the interpretation of dynamics data is not as straightforward as experimental measurements. However, consistent and clear pictures about exciton dynamics are slowly emerging. One commonly used time-resolved laser technique is transient absorption (TA). In TA measurements, a short, usually femtosecond (fs) duration optical pulse (the pump) excites the sample and, after a temporal delay, a second, less powerful short pulse (the probe) is used to monitor the excited population of charge carriers. Changes in the detected signal of the probe pulse, with the accompanying time delay, provide information of the dynamics of the excited carriers being probed.^[188] Because the assignment of the observed signal is complex, the determination of the origin of the TA signal is often accompanied by careful control experiments and other information, *e.g.*, theoretical modeling and simulations. Because the temporal resolution is determined only by the

cross-correlation of the pump and probe pulses, TA measurements provide high temporal resolution that few other techniques can afford. Due to its versatility and its ability to study both films and solutions, TA has been used to study many systems, including metal nanoparticles,^[191-193] semiconductor NCs,^[127,132,194] and metal oxide nanomaterials.^[195-197]

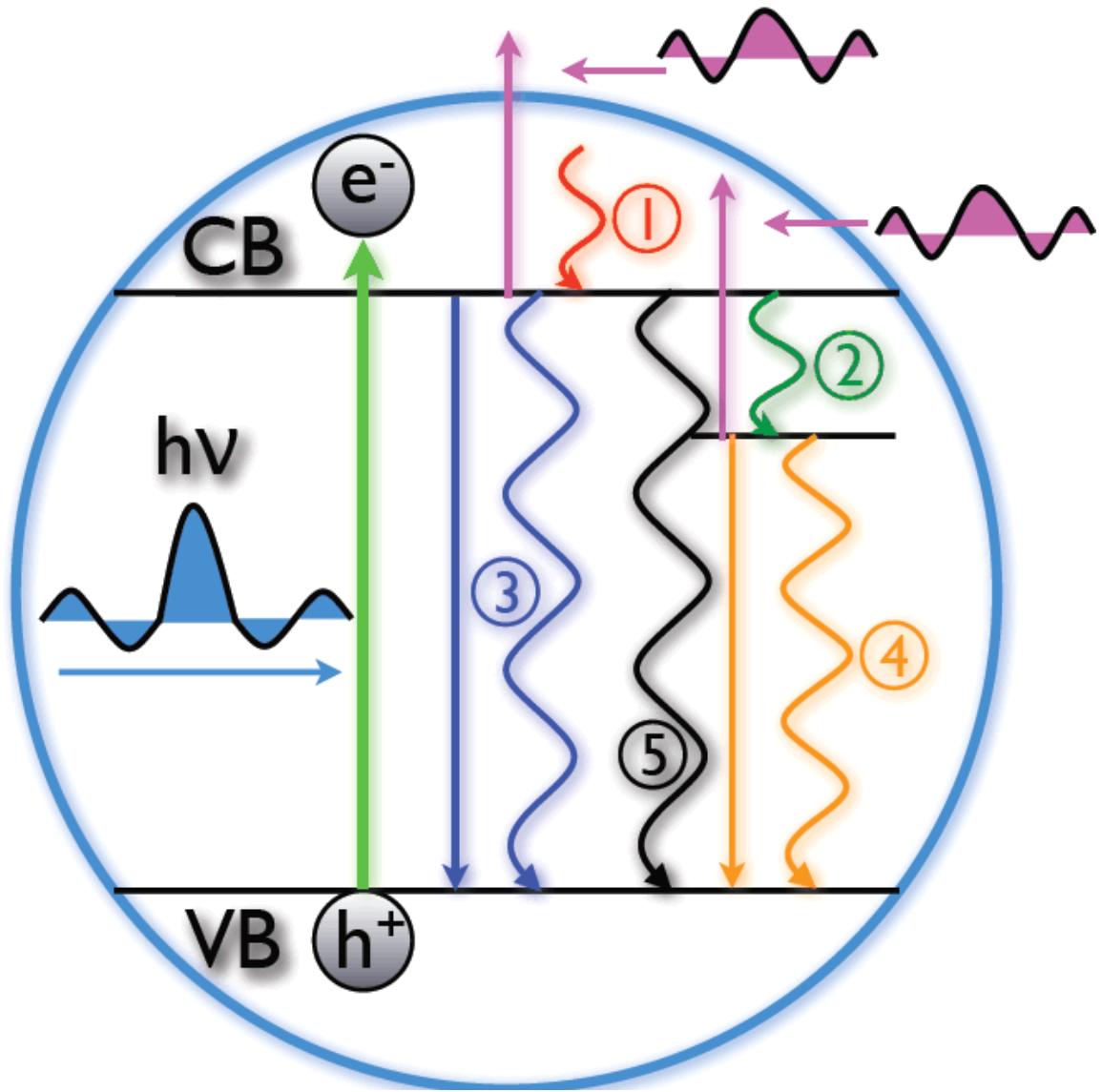
Another technique that is often utilized is time-resolved photoluminescence (PL) measurements.^[198-200] In time-resolved PL, the excitation mechanism is similar to that of TA, although the monitoring of the excited population is different. Instead of monitoring the excited state population with a probe pulse, the time profile of the PL is monitored directly with a photodetector, *e.g.*, a photomultiplier tube (PMT), photodiode, or charge-coupled device (CCD). In these cases, the temporal resolution is limited by the detector, which is often much longer (ps or ns) than the excitation laser pulse. For example, in time correlated single-photon counting (TCSPC), the instrument's resolution is on the order of 25 ps with an instrumental deconvolution lifetime of a few ps. Other methodologies exist, involving luminescence upconversion,^[172] time-resolved photoelectron spectroscopy,^[201] time resolved fluorescence,^[202] four-wave mixing,^[203] and terahertz time-domain spectroscopy.^[204]

8.4.3 Exciton Dynamics

Dynamic processes in semiconductor NCs are generally more complex than in the bulk due to the presence of many bandgap states. These bandgap states are often referred to as surface states or trap states. In a perfect nanocrystal, no such trap states

would exist. However, in real semiconductor NCs, bandgap states are practically impossible to totally avoid, partly due to the intrinsic surface states or dangling bonds. Bandgap states can be harmful or useful, depending on the application of interest. For example, bandgap states often result in quenched photoluminescence, which is undesirable for luminescence applications.^[205] On the other hand, bandgap states can be active and useful for catalytic applications.^[62] Bandgap states are sometimes introduced intentionally for a specific purpose, such as those in doped semiconductors for phosphor applications. As long as the exciton is concerned, presence of bandgap states can significantly alter its dynamics. Some of the key and general dynamic processes are summarized in Figure 4, for which an explanation is offered in the subsequent paragraphs.

Figure 4. Illustration of key dynamic processes in a QD and related pump-probe transient absorption measurement. The excitation or pump is represented as a green arrow and the probe is represented as fuchsia-colored arrows. Different dynamic processes shown include: (1) electron relaxation through electron-phonon coupling within the conduction band (a similar process occurs for the hole in the valence band) following excitation across the bandgap, tens to hundreds of fs; (2) trapping of electrons/holes into trap states due to defects or surface states, hundreds of fs to tens of ps; (3) radiative and nonradiative bandedge electron-hole (or exciton) recombination, tens of ps; (4) radiative and nonradiative trapped electron-hole (or relaxed exciton) recombination, hundreds of ps to a few ns; and (5) nonlinear and nonradiative exciton-exciton annihilation, hundreds of fs to tens of ps.



In the simplest case, above-bandgap excitation with light produces an exciton: an electron in the CB and a hole in the VB, both of which are bound to each other by the forces of Coulombic attraction. Initially, electronic dephasing occurs, which happens on a time scale of a few to a few tens of fs.^[206] Should the electron and hole have excessive kinetic energy, they then undergo intraband relaxation, with the electron relaxing to the bottom of the CB and the hole to the top of the VB.^[207] This relaxation occurs because of electron-phonon interactions and occurs on the time scale of several tens to hundreds of fs. Once the electron reaches the bottom of the CB and hole relaxes to the top of the VB, they may radiatively recombine thereby producing PL through the emission of a photon.^[208] Conversely, the electron and hole can recombine nonradiatively which most usually produces heat.^[209] A near-perfect or high quality NC, which has a very low trap state density, will primarily experience radiative recombination. In this case, the PL quantum yield is very high and the relevant lifetime for a direct bandgap semiconductor is typically on the order of a few to a few tens of ns.^[74] In principle, the hot electron and hole (before relaxing to the bandedges) can also recombine radiatively or non-radiatively, however, the probability is usually very low.

In typical NCs with a relatively higher density of bandgap states, trapping of electrons or holes into these states becomes important and occurs on a time scale of a few ps to a few tens of ps. The time scale for trapping of charge carriers is thus usually faster than that for bandedge radiative recombination.^[102] A typical

consequence of a high density of trap states is that the bandedge PL will be decreased and the overall PL yield is often low.^[210]

Following trapping, charge carriers can either undergo additional trapping, *e.g.*, from shallow traps to traps deeper in the bandgap) or recombine radiatively or nonradiatively. The time scale for further trapping depends strongly on the nature of the trap states involved and can be from a few ps to hundreds of ps.^[211] The lifetime of the charge carries in deep trap states can be very long-lived, from hundreds of ps to ns^[211] or μ s, or even longer.^[212] Should recombination from trap states be radiative, red-shifted PL (relative to bandedge PL) may be observed. Because of this spectral difference, trap state PL can be easily differentiated from bandedge PL. For dipole-forbidden or indirect bandgap transitions, the lifetime can be as long as a few ms.^[213]

The aforementioned scenarios apply to low excitation intensities, where NCs will have, on average, one exciton produced per particle. Quantitatively, one can relate the observed lifetime of a given state, τ_{ob} , to the radiative and nonradiative lifetimes, τ_r and τ_{nr} , respectively by the equation:

$$\frac{1}{\tau_{ob}} = \frac{1}{\tau_r} + \frac{1}{\tau_{nr}}; \quad (\text{Eq. 8})$$

for which the lifetimes are related to the PL quantum yield, Φ_{PL} , by:

$$\Phi_{PL} = \frac{\tau_{ob}}{\tau_r}; \quad (\text{Eq. 9})$$

Here, the radiative lifetime is similar to the observed lifetime only if the nonradiative lifetime is very long or if the PL quantum yield is close to 100%, as is the case for perfect single crystals. In general, the observed lifetime contains

contributions from both radiative and nonradiative lifetimes. Based on Equations 8 and 9, one can calculate the radiative and non-radiative lifetimes once the observed lifetime and fluorescence quantum yield are measured. It should be noted that Equations 8 and 9 apply only to the two states that are involved in PL emission transition.

8.4.3.1 Electronic Dephasing

As the fastest event in dynamics, electronic dephasing is known to occur on a time scale of only a few fs and is typically measured by spectral hole burning techniques^[214,215] or photon echo experiments.^[216-218] Electronic dephasing (electron-electron scattering) is considered as a dynamic process in which the energy is conserved while momentum is changed. Thus, the electronic dephasing following electronic excitation by light absorption is due to electron-electron interaction or scattering. For semiconductor NCs, the line width of the observed bandgap transition can be described by a damping constant, Γ , which is dependent upon the dephasing time, T_2 , which is predicated by the excited state lifetime, T_1 , and the pure dephasing time T_2^* . In the notable example of a two-level system that is coupled to a harmonic bath in the Markovian limit, the coherence diminishes with the total dephasing rate of:^[219,220]

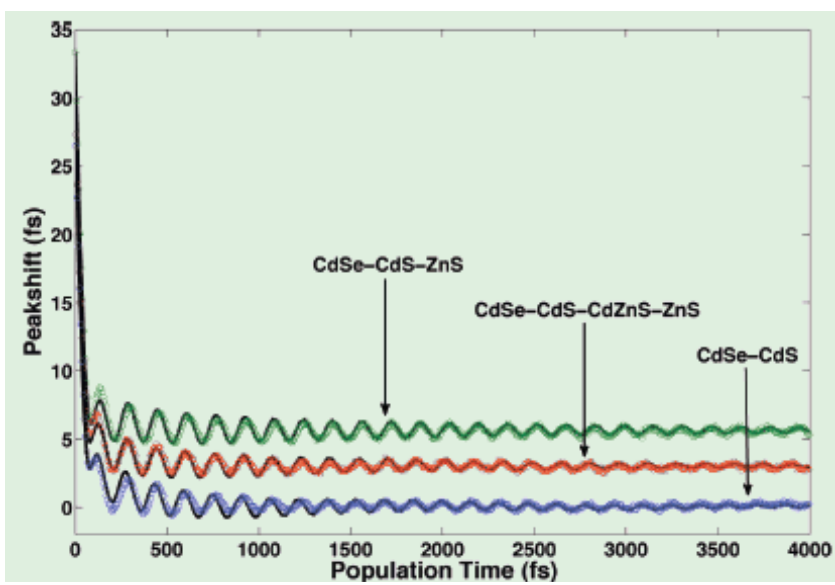
$$\Gamma = \frac{1}{T_2} = \frac{1}{T_1} + \frac{1}{T_2^*}. \quad (\text{Eq. 10})$$

Hole burning techniques have been applied to examine the homogeneous line widths and shapes of an assortment of semiconductor nanoparticles, including CdSe,^[221] CdS,^[222] CdTe,^[223] GaAs,^[224] and porous Si.^[225] The hole burning studies concluded that the quantum confinement of carriers and the strong Coulombic interplay between confined and trapped carriers is necessary for energetic changes as reflected in the spectral hole burning phenomenon.^[214] Hole burning has likewise been exploited to determine the dephasing time of CdSe nanocrystals for which the energetic dependence in the gain region was found to be unvarying for nanocrystals while increasing toward the transparency point for bulk-like samples.^[226]

The electronic dephasing times in CdSe^[216,227] and GaSe^[228] nanocrystals have been measured using time-resolved photon echo experiments. In the case of CdSe,^[216] the dephasing times were related closely with size, with 2 nm NCs dephasing in 85 fs, while larger (4 nm) CdSe NCs dephased in 270 fs. From this, a size-dependence on electronic dephasing can be inferred. Additionally, the dephasing times can be affected by trapping of the electronic excitation due to surface states which increases with increasing size and coupling of the excitation to low-frequency vibrational modes, which peak at intermediate size.^[217] Acoustic phonons tend to be contributing parameters, and govern the homogeneous line width at room temperature.^[216] Figure 5 below is a plot of the three pulse photon echo signal for capped CdSe quantum dots. For this example, the excitation wavelengths were chosen such that the lowest energy transitions were excited, which, for these examples, correspond to 620, 616, and 614 nm, respectively. The quantum beats

resulting from the vibrational contributions are obvious. Fourier transforms of the beating resulted in a low-frequency oscillation attributed to longitudinal acoustic modes.

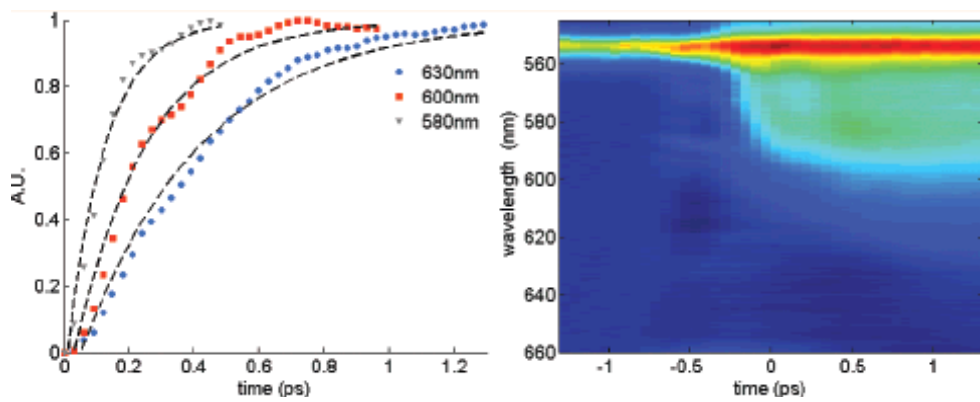
Figure 5. Peak shift data for CdSe-CdS, CdSe-CdS-CdZnS-ZnS, and CdSe-CdS-ZnS as labeled (circles). Also shown are the simulations of the data (solid lines). Reproduced with permission from Ref. 227.



8.4.3.2 Intraband Relaxation

When a semiconductor NC is illuminated with light with enough energy to photoexcite above the bandgap, the electron and/or hole are imparted with excess kinetic energy. The electron can quickly release the excess kinetic energy through electron-phonon interaction and relax to the bottom of the CB while the hole can release the kinetic energy and relax to the top of the VB. Typical time scales for this intraband relaxation are extremely fast, usually a few tens or hundreds of fs.^[229-231] Intraband hot carrier relaxation has been reported in a number of semiconductor nanomaterials, including CdSe with ZnS capping,^[232] PbSe,^[233] GaSe,^[234] Ge nanowires,^[235] CdTe,^[236] Te-doped CdSe,^[237] and many others. For example, in Te-doped CdSe, intraband relaxation was observed. The data collected revealed a fast component lifetime of ~0.3, ~0.4, and ~0.5 ps for QDs with radii of ~2, ~1.7, and ~1.4 nm, respectively. The fast time constants were assigned to intraband recombination following photoexcitation across the bandgap. Figure 6, below, shows the intraband relaxation of Te-doped CdSe nanoparticles where the population dynamics for three different energies across the TA spectrum is presented. The decaying exponent of each energy at $E_{BE} - E$, where E_{BE} is the bandedge excitation absorption energy, is plotted: $E_{BE} - E = 80$ meV (gray triangles), $E_{BE} - E = 170$ meV (red squares), and $E_{BE} - E = 255$ meV (blue circles). These differences correspond to the energetic distance from the bandedge. For the $E_{BE} - E = 255$ meV case, the 255 meV value corresponds to a defect emission center, while the $E_{BE} - E = 80$ meV case represents excitation close to the bandedge.

Figure 6. Rising population (left) probe wavelengths of 580 nm (gray triangles), 600 nm (red squares), and 630 nm (blue circles) for a 1.7 nm sample. False-color image (right) of the relaxation kinetics of the Te-doped CdSe nanoparticles. Reproduced with permission from Ref. 237.



Bandgap trap states can have a strong effect on intraband relaxation. This effect is two-fold: (1) the surface phonon frequencies and distribution are expected to change relative to bulk, thereby affecting the overall electron-phonon interaction and thus primarily the intraband relaxation time; and (2) surface trap states within the bandgap can compete with intraband relaxation by trapping the charge carriers. This has been seen before with CdSe nanoparticles.^[238,239] This is because competing processes, such as $1P_e$ -to-trap state charge transfer can occur which can act to shuttle electrons between the $1P_e$ state and lower-lying states. These defect-assisted relaxations are thus no longer simply intraband relaxations, but rather are a hybrid of intraband relaxation and trapping.

8.4.3.3 Charge Carrier Trapping

Because of the large surface-to-volume ratio of QDs, a high density of surface states due to defects and dangling bonds are created which may lie within the bandgap energetically and act to trap charge carriers following photoexcitation. As a result, charge carrier trapping can play a vital role in the relaxation processes of photoexcited carriers. Trapping is usually a very fast event, on the time scale of a few hundred fs to tens of ps. Factors that influence the trapping time include the DOS and energetic location of trap states within the bandgap.

One intensively-studied system with regard to trapping is CdS QD. A previous study has suggested a trapping time of ~ 30 ps for the electron and 1 ps for the hole based on time-resolved PL measurements^[240-242]. In a recent study, Wu *et al.*

investigated the ultrafast charge separation that occurs when CdS nanorods were capped at one end by a Pt nanoparticle.^[243] An unusually long-lived (μs) charge-separated state observed was attributable to ultrafast hole trapping (~ 0.7 ps) within the CdS nanorods. In studying the decay of the trap-state emission as well as that of the exciton bleach and the photoinduced absorption, they found that the primary decay pathway of photoexcited electrons was through recombination with trapped holes in the CdS. Upon forming a junction with the Pt nanoparticle, the transient bleach spectra of the CdS-Pt system decayed significantly ($\sim 90\%$) while the photoinduced absorption signal remained largely unchanged over the first 100 ps. The decay of the transient bleach signal is taken as an indication of the depopulation of excited electrons without the removal of trapped holes.

Core-shell materials involving CdS are also gaining traction. For example, Yan *et al.* conducted a spectroscopic investigation of CdTe and CdTe-CdS nanocrystals.^[244] For air-exposed CdTe, it is thought that the Te atoms react with ambient oxygen to generate traps for one or both of the excited carriers (electrons or holes), where the air-exposed CdTe displays a consistently faster lifetime following above-bandgap, 400 nm excitation, as opposed to its argon-protected counterpart system. For argon-protected CdTe cores, the charge carriers became trapped within 32 ps. This is an order of magnitude slower than that of the air-exposed CdTe sample, in which trapping occurred within 2.6 ps. In order to study the effect of how altering the surface of the CdTe might affect trapping times, the CdTe cores were passivated with a CdS shell. Upon passivation of the CdTe core with a CdS capping

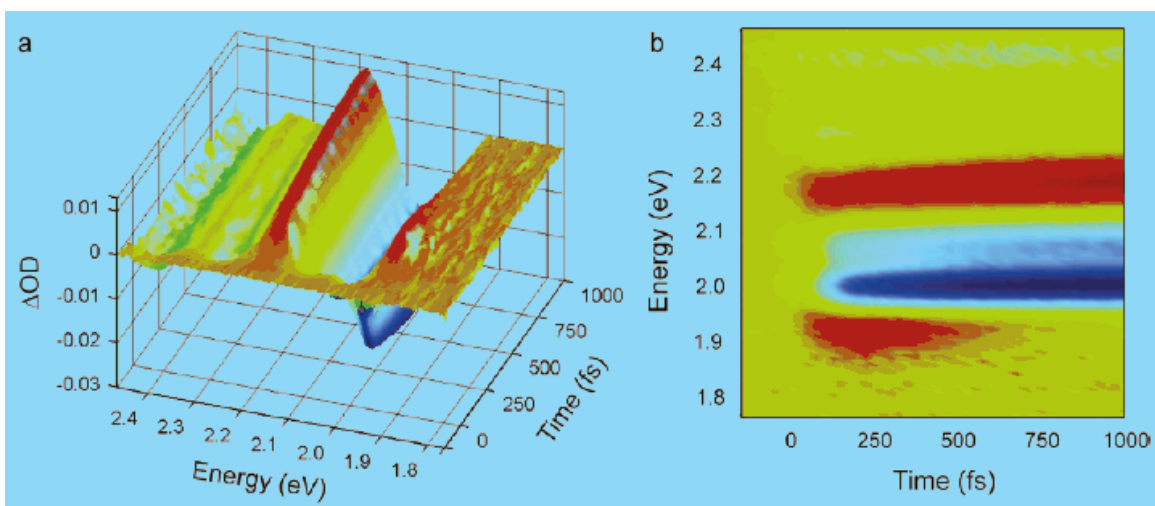
layer, the decay of the QDs was seen to mimic closely that of the argon-protected CdTe cores, regardless of whether the core-shell QDs had been exposed to air or argon. This finding supports the notion that direct binding of oxygen to the CdTe surface is necessary for trapping, likely into shallow trap states, which has a strong influence on the overall rate of recombination. Further, the fact that the CdTe-CdS NCs have very similar kinetics to argon-protected CdTe, regardless of whether the core-shell QDs were exposed to argon or air, is considered as proof that the CdS passivating layer is effective in quenching trapping.

8.4.3.4 Interband Electron-Hole Recombination

Electron-hole recombination can occur either before or after the electron and hole become trapped but usually follow electronic dephasing and intraband relaxation. Because trapping is typically a very fast process, as discussed above, the majority of the recombination takes place after one or both of the charge carriers are trapped. This is particularly true for QD samples that have a high density of trap states. For example, in the study of CdSe QDs studied by pump-probe TA, dephasing and initial intraband recombination were followed by trapping.^[245] Analysis of the data revealed three lifetimes of ~ 200 fs, ~ 1 ps, and ~ 30 ps. In particular, the third component was assigned to interband electron-hole recombination. Representative data are shown in Figure 7.^[245] In the figure, both TA and bleaching signals are observed to first grow in and then decay over time. Following the pump pulse, the continuum probe monitors, in order, the dephasing and initial interband

recombination. Following those events, interband transitions from ~ 520 nm to 690 nm are monitored by the probe pulse, which represent electron-hole recombination.

Figure 7. Representative femtosecond pump-probe TA spectra of colloidal CdSe QDs in dispersion. Here, the continuum probe monitors the interband transitions in the visible. Reproduced with permission from Ref. 245.



Another example of CdSe interband recombination using TA has shown a fast ~ 1 ps component and a long-lived component of >200 ps.^[246] While the ~ 1 ps component was assigned to intraband relaxation, the ~ 200 ps component was assigned to a phonon-assisted nonradiative interband relaxation also termed the “phonon bottleneck.” While this long-lived ~ 200 ps component assigned to interband recombination is approximately $10\times$ longer than the previous example given in this section, that difference could plausibly be related to a much lower density of trap states in this CdSe system. The overall observed interband recombination rate is expected to be strongly sensitive to the density of trap states because the nonradiative decay rate is highly dependent on the density of trap states. Because of that, semiconductor NC systems with a (relatively) lower density of trap states will experience a slower overall interband relaxation.

Studies on 2.5-6 nm Si NCs have also shown, for example, that interband recombination can be directly measured since red-shifted trap state PL is observed upon emission of photons from traps.^[247] In that study, a sub-10 ps relaxation was monitored and attributed to efficient surface trapping potentially due to a very high density of trap states. Another study utilizing PL involving Si NCs was performed to inspect recombination.^[248] In this study, the Si crystallite sizes were also found to be 3-5 nm. An intense luminescence with a lifetime of ~ 100 ps was observed and was assigned to direct interband recombination mediated by a low density of trap states. Since both studies focused on similar-sized crystallites of the same material, the

difference in interband recombination lifetimes may be ascribed to trap state density, as explained in previous paragraphs.

Particle shape may affect interband relaxation for certain materials. For example, the shape dependence of interband relaxation in CdSe QDs *vs.* NRs has been studied.^[249] The QDs in the study were observed to have a double exponential decay of 2.2 and 33 ps at a probe wavelength of 550 nm, for which the 33 ps time was attributed to interband recombination. For the same probe wavelength, the NRs were found to have a double exponential of 4.3 and 43 ps. In other words, the NRs had an interband recombination time that was 10 ps longer than that of the QDs. One potential reason for the difference is that there is less effective surface trapping in the rods than in the QDs due to the rods having a higher overall surface area. However, for PbS NCs, no noticeable change in relaxation dynamics was observed for changing particle shape (NPs *vs.* NRs).^[128] For both systems, an analysis of the data revealed a double exponential decay of 1.2 and 45 ps which was independent of both probe wavelength and pump intensity. In particular, the 45 ps decay was attributed to interband electron-hole recombination mediated by trap states which lay energetically within the bandgap. The independence of the relaxation due to shape was attributed to the dominant surface effects on electron relaxation. From these studies, it seems that the shape-dependence is strongly coupled with and manifests as surface effects. If the dynamics are sensitive to surface characteristics, a shape change may not elicit a large change in the dynamics.

Another, more recent study which investigated the shape-dependence of interband relaxation centered on CdS nanospheres *vs.* nanorods and nanotriangles.^[250] In the study, stretched exponentials were used to analyze the relaxation following a 375 nm excitation, and it was found that for the nanospheres, nanorods, and nanotriangles, the average lifetimes decreased by an order of magnitude, from 13.63 to 3.95, to 2.96 ns, respectively. In an effort to understand this phenomenon more cohesively, a stochastic model was used to determine the number of trap states which directly affected the lifetime. It was found that the number of trap states within the bandgap increased from 11.2 to 21.9 to 34.5 for the nanospheres, nanorods, and nanotriangles, respectively. Because the number of trap states increased, so did the average lifetime decrease as did the overall PL quantum yields.

8.4.4 Nonlinear Exciton Dynamics

When one increases sufficiently the intensity of incident light upon a semiconductor NC, nonlinear absorption and emission characteristics manifest, as discussed in Section 2.2. These nonlinear properties are also evident in time-resolved studies and can be closely monitored and studied. Upon the generation of a high density of excited charge carriers or excitons, the likelihood of observing nonlinear dynamical processes such as Auger recombination or exciton-exciton annihilation becomes high. These processes are higher order kinetic processes in comparison to linear processes discussed above. The overarching conclusion that may be drawn from nonlinear processes is that fast and nonradiative decays are seen to occur,

thereby reducing the overall charge carrier lifetime^[251] and luminescence quantum yield.^[252]

A hallmark of nonlinear behavior is the photogeneration of multiple excitons within the same spatial region at the same time, leading to the strong interaction of excitons. This is typically evidenced as a dynamic process that depends nonlinearly (*i.e.* superlinearly or higher) on the excitation light intensity.^[88,127,132,139,253-255]

Several explanations have been put forth to explain the observation of nonlinear dynamical behavior in semiconductors, including higher order kinetics, Auger recombination,^[256] and exciton-exciton annihilation.^[257] Exciton-exciton annihilation is favorable for some since Auger recombination requires ionization despite the fact that most time-resolved studies do not provide incontrovertible evidence that this occurs to any great degree. On the other hand, Auger recombination is favored by others since it originates from solid state materials theory,^[238] since the threshold energy of Auger recombination is governed by the conservation laws of energy and momentum, the threshold calculations become quasi-classical and are much easier than a quantum mechanical probability calculation.^[213]

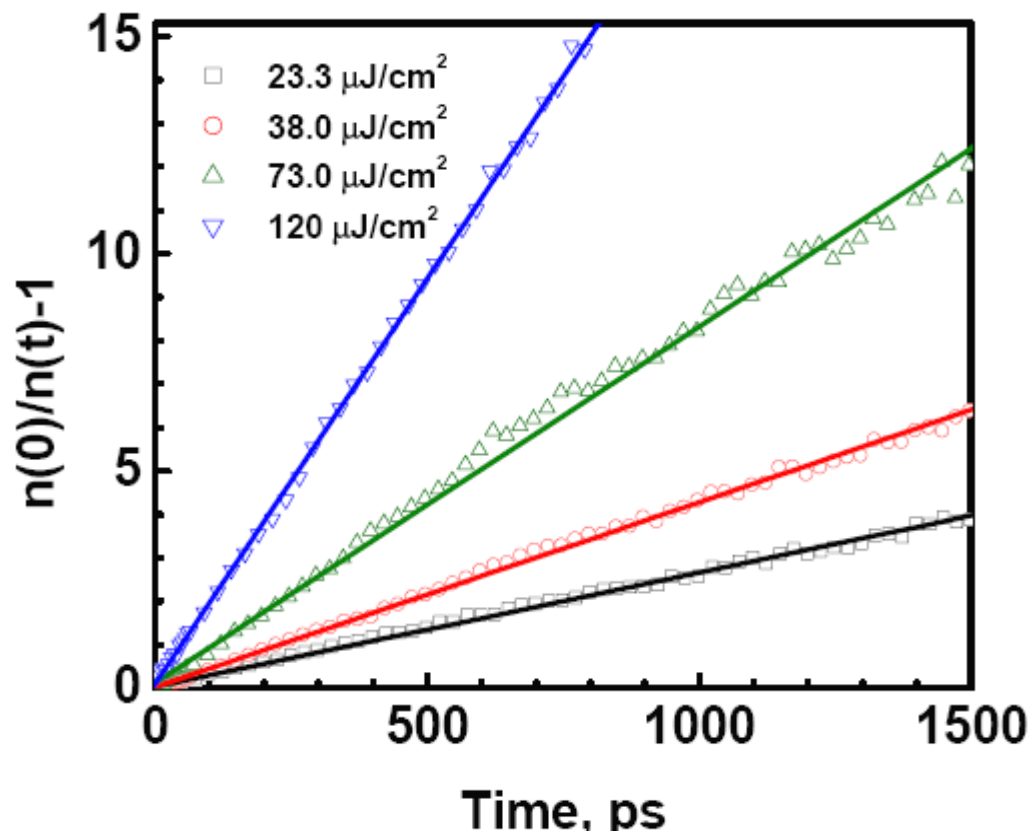
In the exciton-exciton annihilation model, a high excitation intensity for the pump pulse produces multiple excitons per particle that can interact and annihilate, resulting in one exciton excited and another one which is de-excited. If trapping occurs at a higher rate than that of exciton-exciton annihilation, trapping will reduce the likelihood of exciton-exciton annihilation. However, if the trap states become

saturated, exciton-exciton annihilation can occur. Because of this, surface considerations for the particle become important. Nanoparticles which have a higher density of trap states can be expected to have a higher threshold for observing exciton-exciton annihilation or will require a higher pump laser intensity to observe this nonlinear process. Additionally, should the pump pulse have a photon energy in excess of the bandgap, the initial photogenerated exciton will not result in the electron and hole being at bandedge positions initially. In other words, the origin of the TA signal is likely to be from higher excited states or higher energy levels within the VB and CB. Although, at this point, the electron has kinetic energy in excess of what is needed for pumping to the bandedge, direct discernment of the transition involved is not easy without detailed knowledge of the electronic band structure. It should be noted that this statement is true for any QD system in which exciton-exciton annihilation is implied.

The exciton-exciton annihilation process has been demonstrated clearly in CdSe.^[258] In this study which utilized pump-probe transient absorption, nonlinear effects in the initial decay of the CdSe was observed. An analysis of the data revealed fast component decays of 357, 231, 121, and 47 ps for pump fluences of 23.3, 38.0, 73.0, and 120 $\mu\text{J}/\text{cm}^2$. These fast component decays, which were seen to become progressively faster with increasing pump fluence, were attributed to bimolecular (exciton-exciton) annihilation of photogenerated excitons. A plot of the exciton density as a function of time at various pump fluences, with a slope of the Auger constant (recombination probability), is shown below in Figure 8. As can be

seen, the recombination time becomes progressively smaller for increasing pump fluences. Above the $23.3 \mu\text{J}/\text{cm}^2$ level, the dynamics adopt a second-order behavior, signifying that the nonlinear regime has been realized.

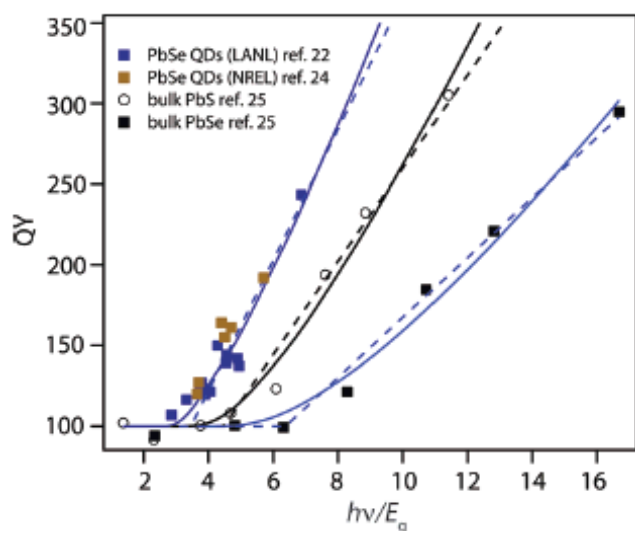
Figure 8. A plot of exciton density as a function of time for CdSe NCs. At low pump fluence (grey squares) the overall recombination time is relatively slow. However, upon gradually increasing the excitation energy, the recombination is observed to become progressively faster, indicating nonlinear recombination. Reproduced with permission from Ref. 258.



Care needs to be taken when assigning exciton-exciton annihilation as a potential process. When differently sized or shaped nanoparticles are analyzed, several considerations should be accounted for. For example, for differently-sized nanoparticles with the same number of photogenerated excitons, the smaller particles are expected to exhibit a more distinct nonlinear effect or lower threshold for observing exciton-exciton annihilation. The smaller particles will have an overall more distinct spatial confinement in which the excitons may interact with one another. Additionally, the smaller particles will have a lower density of states, enabling exciton-exciton annihilation to occur at a lower excitation threshold. However, this needs to be weighed against the fact that larger particles will generate more excitons in totality, thereby undergoing exciton-exciton annihilation more readily. This supports the notion that the volume factor potentially dominates over the effect of trap states. That is, larger particles which have a larger molar absorptivity and can thus absorb more photons will generate more excitons than smaller particles. A strong case for this has been seen in CdS NPs of 3, 5, and 10 nm.^[194] Following a 390 nm pump (5 mJ/(pulse-cm²)) and 780 nm probe, the time constants for the fast component of the decay were found to decrease from 4.3 to 2.5 ps for increasing size (3 to 5 to 10 nm) while the same 143 ps slow time constant applied to all sizes. Since the smaller particles yielded slower fast components, which is indicative of fewer overall excitons being photogenerated, the result will be a less efficient fast decay.

Recently, it has been suggested that a single photon can photoinduce multiple excitons in small bandgap semiconductors such as PbSe,^[259-263] PbS,^[14,264,265] PbTe,^[262] and Si^[266,267] in a process termed multiple exciton generation (MEG) in which the pump photon energy needs to be at least twice that of the bandgap energy ($>2E_g$). The implications for this for solar energy conversion and other applications are immense. Several theoretical models have been put forth as possible explanations for the enhancement of MEG that has been observed in quantum confined semiconductors.^[264,268,269] Given that, it is unclear what the probability or efficiency might be in reality. Because electronic relaxation is characteristically very fast, MEG is likely to be inefficient unless the energy levels concerned can be carefully and intelligently designed to enhance the process. For example, PbSe QDs have been proposed to be materials for which MEG is possible due to its small bandgap.^[263] The experiment, conducted by time-resolved terahertz spectroscopy, reveals the quantum yields (QY) in excess of 100%, indicating that MEG is occurring and that several excitons are being photogenerated for every absorbed photon. Figure 9, below, shows the quantum yield as a function of photon energy/bandgap ($h\nu/E_g$) for PbSe QD samples. The dotted lines are a linear least-squares fit to the data.

Figure 9. Quantum yield vs. $h\nu/E_g$ for PbSe QDs indicating electron-hole pair multiplication (EHPM) following absorption of the PbSe by photons with at least twice the bandgap energy of the PbSe. Reproduced with permission from Ref. 263.



However, the validity of MEG is currently one of controversy. A recently published study by Kambhampati^[270] provided evidence that surface defect-induced charge trapping processes led to false MEG signals, thereby resulting in inaccurate measurements of the MEG process. In the study, it was found that surface defect-induced processes such as trapping, which manifest as transient absorption signals, can falsely be interpreted as MEG signals due to state-filling which manifests as transient bleach signals. They concluded that these large, positive, and broad transient absorption signals have a spectral overlap with negative transient bleach signals which result in spectrally complex bleach signals in QDs. These surface-induced processes lead to additional time scales in the bleach signals that are commonly misinterpreted as MEG signals. To prove their point, the authors conducted control experiments wherein MEG signals were falsely obtained since the pump wavelength in the control was only 1.35 \times that of the bandgap of the CdSe QDs instead of the 2 \times .

Another recent study investigated the dependence of observing false MEG signals on surface treatment. Nozik's group recently investigated the MEG properties of PbSe films and found that the associated quantum yields were affected by the choice of reagent used to treat the surface of the QD.^[271] These changes were attributed to how the reagent could potentially change the film from being *p*-type to *n*-type which could adversely affect the short-timescale and long-time-scale time constants, thereby resulting in incorrectly interpreted MEG quantum yields. Other recent studies^[272,273] have been conducted to determine the contribution to false MEG

signals from surface oxidation of PbSe and PbS QDs, respectively. In the studies, it was found that exposure to air resulted in a ~ 0.5 nm passivation of the outer layer of the QD into an oxide form. Because of this, the MEG performance is affected since the QD had transformed into one with a Pb-chalcogenide with a smaller original core material now being ensconced by an outer oxide shell. The reduction in size of the Pb-chalcogenide and its subsequent envelopment by an oxide shell both increased the overall bandgap and the photon energy threshold necessary for observing MEG.

Others studies have also highlighted the importance of surface properties on recombination rates. A study by Bawendi *et al.*^[238] investigated the time dynamics of CdSe QDs with tri-*n*-octylphosphine oxide (TOPO) or ZnS as capping/shell materials and thereby different densities of surface defect-based trap states. The authors showed unambiguously that a reduction in the degree of surface passivation led to faster initial dynamics of the exciton, indicating that the dynamics are affected greatly by surface trap states. Higher pump fluence experiments also highlighted the dominance of QD volume (and hence trap states) over biexciton decay.

Finally, a study by Klimov *et al.*^[274] provided evidence that photocharging could incorrectly lead to assignments of MEG. Photocharging is a phenomenon whereby when a charged QD absorbs an additional photon, it forms a trion (a single exciton plus an unpaired electron or hole). Unlike a single exciton, a trion can decay rapidly *via* Auger recombination and thus on a timescale concomitant with a biexciton as in a typical MEG process. Trion decay thus produces kinetic traces that

mimic closely those of MEG. Clearly the issues surrounding MEG are still being debated and will certainly be the subject of intense focus.

8.4.5 Exciton Dynamics in Semiconductor Heterojunctions

Semiconductor heterojunctions that involve two semiconductors have emerged as an area of strong interest. One common example is QD-metal oxide (MO) junctions that are of interest for applications such as QD-sensitized solar cells. As discussed in Section 2.1, QDs with small bandgaps can be tuned to absorb a broad range of wavelengths and used to sensitize MOs that have weak or no visible absorption. Exciton dynamics in such systems have been investigated with the goal of better understanding exciton dissociation and subsequent charge injection or transfer.

For example, one recent study by Robel *et al.* showed that following a 387 nm wavelength excitation, the ultrafast exciton relaxation dynamics of CdSe QDs attached to the surface of a TiO₂ film is faster than in CdSe alone.^[275] Moreover, the bleach recovery was sensitive to the size of the CdSe attached to the TiO₂. With decreasing QD size, an increasingly fast recovery was evident. Utilizing a stretched exponential function to fit the experimental data, the time constant of 2281 ± 50 ps was found for 7.5 nm CdSe anchored to TiO₂. In decreasing the size of the CdSe to 3.5, 2.7, and 2.4 nm, the time constant decreased to 1117 ± 21 , 357 ± 11 , and $83 \text{ ps} \pm 3$ ps, respectively. The faster decay rate is attributed to electron injection into TiO₂ following intraband exciton relaxation in the QDs.

Similarly, Guijarro *et al.* investigated the exciton dynamics of CdSe both directly attached and linked to TiO₂ following a 470 nm excitation.^[276] In particular, for directly attached QDs, the decay was fit well to a biexponential function with time constants of 2.8 and 104 ps. However, when the CdSe/TiO₂ junction was created *via* a molecular linker of 3-mercaptopropionic acid (MPA), the decay time constants increased to 4.2 and 204 ps. Finally, for *p*-mercaptopbenzoic acid (MBA) as a linker, the time constants increased to 7.7 and 245 ps. As a point of reference, the time constants obtained for colloidal CdSe were 8.8 and 506 ps. Overall, the CdSe/TiO₂ system displays consistently faster relaxation kinetics because electron transfer from QDs to TiO₂ provides an additional pathway for exciton decay. This pathway, attributed to tunneling from the excited QD to TiO₂, is sensitive to the distance between the electron donor (QD) and acceptor (TiO₂), which is thereby a key parameter affecting the exciton dynamics. Because MBA is longer than MPA, the electron injection is slower with MBA. Later, Pernik *et al.* corroborated the findings by Guijarro and found that the exciton lifetime was predicated greatly upon the nature of the attachment of CdSe QDs to the TiO₂.^[277] Following 387 nm excitation, the exciton decay profile of CdSe directly adsorbed to the surface of TiO₂ can be fit well to a double exponential of 3.1 and 94 ps, while that for CdSe linked to the TiO₂ by 3-mercaptopropionic acid (MPA) had a time constants of 2.6 and 180 ps. The calculated average electron transfer rate of the linked QDs/TiO₂ is $2.3 \times 10^9 \text{ s}^{-1}$, compared to $7.2 \times 10^9 \text{ s}^{-1}$ for the directly attached system. This increase in the electron transfer rate is understandable especially considering that the mechanism for

electron transfer in the case of CdSe QDs on TiO₂ involves quantum tunneling through the QD-TiO₂ junction. Previously, Watson *et al.* had provided similar trends, albeit on a nanosecond timescale, in which an increasing chain length resulted in a decreased injection yield. This picosecond time scale data were able to temporally resolve the electron transfer on an ultrafast scale in order to illustrate the early parts of the electron dynamics.^[278]

For QD/MO heterojunctions, it is often desired to have large contact area and strong interaction between the QD and MO. One approach to achieving this is to co-deposit QD and MO directly together to produce composite structures with a high degree of mixing between the two components. Using one such composite structure composed of CdSe and TiO₂, Fitzmorris *et al.* studied the exciton dynamics of a CdSe/TiO₂ system with 580 nm excitation.^[279] For CdSe alone, the exciton dynamics reflected in transient bleach recovery, with representative data shown in Figure 10, can be fit to a triple exponential with time constants of 7.3, 84, and 1000 ps. For the CdSe/TiO₂ heterojunction system, the exciton time profile was fit to a triple exponential of 0.5, 3.1, and 24 ps.

Figure 10. Transient bleach decay data probed at 695 nm with triple exponential fit functions for CdSe and 44% CdSe/56%TiO₂ arrays. Reproduced with permission from Ref. 279.

For CdSe alone, the two fast decays were attributed to exciton relaxation mediated by the presence of both shallow and deep traps. Meanwhile, the much faster decay for the CdSe/TiO₂ system was believed to originate from electron injection from the conduction band of the CdSe to the conduction band of the TiO₂. An average electron injection rate of $1.7 \times 10^{11} \text{ s}^{-1}$ was estimated, which is very high and attributed to the large interfacial contact area between the CdSe and the TiO₂.

8.4.6 Modeling of Exciton Dynamics

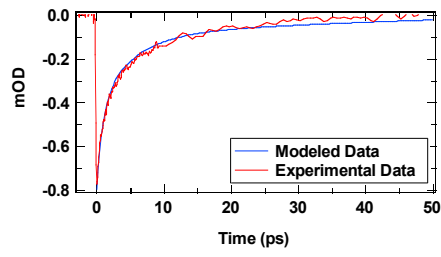
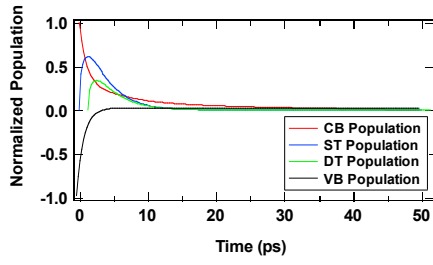
In conjunction with experimental studies, computation and modeling have helped to provide further insight into exciton dynamics in semiconductor NCs. For example, modeling of exciton dynamics has been performed on a number of systems to corroborate experimental results, including semiconductor crystallites,^[280] silver halide nanocrystals,^[281] Cu_xS nanoparticles,^[130] silicon nanowires,^[132] CdSe/CdS/ZnS nanocrystals,^[282] polymeric semiconductor nanoparticles,^[283,284] PbSe and CdSe,^[285] and InAs/GaAs nanopramids,^[286]

Most typically, kinetic modeling can be described by a series of differential equations that relate the concentration of charge carriers, *i.e.* electrons, in different states *via* appropriate rate constants. These “conventional rate equations,” or CREs,^[287-290] apply generally to ensemble-averaged level occupations and are inspired by bulk descriptions. Some very good examples of four-state kinetic modeling – in which the four distinct states are the valence and conduction bands and shallow and deep trap states – have been shown to provide a strong correlation

between experimentally-derived temporal events and actual photophysical processes,^[130,132,281]

For example, in the kinetic modeling of the charge carrier dynamics of porous silicon nanowires (SiNWs), a simple four-state kinetic model was employed in order to gain some insights into the physical processes governing the dynamics of charge carriers measured experimentally.

Figure 11. (Left) Populations of individual states as a function of time. (Right) Experimental data vs. modeled data using a 30/30/20/20 percentage split between the CB, VB, ST, and DT states, respectively. Reproduced with permission from Ref. 132.

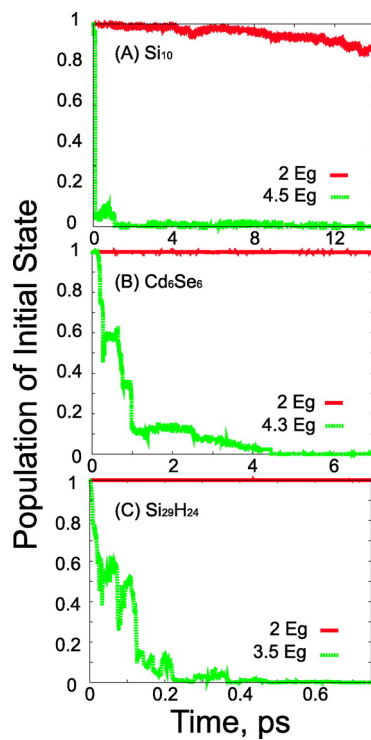
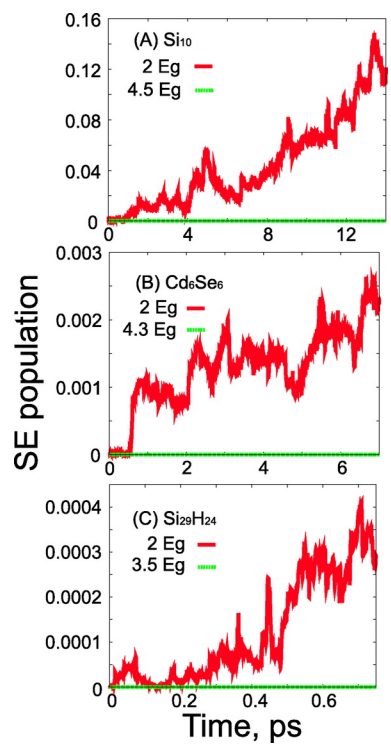


From the final rate constants determined by comparing the modeled data with the experimental data, it is possible to assign rate constants to the key physical processes shown in the right-hand side of Figure 11. From the modeled data, lifetime values of 0.48 ps, 6.4 ps, and 83 ps were obtained that supported the experimental curve-fitting results with time constants of 0.3 ps, 5 ps, and ~75 ps. From these lifetimes, the model suggests that after initial photoexcitation, CB electrons become trapped within shallow trap states within 0.5 ps and are further trapped into deep trap states within 4 ps. The deep trap electrons finally recombine with the hole with a time constant of ~500 ps.

The computation of exciton properties has been conducted with regard to small Si and CdSe QDs.^[291] In this study, multiple exciton generation and recombination (MEG and MER, respectively) dynamics were simulated using *ab initio* time-dependent density functional theory (TDDFT) in combination with nonadiabatic molecular dynamics. The approach used in this study was unique in that it provided atomistic descriptions, employed time-domain representation, allowed for various time-dynamical regimes, and included electron-phonon interactions. Intriguingly, the study found that exponential dynamics start much later than is conventionally believed and occurs when the number of quantum states accessible to the system's dynamics becomes large, after approximately 2 ps. The authors were able to show that MEG occurs on a picosecond time scale in small QDs and that the process speeds up considerably with increasing energy since the ratio of the final double exciton to initial single exciton state densities grows with energy. Perhaps most interestingly, it

was also shown that MEG can occur at energies below the purely electronic energy threshold and that the electronic degrees of freedom can “borrow” energy from phonons. Such phonon-assisted MEG is best promoted by high-frequency phonons of surface ligands. This is shown below in Figure 12. The left panels show plots the MER dynamics starting from a double exciton state and plots the total population of single exciton states as a function of time and energy for different materials. The plot shows that MER is possible only from low energy double excitons. Thus, higher energy double excitons need to lose some of their energy before they can annihilate and form single excitons. The right panel, meanwhile, illustrates the evolution of the population of the initially excited double exciton states.

Figure 12. Left: growth of the total population of all single exciton states starting from a double exciton state of the energy indicated in the figure. The growth is due to MER. MER becomes efficient only at energies near $2E_g$. The MER dynamics are faster in Si_{10} than in Cd_6Se_6 . $\text{Si}_{29}\text{H}_{24}$ shows the slowest MER. Right: population decay of the initially excited double exciton states. The decay is faster at higher energies. Note that at high energies the decay of the population of the initially excited DE states is not due to MER but rather is a result of population transfer from the initial DE to other DEs. Reproduced with permission from Ref. 291.

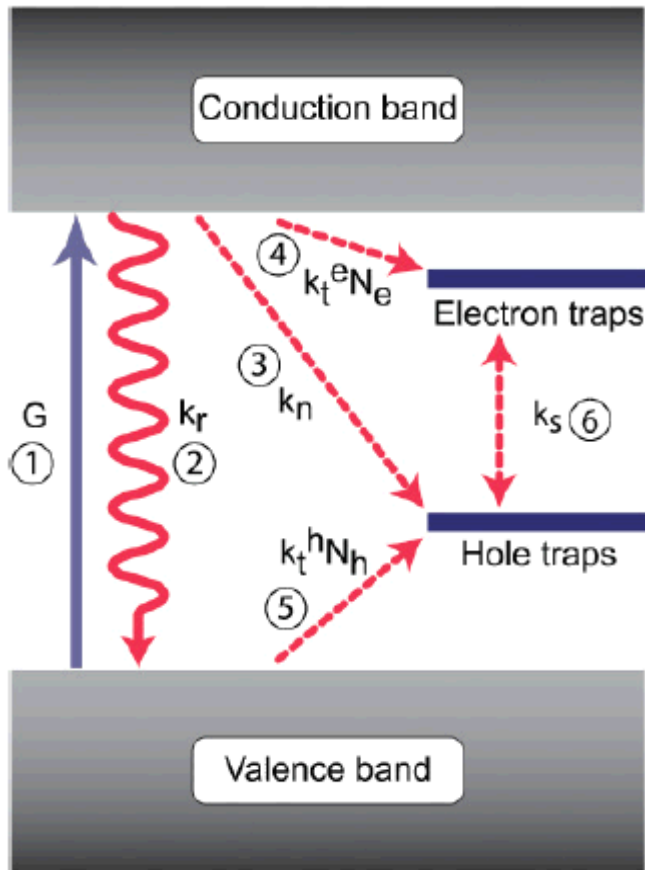


Modeling of linear and nonlinear excitonic recombination has been conducted in 1D semiconductor nanostructures as well.^[292] In studying the exciton dynamics in CdSe nanowires, a kinetic model, described in this paragraph, highlighting the various radiative and nonradiative decay pathways was developed to provide further insight into the role that rapid hole trapping has on excitonic decays. In particular, the proposed model accounted for the generation of carriers *via* laser excitation and their subsequent bimolecular radiative recombination. A further assumption was that both electrons and holes became trapped into defect states. By assuming nominal values for the rate constants, the proposed model was used to rationalize the experimental results also obtained in the study. Using the model, the superlinear growth of the emission intensity was explainable. In the model, at very low excitation fluences, carrier trapping (of both electrons and holes) and subsequent nonradiative recombination dominated the excitonic decay kinetics following generation. The model was instrumental in accounting for the excitation-intensity-dependence of the nanowire quantum yield.

The model (Figure 13, below) was used further to probe variable-order Auger kinetics in TA studies of CdSe nanowires. In particular, the transition from a high pump fluence bimolecular recombination regime to a low-fluence region where apparent three-carrier (third order) kinetics occurs upon fast hole trapping (~10 ps). In other words, at high pump fluences, the TA kinetics are predominantly bimolecular in nature due to the recombination of free electrons and trapped holes. At lower pump fluences, however, deviations from bimolecular kinetics can occur and may

lead to decays which follow apparent third-order kinetics since a decay is directly proportional to trapped holes as well as a second-order rate constant of electron trapping. The insights that were gained from this model center around the fact that photogenerated charge carriers in large diameter nanowires are primarily free electrons and holes. This explanation helped account for the observation of the excitation intensity-dependence of the quantum yield of the nanowires.

Figure 13. Illustration of the kinetic model used to support experimental observations. Following generation (G), free carriers at the band edge recombine radiatively with a second-order rate constant, k_r . They can also be trapped with effective first-order rate constants combining contributions of both electrons and holes. Additional nonradiative recombination channels involve trapped holes that recombine with free electrons (associated rate constant k_n) as well as with trapped electrons (associated rate constant k_s). Here, $k_t^e N_e$ and $k_t^h N_h$ are second-order rate constants for trapped electrons and holes, respectively, while N_e and N_h are the number of electron and hole traps, respectively. Reproduced with permission from Ref. 292.



8.5 Concluding Remarks

In this review, we have provided an overview on recent advances on the study and understanding of exciton dynamics in semiconductor NCs. In addition to examining the static optical properties of semiconductors, we placed special emphasis on the time-resolved studies of exciton dynamics of these materials in comparison to that in bulk materials. We attempted to provide a unifying picture of the key dynamic processes of photogenerated excitons, including electronic dephasing, intraband relaxation, trapping, and recombination of free and trapped charge carriers. Nonlinear dynamic processes are also covered in relation to the generation of multiple excitons. Additionally, we discuss some examples of modeling and computation of exciton dynamics to gain further insight. A deeper understanding of the fundamental exciton dynamics in semiconductor NCs is essential for exploiting their applications in a number of important technological fields, including optical detectors, solar energy conversion, sensors, and many others.

8.6 References

- [1] H. Yoshioka; N. Morioka; J. Suda; T. Kimoto, *Journal of Applied Physics*, **2011**, *109*, 064312.
- [2] K. Takei; H. Fang; S. B. Kumar; R. Kapadia; Q. Gao; M. Madsen; H. S. Kim; C. H. Liu; Y. L. Chueh; E. Plis, *Nano Letters*, **2011**,
- [3] M. A. Holmes; T. K. Townsend; F. E. Osterloh, *Chemical Communications*, **2012**,

- [4] P. F. Zhang; Z. Liu; W. Duan; F. Liu; J. Wu, *Physical Review B*, **2012**, 85, 201410.
- [5] A. Sahu; A. Khare; D. Deng; D. Norris, *Chemical Communications*, **2012**,
- [6] O. Chen; Y. Yang; T. Wang; H. Wu; C. Niu; J. Yang; Y. C. Cao, *Journal of the American Chemical Society*, **2011**,
- [7] B. M. Cossairt; P. Juhas; S. J. L. Billinge; J. S. Owen, *The Journal of Physical Chemistry Letters*, **2011**,
- [8] H. Ruda; A. Shik, *Applied Physics Letters*, **2011**, 99, 213111-213111-213113.
- [9] L. Zhang; H. Jing; G. Boisvert; J. Z. He; H. Wang, *ACS Nano*, **2012**, 6, 3514-3527.
- [10] M. Grätzel, *Inorganic Chemistry*, **2005**, 44, 6841-6851.
- [11] A. J. Bard, *The Journal of Physical Chemistry*, **1982**, 86, 172-177.
- [12] R. D. Schaller; V. I. Klimov, *Physical Review Letters*, **2004**, 92, 186601.
- [13] A. J. Nozik, *Annual Review of Physical Chemistry*, **1978**, 29, 189-222.
- [14] V. I. Klimov, *The Journal of Physical Chemistry B*, **2006**, 110, 16827.
- [15] A. I. Hochbaum; P. Yang, *Chemical Reviews*, **2010**, 110, 527.
- [16] R. Memming, *Electrochimica Acta*, **1980**, 25, 77-88.
- [17] G. J. Meyer, *Inorganic Chemistry*, **2005**, 44, 6852-6864.
- [18] P. V. Kamat; N. M. Dimitrijević, *Solar Energy*, **1990**, 44, 83-98.

- [19] P. V. Kamat, *The Journal of Physical Chemistry C*, **2007**, *111*, 2834-2860.
- [20] H. Hasegawa; M. Akazawa, *Applied Surface Science*, **2008**, *255*, 628-632.
- [21] H. Hasegawa; M. Akazawa, *Applied Surface Science*, **2008**, *254*, 8005-8015.
- [22] W. Lu; C. M. Lieber, *Nature materials*, **2007**, *6*, 841-850.
- [23] J. D. Meindl; Q. Chen; J. A. Davis, *Science*, **2001**, *293*, 2044-2049.
- [24] W. Lee; Y. Lee; Y. Wu; P. Chang; Y. Huang; Y. Hsu; J. Mannaerts; R. Lo; F. Chen; S. Maikap, *Journal of crystal growth*, **2005**, *278*, 619-623.
- [25] B. Yu; M. Meyyappan, *Solid-state electronics*, **2006**, *50*, 536-544.
- [26] V. V. Zhirnov; D. J. C. Herr, *Computer*, **2001**, *34*, 34-43.
- [27] C. Hu, *Nanotechnology*, **1999**, *10*, 113.
- [28] R. Chau; S. Datta; A. Majumdar. "Opportunities and challenges of III-V nanoelectronics for future high-speed, low-power logic applications", 2005.
- [29] Y. Huang; S. T. Ho, *Opt. Express*, **2006**, *14*, 3569-3587.
- [30] D. J. Sirbuly; M. Law; H. Yan; P. Yang, *The Journal of Physical Chemistry B*, **2005**, *109*, 15190-15213.
- [31] B. E. A. Saleh; M. C. Teich; B. E. Saleh *Fundamentals of photonics*; Wiley Online Library, 1991; Vol. 22.
- [32] B. Jalali; S. Fathpour, *Lightwave Technology, Journal of*, **2006**, *24*, 4600-4615.

- [33] A. J. Shields, *Nature Photonics*, **2007**, *1*, 215-223.
- [34] R. Yan; D. Gargas; P. Yang, *Nature Photonics*, **2009**, *3*, 569-576.
- [35] T. Prevenslik, *Advanced Materials Research*, **2008**, *31*, 1-3.
- [36] M. Law; D. J. Sirbuly; J. C. Johnson; J. Goldberger; R. J. Saykally; P. Yang, *Science*, **2004**, *305*, 1269-1273.
- [37] A. Stroyuk; A. Kryukov; S. Y. Kuchmii; V. Pokhodenko, *Theoretical and Experimental Chemistry*, **2005**, *41*, 67-91.
- [38] P. Alivisatos, *Nature biotechnology*, **2003**, *22*, 47-52.
- [39] Y. Cui; Q. Wei; H. Park; C. M. Lieber, *Science*, **2001**, *293*, 1289-1292.
- [40] S. Pearton; F. Ren; Y. L. Wang; B. Chu; K. Chen; C. Chang; W. Lim; J. Lin; D. Norton, *Progress in Materials Science*, **2010**, *55*, 1-59.
- [41] S. Pearton; B. Kang; S. Kim; F. Ren; B. Gila; C. Abernathy; J. Lin; S. Chu, *Journal of Physics: Condensed Matter*, **2004**, *16*, R961.
- [42] P. Yang; R. Yan; M. Fardy, *Nano Letters*, **2010**, *10*, 1529-1536.
- [43] X. Gao; W. C. W. Chan; S. Nie, *Journal of Biomedical Optics*, **2002**, *7*, 532.
- [44] M. G. Nikolaides; S. Rauschenbach; S. Luber; K. Buchholz; M. Tornow; G. Abstreiter; A. R. Bausch, *ChemPhysChem*, **2003**, *4*, 1104-1106.
- [45] I. L. Medintz; H. T. Uyeda; E. R. Goldman; H. Mattoussi, *Nature materials*, **2005**, *4*, 435-446.
- [46] F. Patolsky; G. Zheng; C. M. Lieber, *Nanomedicine*, **2006**, *1*, 51-65.

- [47] F. Patolsky; G. Zheng; C. M. Lieber, *Nature Protocols*, **2006**, *1*, 1711-1724.
- [48] H. Kosaka; A. A. Kiselev; F. A. Baron; K. W. Kim; E. Yablonovitch, *Electronics Letters*, **2001**, *37*, 464-465.
- [49] W. Tsang *Semiconductors and semimetals: lightwave communications technology. photodetectors*; Academic Pr, 1985; Vol. 22.
- [50] P. Dowd; S. Johnson; S. Feld; M. Adamcyk; S. Chaparro; J. Joseph; K. Hilgers; M. Horning; K. Shiralagi; Y. H. Zhang, *Electronics Letters*, **2003**, *39*, 987-988.
- [51] R. Hui; S. Taherion; Y. Wan; J. Li; S. Jin; J. Lin; H. Jiang, *Applied Physics Letters*, **2003**, *82*, 1326.
- [52] J. B. D. Soole; H. Schumacher, *Quantum Electronics, IEEE Journal of*, **1991**, *27*, 737-752.
- [53] E. Yablonovitch; E. Kane, *Lightwave Technology, Journal of*, **1988**, *6*, 1292-1299.
- [54] A. J. Bard, *Journal of Photochemistry*, **1979**, *10*, 59-75.
- [55] T. Wolkenstein, *Advances in Catalysis*, **1960**, *12*, 189-264.
- [56] A. Mills; R. H. Davies; D. Worsley, *Chem. Soc. Rev.*, **1993**, *22*, 417-425.
- [57] A. Mills; S. L. Hunte, *Journal of Photochemistry and Photobiology-Chemistry Section*, **1997**, *108*, 1-36.
- [58] H. Yoneyama, *Catalysis today*, **1997**, *39*, 169-175.

- [59] L. Khalil; W. Mourad; M. Rophael, *Applied Catalysis B: Environmental*, **1998**, *17*, 267-273.
- [60] M. Pileni, *Catalysis today*, **2000**, *58*, 151-166.
- [61] N. A. Vante; H. Tributsch, *Nature*, **1986**, *323*, 431-432.
- [62] M. R. Hoffmann; S. T. Martin; W. Choi; D. W. Bahnemann, *Chemical Reviews*, **1995**, *95*, 69-96.
- [63] P. V. Kamat; D. Meisel, *Comptes Rendus Chimie*, **2003**, *6*, 999-1007.
- [64] K. Rajeshwar; N. R. de Tacconi, *Chem. Soc. Rev.*, **2009**, *38*, 1984-1998.
- [65] S. O. Obare; T. Ito; G. J. Meyer, *Environmental Science & Technology*, **2005**, *39*, 6266-6272.
- [66] C. L. Torres-Martinez; R. Kho; O. I. Mian; R. K. Mehra, *Journal of Colloid and Interface Science*, **2001**, *240*, 525-532.
- [67] C. Nasr; K. Vinodgopal; L. Fisher; S. Hotchandani; A. Chattopadhyay; P. V. Kamat, *The Journal of Physical Chemistry*, **1996**, *100*, 8436-8442.
- [68] X. Hu; G. Li; J. C. Yu, *Langmuir*, **2009**, *26*, 3031-3039.
- [69] M. A. El-Sayed, *Accounts of Chemical Research*, **2004**, *37*, 326-333.
- [70] S. Kan; T. Mokari; E. Rothenberg; U. Banin, *Nature materials*, **2003**, *2*, 155-158.
- [71] X. Peng, *Advanced Materials*, **2003**, *15*, 459-463.
- [72] L. Manna; E. C. Scher; A. P. Alivisatos, *Journal of Cluster Science*, **2002**, *13*, 521-532.

- [73] Z. A. Peng; X. Peng, *Journal of the American Chemical Society*, **2002**, *124*, 3343-3353.
- [74] J. Z. Zhang *Optical properties and spectroscopy of nanomaterials*; World Scientific Publishing Co.: Hackensack, NJ, 2009.
- [75] J. Rogers; M. Lagally; R. Nuzzo, *Nature*, **2011**, *477*, 45-53.
- [76] M. Niu; F. Huang; L. Cui; P. Huang; Y. Yu; Y. Wang, *ACS Nano*, **2010**, *4*, 681-688.
- [77] A. Sahu; L. Qi; M. S. Kang; D. Deng; D. J. Norris, *Journal of the American Chemical Society*, **2011**,
- [78] D. Ness; J. Niehaus; V. H. Tran; H. Weller. "Sustainable Synthesis of Semiconductor Nanoparticles in a Continuous Flow Reactor", 2012.
- [79] Z. Zhuang; Q. Peng; Y. Li, *Chem. Soc. Rev.*, **2011**, *40*, 5492-5513.
- [80] B. P. Khanal; A. Pandey; L. Li; Q. Lin; W. K. Bae; H. Luo; V. I. Klimov; J. M. Pietryga, *ACS Nano*, **2012**,
- [81] Z. Li; X. Ma; Q. Sun; Z. Wang; J. Liu; Z. Zhu; S. Z. Qiao; S. C. Smith; G. M. Lu; A. Mews, *European Journal of Inorganic Chemistry*, **2010**, *2010*, 4325-4331.
- [82] S. Liu; J. Yu; B. Cheng; M. Jaroniec, *Advances in Colloid and Interface Science*, **2012**, *173*, 35-53.
- [83] T. Sasamura; K. I. Okazaki; S. Kuwabata; T. Torimoto, *Journal of The Society of Photographic Science and Technology of Japan*, **2012**, *73*, 290-296.

- [84] J. S. Son; J. H. Yu; S. G. Kwon; J. Lee; J. Joo; T. Hyeon, *Advanced Materials*, **2011**,
- [85] A. L. Efros; A. L. Efros, *Fizika i Tekhnika Poluprovodnikov*, **1982**, *16*, 1209.
- [86] L. E. Brus, *The Journal of Chemical Physics*, **1984**, *80*, 4403.
- [87] S. Shinde; P. Shinde; V. Sathe; S. Barman; C. Bhosale; K. Rajpure, *Journal of Molecular Structure*, **2010**, *984*, 186-193.
- [88] J. Z. Zhang, *Accounts of Chemical Research*, **1997**, *30*, 423-429.
- [89] G. Nootz; L. A. Padilha; L. Levina; V. Sukhovatkin; S. Webster; L. Brzozowski; E. H. Sargent; D. J. Hagan; E. W. Van Stryland, *Physical Review B*, **2011**, *83*, 155302.
- [90] M. M. Abdulla; N. H. Hasan; H. I. Mohammed; G. H. Mohamed; K. A. Al-Hamdani; A. F. Abdulameer, *Journal of Electron Devices*, **2012**, *12*, 761-766.
- [91] H. Mathieu; T. Richard; J. Allegre; P. Lefebvre; G. Arnaud; W. Granier; L. Boudes; J. Marc; A. Pradel; M. Ribes, *Journal of Applied Physics*, **1995**, *77*, 287-293.
- [92] U. Thupakula; A. H. Khan; J. K. Bal; K. Ariga; S. Acharya, *Journal of Nanoscience and Nanotechnology*, **2011**, *11*, 7709-7714.
- [93] J. Puthussery; T. H. Kosel; M. Kuno, *Small*, **2009**, *5*, 1112-1116.
- [94] Z. Deng; H. Yan; Y. Liu, *Angewandte Chemie*, **2010**, *122*, 8877-8880.
- [95] F. Shen; W. Que; X. Yin; Y. Huang; Q. Jia, *Journal of Alloys and Compounds*, **2011**,

- [96] S. S. Walavalkar; C. E. Hofmann; A. P. Homyk; M. D. Henry; H. A. Atwater; A. Scherer, *Nano Letters*, **2010**,
- [97] A. Wolcott; D. Gerion; M. Visconte; J. Sun; A. Schwartzberg; S. Chen; J. Z. Zhang, *The Journal of Physical Chemistry B*, **2006**, *110*, 5779-5789.
- [98] H. Mathieu; P. Lefebvre; P. Christol, *Physical Review B*, **1992**, *46*, 4092.
- [99] M. Ueta; H. Kanzaki; K. Kobayashi; Y. Toyozawa; E. Hanamura *Excitonic processes in solids*; Springer-Verlag Berlin, 1986; Vol. 60.
- [100] E. Rosencher; B. Vinter *Optoelectronics*; Cambridge University Press: Cambridge, 2002.
- [101] A. S. Heintz; M. J. Fink; B. S. Mitchell, *Applied Organometallic Chemistry*, **2010**, *24*, 236-240.
- [102] C. D. Grant; J. Z. Zhang *Annual Review of Nano Research*; World Scientific Publisher: Singapore, 2008; Vol. 2.
- [103] C. Leatherdale; W. K. Woo; F. Mikulec; M. Bawendi, *The Journal of Physical Chemistry B*, **2002**, *106*, 7619-7622.
- [104] T. Takagahara, *Physical Review B*, **1987**, *36*, 9293.
- [105] Y. Kayanuma, *Physical Review B*, **1988**, *38*, 9797-9805.
- [106] Q. Dai; Y. Wang; X. Li; Y. Zhang; D. J. Pellegrino; M. Zhao; B. Zou; J. T. Seo; W. W. Yu, *ACS Nano*, **2009**, *3*, 1518-1524.
- [107] C. Yang; Y. W. Mai, *Chemical Physics Letters*, **2012**,

- [108] W. Ma; S. L. Swisher; T. Ewers; J. Engel; V. E. Ferry; H. A. Atwater; A. P. Alivisatos, *ACS Nano*, **2011**,
- [109] R. Chen; M. I. Bakti Utama; Z. Peng; B. Peng; Q. Xiong; H. Sun, *Advanced Materials*, **2011**, *23*, 1404-1408.
- [110] L. Hu; H. Wu; L. Du; H. Ge; X. Chen; N. Dai, *Nanotechnology*, **2011**, *22*, 125202.
- [111] J. Zhang; A. A. Lutich; A. S. Susha; M. Doblinger; Y. P. Rakovich; Y. Volkov; J. F. Donegan; F. Jackel; J. Feldmann; A. L. Rogach. "Solution-grown CdTe nanowires: Self-assembly, optical properties and strong temperature dependent electronic coupling", 2010.
- [112] D. R. Baker; P. V. Kamat, *Langmuir*, **2010**, *26*, 11272-11276.
- [113] N. Maseko; N. Revaprasadu; V. Pullabhotla; R. Karthik; P. O'Brien, *Materials Letters*, **2010**, *64*, 1037-1040.
- [114] X. Luo; P. Liu; N. T. N. Truong; U. Farva; C. Park, *The Journal of Physical Chemistry C*, **2011**,
- [115] A. Mandal; N. Tamai, *Chemical Physics Letters*, **2011**,
- [116] J. Labéguerie-Eg ea; H. M. McEvoy; C. McDonagh, *Journal of Nanoparticle Research*, **2011**, 1-11.
- [117] S. Mehta; S. Kumar, *Journal of luminescence*, **2010**, *130*, 2377-2384.
- [118] M. Zhong; J. Shi; F. Xiong; W. Zhang; C. Li, *Solar Energy*, **2011**,
- [119] M. Wang; G. Abbineni; A. Clevenger; C. Mao; S. Xu, *Nanomedicine: Nanotechnology, Biology and Medicine*, **2011**,

- [120] F. Fabbri; F. Rossi; G. Attolini; G. Salviati; S. Iannotta; L. Aversa; R. Verucchi; M. Nardi; N. Fukata; B. Dierre, *Nanotechnology*, **2010**, *21*, 345702.
- [121] Y. Tian; B. Chen; R. Hua; J. Sun; L. Cheng; H. Zhong; X. Li; J. Zhang; Q. Meng; M. Chen, *Journal of Nanoscience and Nanotechnology*, **2011**, *11*, 9631-9635.
- [122] D. Yang; C. Li; G. Li; M. Shang; X. Kang; J. Lin, *J. Mater. Chem.*, **2011**, *21*, 5923-5927.
- [123] H. Zhang; D. Chen; J. Zhang; Z. Wang; Y. Cui; L. Shen, *Journal of Nanoscience and Nanotechnology*, **2010**, *10*, 7587-7591.
- [124] M. A. Hines; P. Guyot-Sionnest, *The Journal of Physical Chemistry B*, **1998**, *102*, 3655-3657.
- [125] Y. Wang; G. Meng; L. Zhang; C. Liang; J. Zhang, *Chemistry of Materials*, **2002**, *14*, 1773-1777.
- [126] D. V. Talapin; A. L. Rogach; E. V. Shevchenko; A. Kornowski; M. Haase; H. Weller, *Journal of the American Chemical Society*, **2002**, *124*, 5782-5790.
- [127] D. Wheeler; B. Fitzmorris; H. Zhao; D. Ma; J. Zhang, *SCIENCE CHINA Chemistry*, **2011**, *54*, 2009-2015.
- [128] A. A. Patel; F. Wu; J. Z. Zhang; C. L. Torres-Martinez; R. K. Mehra; Y. Yang; S. H. Risbud, *The Journal of Physical Chemistry B*, **2000**, *104*, 11598.
- [129] A. Sengupta; B. Jiang; K. Mandal; J. Zhang, *The Journal of Physical Chemistry B*, **1999**, *103*, 3128-3137.

- [130] M. C. Brelle; C. L. Torres-Martinez; J. C. McNulty; R. K. Mehra; J. Z. Zhang, *Pure Appl. Chem.*, **2000**, *72*, 101-117.
- [131] M. C. Brelle; J. Z. Zhang; L. Nguyen; R. K. Mehra, *The Journal of Physical Chemistry A*, **1999**, *103*, 10194-10201.
- [132] D. A. Wheeler; J.-A. Huang; R. J. Newhouse; W.-F. Zhang; S.-T. Lee; J. Z. Zhang, *The Journal of Physical Chemistry Letters*, **2012**, *3*, 766-771.
- [133] J. Haynes; W. Westphal, *Physical Review*, **1956**, *101*, 1676.
- [134] L. Spanhel; M. Haase; H. Weller; A. Henglein, *Journal of the American Chemical Society*, **1987**, *109*, 5649.
- [135] P. V. Kamat; N. M. Dimitrijevic, *The Journal of Physical Chemistry*, **1989**, *93*, 4259-4263.
- [136] P. V. Kamat; M. D. v. Wijngaarden; S. Hotchandani, *Israel J. Chem*, **1993**, *33*, 47.
- [137] C. Luangdilok; D. Meisel, *Israel J. Chem.*, **1993**, *33*, 53.
- [138] M. Gao; S. Kirstein; H. M \ddot{u} llhwald; A. L. Rogach; A. Kornowski; A. Eychm \ddot{u} ller; H. Weller, *The Journal of Physical Chemistry B*, **1998**, *102*, 8360.
- [139] T. Roberti; N. Cherepy; J. Zhang, *J. Chem. Phys.*, **1998**, *108*, 2143.
- [140] B. Chon; J. Bang; J. Park; C. Jeong; J. H. Choi; J. B. Lee; T. Joo; S. Kim, *The Journal of Physical Chemistry C*, **2011**,
- [141] N. Hauke; T. Zabel; K. M \ddot{u} ller; M. Kaniber; A. Laucht; D. Bougeard; G. Abstreiter; J. Finley; Y. Arakawa, *New Journal of Physics*, **2010**, *12*, 053005.

- [142] H. Z. Zhuang; B. L. Li; C. S. Xue; S. Y. Zhang; D. X. Wang; J. B. Shen, *Vacuum*, **2008**, *82*, 1224-1228.
- [143] P. C. Ou; W. R. Liu; H. J. Ton; J. H. Lin; W. F. Hsieh, *Journal of Applied Physics*, **2011**, *109*, 013102-013102-013105.
- [144] H. Yoneda; Y. Inubushi; T. Tanaka; Y. Yamaguchi; F. Sato; S. Morimoto; T. Kumagai; M. Nagasono; A. Higashiya; M. Yabashi, *Optics Express*, **2009**, *17*, 23443-23448.
- [145] E. Jelமாக; R. Tomas[□]iun[□]as; E. Rafailov; I. Krestnikov. “Photoinduced absorption saturation dynamics of InGaAs quantum dot structure dedicated for wavelength 1070 nm”, 2010.
- [146] H. Gibbs; G. Khitrova; S. Koch, *Nature Photonics*, **2011**, *5*, 273-273.
- [147] Y. Yakar; B. ÇakIr; A. Özmen, *Optics Communications*, **2010**, *283*, 1795-1800.
- [148] V. Dneprovskii; N. Gushina; O. Pavlov; V. Poborchii; I. Salamatina; E. Zhukov, *Physics Letters A*, **1995**, *204*, 59-62.
- [149] V. Dneprovskii; A. Eev; N. Gushina; D. Okorokov; V. Panov; V. Karavanskii; A. Maslov; V. Sokolov; E. Dovidenko, *physica status solidi (b)*, **1995**, *188*, 297-306.
- [150] F. Z. Henari; K. Morgenstern; W. J. Blau; V. A. Karavanskii; V. S. Dneprovskii, *Applied Physics Letters*, **1995**, *67*, 323.
- [151] M. Nyk; D. Wawrzynczyk; J. Szeremeta; M. Samoc, *Applied Physics Letters*, **2012**, *100*, 041102-041102-041104.

- [152] G. Lin; F. Luo; H. Pan; M. M. Smedskjaer; Y. Teng; D. Chen; J. Qiu; Q. Zhao, *The Journal of Physical Chemistry C*, **2011**,
- [153] H. Sekhar; P. P. Kiran; D. N. Rao, *Materials Chemistry and Physics*, **2011**,
- [154] M. Jacobsohn; U. Banin, *The Journal of Physical Chemistry B*, **2000**, *104*, 1-5.
- [155] Z. Yu; F. Degang; W. Xin; L. Juzheng; L. Zuhong, *Colloids and Surfaces A: Physicochemical and Engineering Aspects*, **2001**, *181*, 145-149.
- [156] A. Baron; A. Ryasnyanskiy; N. Dubreuil; P. Delaye; Q. Vy Tran; S. Combrié; A. De Rossi; R. Frey; G. Roosen, *Optics Express*, **2009**, *17*, 552-557.
- [157] L. Guo; K. Ibrahim; F. Liu; X. Ai; Q. Li; H. Zhu; Y. Zou, *Journal of luminescence*, **1999**, *82*, 111-114.
- [158] T. Yamaki; K. Asai; K. Ishigure; K. Sano; K. Ema, *Synthetic metals*, **1999**, *103*, 2690-2691.
- [159] Z. Deng; L. Tong; M. Flores; S. Lin; J. X. Cheng; H. Yan; Y. Liu, *Journal of the American Chemical Society*, **2011**,
- [160] Z. Yang; J. Zhu; D. Yan; H. Wu; R. Wang; Z. Song; X. Yu; Y. Yang; D. Zhou; Z. Yin, *Optical Materials*, **2012**,
- [161] L. G. Quagliano; H. Nather, *Applied Physics Letters*, **1984**, *45*, 555-557.
- [162] E. Johnson; J. Kafalas; R. Davies; W. Dyes, *Applied Physics Letters*, **1982**, *40*, 993-995.

- [163] H. H. Fang; Q. D. Chen; J. Yang; H. Xia; Y. G. Ma; H. Y. Wang; H. B. Sun, *Optics letters*, **2010**, *35*, 441-443.
- [164] Y. Xu; D. Chen; Q. Zhang; W. Wang; H. Zeng; C. Shen; G. Chen, *Chemical Physics Letters*, **2009**, *472*, 104-106.
- [165] Y. H. Cho; D. Kim; B. D. Choe; H. Lim; J. Lee; D. Kim, *Physical Review B*, **1997**, *56*, 4375-4378.
- [166] M. Potemski; R. Stepniowski; J. Maan; G. Martinez; P. Wyder; B. Etienne, *Physical Review Letters*, **1991**, *66*, 2239-2242.
- [167] P. Vagos; P. Boucaud; F. Julien; J. M. Lourtioz; R. Planel, *Physical Review Letters*, **1993**, *70*, 1018-1021.
- [168] W. Seidel; A. Titkov; J. Andre; P. Voisin; M. Voos, *Physical Review Letters*, **1994**, *73*, 2356.
- [169] A. Vinattieri; J. Shah; T. Damen; D. Kim; L. Pfeiffer; M. Maialle; L. Sham, *Physical Review B*, **1994**, *50*, 10868.
- [170] J. Li, *Physical Review B*, **2007**, *75*, 155315.
- [171] S. Eshlaghi; W. Worthoff; A. Wieck; D. Suter, *Physical Review B*, **2008**, *77*, 245317.
- [172] W. Wu; Y. Gao; Q. Chang; H. Ye; Z. Zheng; W. Liu; A. Li; Y. Yang, *Journal of Nanoparticle Research*, **2011**, *13*, 1049-1061.
- [173] D. A. Fishman; C. M. Cirloganu; S. Webster; L. A. Padilha; M. Monroe; D. J. Hagan; E. W. Van Stryland, *Nature Photonics*, **2011**, *5*, 561-565.

- [174] H. M. Cheong; B. Fluegel; M. C. Hanna; A. Mascarenhas, *Physical Review B*, **1998**, *58*, 4254-4257.
- [175] M. D. Garrett; M. J. Bowers; J. R. McBride; R. L. Orndorff; S. J. Pennycook; S. J. Rosenthal, *The Journal of Physical Chemistry C*, **2008**, *112*, 436-442.
- [176] J. He; G. D. Scholes; Y. Qu; W. Ji, *Journal of Applied Physics*, **2008**, *104*, 023110-023110-023114.
- [177] E. Poles; D. C. Selmarten; O. I. Mičić; A. J. Nozik, *Applied Physics Letters*, **1999**, *75*, 971.
- [178] P. Paskov; P. Holtz; B. Monemar; J. M. García; W. Schoenfeld; P. Petroff, *Applied Physics Letters*, **2000**, *77*, 812.
- [179] F. W. Huang; J. K. Sheu; M. L. Lee; S. J. Tu; W. C. Lai; W. C. Tsai; W. H. Chang, *Optics Express*, **2011**, *19*, A1211-A1218.
- [180] N. Thantu, *Journal of luminescence*, **2005**, *111*, 17-24.
- [181] L. Bokatial; S. Rai, *Journal of Fluorescence*, **2012**, 1-7.
- [182] P. Zhang; S. Rogelj; K. Nguyen; D. Wheeler, *Journal of the American Chemical Society*, **2006**, *128*, 12410-12411.
- [183] F. Wang; R. Deng; J. Wang; Q. Wang; Y. Han; H. Zhu; X. Chen; X. Liu, *Nat Mater*, **2011**, *10*, 968-973.
- [184] R. T. Wegh; H. Donker; K. D. Oskam; A. Meijerink, *Science*, **1999**, *283*, 663-666.

- [185] C. P. Poole; F. J. Owens *Introduction to nanotechnology*; Wiley-Interscience, 2003.
- [186] M. Grätzel *Heterogeneous photochemical electron transfer*; CRC Press Boca Raton, FL, 1989; Vol. 91.
- [187] S. D. Baranovskii; M. Wiemer; A. V. Nenashev; F. Jansson; F. Gebhard, *The Journal of Physical Chemistry Letters*, **2012**, 3, 1214-1221.
- [188] J. Z. Zhang, *The Journal of Physical Chemistry B*, **2000**, 104, 7239-7253.
- [189] V. I. Klimov; D. W. McBranch, *Optics letters*, **1998**, 23, 277-279.
- [190] K. Kaiser *Ultrashort Laser Pulses: Generation and Applications*; Springer-Verlag: Berlin, 1993.
- [191] R. J. Newhouse; H. Wang; J. K. Hensel; D. A. Wheeler; S. Zou; J. Z. Zhang, *The Journal of Physical Chemistry Letters*, **2011**, 2, 228.
- [192] J. Hodak; I. Martini; G. V. Hartland, *Chemical Physics Letters*, **1998**, 284, 135.
- [193] S. Link; A. Furube; M. B. Mohamed; T. Asahi; H. Masuhara; M. A. El-Sayed, *The Journal of Physical Chemistry B*, **2002**, 106, 945.
- [194] F. Wu; J. H. Yu; J. Joo; T. Hyeon; J. Z. Zhang, *Optical Materials*, **2007**, 29, 858.
- [195] D. A. Wheeler; G. Wang; B. C. Fitzmorris; S. A. Adams; Y. Li; J. Z. Zhang, *MRS Proc.*, **2012**, *In press*,

- [196] G. Wang; Y. Ling; D. A. Wheeler; K. E. N. George; K. Horsley; C. Heske; J. Z. Zhang; Y. Li, *Nano Letters*, **2011**, *11*, 3503-3509.
- [197] Y. Ling; G. Wang; D. A. Wheeler; J. Z. Zhang; Y. Li, *Nano Letters*, **2011**, null.
- [198] A. Juris; M. Maestri, *The Exploration of Supramolecular Systems and Nanostructures by Photochemical Techniques*, **2012**, 167-184.
- [199] C. Galland; Y. Ghosh; A. Steinbrück; M. Sykora; J. A. Hollingsworth; V. I. Klimov; H. Htoon, *Nature*, **2011**, *479*, 203-207.
- [200] A. Y. Koposov; P. Szymanski; T. Cardolaccia; T. J. Meyer; V. I. Klimov; M. Sykora, *Advanced Functional Materials*, **2011**,
- [201] S. Tanaka, *Journal of Electron Spectroscopy and Related Phenomena*, **2012**,
- [202] Ł. Bujak; M. Olejnik; R. Litvin; D. Piątkowski; N. A. Kotov; S. Mackowski, *Central European Journal of Physics*, **2011**, *9*, 287-292.
- [203] C. Meuer; C. Schmidt-Langhorst; H. Schmeckeber; G. Fiol; D. Arsenijević; C. Schubert; D. Bimberg, *Optics Express*, **2011**, *19*, 3788-3798.
- [204] A. I. McIntosh; B. Yang; S. M. Goldup; M. Watkinson; R. S. Donnan, *Chem. Soc. Rev.*, **2012**, *41*, 2072-2082.
- [205] F. Wu; J. Zhang; R. Kho; R. Mehra, *Chemical Physics Letters*, **2000**, *330*, 237-242.
- [206] F. Masia; W. Langbein; I. Moreels; Z. Hens; P. Borri, *Physical Review B*, **2011**, *83*, 201309.

- [207] P. Kambhampati, *Accounts of Chemical Research*, **2010**, *44*, 1-13.
- [208] C. H. Chia; W. C. Fan; Y. C. Lin; W. C. Chou, *Journal of luminescence*, **2011**,
- [209] P. Dahan; V. Fleurov; P. Thurian; R. Heitz; A. Hoffmann; I. Broser, *Journal of Physics: Condensed Matter*, **1998**, *10*, 2007.
- [210] J. K. Cooper; A. M. Franco; S. Gul; C. Corrado; J. Z. Zhang, *Langmuir*, **2011**,
- [211] S. H. Chi; L. Mazeina; S. M. Prokes; J. D. Caldwell; G. Beadie; S. R. Flom; J. S. Shirk. "Below Bandgap Excitation of SnO₂ Nanowires: The Relaxation of Trap States", 2011.
- [212] B. Liu; C. He; M. Jin; D. Ding; C. Gao, *physica status solidi (b)*, **2011**, *248*, 1102-1105.
- [213] P. T. Landsberg *Recombination in semiconductors*; Cambridge Univ Pr, 2003.
- [214] Y. Masumoto, *Journal of luminescence*, **1996**, *70*, 386-399.
- [215] P. Palinginis; H. Wang, *Appl. Phys. Lett*, **2001**, *78*, 1541-1543.
- [216] R. Schoenlein; D. Mittleman; J. Shiang; A. Alivisatos; C. Shank, *Physical Review Letters*, **1993**, *70*, 1014-1017.
- [217] D. Mittleman; R. Schoenlein; J. Shiang; V. Colvin; A. Alivisatos; C. Shank, *Physical Review B*, **1994**, *49*, 14435.
- [218] M. Toutounji, *The Journal of Physical Chemistry C*, **2010**,
- [219] G. Stock, *The Journal of Chemical Physics*, **1994**, *101*, 246.

- [220] L. Allen; J. H. Eberly *Optical resonance and two-level atoms*; Dover Publications, 1987.
- [221] M. Bawendi; W. Wilson; L. Rothberg; P. Carroll; T. M. Jedju; M. Steigerwald; L. Brus, *Physical Review Letters*, **1990**, *65*, 1623-1626.
- [222] K. Kang; A. Kepner; Y. Hu; S. Koch; N. Peyghambarian; C. Y. Li; T. Takada; Y. Kao; J. Mackenzie, *Applied Physics Letters*, **1994**, *64*, 1487-1489.
- [223] Y. Masumoto; K. Sonobe, *Physical Review B*, **1997**, *56*, 9734.
- [224] J. Oudar; D. Hulin; A. Migus; A. Antonetti; F. Alexandre, *Physical Review Letters*, **1985**, *55*, 2074-2077.
- [225] D. Kovalev; H. Heckler; B. Averboukh; M. Ben-Chorin; M. Schwartzkopff; F. Koch, *Physical Review B*, **1998**, *57*, 3741.
- [226] H. Giessen; B. Fluegel; G. Mohs; Y. Hu; N. Peyghambarian; U. Woggon; C. Klingshirn; P. Thomas; S. Koch, *JOSA B*, **1996**, *13*, 1039-1044.
- [227] L. J. McKimmie; C. N. Lincoln; J. Jasieniak; T. A. Smith, *The Journal of Physical Chemistry C*, **2009**, *114*, 82-88.
- [228] H. Tahara; Y. Ogawa; F. Minami, *Physical Review Letters*, **2011**, *107*, 37402.
- [229] S. Xu; A. Mikhailovsky; J. Hollingsworth; V. Klimov, *Physical Review B*, **2002**, *65*, 045319.
- [230] P. Yu; J. M. Nedeljkovic; P. A. Ahrenkiel; R. J. Ellingson; A. J. Nozik, *Nano Letters*, **2004**, *4*, 1089-1092.

- [231] A. W. Schill; C. S. Gaddis; W. Qian; M. A. El-Sayed; Y. Cai; V. T. Milam; K. Sandhage, *Nano Letters*, **2006**, *6*, 1940-1949.
- [232] V. Klimov; A. Mikhailovsky; D. McBranch; C. Leatherdale; M. Bawendi, *Physical Review B*, **2000**, *61*, 13349-13352.
- [233] J. Stewart; L. Padilha; D. Lee; B. Khanal; J. Pietryga; V. Klimov, *Bulletin of the American Physical Society*, **2011**, *56*,
- [234] V. Chikan; D. Kelley, *Nano Letters*, **2002**, *2*, 1015-1020.
- [235] M. T. Mihnev; W. Fung; W. Lu; T. B. Norris. "Ultrafast Optical-Pump Terahertz-Probe Spectroscopy of Oriented Ge and Ge/Si Core/Shell Nanowires", 2011.
- [236] Y. Yan; G. Chen; P. G. Van Patten, *The Journal of Physical Chemistry C*, **2011**,
- [237] A. Avidan; I. Pinkas; D. Oron, *ACS Nano*, **2012**, *6*, 3063-3069.
- [238] V. Klimov; A. Mikhailovsky; D. McBranch; C. Leatherdale; M. Bawendi, *Science*, **2000**, *287*, 1011-1013.
- [239] C. Burda; S. Link; M. Mohamed; M. El-Sayed, *The Journal of Physical Chemistry B*, **2001**, *105*, 12286.
- [240] M. O'Neil; J. Marohn; G. McLendon, *Chemical Physics Letters*, **1990**, *168*, 208-210.
- [241] V. Klimov; P. H. Bolivar; H. Kurz, *Physical Review B*, **1996**, *53*, 1463.

- [242] S. Logunov; T. Green; S. Marguet; M. El-Sayed, *The Journal of Physical Chemistry A*, **1998**, *102*, 5652-5658.
- [243] K. Wu; H. Zhu; Z. Liu; W. Rodríguez-Córdoba; T. Lian, *Journal of the American Chemical Society*, **2012**, *134*, 10337-10340.
- [244] Y. Yan; L. Wang; C. B. Vaughn; G. Chen; P. G. Van Patten, *The Journal of Physical Chemistry C*, **2011**, *115*, 24521-24527.
- [245] P. Kambhampati, *The Journal of Physical Chemistry C*, **2011**, *115*, 22089-22109.
- [246] P. Guyot-Sionnest; M. Shim; C. Matranga; M. Hines, *Physical Review B*, **1999**, *60*, 2181-2184.
- [247] V. Klimov; C. Schwarz; D. McBranch; C. White, *Appl. Phys. Lett.*, **1998**, *73*, 2603.
- [248] X. Zhao; O. Schoenfeld; S. Nomura; S. Komuro; Y. Aoyagi; T. Sugano, *Materials Science and Engineering: B*, **1995**, *35*, 467-471.
- [249] M. B. Mohamed; C. Burda; M. A. El-Sayed, *Nano Letters*, **2001**, *1*, 589-593.
- [250] S. Sadhu; A. Patra, *The Journal of Physical Chemistry C*, **2011**, *115*, 16867-16872.
- [251] M. W. Graham; J. Chmeliov; Y. Z. Ma; H. Shinohara; A. A. Green; M. C. Hersam; L. Valkunas; G. R. Fleming, *The Journal of Physical Chemistry B*, **2010**, *115*, 5201-5211.

- [252] A. Mandal; J. Nakayama; N. Tamai; V. Biju; M. Isikawa, *The Journal of Physical Chemistry B*, **2007**, *111*, 12765-12771.
- [253] J. Z. Zhang; R. H. O'Neil; T. W. Roberti, *The Journal of Physical Chemistry*, **1994**, *98*, 3859.
- [254] D. E. Skinner; D. P. Colombo; J. J. Cavaleri; R. M. Bowman, *J. Phys. Chem.*, **1995**, *99*, 7853-7856.
- [255] R. C. Fitzmorris; G. Larsen; D. A. Wheeler; Y. Zhao; J. Z. Zhang, *The Journal of Physical Chemistry C*, **2012**,
- [256] V. I. Klimov, *The Journal of Physical Chemistry B*, **2000**, *104*, 6112-6123.
- [257] Y. Yang; W. Rodríguez-Córdoba; T. Lian, *Nano Letters*, **2012**, *12*, 4235-4241.
- [258] I. Robel; B. A. Bunker; P. V. Kamat; M. Kuno, *Nano Letters*, **2006**, *6*, 1344-1349.
- [259] J. M. Luther; M. C. Beard; Q. Song; M. Law; R. J. Ellingson; A. J. Nozik, *Nano Letters*, **2007**, *7*, 1779.
- [260] A. Luque; A. Martí; A. J. Nozik, *MRS Bulletin*, **2007**, *32*, 236-241.
- [261] G. Allan; C. Delerue, *Physical Review B*, **2006**, *73*, 205423.
- [262] J. E. Murphy; M. C. Beard; A. G. Norman; S. P. Ahrenkiel; J. C. Johnson; P. Yu; O. I. Micic; R. J. Ellingson; A. J. Nozik, *Journal of the American Chemical Society*, **2006**, *128*, 3241.

- [263] M. C. Beard; A. G. Midgett; M. C. Hanna; J. M. Luther; B. K. Hughes; A. J. Nozik, *Nano Letters*, **2010**,
- [264] R. J. Ellingson; M. C. Beard; J. C. Johnson; P. Yu; O. I. Micic; A. J. Nozik; A. Shabaev; A. L. Efros, *Nano Letters*, **2005**, *5*, 865.
- [265] A. J. Nozik, *Chemical Physics Letters*, **2008**, *457*, 3.
- [266] M. C. Beard; K. P. Knutsen; P. Yu; J. M. Luther; Q. Song; W. K. Metzger; R. J. Ellingson; A. J. Nozik, *Nano Letters*, **2007**, *7*, 2506.
- [267] M. C. Beard; P. K. Kelly; Y. Pingrong; S. Qing; M. L. Joseph; J. E. Randy; J. N. Arthur. "Multiple Exciton Generation in Silicon Nanocrystals"; *Frontiers in Optics*, 2007.
- [268] R. D. Schaller; M. Sykora; S. Jeong; V. I. Klimov, *The Journal of Physical Chemistry B*, **2006**, *110*, 25332-25338.
- [269] A. Shabaev; A. L. Efros; A. Nozik, *Nano Letters*, **2006**, *6*, 2856-2863.
- [270] P. Tyagi; P. Kambhampati, *The Journal of Chemical Physics*, **2011**, *134*, 094706-094710.
- [271] M. C. Beard; A. G. Midgett; M. Law; O. E. Semonin; R. J. Ellingson; A. J. Nozik, *Nano Letters*, **2009**, *9*, 836-845.
- [272] M. Sykora; A. Y. Kuposov; J. A. McGuire; R. K. Schulze; O. Tretiak; J. M. Pietryga; V. I. Klimov, *ACS Nano*, **2010**, *4*, 2021-2034.
- [273] S. J. O. Hardman; D. M. Graham; S. K. Stubbs; B. F. Spencer; E. A. Seddon; H. T. Fung; S. Gardonio; F. Sirotti; M. G. Silly; P. O'Brien, *Physical Chemistry Chemical Physics*, **2011**, *13*, 20275-20283.

- [274] J. A. McGuire; M. Sykora; J. Joo; J. M. Pietryga; V. I. Klimov, *Nano Letters*, **2010**, *10*, 2049-2057.
- [275] I. Robel; M. Kuno; P. V. Kamat, *Journal of the American Chemical Society*, **2007**, *129*, 4136-4137.
- [276] N. s. Guijarro; Q. Shen; S. Giménez; I. n. Mora-Seró; J. Bisquert; T. Lana-Villarreal; T. Toyoda; R. Gómez, *The Journal of Physical Chemistry C*, **2010**, *114*, 22352-22360.
- [277] D. R. Pernik; K. Tvrdy; J. G. Radich; P. V. Kamat, *The Journal of Physical Chemistry C*, **2011**, *115*, 13511-13519.
- [278] R. S. Dibbell; D. F. Watson, *The Journal of Physical Chemistry C*, **2009**, *113*, 3139-3149.
- [279] B. C. Fitzmorris; G. K. Larsen; D. A. Wheeler; Y. Zhao; J. Z. Zhang, *The Journal of Physical Chemistry C*, **2012**, *116*, 5033-5041.
- [280] L. Brus, *The Journal of Chemical Physics*, **1983**, *79*, 5566.
- [281] M. C. Brelle; J. Z. Zhang, *The Journal of Chemical Physics*, **1998**, *108*, 3119-3126.
- [282] M. Jones; S. S. Lo; G. D. Scholes, *Proceedings of the National Academy of Sciences*, **2009**, *106*, 3011.
- [283] M. A. Stevens; C. Silva; D. M. Russell; R. H. Friend, *Physical Review B*, **2001**, *63*, 165213.
- [284] B. G. Sumpter; P. Kumar; A. Mehta; M. D. Barnes; W. A. Shelton; R. J. Harrison, *The Journal of Physical Chemistry B*, **2005**, *109*, 7671-7685.

- [285] V. Klimov; J. McGuire; R. Schaller; V. Rupasov, *Physical Review B*, **2008**, *77*, 195324.
- [286] M. Grundmann; R. Heitz; D. Bimberg; J. Sandmann; J. Feldmann, *physica status solidi (b)*, **1997**, *203*, 121-132.
- [287] G. Wang; S. Fafard; D. Leonard; J. Bowers; J. Merz; P. Petroff, *Applied Physics Letters*, **1994**, *64*, 2815-2817.
- [288] F. Adler; M. Geiger; A. Bauknecht; F. Scholz; H. Schweizer; M. Pilkuhn; B. Ohnesorge; A. Forchel, *Journal of Applied Physics*, **1996**, *80*, 4019-4026.
- [289] S. Grosse; J. Sandmann; G. Von Plessen; J. Feldmann; H. Lipsanen; M. Sopanen; J. Tulkki; J. Ahopelto, *Physical Review B*, **1997**, *55*, 4473.
- [290] K. Mukai; N. Ohtsuka; H. Shoji; M. Sugawara, *Applied Physics Letters*, **1996**, *68*, 3013-3015.
- [291] K. Hyeon-Deuk; O. V. Prezhdo, *ACS Nano*, **2012**, *6*, 1239-1250.
- [292] F. Vietmeyer; P. A. Frantsuzov; B. Janko; M. Kuno, *Physical Review B*, **2011**, *83*, 115319.

CHAPTER 9. Ultrafast Exciton Dynamics in Silicon Nanowires

9.1 Abstract

Ultrafast exciton dynamics in one-dimensional (1D) silicon nanowires (SiNWs) have been investigated using femtosecond transient absorption techniques. A strong transient bleach feature was observed from 500 to 770 nm following excitation at 470 nm. The bleach recovery was dominated by an extremely fast feature that can be fit to a triple exponential with time constants of 0.3, 5.4, and ~ 75 ps which are independent of probe wavelength. The amplitude and lifetime of the fast component were excitation intensity-dependent, with the amplitude increasing more than linearly and the lifetime decreasing with increasing excitation intensity. The fast decay is attributed to exciton-exciton annihilation upon trap state saturation. The threshold for observing this nonlinear process is sensitive to porosity and surface properties of the sample. To help gain insights into the relaxation pathways, a four-state kinetic model was developed to explain the main features of the experimental dynamics data. The model suggests that after initial photoexcitation, conduction band (CB) electrons become trapped in the shallow trap (ST) states within 0.5 ps and are further trapped into deep trap (DT) states within 4 ps. The deep trapped electrons finally recombine with the hole with a time constant of ~ 500 ps, confirming the photophysical processes we assigned the decays to.

9.2 Introduction

Nanostructured silicon has been the focus of recent interest since the discovery of its photoluminescent (PL) properties in 1990 by Canham¹. It has potential applications in biological sensors²⁻⁴, field-effect transistors (FETs)⁵⁻⁷, integrated logic circuits⁸, and photodynamic therapy⁹. Bulk silicon is known to be an indirect bandgap semiconductor¹⁰ with weak PL. Because of this, quantum confinement effects are thought to be the cause of PL in silicon nanocrystals¹¹⁻¹⁴. Surface effects have also been suggested to play an important role in PL of nanostructured Si¹⁵⁻¹⁸. For instance, cathode luminescence and time-resolved PL spectroscopy have shown that luminescence in SiNWs is due to interface states and surface radiative recombination centers located at the interface of the silicon core and the SiO₂ cladding layer^{19,20}.

Ultrafast dynamics of excitons and charge carriers in nanostructured silicon have been studied, particularly in relation to its PL properties. Fast carrier thermalization times of ~150 fs *via* phonon emission have been seen before²¹ along with intraband relaxation times of ~240 fs²². Silicon grains showed a fast decay component of 400 fs, attributed to the quenching of the interior exciton radiative recombination by carrier trapping,²³ while another study found a 500 fs component attributed to nanocrystallite defect scattering²⁴. Other investigations observed a femtosecond component which was proposed to be due to molecule-like silicon complexes or clusters in the material^{25,26}. Additionally, a feature that decayed in ~3 ps was monitored and found to be dependent on the porosity of the sample²⁷.

One-dimensional (1D) silicon structures, such as nanowires, in particular hold interest over zero-dimensional (0D) structures due to their potential advantage of

better charge transport along the long axis, which is important for certain applications such as nanoscale transistors^{6,28,29}, sensors^{4,30}, power sources³¹ and battery anodes³². Despite this, little work has been done on the ultrafast dynamics of excitons and charge carriers in 1D porous silicon nanowires (SiNWs).

In this work, we studied the early time exciton dynamics of 1D SiNWs using ultrafast laser techniques. The ultrafast exciton dynamics are dominated by an extremely fast feature that can be fit with a triple exponential with fast and slow components. The threshold for observing the fast component (~ 300 fs), attributed to nonlinear exciton-exciton annihilation, was found to be dependent on pump power. The slower and pump power-independent decay, ~ 5 ps, is attributed to exciton relaxation from the ST to the DT. A much slower and small amplitude delay with a time constant on the order of ~ 75 ps is likely associated with recombination from the DT to the valence band (VB) and is related to the weak PL observed. Finally, a kinetic modeling scheme was developed that supports the experimental decay profiles and mechanism and helps account for the main features of the experimental dynamics.

9.3 Results

Figure 1 shows SEM and TEM images of the 1-D SiNWs. Figure 1a reveals vertically aligned SiNWs with a length of approximately $15 \mu\text{m}$ and an average diameter of ~ 150 nm. The SiNWs shown in Figures 1b-e exhibit a high degree of surface roughness, porosity, and polycrystallinity and are covered by a cladding layer

of SiO₂. High-resolution TEM (HRTEM) shows the irregularly-shaped pores of the SiNWs which are 5 to 10 nm in size. Image analysis indicates an average porosity of ~18% for the SiNWs.

Figure 1. (a) SEM and (b-e) TEM images of 1D silicon nanowires that show vertical alignment (a) as well as a mesoporous structure (b-e).

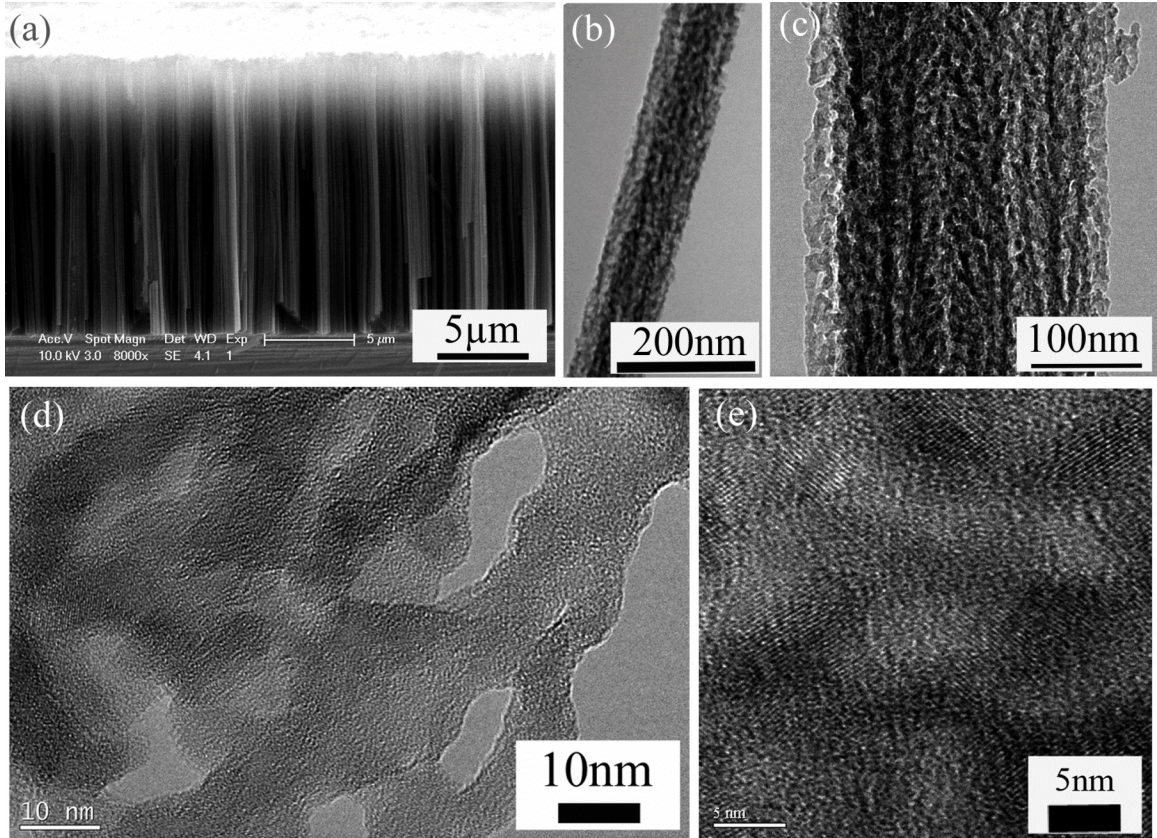


Figure 2 shows the PL spectrum (red line) of the SiNWs which displays weak NIR emission with peaks centered at 732 and 800 nm that are in good agreement with previously reported spectra³³⁻³⁵. The small peak at 732 nm arises from the SiNWs' thin oxide coating while the broad peak at 805 nm is likely due to the emission from the localized excitation in the porous sample³³. Figure 2 also displays the UV-Vis spectrum (blue line) of the SiNWs that shows a broad absorption ranging from 300 to 800 nm with a peak centered near 460 nm. The spectrum of the SiNWs matches well with previously reported spectra for NWs and shows a long absorption tail persisting beyond 800 nm attributed to the indirect nature of the bandgap³⁶.

Figure 2. Electronic absorption (blue line) and fluorescence (red line, with $\lambda_{\text{ex}} = 514.5$ nm) spectra.

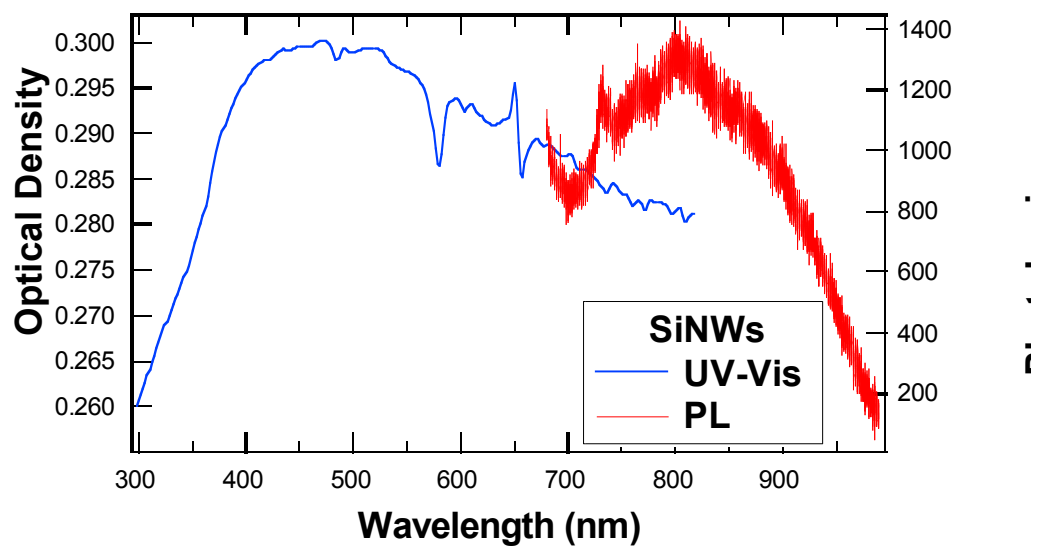


Figure 3 is a 3D plot of the transient time decay profile (in ps) for the SiNWs following excitation at 470 nm (maintained at a pulse energy of 200 nJ/pulse) at probe wavelengths of 600-700 nm. A pulse-width-limited (<180 fs) transient bleach is followed by an exponential fast recovery (~0.3 ps) a slow exponential recovery (~ 5 ps), and a third small amplitude, slower (~75 ps) exponential recovery. Similar decay profiles have been observed for other pump powers including the notion that the amplitude and time constant for the fast component change with pump power. The transient bleach data showed that the observed time constants are independent of probe wavelength while their amplitudes vary with probe wavelength, indicating that the transient species has a broad spectrum and the spectral intensity is wavelength dependent. Figure 3 also shows that the maximum intensity of the signal is larger for redder probe wavelengths, increasing by ~60% over a span of 100 nm.

Figure 3. 3D transient bleach relaxation traces of 1D SiNWs at probe wavelengths spanning 600-700 nm following a 470 nm, 200 nJ/pulse pump.

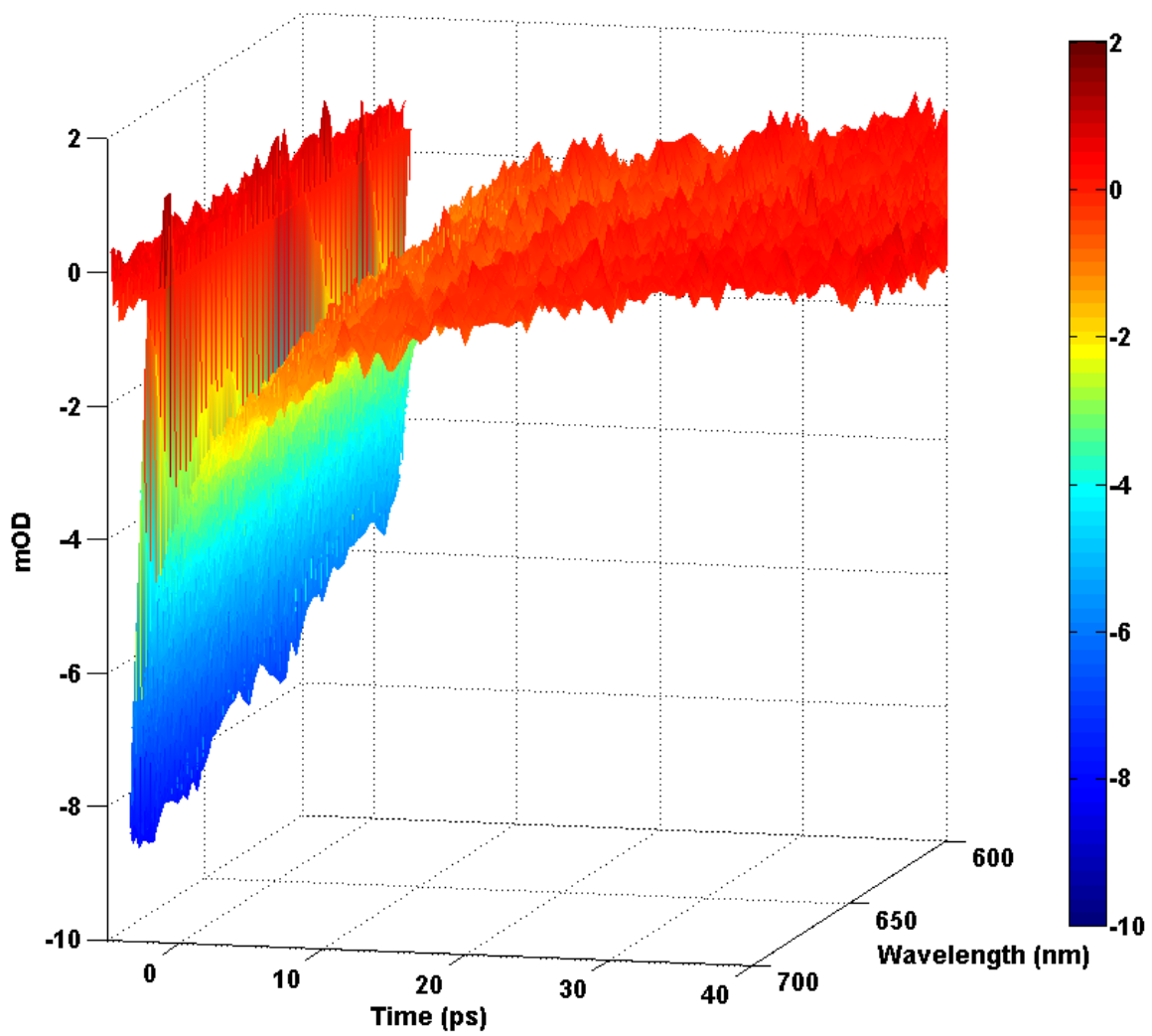
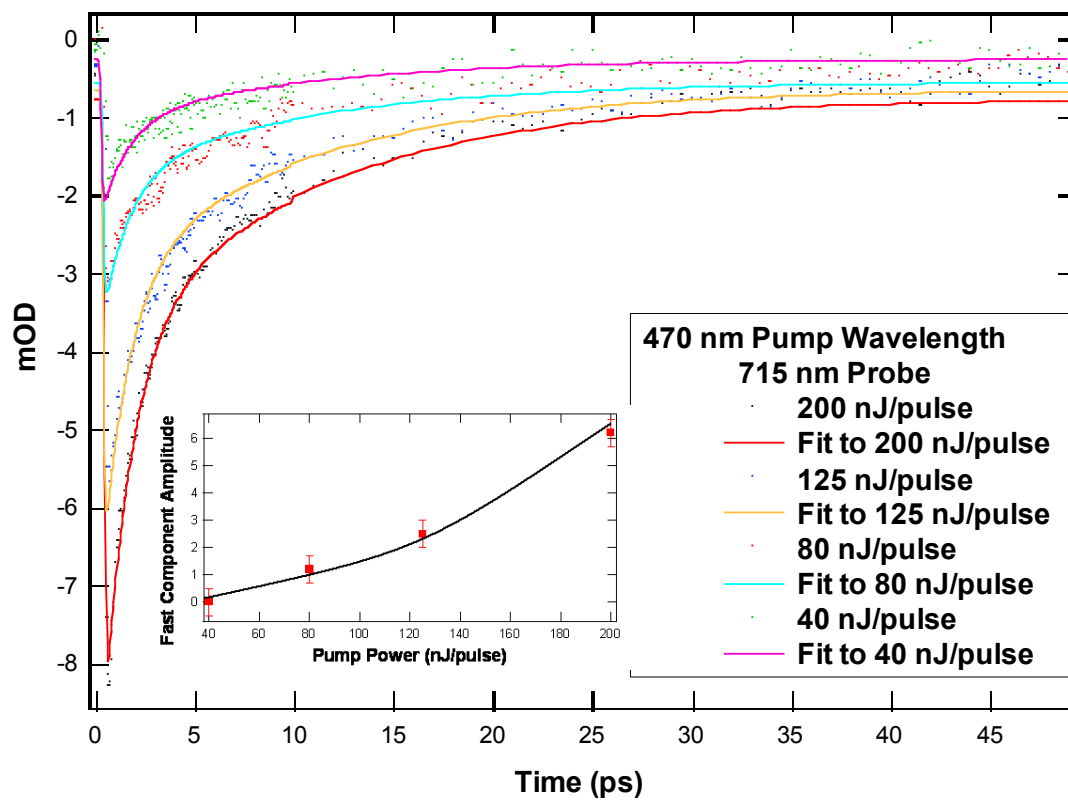


Figure 4 shows that as the pump power was decreased from 200 nJ/pulse to 125, 80, and 40 nJ/pulse, the amplitude of the fast component decreased superlinearly. Additionally, while the 200 nJ/pulse's fast decay component was 0.3 ps, the 125 and 80 nJ/pulse data had fast components of 0.5 and 1.8 ps, slow components of 6.9 and 8.6 ps, and long-time components of ~ 75 ps. Finally, for the lowest pump power of 40 nJ/pulse, the fast component had disappeared, making the 40 nJ/pulse data a biexponential decay comprised solely of the two slow decay components with time constants of 9.2 and ~ 75 ps. Figure 4 and its inset also show that the amplitude of the fast component increases faster than that of the slower component with increased excitation intensities. For the reported lifetimes, a nominal error of $\sim 10\%$ is ascribed to the data.

Figure 4. Transient bleach relaxation traces of 1D SiNWs at a probe wavelength of 715 nm at powers of 200, 125, 80, and 40 nJ/pulse following a 470 nm pump. Inset: Nonlinear power dependence of the maximum intensity of the signal as a function of pulse power following a 470 nm excitation and 715 nm probe.



9.4 Discussion

PL spectroscopy indicated that the SiNWs are weakly luminescent. Two factors are responsible for high PL in nanostructured silicon: increased porosity³³ and passivation of the surface with an oxide layer³⁷. Studies have shown a dependence of PL intensity on the porosity of the silicon^{25,27}. The stronger trap state emission from the porosity is associated with a net increase in the number of trap states. Therefore, more porous SiNWs can be expected to have increased trap state PL. However, passivation of the surface of the SiNWs with an oxide layer will lead to a decreased density of deep trap states, resulting in a net decrease in trap state PL intensity. Nevertheless, the PL that is observed (modeled in Figure 5) is believed to arise from the recombination from the Si/SiO₂ interface states, which act as deep traps, for which this assignment has been made before^{19,20}. SiNW samples with lower relative porosity will thus have low overall PL yet will exhibit characteristic SiO₂ peaks (Figure 2).

Our dynamics data show that the lifetime of the fast component decreases with increasing pump power (Figure 4). This is similar to what has been observed in previous studies of CdS quantum dots by Roberti *et al.*³⁸. With further increasing pump power, higher order kinetic processes can take place and result in faster decay or even shorter lifetime³⁹⁻⁴¹. Nonlinear behaviors, such as exciton-exciton annihilation, occur when multiple excitons are generated where there is strong interaction between the excitons. This is typically reflected as an ultrafast dynamic process with a lifetime of hundreds of fs up to a few ps and depends nonlinearly on

the excitation light intensity^{39,41,42}. The reported nonlinear decay kinetics can change considerably depending upon the system being studied. For example, TiO₂ nanoclusters have reported lifetimes of 0.5 ps⁴³, AgI/Ag₂S core/shell particles with lifetimes of 0.8 ps⁴⁴, and CdS quantum dots with lifetimes of 2.5 ps³⁹.

In the meantime, the amplitude of the fast component grows more than linearly with increasing pump power (inset, Figure 4). The nonlinear increase in amplitude for the fast component with excitation intensity is also consistent with nonradiative exciton-exciton annihilation or Auger recombination, similar to what has been observed in other semiconductor nanostructures previously^{38,45-47}. At low pump power, excitons generated can quickly dissociate into electrons and holes that can be trapped into trap states^{48,49}. As

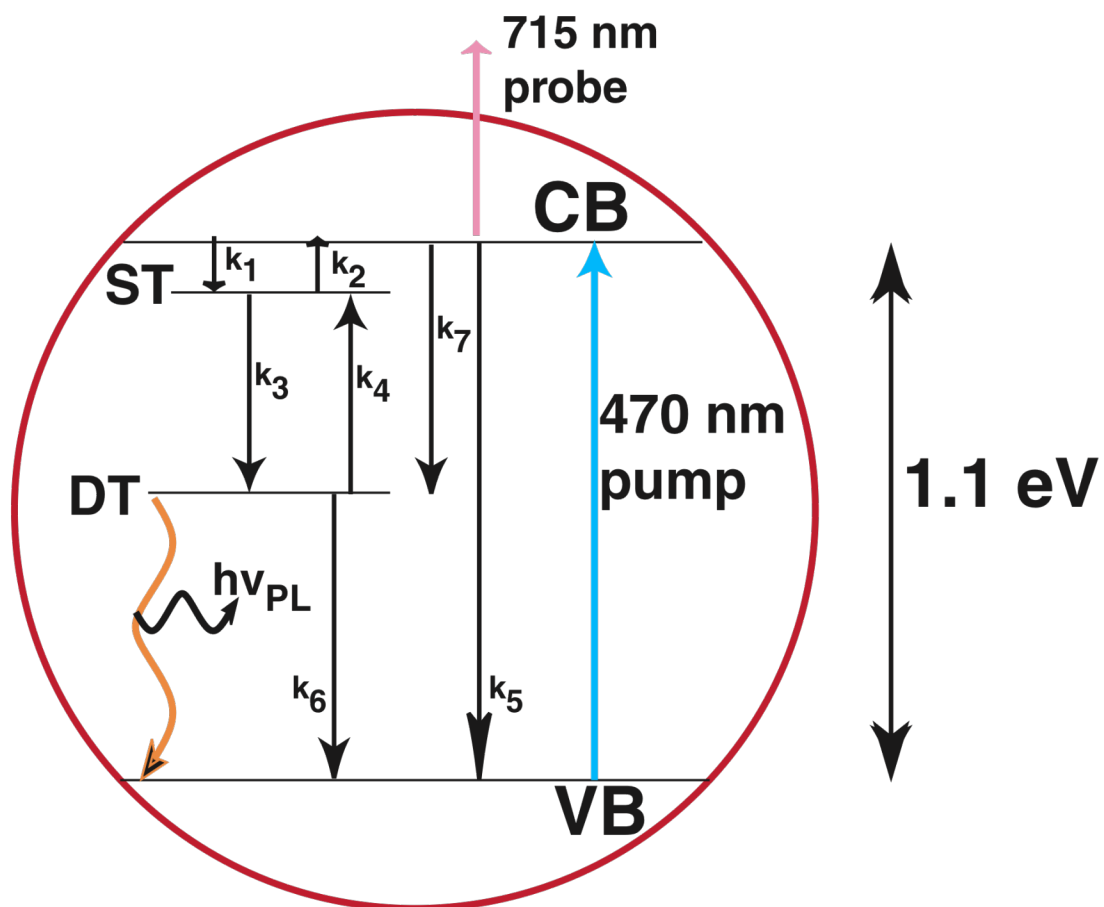
the pump power is increased, an increased number of excitons are generated per particle or NW, which could generate enough electrons and holes to saturate the trap states. Upon saturation of the trap states, excitons can accumulate and exciton-exciton annihilation can occur, which is often reflected as a pump power-dependent fast decay in transient absorption measurements^{38,45}. The slower 5 ps decay observed for SiNWs in this study is assigned to nonradiative recombination from trap states⁵⁰. The recombination time is relatively short due to a high density of trap states that mediate the decay. Finally, the longer decay of ~75 ps is likely due to the presence of a high density of deep trap states or defect states.

Figure 5 is an energy model diagram for the SiNWs. After an initial 470 nm pump, a decay with an average of 5 ps occurs. Following that process, a slower 75 ps

decay takes place. The faster 5 ps decay is attributable to nonradiative exciton decay or electron-hole recombination mediated by trap states occurs while a slower 75 ps decay related to deep trapping occurs. We believe the 75 ps component is related to the weak PL.

Figure 5. Proposed model for energy levels related to the optical properties and dynamics studies. CB and VB represent the conduction band and valence band, respectively, while ST represents shallow trap DT stands for deep trap related to the Si-SiO₂ interface. At low power, the pump laser beam excites an electron from the VB into the CB, which is followed by nonradiative exciton decay or electron-hole recombination mediated by shallow and deep trap states. At high pump power, an additional, faster delay, attributed to exciton-exciton annihilation, takes place. The observed weak PL is attributed to radiative recombination from deep trap states related to the Si-SiO₂ interface.

Silicon NWs



To gain further insight into the energy relaxation mechanism of the SiNWs, we utilized a four-state kinetic scheme to model the observed dynamics, as shown in Figure 5 and explained in more detail in the Supplemental Information. The proposed scheme includes the valence band (VB), conduction band (CB), shallow traps (ST), and deep traps (DT). After combining the contributions of each of the states at varying percentages with a set of rate constants, we were able to closely model our experimental data. The rate constants were chosen based on the experimental results in this Letter as well as other experiments^{23,51-53}.

In modeling the data for the SiNWs, the VB needs to be explicitly included since it is probed by the probe pulse and is reflected as a transient bleach signal. By combining 30% contribution from the VB, 30% from the CB, and 20% from both the STs and DTs, a curve could be generated which modeled closely our observed data. It should be noted that the model, as constructed, works for low laser power only. This is because adequate modeling at progressively higher powers would require an additional state to account for exciton-exciton annihilation, which is a second-order process.

In terms of the mechanism of the modeled decay, and from the final rate constants determined by comparing the modeled data with the experimental data, we are able to unambiguously assign rate constants to the key physical processes shown in Figure 5. In particular, the time constant from the CB to the ST was modeled to be 0.5 ps, while the decay from the ST to the DT is 4 ps and the DT to VB was 500 ps. Although the time constants may not be unique due to several assumptions made in

the modeling scheme, we believe they are indicative of key physical processes that are occurring during the transient absorption decay profile.

In modeling the dynamics at low power, we discovered that the saturation of the STs results in accumulation of electrons in the CB. The result is that it increases the transient absorption over the bleach. Overall, this is most likely because the relaxation from the CB to the ST is an order of magnitude faster than that from the ST to the DT, and high-intensity excitation facilitates the accumulation of electrons in the ST states. This thereby leads to ST saturation more easily than that of DT. From modeling the individual states, we generated a series of plots which represent individual components that, when added, generates an overall curve that models the experimental data (Figure S1). Fitting the overall modeled curve with the same algorithm that fit the experimental data generated time constants, effectively allowing for a direct comparison between modeled and experimental data. From the modeled data, we obtained lifetime values of 0.48 ps, 6.4 ps, and 83 ps that support our experimental curve-fitting results with time constants of 0.3 ps, 5 ps, and ~75 ps. Any discrepancy is likely due to the model being a first-approximation. Nevertheless, both modeled as well as experimental data seem to reflect one another well.

Finally, in comparison to previous studies of high-power, nonlinear dynamical exciton dynamics of silicon nanoparticles^{17,51,52,54} (SiNPs), the SiNWs seem to show a faster average decay time. Although rigorous quantitative comparisons are not easy since factors such as the laser power, spot size, and the surface conditions of the samples can be different and are important, faster exciton-exciton annihilation may be

anticipated for SiNWs. This is because SiNWs are larger than typical SiNPs, and a stronger nonlinear effect is expected due to a higher number of excitons generated in one SiNW than in a SiNP, assuming the samples have similar optical density and similar surface properties in terms of density of trap states⁵⁵.

Ultrafast exciton dynamics in SiNWs were studied using transient absorption pump-probe spectroscopy. A broad transient bleach was observed for probe wavelengths in the range of 500-770 nm following an initial excitation wavelength of 470 nm and can be fit to a triple exponential decay of 0.3, 5.4, and ~75 ps. The time constants were probe wavelength-independent, indicating broad absorption features of the transient species probed. Power dependence studies showed that the amplitude of the fast component increases superlinearly with increasing pump power, indicating a nonlinear process that is attributed to exciton-exciton annihilation upon trap state saturation. Despite the porosity of the sample, the surface passivation of the SiNWs with an oxide layer is believed to be critical in determining the threshold for observing exciton-exciton annihilation. Kinetic modeling of the relaxation mechanism of the SiNWs reinforced our experimental data fitting and also provided insights into the mechanism of the decay profile evolution of each of the states over time. The modeling determined that the relaxation from the CB to the ST occurred after 500 fs, while the ST-to-DT relaxation transition occurs with a time constant of 4 ps, and the DT-to-VB relaxation occurs with a time constant of 500 ps. These modeled findings are important in that they aid in assigning physical processes to

time constants in the experimental data, helping unambiguously determine the major relaxation mechanism.

9.6 Methods

9.6.1 SiNW Preparation

The SiNWs were synthesized by using electrochemical etching techniques following a previously reported synthetic protocol.⁵⁶ Briefly, a clean n-Si(100) wafer with 0.005–0.02 $\Omega\cdot\text{cm}$ resistivity was immersed in a silver deposition solution containing 4.8M HF and 0.005M AgNO₃ for 1 minute, and then etched in 4.8M HF and 0.3 M H₂O₂ for 30 minutes. The dried SiNWs were cut off from the wafer and dispersed in approximately 100 μL of ethanol and sonicated for 30 minutes. Subsequently, 25 μL of the dispersed SiNWs were dried on a ZrO₂ film. The procedure was repeated once again to increase the SiNW film thickness until a yellow-brown color was observed.

9.6.2 UV-Vis, Electron Microscopy (EM), and PL Measurements

UV-Vis spectra of the dried, deposited SiNWs were collected using an HP 8452A diode array spectrophotometer with spectral resolution set at 2 nm. Scanning electron microscopy (SEM) was carried out using a Philips XL30 FEG microscope. High-resolution TEM was performed on a Philips CM200-FEG. Porosity was measured using imageJ⁵⁷. The PL spectra of the SiNWs were collected on a Renishaw InVia Raman microscope system using an excitation wavelength of 514.5 nm (Ar⁺).

9.6.3 Femtosecond laser System and Transient Absorption Measurements

Ultrafast transient bleach measurements were conducted using an amplified femtosecond Ti-sapphire laser system described previously⁵⁸. In all experiments, a pump wavelength of 470 nm was selected from an OPA (optical parametric amplifier) and used. In the wavelength-dependent study, an output pulse duration of <180 fs and a pulse energy of 200 nJ/pulse was used for all wavelengths used. A white light continuum (WLC) generated from a sapphire crystal was used as the probe pulse that was detected using a CCD detector. Pump power-dependence studies were conducted with pump pulse energies of 200, 125, 80, and 40 nJ/pulse, which were varied using neutral density filters.

9.7 References

- (1) Canham, L. T. Silicon quantum wire array fabrication by electrochemical and chemical dissolution of wafers. *Appl. Phys. Lett.* **1990** *57*, 1046-1048.
- (2) Li, Z.; Chen, Y.; Li, X.; Kamins, T. I.; Nauka, K.; Williams, R. S. Sequence-Specific Label-Free DNA Sensors Based on Silicon Nanowires. *Nano Letters.* **2004**, *4*, 245-247.
- (3) Hahn, J.-i.; Lieber, C. M. Direct Ultrasensitive Electrical Detection of DNA and DNA Sequence Variations Using Nanowire Nanosensors. *Nano Letters.* **2003**, *4*, 51-54.

- (4) Cui, Y.; Wei, Q.; Park, H.; Lieber, C. M. Nanowire Nanosensors for Highly Sensitive and Selective Detection of Biological and Chemical Species. *Science*. **2001**, *293*, 1289-1292.
- (5) Koo, S.-M.; Li, Q.; Edelstein, M. D.; Richter, C. A.; Vogel, E. M. Enhanced Channel Modulation in Dual-Gated Silicon Nanowire Transistors. *Nano Letters*. **2005**, *5*, 2519-2523.
- (6) Cui, Y.; Zhong, Z.; Wang, D.; Wang, W. U.; Lieber, C. M. High Performance Silicon Nanowire Field Effect Transistors. *Nano Letters*. **2003**, *3*, 149-152.
- (7) Duan, X.; Huang, Y.; Lieber, C. M. Nonvolatile Memory and Programmable Logic from Molecule-Gated Nanowires. *Nano Letters*. **2002**, *2*, 487-490.
- (8) Huang, Y.; Duan, X.; Cui, Y.; Lauhon, L. J.; Kim, K.-H.; Lieber, C. M. Logic Gates and Computation from Assembled Nanowire Building Blocks. *Science*. **2001**, *294*, 1313-1317.
- (9) Kovalev, D.; Fuji, M. *Annual Review of Nano Research*; World Scientific: Singapore, 2008; Vol. 159.
- (10) Brus, L. Luminescence of Silicon Materials: Chains, Sheets, Nanocrystals, Nanowires, Microcrystals, and Porous Silicon. *The Journal of Physical Chemistry*. **1994**, *98*, 3575-3581.
- (11) Allan, G.; Delerue, C. Efficient intraband optical transitions in Si nanocrystals. *Physical Review B*. **2002**, *66*, 233303-233306.

- (12) Sa'ar, A.; Dovrat, M.; Jedrzejewski, J.; Balberg, I. Optical inter- and intra-band transitions in silicon nanocrystals: The role of surface vibrations. *Physica E: Low-dimensional Systems and Nanostructures*. **2007**, *38*, 122-127.
- (13) Sa'ar, A.; Reichman, Y.; Dovrat, M.; Krapf, D.; Jedrzejewski, J.; Balberg, I. Resonant Coupling between Surface Vibrations and Electronic States in Silicon Nanocrystals at the Strong Confinement Regime. *Nano Letters*. **2005**, *5*, 2443-2447.
- (14) Wolkin, M. V.; Jorne, J.; Fauchet, P. M.; Allan, G.; Delerue, C. Electronic States and Luminescence in Porous Silicon Quantum Dots: The Role of Oxygen. *Physical Review Letters*. **1999**, *82*, 197-200.
- (15) Kanemitsu, Y.; Suzuki, K.; Uto, H.; Masumoto, Y.; Matsumoto, T.; Kyushin, S.; Higuchi, K.; Matsumoto, H. Visible photoluminescence of silicon-based nanostructures: Porous silicon and small silicon-based clusters. *Appl. Phys. Lett.* **1992**, *61*, 2446-2448.
- (16) Malý, P.; Trojánek, F.; Hospodková, A.; Kohlová, V.; Pelant, I. Transmission study of picosecond photocarrier dynamics in free-standing porous silicon. *Solid State Communications*. **1994**, *89*, 709-712.
- (17) Matsumoto, T.; Wright, O. B.; Futagi, T.; Mimura, H.; Kanemitsu, Y. Ultrafast electronic relaxation processes in porous silicon. *Journal of Non-Crystalline Solids*. **1993**, *164-166*, 953-956.

- (18) Tsybeskov, L.; Vandyshev, J. V.; Fauchet, P. M. Blue emission in porous silicon: Oxygen-related photoluminescence. *Physical Review B*. **1994**, *49*, 7821-7824.
- (19) Dovrat, M.; Arad, N.; Zhang, X. H.; Lee, S. T.; Sa'ar, A. Optical properties of silicon nanowires from cathodoluminescence imaging and time-resolved photoluminescence spectroscopy. *Physical Review B*. **2007**, *75*, 205343-205347.
- (20) Dovrat, M.; Shalibo, Y.; Arad, N.; Popov, I.; Lee, S. T.; Sa'ar, A. Excitonic transitions in silicon nanostructures probed by time-resolved photoluminescence spectroscopy. *physica status solidi (c)*. **2009**, *6*, 1615-1619.
- (21) Dexheimer, S. L.; Zhang, C. P.; Liu, J.; Young, J. E.; Nelson, B. P. Ultrafast Carrier Thermalization in Hydrogenated Amorphous Silicon. *MRS Proc.* **2002**, *715*, A2.1.
- (22) Myers, K. E.; Wang, Q.; Dexheimer, S. L. Ultrafast carrier dynamics in nanocrystalline silicon. *Physical Review B*. **2001**, *64*, 161309-161312.
- (23) Trojánek, F.; Neudert, K.; Malý, P.; Dohnalová, K.; Pelant, I. Ultrafast photoluminescence in silicon nanocrystals studied by femtosecond up-conversion technique. *J. Appl. Phys.* **2006**, *99*, 116108-116110.
- (24) Kovalenko, S. A.; Dobryakov, A. L.; Karavanskii, V. A.; Lisin, D. V.; Merkulova, S. P.; Lozovik, Y. E. Femtosecond Spectroscopy of Porous Silicon. *Phys. Scr.* **1999**, *60*, 589-592.

- (25) Klimov, V.; McBranch, D.; Karavanskii, V. Strong optical nonlinearities in porous silicon: Femtosecond nonlinear transmission study. *Physical Review B*. **1995**, *52*, R16989-R16992.
- (26) Klimov, V. I.; Dneprovskii, V. S.; Karavinskii, V. A. Nonlinear transmission spectra of porous silicon: Manifestation of size quantization. *Appl. Phys. Lett.* **1994**, *64*, 2691-2693.
- (27) Van Dao, L.; Hannaford, P. Femtosecond nonlinear coherence spectroscopy of carrier dynamics in porous silicon. *J. Appl. Phys.* **2005**, *98*, 083508-083512.
- (28) Huang, Y.; Lieber, C. M. Integrated nanoscale electronics and optoelectronics: Exploring nanoscale science and technology through semiconductor nanowires. *Pure Appl. Chem.* **2004**, *76*, 2051-2068.
- (29) Wang, D.; Wang, Q.; Javey, A.; Tu, R.; Dai, H.; Kim, H.; McIntyre, P. C.; Krishnamohan, T.; Saraswat, K. C. Germanium nanowire field-effect transistors with SiO₂ and high-k HfO₂ gate dielectrics. *Appl. Phys. Lett.* **2003**, *83*, 2432-2434.
- (30) Patolsky, F.; Timko, B. P.; Yu, G.; Fang, Y.; Greytak, A. B.; Zheng, G.; Lieber, C. M. Detection, Stimulation, and Inhibition of Neuronal Signals with High-Density Nanowire Transistor Arrays. *Science*. **2006**, *313*, 1100-1104.
- (31) Tian, B.; Zheng, X.; Kempa, T. J.; Fang, Y.; Yu, N.; Yu, G.; Huang, J.; Lieber, C. M. Coaxial silicon nanowires as solar cells and nanoelectronic power sources. *Nature*. **2007**, *449*, 885-889.

- (32) Chan, C. K.; Peng, H.; Liu, G.; McIlwrath, K.; Zhang, X. F.; Huggins, R. A.; Cui, Y. High-performance lithium battery anodes using silicon nanowires. *Nat Nano*. **2008**, *3*, 31-35.
- (33) Lin, L.; Guo, S.; Sun, X.; Feng, J.; Wang, Y. Synthesis and Photoluminescence Properties of Porous Silicon Nanowire Arrays. *Nanoscale Research Letters*. **2010**, *5*, 1822-1828.
- (34) Beard, M. C.; Knutsen, K. P.; Yu, P.; Luther, J. M.; Song, Q.; Metzger, W. K.; Ellingson, R. J.; Nozik, A. J. Multiple Exciton Generation in Colloidal Silicon Nanocrystals. *Nano Letters*. **2007**, *7*, 2506-2512.
- (35) Sivakov, V. A.; Voigt, F.; Berger, A.; Bauer, G.; Christiansen, S. H. Roughness of silicon nanowire sidewalls and room temperature photoluminescence. *Physical Review B*. *82*, 125446-125451.
- (36) Zhang, X.; Tian, H.; He, J.; Fang, X. Spectroscopic Changes of Silicon Nanowires Induced by Femtosecond Laser Pulses. *Chemistry Letters*. **2010**, *39*, 890-891.
- (37) Shih, S.; Jung, K.; Yan, J.; Kwong, D.; Kovar, M.; White, J.; George, T.; Kim, S. Photoinduced luminescence enhancement from anodically oxidized porous Si. *Appl. Phys. Lett.* **1993**, *63*, 3306-3308.
- (38) Roberti, T.; Cherepy, N.; Zhang, J. TI - Nature of the power-dependent ultrafast relaxation process of photoexcited charge carriers in II-VI semiconductor quantum dots: Effects of particle size, surface, and electronic structure. *J. Chem. Phys.* **1998**, *108*, 2143-2151.

- (39) Zhang, J. Z.; O'Neil, R. H.; Roberti, T. W. Femtosecond Studies of Photoinduced Electron Dynamics at the Liquid-Solid Interface of Aqueous CdS Colloids. *The Journal of Physical Chemistry*. **1994**, *98*, 3859-3864.
- (40) Xu, X.; Zhao, Y.; Sie, E. J.; Lu, Y.; Liu, B.; Ekahana, S. A.; Ju, X.; Jiang, Q.; Wang, J.; Sun, H.; Sum, T. C.; Huan, C. *et al.*. Dynamics of Bound Exciton Complexes in CdS Nanobelts. *ACS Nano*. **2011**, *5*, 3660-3669.
- (41) Wheeler, D.; Fitzmorris, B.; Zhao, H.; Ma, D.; Zhang, J. Ultrafast exciton relaxation dynamics of PbS and core/shell PbS/CdS quantum dots. *SCIENCE CHINA Chemistry*. **2011**, *54*, 2009-2015.
- (42) Skinner, D. E.; Colombo, D. P.; Cavaleri, J. J.; Bowman, R. M. Femtosecond Investigation of Electron Trapping in Semiconductor Nanoclusters. *J. Phys. Chem.* **1995**, *99*, 7853-7856.
- (43) Philip Colombo Jr, D.; Roussel, K. A.; Saeh, J.; Skinner, D. E.; Cavaleri, J. J.; Bowman, R. M. Femtosecond study of the intensity dependence of electron-hole dynamics in TiO₂ nanoclusters. *Chemical Physics Letters*. **1995**, *232*, 207-214.
- (44) Brelle, M. C.; Zhang, J. Z. Femtosecond study of photo-induced electron dynamics in AgI and core/shell structured AgI/Ag₂S and AgBr/Ag₂S colloidal nanoparticles. *The Journal of Chemical Physics*. **1998**, *108*, 3119-3126.
- (45) Zheng, J.; Kwok, H. Exciton and biexciton recombination in semiconductor nanocrystals. *Appl. Phys. Lett.* **1994**, *65*, 1151-1153.

- (46) Burda, C.; Link, S.; Mohamed, M.; El-Sayed, M. The pump power dependence of the femtosecond relaxation of CdSe nanoparticles observed in the spectral range from visible to infrared *J. Chem. Phys.* **2002**, *116*, 3828-3833.
- (47) Burda, C.; Link, S.; Green, T. C.; El-Sayed, M. A. New Transient Absorption Observed in the Spectrum of Colloidal CdSe Nanoparticles Pumped with High-Power Femtosecond Pulses. *The Journal of Physical Chemistry B.* **1999**, *103*, 10775-10780.
- (48) Thibert, A. J.; Frame, F. A.; Busby, E.; Larsen, D. S. Primary Photodynamics of Water Solubilized Two-Dimensional CdSe Nanoribbons. *The Journal of Physical Chemistry C.* **2011**, *115*, 19647-19658.
- (49) Liu, R.; Chen, Y.; Wang, F.; Cao, L.; Pan, A.; Yang, G.; Wang, T.; Zou, B. Stimulated emission from trapped excitons in SnO₂ nanowires. *Physica E: Low-dimensional Systems and Nanostructures.* **2007**, *39*, 223-229.
- (50) Grant, C. D.; Zhang, J. Z. *Annual Review of Nano Research*; World Scientific Publisher: Singapore, 2008; Vol. 2.
- (51) Kuntermann, V.; Cimpean, C.; Brehm, G.; Sauer, G.; Kryschi, C.; Wiggers, H. Femtosecond transient absorption spectroscopy of silanized silicon quantum dots. *Physical Review B.* **2008**, *77*, 115343-115350.
- (52) Cimpean, C.; Groenewegen, V.; Kuntermann, V.; Sommer, A.; Kryschi, C. Ultrafast exciton relaxation dynamics in silicon quantum dots. *Laser & Photonics Reviews.* **2009**, *3*, 138-145.

- (53) Owrutsky, J. C.; Rice, J. K.; Guha, S.; Steiner, P.; Lang, W. Ultrafast absorption in free-standing porous silicon films. *Applied Physics Letters*. **1995**, *67*, 1966-1968.
- (54) Klimov, V.; Schwarz, C.; McBranch, D.; White, C. Initial carrier relaxation dynamics in ion-implanted Si nanocrystals: Femtosecond transient absorption study *Appl. Phys. Lett.* **1998**, *73*, 2603-2605.
- (55) Wu, F.; Yu, J. H.; Joo, J.; Hyeon, T.; Zhang, J. Z. Ultrafast electronic dynamics of monodisperse PbS and CdS nanoparticles/nanorods: Effects of size on nonlinear relaxation. *Optical Materials*. **2007**, *29*, 858-866.
- (56) Zhang, M.-L.; Peng, K.-Q.; Fan, X.; Jie, J.-S.; Zhang, R.-Q.; Lee, S.-T.; Wong, N.-B. Preparation of Large-Area Uniform Silicon Nanowires Arrays through Metal-Assisted Chemical Etching. *The Journal of Physical Chemistry C*. **2008**, *112*, 4444-4450.
- (57) Rasband, W. S. imageJ. *imageJ*. **1997-2009**, U.S. National Institute of Health, Bethesda, Maryland, USA, <http://rsb.info.nih.gov/ij/>.
- (58) Newhouse, R. J.; Wang, H.; Hensel, J. K.; Wheeler, D. A.; Zou, S.; Zhang, J. Z. Coherent Vibrational Oscillations of Hollow Gold Nanospheres. *The Journal of Physical Chemistry Letters*. **2011**, *2*, 228-235.

9.8 Supporting Information

9.8.1 Kinetic Modeling of Charge Carrier Dynamics

In order to gain some insights into the physical processes governing the dynamics of charge carriers measured experimentally, we carried out modeling using a simple four-state kinetic model following the work by Brelle *et al.*^{1,2}, as shown in Figure 5 of the main text. Kinetics can be described by a series of differential equations that relate the concentration of charge carriers, *i.e.* electrons in this case, in different states *via* appropriate rate constants. Here, we treat each step, forward or backward, as a first-order process so the rate constant is just inversely proportional to the time constant. The choice of the rate constants may not be unique but is made to match the experimental data through iterative fitting using curves generated from the model. The initial set of rate constants are chosen based on literature values for similar systems³⁻⁶. After several iterations, the final time constants that best fit the experimental data are as follows: $k_1 = 2 \text{ ps}^{-1}$, $k_2 = 0.1 \text{ ps}^{-1}$, $k_3 = 2.5 \times 10^{-1} \text{ ps}^{-1}$, $k_4 = 2.5 \times 10^{-2} \text{ ps}^{-1}$, $k_5 = 1 \times 10^{-3} \text{ ps}^{-1}$, $k_6 = 2 \times 10^{-3} \text{ ps}^{-1}$, and $k_7 = 2 \times 10^{-3} \text{ ps}^{-1}$.

Several assumptions were made regarding the modeling in order to compare to the experimental data in a manner that is simple and yet able to provide some new insights. First, we assumed the absorption cross-section of each state to be equivalent. In doing this, the modeled signal is proportional to only the carrier concentration. Second, we assume that the backward rate constants are approximately an order of magnitude smaller than the forward rate constants. This is simply because the carriers are expected to relax more easily from a high energy state to a lower energy state than the other way around. Finally the initial state with population (conduction band, or CB) is assumed to have a positive signal value

(chosen as 1.0 for convenience) with the two intragap states: shallow trap and deep trap (ST, DT, respectively) with zero initial population have signal value of zero. Lastly, the valence band (VB) with a negative initial population has a signal value of -1. In a transient absorption (TA) measurement, however, the signal for the VB is manifested as -1 (known as a bleach signal) due to the way TA works and the manner we plot our data (transient absorption as a positive signal and transient bleach as a negative signal). In this scheme of presenting the data, an increase in population for a given state over time goes with a positive slope of the data curve, while a decrease in population over time is associated with a negative slope of the data curve.

The initial time constants used for generating the model data using the following equations are estimates or “guesses” based upon the apparent time constants that were generated from mathematical fitting of the experimental data as well as time constants previously reported for other semiconductor nanostructure³⁻⁶.

$$d[CB]/dt = -k_1[CB] + k_2[ST] - k_5[CB] - k_7[CB]$$

$$d[ST]/dt = k_1[CB] - k_2[ST] - k_3[ST] + k_4[DT]$$

$$d[DT]/dt = k_3[ST] - k_4[DT] - k_6[DT] + k_7[CB]$$

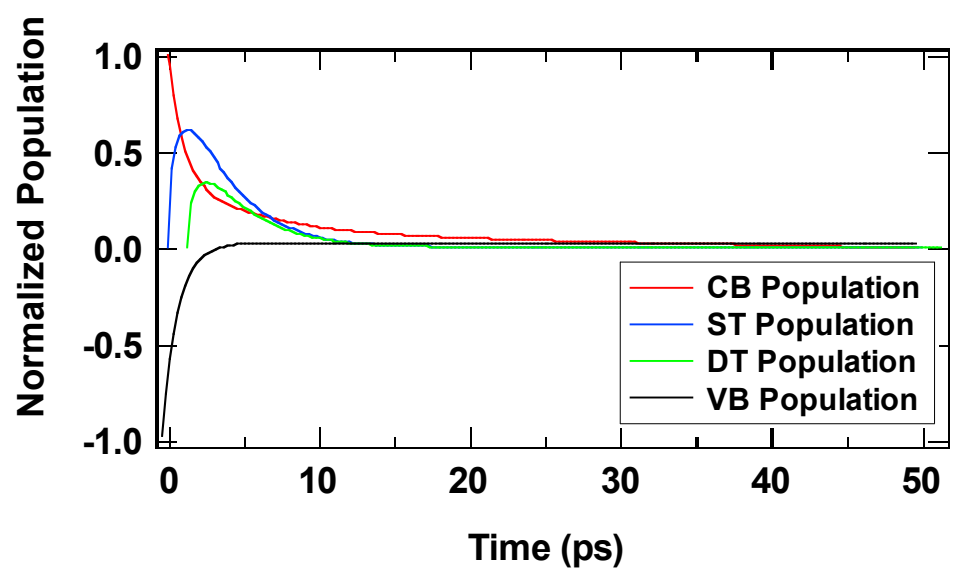
$$d[VB]/dt = k_5[DT] + k_6[CB]$$

Where [CB], [ST], [DT], and [VB] refer to the concentrations of the conduction band, shallow trap, deep trap, and valence band, respectively. The solutions to these equations yield curves for the population of each state as a function of time, akin to a “basis set.” The contribution is the initial concentration of the state and was normalized to the CB, *e.g.* [CB]₀ = 1, [ST]₀ = 0, [DT]₀ = 0, and [VB]₀ = -1. [VB]₀ was shifted to -1 in order to match the experiment and make comparisons with

experiment more direct. From the solutions to the system of equations, the population of each state as a function of time could be generated.

From this, it becomes possible to obtain a graphical representation of the population increase and subsequent depopulation of each of the states as shown below in Figure S1. As can be seen in the figure, the CB population curve behaves as an exponential decay. As the CB population decays, the ST population increases. Subsequent to the ST population increase, the charge carriers relax into the DT, represented by a simultaneous decrease in ST population and increase in DT population. Finally, as the DT population decreases, the VB population increases. The initial concentration values were chosen to match the experimental conditions. It is assumed that the initial photoexcitation is instantaneous, resulting in a [CB] of 1. Also assumed is that there is no population of charge carriers occupying the ST or DT, which is why those values were taken to be 0 initially. Finally, the net result of the initial photoexcitation is the complete depopulation of the VB, resulting in an initial population concentration of -1.

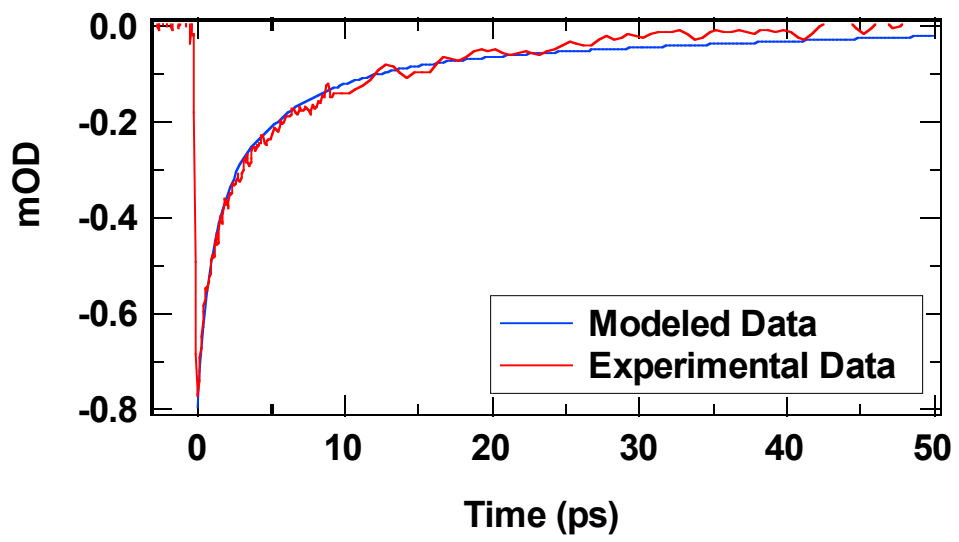
Figure 6. Populations of individual states as a function of time.



In TA measurement, the probe pulse could be interrogating more than one state at a given time, which is actually expected due to the relative high density of states in semiconductor nanostructures like SiNWs. To account for this fact, we need to mix signals from the different states in the kinetic model in order to generate curves or modeled data that can be more realistically compared to the experimental data. The percentage of contribution from each state is varied iteratively until the “data” generated from the model matches that of the experiment.

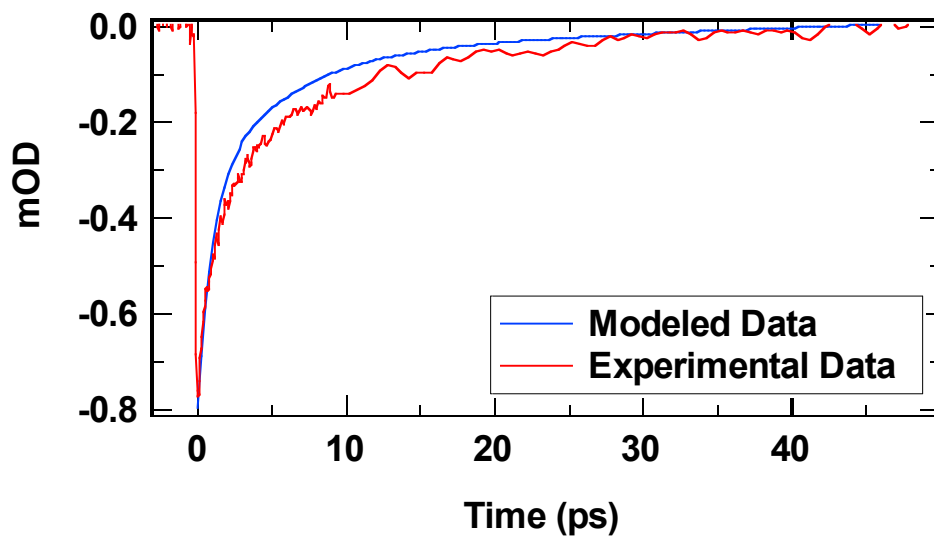
For example, after several iterations, we found that combining 30% from the CB and VB each, and 20% from the ST and DT each, a curve could be generated that best fit the observed low-excitation intensity data, as shown in Figure S2. We chose the low intensity data to compare to avoid the need to deal with the second-order non-linear exciton-exciton annihilation process that occurs at high excitation intensities, which is not included in the simple kinetic model we proposed here. The second-order process at high excitation intensity could be modeled but would require modification of the model to include an additional kinetic process. When we fit the modeled data mathematically as we did for the experimental data, we obtained time constants of 0.48 ps, 6.4 ps, and 83 ps, which are very similar to the apparent time constants obtained from fitting the experimental data as shown in the Results section of the main text.

Figure 7. Experimental data vs. modeled data using a 30/30/20/20 split between the CB, VB, ST, and DT states, respectively.



To demonstrate that the modeled data indeed sensitively depends on the percentage contribution from each state involved, we changed the percentage contributions from the CB, VB, ST, and DT from 30, 30, 20, and 20%, respectively to 40, 40, 10, and 10%, respectively, and we can easily see that the modeled data no longer matches the experimental data, as shown in Figure S3. In this particular case, the contribution from the CB and VB are increased while the ST and DT contributions are diminished. This manifests as an overall faster decay in short time periods as well as decreased signal intensity, when compared to the experimental data, in the 2-30 ps range. This exercise helps prove that the percentage contributions from each state can have drastic effects in helping the modeled data closely match the experimental data, and that the percentage contribution parameters play an important role in the model.

Figure 8. Experimental data *vs.* modeled data using a 40/40/10/10 split between the CB, VB, ST, and DT, respectively.



From the final rate constants determined by comparing the modeled data with the experimental data, we obtained an estimate of the time constants for the several important physical processes shown in Figure 5. For example, the time constant of relaxation from CB to ST is 0.5 ps while the time constant for the relaxation from the ST to the DT is 4 ps. Other related time constants can also be simply obtained by taking reciprocal of the corresponding rate constant, due to the assumption of first-order process. While these time constants may not be unique due to the many modeling parameters involved and assumptions made, we believe that they do provide some reasonable estimates of the most important physical processes involved in the charge carrier dynamics in SiNWs. The model is general and can be applied to other systems with changes in rate or time constants.

9.9 Supporting Information References

(1) Brelle, M. C.; Zhang, J. Z. *The Journal of Chemical Physics* Femtosecond study of photo-induced electron dynamics in AgI and core/shell structured AgI/Ag₂S and AgBr/Ag₂S colloidal nanoparticles. **1998**, *108*, 3119-3126.

(2) Brelle, M. C.; Torres-Martinez, C. L.; McNulty, J. C.; Mehra, R. K.; Zhang, J. Z. *Pure Appl. Chem.* Synthesis and characterization of Cu_xS nanoparticles. Nature of the infrared band and charge-carrier dynamics. **2000**, *72*, 101-117.

- (3) Trojánek, F.; Neudert, K.; Malý, P.; Dohnalová, K.; Pelant, I. *J. Appl. Phys* Ultrafast photoluminescence in silicon nanocrystals studied by femtosecond up-conversion technique. **2006**, *99*, 116108.
- (4) Kuntermann, V.; Cimpean, C.; Brehm, G.; Sauer, G.; Kryschi, C.; Wiggers, H. *Physical Review B* Femtosecond transient absorption spectroscopy of silanized silicon quantum dots. **2008**, *77*, 115343.
- (5) Cimpean, C.; Groenewegen, V.; Kuntermann, V.; Sommer, A.; Kryschi, C. *Laser & Photonics Reviews* Ultrafast exciton relaxation dynamics in silicon quantum dots. **2009**, *3*, 138.
- (6) Owrutsky, J. C.; Rice, J. K.; Guha, S.; Steiner, P.; Lang, W. *Applied Physics Letters* Ultrafast absorption in free-standing porous silicon films. **1995**, *67*, 1966-1968.

CHAPTER 10. Ultrafast Exciton Relaxation Dynamics of PbS and Core/Shell PbS/CdS Quantum Dots

10.1 Abstract

Optical properties and ultrafast exciton relaxation dynamics in PbS and core/shell PbS/CdS quantum dots (QDs) have been studied using UV-Vis absorption and fluorescence spectroscopy as well as femtosecond (fs) transient absorption spectroscopy. The electronic absorption spectrum of PbS QDs features broad absorption in the entire near IR-Vis-UV region with monotonic increase in intensity towards shorter wavelength. Relative to PbS, the absorption of the core/shell PbS/CdS QDs shows a slight blue shift in the 600-800 nm region, due to the decrease of the PbS crystal size caused by the synthetic process of the core/shell structure, and increased absorption near 400 nm due to the CdS shell. The PL of the PbS/CdS QDs was ~ 2.6 times more intense than that of the PbS QDs, due to surface passivation of PbS by CdS, and blue-shift, attributable to smaller PbS size and thereby stronger quantum confinement in the core/shell QDs. Fs transient absorption measurements of both systems showed a strong transient absorption feature from 600 to 750 nm following excitation at 750 nm. The transient absorption decays can be fit to a biexponential with time constants of 8 ps and 100 ps for PbS and 6 and 80 ps for PbS/CdS. The amplitude and lifetime of the fast component were excitation intensity dependent, with the amplitude increasing more than linearly with

increasing excitation intensity and the lifetime decreasing with increasing intensity. The fast decay is attributed to exciton-exciton annihilation and it occurs more readily for the PbS/CdS than the PbS QDs, which is attributed to a lower density of trap states in the core/shell QDs, as supported by their stronger PL.

10.2 Introduction

Near-infrared (NIR) emitting quantum dots (QDs) have been an area of intense research due to their potential applications in biological labeling¹ and solar energy harvesting^{2,3}. The NIR emission of the QDs allows for the emission to pass through biological tissues and thereby is beneficial for *in vivo* imaging^{4,5}. The small bandgap of these materials is also attractive for sensitizing larger bandgap semiconductors to the NIR component of solar light in photovoltaic applications⁶. The large Bohr radii of the lead chalcogenides⁷ (PbS, PbSe, and PbTe) make these materials especially attractive among the NIR-emitting QDs because the emission is tunable⁸ at a relatively large particle size.

Although lead chalcogenide QDs have many attractive properties, they suffer from very low quantum yield (QY) due to charge carrier trapping at the QD surface⁹. In order to remedy this issue, the QDs must be modified by covering the surface with organic capping ligands or by adding an inorganic shell. There are two categories of inorganic shells that are appropriate for different applications. Type I core/shell QDs consist of a smaller bandgap core surrounded by a larger bandgap shell where the

conduction band of the shell is of higher energy than that of the core and the valence band of the shell is of lower energy than that of the core¹⁰. Type I QDs are ideal for labeling applications where the electron-hole pair is confined to the core where it cannot interact with the surroundings.

Type II core/shell QDs consist of a smaller bandgap core material and a larger bandgap shell material where both the conduction and valence bands of the shell should be higher or lower than those of the core¹¹. In this Type II configuration, electron-hole pairs are generated in the core of the nanocrystal but only one of the charge carriers (either the electron or the hole) is confined to the core; the other is able to move into the shell material. Whether Type I or Type II, an inorganic shell passivates the nanocrystal surface and protects it from the surroundings¹².

One of the most powerful techniques for studying the electronic properties and exciton dynamics of QDs is ultrafast pump-probe spectroscopy¹³⁻¹⁶. Earlier studies investigated how properties such as size¹⁷, surface passivation¹⁸, and pump intensity¹⁹ affect the exciton and charge carrier lifetime of QDs²⁰. Recent studies have investigated more complex nanostructures such as one dimensional structures and core/shell quantum dots to determine how the exciton lifetime many depend on the structural properties²¹.

In this study, we investigate the power-dependent ultrafast exciton dynamics in PbS and PbS/CdS core/shell QDs to determine how the CdS passivation of the PbS core material affects the exciton lifetime. Previous studies have shown that the exciton lifetime in PbS is mostly independent of size and is dominated by charge

carrier trapping^{20,22}. The present study of core/shell PbS/CdS QDs has shown that the improved surface passivation from the CdS shell decreases the density of trap states and lowers the threshold for observing exciton-exciton annihilation or shortens the apparent observed exciton lifetime because the trap states are more easily saturated.

10.3 Experimental

10.3.1 Synthesis of Quantum Dots

10.3.1.1 Synthesis of PbS Quantum Dots

PbS QDs were synthesized by using oleylamine (OLA) as a ligand as previously reported^{9,23}. Typically, PbCl₂ (3.6 mmol) in OLA (2.4 mL) and sulfur (0.36 mmol) in OLA (0.24 mL) were purged, respectively, by N₂ at room temperature for 30 min. The PbCl₂-OLA suspension was heated to 160 °C and kept at this temperature for at least 1 hour. The homogeneous PbCl₂-OLA suspension was cooled to 120 °C under vacuum for 15 minutes. The flask was then reopened and the N₂ flux was restored. Sulfur in OLA at room temperature was quickly injected into the PbCl₂-OLA suspension under vigorous stirring. The reaction cell was quenched with cold water after the growth reaction proceeded at 100 °C for 10 minutes to obtain 5.2-nm PbS QDs. Alcohol was added (QDs solution:alcohol = 1:5 by volume), the suspension was centrifuged, and the supernatant was removed. The QDs were re-dissolved in hexane. This process was repeated twice. The QDs were finally redissolved in toluene.

10.3.1.2 Synthesis of PbS/CdS quantum dots

PbS/CdS QDs were synthesized *via* a cation exchange method, reported previously^{24,25}. Typically, CdO (2.3 mmol), oleic acid (OA, 2 mL), and phenyl ether (10 mL) were heated to 255 °C under N₂ for 20 minutes. The clear solution was cooled to 155 °C under vacuum for 15 minutes. The flask was subsequently reopened and the N₂ flux was restored. PbS QDs suspended in toluene (1 mL, optical density of 3.0) were diluted in 10 mL toluene, bubbled with N₂ for 30 minutes and then heated to 100 °C immediately. The Cd/OA mixture was subsequently injected. The reaction cell was quenched with cold water after the growth reaction was conducted at 100 °C for 4 hours. Alcohol was added, the suspension was centrifuged, and the supernatant was removed. QDs were re-dissolved in hexane. This process was repeated for two times. The final QDs were re-dissolved in toluene.

10.3.2 UV-Vis, Photoluminescence, Electron Microscopy, and ICP-OES Measurements

UV-Vis spectra of the as-prepared samples of PbS and PbS/CdS in toluene were collected using an HP 8452A diode array spectrophotometer with spectral resolution set at 2 nm. PbS and PbS/CdS QDs were characterized by transmission electron microscopy (TEM) using a JEOL 2100F microscope. Particle sizes were measured using imageJ²⁶. The Pb/Cd ratio was measured by using inductively coupled plasma optical emission spectroscopy on a Perkin Elmer Model Optima 7300 DV. PL

spectra were collected on a Fluorolog-3 (Horiba Jobin Yvon) system using an excitation wavelength of 674 nm.

10.3.3 Femtosecond Laser and Transient Absorption

Femtosecond pump-probe relaxation dynamics were collected on a system described previously²⁷. In all experiments, a pump wavelength of 750 nm was used with an output pulse duration of <150 fs and pump energies of 100, 125, and 200 nJ/pulse along with a white light continuum probe pulse. Peak power was varied by usage of absorptive neutral density filters. The optical density of the colloidal solutions at 750 nm during laser experiments was 1.0.

10.4 Results

Figure 1 shows representative TEM images of the monodisperse PbS and core/shell PbS/CdS QDs. The PbS QDs have an average diameter of 5.2 nm with a polydispersity of ~7.5%, while the PbS/CdS QDs have a core PbS diameter of 3.8 nm with a CdS shell of 0.7 nm in thickness, therefore a total diameter of 5.2 nm. The overall polydispersity of the PbS/CdS QDs is ~4.3%. The PbS QDs have 36.8% more surface area than the PbS cores in the PbS/CdS QDs assuming spherical shape. The scale bars are 20 nm.

Figure 1. TEM image of PbS (top) and PbS/CdS (bottom) QDs.

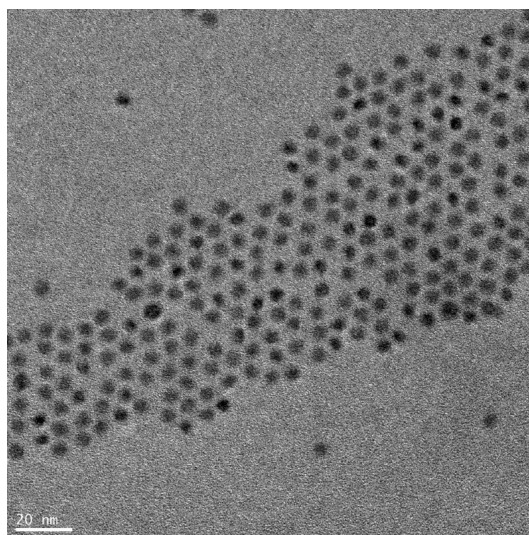
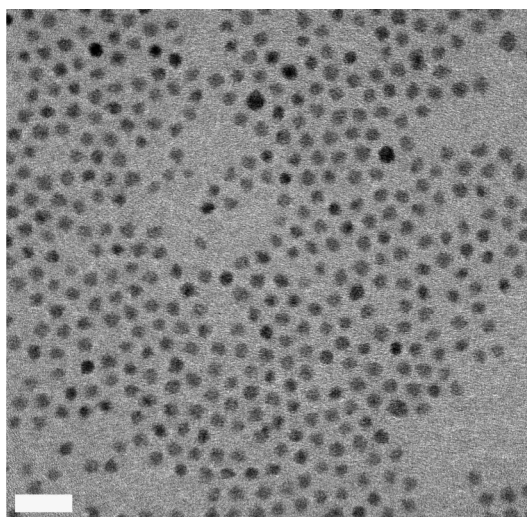


Figure 2 displays the UV-Vis spectra of as-prepared PbS and PbS/CdS QDs in solution. The absorption spectra feature no obvious excitonic peak in the near UV and visible regions spanning 300–800 nm except for a shoulder at ~600 nm. Additionally, the increased absorption due to the CdS is noticeable in the PbS/CdS spectrum and manifests as a red-shift at the spectral region of ~400 nm²⁸. The spectra of the PbS and PbS/CdS QDs match well with previously reported spectra^{22,25} and show a long absorption tail persisting beyond 600 nm attributed to the direct bandgap of PbS. Excitonic peaks at 1300 nm along with a corresponding fluorescence peak at 1350 nm have been reported previously²⁹. Because of this, the first excitonic absorption peak might occur at wavelengths too red for our detection. Thus, the shoulder at 600 nm could be due to higher energy excitons. In the 600-800 nm region, the absorption for PbS/CdS is slightly lower than that of PbS, likely due to decrease of the PbS core size in PbS/CdS in comparison to the parent PbS QDs.

Figure 2. UV-Vis absorption spectra of PbS (red curve) and PbS/CdS (blue curve) nanoparticles.

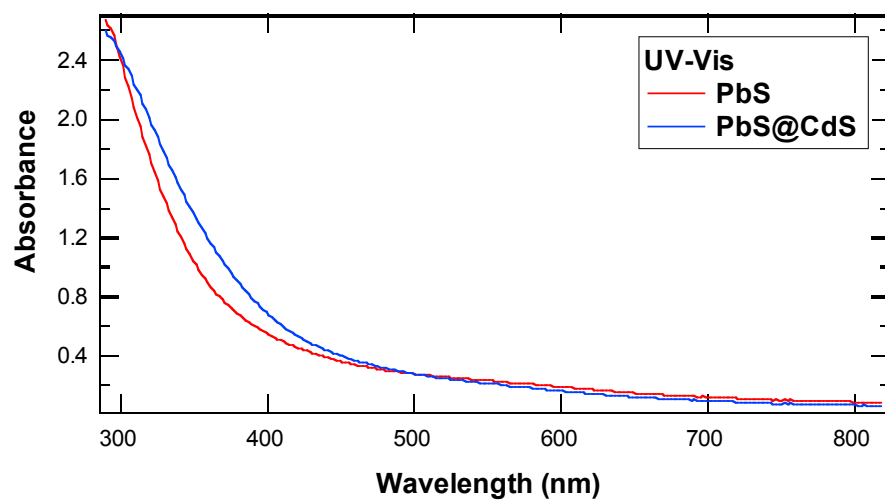


Figure 3 shows the PL spectra of both the PbS and PbS/CdS QDs which display NIR emission with the PL peaks centered at 1428 and 1315 nm, respectively. The PbS/CdS spectrum has PL that is ~ 2.6 times more intense than the PbS QDs. The PbS/CdS spectrum also has a tail extending to the red which is assigned to a minority of particles with little or no CdS shell. The blue-shift of the PbS/CdS PL relative to that of the PbS is easily explainable since the PbS core in the core/shell QDs is smaller and hence more quantum confined than the parent PbS QDs.

Figure 3. PL spectra of PbS (red curve) and PbS/CdS (blue curve) QDs.

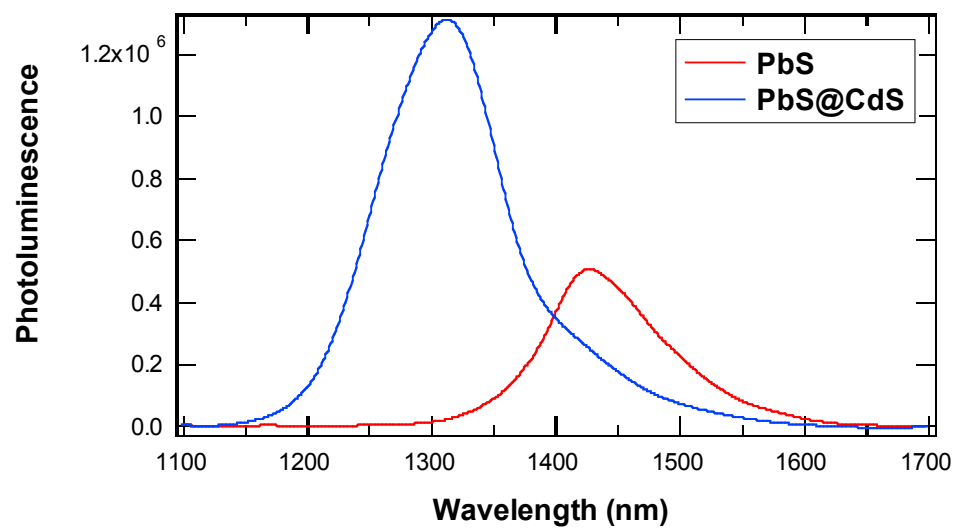


Figure 4 is a plot of the transient time decay profiles (in ps) for the PbS and PbS/CdS QDs following an excitation wavelength of 750 nm (maintained at a pulse energy of 100 nJ/pulse) and a probe wavelength of 600 nm. The lifetime of the transient absorption feature was independent of the probe wavelength in the range of 600-750 nm and was fit to decays of 8 and 100 ps versus 6 and 80 ps for the PbS and PbS/CdS QDs, respectively. Figures 5 a and b are three-dimensional plots of the PbS and PbS/CdS relaxation profiles. A pulse-width-limited (<150 fs) rise followed by an exponential fast decay (~7 ps) and another slower exponential decay can be seen and illustrates the probe wavelength-independence of the transient absorption kinetic decay processes across part of the visible spectrum as well as the overall faster decay for the PbS/CdS QDs compared to the PbS QDs.

Figure 4. Transient absorption relaxation traces of PbS (red curve) and PbS/CdS (blue curve) at a probe wavelength of 600 nm following a 750 nm, 200 nJ/pulse pump.

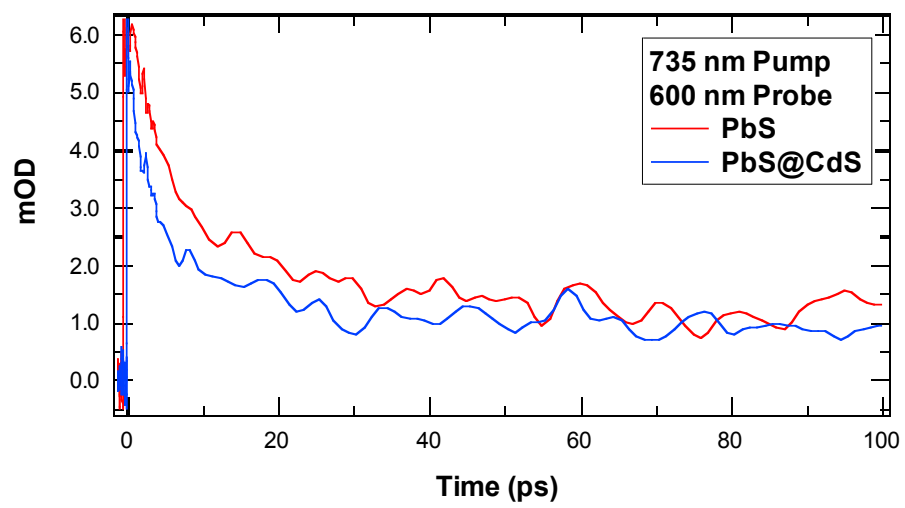
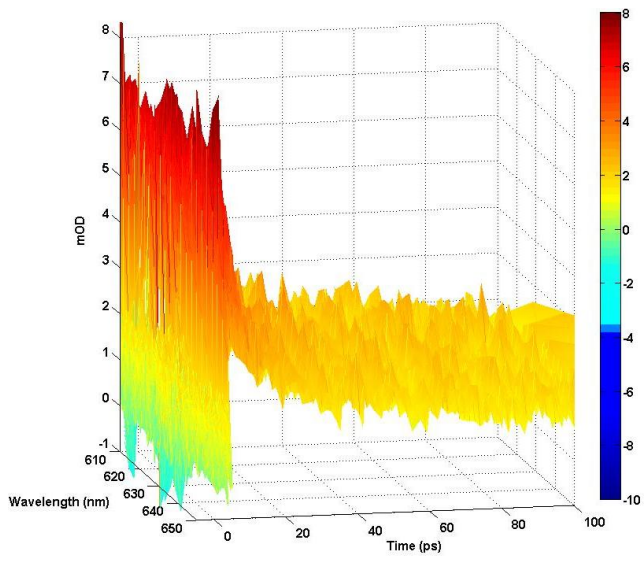
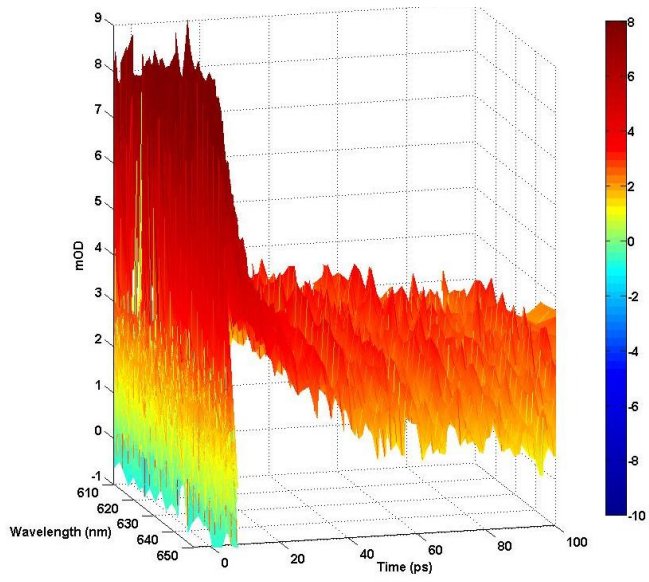
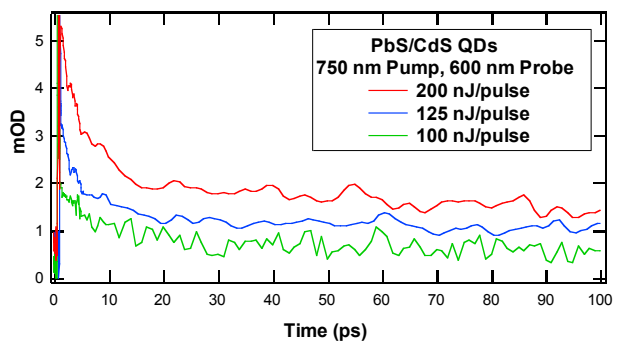
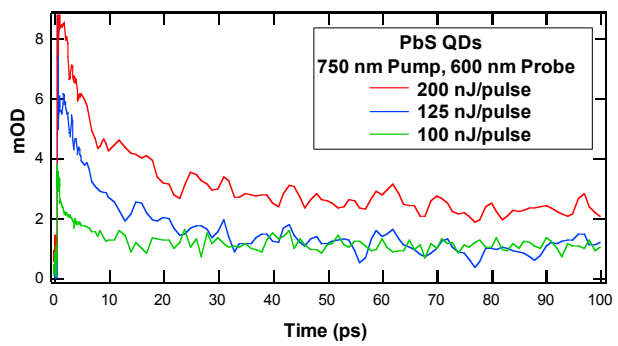


Figure 5. Three-dimensional plots of the transient absorption decay profiles of PbS QDs (top) and PbS/CdS QDs (bottom).



Figures 6a and b are plots of the power-dependent relaxation dynamics of the PbS and PbS/CdS QDs, each observed at three pump powers: 100, 125, and 200 nJ/pulse with a pump of 750 nm and a probe of 600 nm. For the range of pump powers, the PbS QDs exhibited a fast decay of 8, 10, and 14 ps, respectively. In comparison, the PbS/CdS QDs had a fast decay of 6, 8, and 13 ps. In both cases, the amplitude of the fast component was found to increase more than linearly with increasing pump power. Due to the low signal-to-noise ratio for the overall transient signal, the lifetimes of both the fast and slow components have error of about $\pm 10\%$. For the same excitation intensity, the PbS/CdS QDs with a PbS core smaller than the parent PbS shows a faster fast decay.

Figure 6. Transient absorption decay profiles for three different pump powers for the PbS (top) and PbS/CdS QDs (bottom).



10.5 Discussion

Assignment of the transition and the species being probed (*e.g.* electron, hole, or exciton) is non-trivial. However, because our pump wavelength is more energetic than the bandgap, we are not pumping the bandedge. In other words, the origin of the signal is from higher excited states. Although the electron has kinetic energy in excess of what is needed for pumping at the bandedge, direct discernment of the transition is not clear. Previous work has shown that the visible region has contributions from both the electron and hole³⁰, while other studies have concluded that the exciton is the species being probed^{19,31}. Given the confinement in space, the delocalized nature of the conduction and valence bands, and the short time scale, we believe that the species being probed is the exciton. As time evolves and the electron and hole become trapped, the bands become more localized and the spectra of both the electron and hole can evolve to identify more clearly which species is monitored. This assignment of probing the exciton is further supported since the following discussion on exciton-exciton annihilation indicates that excitons are interacting within the same spatial region

In this study, we compared two QD samples: 5.2 nm diameter PbS *vs.* 5.2 nm diameter core/shell PbS/CdS QDs where the Pb²⁺ ions in the outer 0.7 nm of the particles have been exchanged with Cd²⁺ ions. When taking into consideration the photon flux per second of the laser system, the optical density (*i.e.*, concentration) of the QDs, radius, and path length of the cell, the PbS QDs were exposed to, on average, ~3 times more photons per QD.

The time constants of the PbS fit to a biexponential decay profile and generally agree well with previously reported values for PbS²². In comparison to the PbS QDs, the PbS/CdS QDs show a faster decay under the same excitation intensity. Although the PbS QDs have a diameter of 5.2 nm while the PbS core crystals in the PbS/CdS QDs have a diameter of 3.8 nm (0.7 nm CdS shell, hence 5.2 nm in overall diameter), the difference in time constants is likely not due to a size-dependence, since previous reports²² indicate that the decay profiles of PbS have no dependence on the size of the PbS colloid. Because of this, the decay profiles are likely dominated by surface states or trap states.

A factor related to the trap states involves the surface chemistry of the PbS QDs and the effect of the CdS shell. At the surface of the PbS QDs, dangling bonds introduce electronic states within the bandgap where electrons or holes can be trapped. The PbS QDs were capped with OLA which are bound to these surface atoms and can reduce surface states within the bandgap and enhance band edge recombination. However, it is practically very difficult to achieve complete ligand coverage in a QD system because of the dynamic binding of the ligands and more effective surface passivation is achieved through the cation exchange used to produce the PbS/CdS QDs. The PL of the two QD systems provides evidence of improved surface passivation in the PbS/CdS samples. Figure 2 shows that the PbS/CdS QDs have a PL intensity 2.6 times higher than the PbS QDs. Enhancement of PL as well as the ratio of bandedge over trap state emission is known to arise from controlling the surface by removing surface trap states^{19,32,33}. The fewer trap states in the

PbS/CdS will result in saturation of the trap states at lower pump power for the PbS/CdS QDs compared to the PbS QDs (for the same optical density, *i.e.*, concentration). In other words, a stronger nonlinear effect, usually reflected as a faster decay due to exciton-exciton annihilation, is expected in the core/shell PbS/CdS QDs than in PbS for the same or similar excitation intensity. In the exciton-exciton annihilation model, high excitation intensity for the pump pulse produces multiple excitons per particle that can interact and annihilate, resulting in one exciton excited and another one deexcited. If the rate of trapping is higher than the rate of exciton-exciton annihilation, trapping can reduce the probability of exciton-exciton annihilation. However, if the trap states become saturated, exciton-exciton annihilation can occur. Thus, while the PbS QDs are exposed to more photons per QD that should lead to a faster decay or stronger non-linear effect, the core/shell PbS/CdS QDs actually exhibit a faster decay and stronger non-linear effect apparently due to the lower density of trap states. That is, the surface effect seems to dominate the size effect in comparison between PbS and PbS/CdS, which is similar to previous observations[22].

Recently, there have been several studies suggesting multiple exciton generation (MEG) by a single photon when the photon energy exceeds the bandgap energy of a semiconductor QD by at least a factor of two, especially in small bandgap semiconductors such as silicon nanocrystals and the lead chalcogenides³⁴⁻³⁹. In our present study, even though our excitation energy is more than twice the bandgap energy of PbS, we observe no specific indication of MEG by a single photon. The

exciton-exciton annihilation we report here is clearly due to multiple photons based on the non-linear power dependence.

10.6 Conclusion

We have investigated the ultrafast exciton dynamics in both PbS and core/shell PbS/CdS QDs with emphasis on understanding the effect of the CdS shell. For both systems, a broad transient absorption feature was observed from 600 to 750 nm following an excitation at 750 nm. The transient absorption decays exhibit a biexponential decay, with a fast time constant of 8 ps for the PbS and 6 ps for the PbS/CdS, respectively. In conjunction with PL spectroscopy, the relatively faster decay of PbS/CdS was attributed to the decreased density of trap states as a result of surface passivation by CdS. By having a lower density of trap states, the trap states in the PbS/CdS QDs were more readily saturated, thus leading to a lower threshold for exciton-exciton annihilation and a faster decay profile. A power-dependent study showed that the PbS/CdS QDs had a consistently faster decay than the PbS QDs across a range of pump powers investigated herein, further supporting the above explanation. The surface effect seems to dominate over the size effect on the exciton dynamics in these two QD systems studied. Understanding the exciton dynamics has important implications in light energy conversion and other optical applications of semiconductor QDs.

10.7 References

1. Sun J, Zhu MQ, Fu K, Lewinski N, Drezek RA. Lead sulfide near-infrared quantum dot bioconjugates for targeted molecular imaging. *International Journal of Nanomedicine*, 2007, 2: 235-240.
2. Watt AAR, Blake D, Warner JH, Thomsen EA, Tavenner EL, Rubinsztein-Dunlop H, Meredith P. Lead sulfide nanocrystal: conducting polymer solar cells. *Journal of Physics D: Applied Physics*, 2005, 38: 2006-2011.
3. Plass R, Pelet S, Krueger J, Grätzel M, Bach U. Quantum dot sensitization of organic-inorganic hybrid solar cells. *The Journal of Physical Chemistry B*, 2002, 106: 7578-7580.
4. Ntziachristos V, Bremer C, Weissleder R. Fluorescence imaging with near-infrared light: new technological advances that enable in vivo molecular imaging. *European radiology*, 2003, 13: 195-208.
5. Walling M, Novak J, Shepard JRE. Quantum Dots for Live Cell and In Vivo Imaging. *International Journal of Molecular Sciences*, 2009, 10: 441-491.
6. Kamat PV. Quantum Dot Solar Cells. Semiconductor Nanocrystals as Light Harvesters. *The Journal of Physical Chemistry C*, 2008, 112: 18737-18753.
7. Wise FW. Lead Salt Quantum Dots: the Limit of Strong Quantum Confinement. *Accounts of Chemical Research*, 2000, 33: 773-780.
8. Kellermann K, Alchalabi K, Zimin D, Zogg H. Tunable optically pumped lead-chalcogenide mid-infrared emitters on Si-substrates. *Spectrochimica Acta Part A: Molecular and Biomolecular Spectroscopy*, 2004, 60: 3341-3344.

9. Zhao H, Chaker M, Ma D. Bimodal Photoluminescence during the Growth of PbS Quantum Dots. *The Journal of Physical Chemistry C*, 2009, 113: 6497-6504.
10. Tytus M, Krasnyj, J, Jacak W, Chuchmala A, Donderowicz, W, Jacak L. Differences between photoluminescence spectra of type-I and type-II quantum dots. *Journal of Physics: Conference Series*, 2008, 104: 012011-012014.
11. Kim S, Fisher B, Eisler H-Jr, Bawendi M. Type-II Quantum Dots: CdTe/CdSe(Core/Shell) and CdSe/ZnTe(Core/Shell) Heterostructures. *Journal of the American Chemical Society*, 2003, 125: 11466-11467.
12. Fernee MJ, Watt A, Warner J, Heckenberg, N, Rubinsztein-Dunlop H. Evidence for energy relaxation via a radiative cascade in surface-passivated PbS quantum dots. *Nanotechnology*, 2004, 15: 1328-1331.
13. Rawalekar S, Kaniyankandy S, Verma S, Ghosh HN. Ultrafast Charge Carrier Relaxation and Charge Transfer Dynamics of CdTe/CdS Core-Shell Quantum Dots as Studied by Femtosecond Transient Absorption Spectroscopy. *The Journal of Physical Chemistry C*, 2009, 114: 1460-1466.
14. Francesco M, Iwan M, Zeger H, Wolfgang L, Paola B. Ultrafast Exciton Dephasing in PbS Colloidal Quantum Dots. CLEO/Europe and EQEC 2011 Conference Digest, Vol.: Optical Society of America:EI3_2.
15. Nevou L, Mangeney J, Tchernycheva M, Julien FH, Guillot F, Monroy E. Ultrafast relaxation and optical saturation of intraband absorption of GaN/AlN quantum dots. *Appl Phys Lett*, 2009, 94: 132104-132107.

16. Gero N, Lazaro AP, Scott W, David JH, Eric WVS, Larissa L, Vlad S, Edward HS. Evidence of Symmetry Breaking and Carrier Dynamics in Lead Salt Quantum Dots. Conference on Lasers and Electro-Optics/International Quantum Electronics Conference, Vol.: Optical Society of America, 2009:ITuL4.
17. de Mello D, C., Bode M, Meijerink A. Size- and temperature-dependence of exciton lifetimes in CdSe quantum dots. *Physical Review B*, 2006, 74: 085320-085328.
18. Morello G, Anni M, Cozzoli P, Manna L, Cingolani R, De Giorgi M. The Role of Intrinsic and Surface States on the Emission Properties of Colloidal CdSe and CdSe/ZnS Quantum Dots. *Nanoscale Research Letters*, 2007, 2: 512 - 514.
19. Roberti T, Cherepy N, Zhang J. TI - Nature of the power-dependent ultrafast relaxation process of photoexcited charge carriers in II-VI semiconductor quantum dots: Effects of particle size, surface, and electronic structure. *J Chem Phys*, 1998, 108: 2143-2151.
20. Patel AA, Wu F, Zhang JZ, Torres-Martinez CL, Mehra RK, Yang Y, Risbud SH. Synthesis, Optical Spectroscopy and Ultrafast Electron Dynamics of PbS Nanoparticles with Different Surface Capping. *The Journal of Physical Chemistry B*, 2000, 104: 11598-11605.
21. Cretí A, Anni M, Rossi MZ, Lanzani G, Leo G, Della Sala F, Manna L, Lomascolo M. Ultrafast carrier dynamics in core and core/shell CdSe

- quantum rods: Role of the surface and interface defects. *Physical Review B*, 2005, 72: 125346-125355.
22. Wu F, Yu JH, Joo J, Hyeon T, Zhang JZ. Ultrafast electronic dynamics of monodisperse PbS and CdS nanoparticles/nanorods: Effects of size on nonlinear relaxation. *Optical Materials*, 2007, 29: 858-866.
 23. Cademartiri L, Bertolotti J, Sapienza R, Wiersma DS, von Freymann G, Ozin GA. Multigram Scale, Solventless, and Diffusion-Controlled Route to Highly Monodisperse PbS Nanocrystals. *The Journal of Physical Chemistry B*, 2005, 110: 671-673.
 24. Pietryga JM, Werder DJ, Williams DJ, Casson JL, Schaller RD, Klimov VI, Hollingsworth JA. Utilizing the Lability of Lead Selenide to Produce Heterostructured Nanocrystals with Bright, Stable Infrared Emission. *Journal of the American Chemical Society*, 2008, 130: 4879-4885.
 25. Zhao H, Chaker M, Wu N, Ma D. Towards controlled synthesis and better understanding of highly luminescent PbS/CdS core/shell quantum dots. *Journal of Materials Chemistry*, 2011, 21: 8898-8904.
 26. Newhouse RJ, Wang H, Hensel JK, Wheeler DA, Zou S, Zhang JZ. Coherent Vibrational Oscillations of Hollow Gold Nanospheres. *The Journal of Physical Chemistry Letters*, 2011, 2: 228-235.
 27. Rasband WS. imageJ. *imageJ*, 1997-2009: U.S. National Institute of Health, Bethesda, Maryland, USA, <http://rsb.info.nih.gov/ij/>.

28. Ramanathan S, Bandyopadhyay S, Edwards JD, Nelson J, Anderson J. Exciton binding energy in semiconductor nanowires in the presence of dielectric deconfinement. *Nanotechnology*, 2006 IEEE-NANO 2006 Sixth IEEE Conference on, Vol. 1, 2006:110-112.
29. Hines MA, Scholes GD. Colloidal PbS Nanocrystals with Size-Tunable Near-Infrared Emission: Observation of Post-Synthesis Self-Narrowing of the Particle Size Distribution. *Advanced Materials*, 2003, 15: 1844-1849.
30. Spanhel L, Haase M, Weller H, Henglein A. Photochemistry of colloidal semiconductors. 20. Surface modification and stability of strong luminescing CdS particles. *Journal of the American Chemical Society*, 1987, 109: 5649-5655.
31. Gao M, Kirstein S, Mohwald H. Strongly Photoluminescent CdTe Nanocrystals by Proper Surface Modification. *The Journal of Physical Chemistry B*, 1998, 102: 8360-8363.
32. Beard MC, Knutsen KP, Yu P, Luther JM, Song Q, Metzger WK, Ellingson, RJ, Nozik, AJ. Multiple Exciton Generation in Colloidal Silicon Nanocrystals. *Nano Letters*, 2007, 7: 2506-2512.
33. Luther JM, Beard MC, Song Q, Law M, Ellingson RJ, Nozik AJ. Multiple Exciton Generation in Films of Electronically Coupled PbSe Quantum Dots. *Nano Letters*, 2007, 7: 1779-1784.

34. Luque A, Marti A, Nozik AJ. Solar Cells Based on Quantum Dots: Multiple Exciton Generation and Intermediate Bands. *MRS Bulletin*, 2007, 32: 236-241.
35. Allan G, Delerue C. Role of impact ionization in multiple exciton generation in PbSe nanocrystals. *Physical Review B*, 2006, 73: 205423-205427.
36. Murphy JE, Beard MC, Norman AG, Ahrenkiel SP, Johnson JC, Yu P, Micic, OI, Ellingson, RJ, Nozik, AJ. PbTe Colloidal Nanocrystals: Synthesis, Characterization, and Multiple Exciton Generation. *Journal of the American Chemical Society*, 2006, 128: 3241-3247.
37. Ellingson RJ, Beard MC, Johnson JC, Yu P, Micic OI, Nozik AJ, Shabaev, A, Efros, AL. Highly Efficient Multiple Exciton Generation in Colloidal PbSe and PbS Quantum Dots. *Nano Letters*, 2005, 5: 865-871.
38. Klimov VI. Mechanisms for Photogeneration and Recombination of Multiexcitons in Semiconductor Nanocrystals: Implications for Lasing and Solar Energy Conversion. *The Journal of Physical Chemistry B*, 2006, 110: 16827-16845.